

**A THEORETICAL AND
EXPERIMENTAL INVESTIGATION
OF PRESSURE SOLUTION**

by

Owen J. Steele ©

Submitted in partial fulfillment of the
requirements for the degree of

Master of Science

December 1988

Department of Geology
Lakehead University
Thunder Bay, Ontario, Canada

ProQuest Number: 10611783

All rights reserved

INFORMATION TO ALL USERS

The quality of this reproduction is dependent upon the quality of the copy submitted.

In the unlikely event that the author did not send a complete manuscript and there are missing pages, these will be noted. Also, if material had to be removed, a note will indicate the deletion.



ProQuest 10611783

Published by ProQuest LLC (2017). Copyright of the Dissertation is held by the Author.

All rights reserved.

This work is protected against unauthorized copying under Title 17, United States Code
Microform Edition © ProQuest LLC.

ProQuest LLC.
789 East Eisenhower Parkway
P.O. Box 1346
Ann Arbor, MI 48106 - 1346

Permission has been granted to the National Library of Canada to microfilm this thesis and to lend or sell copies of the film.

The author (copyright owner) has reserved other publication rights, and neither the thesis nor extensive extracts from it may be printed or otherwise reproduced without his/her written permission.

L'autorisation a été accordée à la Bibliothèque nationale du Canada de microfilmer cette thèse et de prêter ou de vendre des exemplaires du film.

L'auteur (titulaire du droit d'auteur) se réserve les autres droits de publication; ni la thèse ni de longs extraits de celle-ci ne doivent être imprimés ou autrement reproduits sans son autorisation écrite.

ISBN 0-315-51233-4

ABSTRACT

Consideration of the existing thermodynamic theory of pressure solution (PS) shows that this theory is applicable to the development of PS structures as well as to local grain-scale diffusive transfer. Local precipitation of pressure solved material ceases when pores are reduced to equilibrium size, if not before by kinetic considerations. Longer range diffusion may then occur if a site of non-equilibrium porosity is available. Such porosity may be generated by particulate flow or by hydraulic fracturing. Long range diffusion may also depend on greater ease of diffusion, as may occur along stylolites.

Measurement of PS strain rates was attempted by stress relaxation tests (SRTs) at room temperature of both Carrara marble and compacted aggregates of calcite and quartz sands. Neither material gave results indicative of PS although strain rates as low as $10^{-8.5} \text{ s}^{-1}$ were obtained. Work hardening during loading resulted in alternating increase and decrease of strain rate concomitant with steadily declining differential stress during the SRTs. The variation in strain rate, termed cycling, was interpreted to be the result of non-steady state flow during loading. Thermal expansion and contraction were shown to be the cause of pressure fluctuation in a long term quantitative experiment on PS begun during this study. Such expansion and

contraction should be avoided in quantitative studies, particularly at low strain rates.

ACKNOWLEDGEMENTS

Thanks are due to Dr. G. Borradaile for his suggestion of this experimental topic, and his guidance and criticism during the supervision of this experimental study. Financial support was provided by NSERC grant A6861 to Dr. Borradaile. I also wish to record my appreciation for the assistance and support of my co-supervisor, Dr. B. Kronberg, and the interest and criticism of Dr. P. Fralick. Technical support was ably provided in various capacities by A. Hammond, R. Viitala, T. Griffiths, A. MacKenzie, and A. Raitsakas. Finally, but not least, I wish to note my gratitude for the advice and moral support of family and friends, including my fellow graduate students here at Lakehead University.

CONTENTS

	<u>page</u>
Abstract	
Acknowledgements	
Contents	
1. INTRODUCTION	1
1.1 Deformation by Pressure Solution	1
1.2 Aim and Scope of the Thesis	3
2. THEORETICAL AND EXPERIMENTAL ASPECTS OF PRESSURE SOLUTION	6
2.1 Introduction	6
2.2 Natural Deformation	8
2.2.1 Deformation Mechanisms	9
2.2.2 Constitutive Equations and Flow Laws	16
2.2.3 Deformation Mechanism Maps	19
2.3 Theory of Pressure Solution	27
2.3.1 Phenomenological Models	27
2.3.2 Thermodynamics	36
2.3.3 Textural and Mineralogical Limitations on Pressure Solution	40
2.4 Dynamic Aspects of Pressure Solution	46
2.4.1 Qualitative Controls on Material Flux during Pressure Solution	46
2.4.2 Quantitative Controls on the Rate of Pressure Solution	49
2.4.3 Bulk Behavior During Pressure Solution	58
2.5 Previous Experimental Work	66

3. EXPERIMENTAL APPARATUS	74
3.1 Deformation Machines	74
3.2 Materials and Sample Preparation	77
4. STRESS RELAXATION TESTING AND PRESSURE SOLUTION	81
4.1 The Stress Relaxation Test	81
4.1.1 Theory	81
4.1.2 Application of the SRT	84
4.1.3 Limitations of the SRT	85
4.2 Stress Relaxation Tests on Carrara Marble	91
4.2.1 Introduction	91
4.2.2 Results of Deformation of Carrara marble	92
4.2.3 Discussion	108
4.3 Stress Relaxation Tests on Calcite-Quartz Aggregates	109
4.3.1 Introduction	109
4.3.2 Results of Deformation of CQA samples	110
4.3.3 Discussion	113
5. CONCLUSIONS	115
REFERENCES	121
APPENDICES	
Appendix A: Calculation of a deformation mechanism map for calcite	138
Appendix B: Treatment of SRT data	144
Appendix C: Dependence of T and P_c during the long-term hydrostatic test	150

CHAPTER 1: INTRODUCTION

1.1 Deformation by Pressure Solution

Pressure solution (PS) is an intergranular mechanism of deformation which is slow but capable of producing large strains over geological time. It can contribute significantly to deformation during the diagenesis and low-grade metamorphism of supracrustal rocks, and has been suggested to produce aseismic creep in fault zones (Rutter and Mainprice, 1978). PS is a form of diffusive mass transfer. It involves the dependent steps of dissolution, diffusion and precipitation, all three of which occur along grain boundaries. PS fabrics fall in one of two categories: dissolution-generated and precipitation-generated. Dissolution-generated fabrics include stylolites, which are narrow seams of insoluble material accumulated as more soluble material is dissolved and diffused away, and preferred dimensional orientation of grains. Precipitation-generated fabrics include grain overgrowths and pressure shadows.

Unlike the solid-state diffusive mass transfer mechanisms of Coble creep and Nabarro-Herring creep, PS operates in the presence of an adsorbed intergranular aqueous film (McClay, 1977). The nature of this film is incompletely known. It is thought to be

responsible for enhanced rates of intergranular diffusion. For example, Rutter (1976) has calculated a 2 nm film of water along a calcite grain boundary would raise the mass diffusion rate by ten to twelve orders of magnitude over that for solid-state grain boundary diffusion. The aqueous film is also generally thought to be responsible for greater (sometimes macroscopic) distances of diffusion than occur during solid-state diffusion. In some circumstances a film is capable of withstanding normal loads of 100 MPa (Rutter, 1983). Greater temperature and pressure (associated with higher metamorphic grade) may lead to deterioration of the film and consequently its capacity for diffusive transport. This will therefore be an influence on the conditions under which transition to other deformation mechanisms will occur.

The deformation which produces PS fabrics occurs in two ways. One form of deformation is strain, which is volume-conservative change of shape. Strain is produced by differential stress. Diffusion between grain contacts and adjacent pores is driven by the differential stress which exists at the edge of a contact, and also by a normal stress gradient which tends to exist along the surface of a contact. In addition, larger masses of rock may be subject to a bulk differential stress. Such a differential stress is manifested at the scale of individual grains by a correlation between normal stress across grain contacts and

contact orientation; as contacts approach perpendicularity to the bulk maximum principal stress, the normal stress on grain contacts will tend to be greater. The second form of deformation by PS is negative dilation. Dilation is a change in size which preserves shape. Individual grains undergoing PS will not undergo negative dilation although material may be redistributed. (This loss of spatial continuity is referred to as discontinuous strain.) Larger volumes of rock may undergo a negative dilation during PS. Bulk negative dilation occurs if dissolved material is precipitated in pores of the rock or transported outside the field of observation by diffusion or fluid flow. This negative dilation is a product of the strain of individual grains.

1.2 Aim and Scope of the Thesis

This investigation has been directed towards experimental production of PS fabrics, and determination of the conditions under which PS occurs. While much previously reported work was intended to produce deformation by PS, there has been little success (see section 2.5). Because previous experimental studies have been largely qualitative, a quantitative approach was chosen, and stress relaxation tests are a potentially suitable technique to

this end. These tests permit deformation at lower strain rates than is possible with conventional loading tests. A series of stress relaxation tests was performed for this thesis.

A second experimental approach, following the lead of de Boer (1975) and Gratier and Guiguet (1986), has been to perform a long-term test under approximately constant external hydrostatic pressure. This test will not provide any quantitative data on PS strain rates. Instead, it is hoped that convincing textural evidence of PS will be produced, thus indicating conditions under which the process may occur. The experimental procedure is similar to that of de Boer (1975). However, unlike the experiment of de Boer, twelve samples rather than one have been deformed and the sand being deformed is calcite rather than quartz. The greater number of samples has two advantages. It provides insurance against loss of a sample, e.g. resulting from failure of the jacket enclosing the sample. It also allows variation of sample composition, thus possibly indicating controls on PS. Results from the long term test are not discussed in this thesis with the exception of the effect of variation of ambient temperature on confining pressure.

The slow rate of PS was the most important consideration in design of both the long term test and the stress relaxation tests. Among the factors which affect PS strain rate, grain size is probably the strongest influence; if diffusion is the rate controlling process of PS, strain rate is proportional to the

reciprocal of the cube of grain size (Rutter, 1976). Consequently a fine grain size is advantageous for experimentation. The choice of material was also important. Calcite was selected because both theoretical and natural evidence indicates that calcite is more susceptible than quartz to PS (Kerrich, 1978). Clay was added to the long term samples because it is thought to aid diffusion. It is also possible to counter the effect of low strain rate by deforming a sample for a longer time. For this reason long term experiments are an attractive approach to qualitative investigation.

CHAPTER 2: THEORETICAL AND EXPERIMENTAL ASPECTS OF PRESSURE SOLUTION

2.1 Introduction

The literature on PS includes some debate on its definition. PS is generally understood to denote diffusive mass transfer driven through an adsorbed aqueous film by differential stress (McClay, 1977). However, Elliot (1973) has defined PS to include the processes of grain boundary diffusion in the absence of an adsorbed fluid (Coble creep) and lattice diffusion (Nabarro-Herring creep) in addition to fluid-enhanced boundary diffusion. Despite the difficulty of differentiating between Coble creep and PS textures (see subsection on deformation mechanisms), this terminology has not been accepted. Durney (1976) has defined PS as "the dissolution and removal of mineral substance at a grain contact subjected to 'pressure' " (p.231), with an accompanying definition of "pressure growth" as deposition of diffused material under pressure. Durney (1972), also cited by Kerrich (1978), further confuses the terminology by designating deformation through mass flux as "solution transfer". Despite this, the former

definition remains entrenched.

Though recognized since the 1860's (by Sorby) and subjected to considerable study, PS remains incompletely understood. Fieldwork and routine petrographic techniques have provided comprehensive descriptions of the fabrics produced by PS, and of the environment in which it occurs. This work provides a basis for much of our understanding of the process but unfortunately provides no details as to what actually happens during PS. Another line of investigation is theoretical modelling. Its contribution is difficult to assess, largely because of limited understanding of the intergranular film which is generally inferred to be present under conditions favouring PS (Kerrich, 1978; Green, 1984). PS has also been studied experimentally. This approach has met with some success but unequivocal evidence for PS is generally lacking. The conditions favouring PS - extremely slow strain rate and fine grain size - have hindered attempts to produce PS. For example, production of only 1% strain, assuming a strain rate of 10^{-10} s^{-1} , would require 10^8 s (approximately 3.2 years). Even lower strain rates will require correspondingly longer periods. Likewise, finer grain size (which modelling suggests strongly favours increased strain rate) makes observation of any deformation textures more difficult. Other experimental work has been directed towards revealing the enigmatic nature of the adsorbed boundary layer

(Rutter, 1976,1983). There are also studies of mass and chemical balance associated with PS in both natural and artificial situations. Such work appears to be in its infancy.

The purpose of this chapter is not to review PS. This has already been done by Kerrich (1978) and McClay (1977), among others. In particular, summaries of PS fabric have been presented by Ramsay (1977), McClay (1977), Durney (1972) and Kerrich (1978). Subsequent sections of this chapter describe aspects of both theoretical and experimental modelling of PS. A summary of deformation mechanisms is an appropriate starting point.

2.2 Natural deformation

Various deformation mechanisms are responsible for permanent deformation of rock. Each mechanism is favoured by particular sets of conditions. For a given material, these conditions can be shown on deformation mechanism maps (DMMs). To begin, a summary of deformation mechanisms is presented.

2.2.1 Deformation Mechanisms

At microscopic scale, deformation involves different intra- and intergranular processes known as deformation mechanisms. There are five groups of these mechanisms; by definition, their effects are distinguishable (Ashby, 1972). While a sample may have been affected by only one mechanism at a given time, all but the simplest deformation history will involve several processes.

To understand deformation mechanisms it is important to distinguish between dependent and independent processes. Independent processes are able to proceed autonomously; dependent ones are not (Stocker and Ashby, 1973). Consequently, the fastest process of a group of independent processes will determine the minimum overall rate; the slowest of a group of dependent processes will set the overall rate (Elliot, 1973). This idea of dependence and independence may be seen to operate at two levels. An individual deformation mechanism may occur through a sequence of dependent, lattice-level processes. PS, for example, is thought to consist of three steps - dissolution followed by diffusive transport within the adsorbed fluid and subsequent precipitation - with the middle process, diffusive flow, limiting the overall rate (Rutter, 1976). In contrast, some deformation mechanisms result from the simultaneous operation of two

dependent deformation mechanisms. (Perhaps a distinction could be drawn between deformation mechanisms by using the adjectives "simple" and "complex".) Superplastic flow, which proceeds through simultaneous lattice diffusion and particulate flow (Ashby and Verall, 1973), illustrates this. The five groups of mechanisms referred to above are, by themselves, independent.

Both field and experimental studies require identification of the mechanism by which a material has deformed. Fortunately, characteristic microstructures provide convenient criteria to distinguish some of the operative mechanisms. The following is a summary of the five groups, and of the conditions which produce them.

Cataclasis: Cataclasis refers to both intra- and intergranular fracture. It is thus a fine-scale equivalent of bulk brittle behavior. Bulk ductile behavior can be generated through pervasive local cataclasis in conjunction with particulate flow (see below; Paterson, 1976; White, 1976a). The observation of fractures is straightforward. Additionally, their presence may be marked in natural samples by alteration or infilling. In thin section the identification of fractures may be aided by prior impregnation of the sample with a dye (Borradaile, pers. comm.). Cataclasis is favoured at low confining pressures (P_c), low

temperatures and high strain rate (Borg et al, 1960; White, 1976b; Paterson, 1978). Donath and Fruth (1971) have noted that rapid increase of bulk differential stress rate may be responsible for cataclasis during experimental procedures.

Particulate flow: Particulate flow refers to discontinuous deformation between adjacent grains. It includes both translation (relative to adjacent grains) and rotation of separate grains. Borradaile (1981) has identified particulate flow as an independent mechanism and so distinguished it from cataclasis. Like cataclasis, particulate flow may produce discontinuous ductile flow. This may be accomplished without intragranular deformation (referred to as independent particulate flow), or controlled completely by intragranular deformation (dependent particulate flow), or limited by intragranular deformation but encouraged by other factors (controlled particulate flow; Borradaile, 1981). Independent particulate flow is favoured by low effective normal stress. Consequently, pore fluid pressure (P_f) will tend to hasten particulate flow (but if too high will lead to hydraulic fracturing). The other two classes of particulate flow are limited by the rate of the coupled mechanism (Borradaile, 1981).

An experimental (and natural) manifestation of particulate

flow is dilation hardening (Brace, 1968; Frank, 1965). Because of the limited rate of permeability of a rock, a rapid change in pore pressure is not communicated immediately to a fluid reservoir. When particulate flow associated with high strain rates causes an increase in the pore space available to a pressurized pore fluid, sample pore pressure will drop and the effective stress will increase. The measured pore pressure appears to be high, however, and an apparent bulk hardening of the sample is inferred.

As particulate flow causes no change in grain shape, detection of intergranular movement may be difficult (Borradaile, 1981). The occurrence of particulate flow during experimental deformation may be detected by the offset of markers, such as scored lines on sample surfaces (Heard and Raleigh, 1972), and thin metal foils inserted between two halves of a granular specimen (Raleigh, 1965; Schmid et al., 1980).

Crystal plasticity: Crystal plasticity, more properly referred to as intracrystalline plasticity, is one of two methods by which grain shape is modified without volume change. It is caused by the generation and movement of dislocations within the crystal lattice. (Intracrystalline plasticity is not to be confused with plasticity in the rheological sense.) Dislocations move by glide, which is movement confined between adjacent rows of

atoms, and by climb, which is movement that continues across nearby atomic layers within the lattice. The mechanism of dislocation creep involves glide and climb. Nicolas and Poirier (1976) provide a full account of crystal plasticity. Evidence for crystal plasticity is varied. Optical microscope examination will show undulose extinction, deformation bands, deformation lamellae, subgrains and twinning (White, 1976a). The transmission electron microscope is able to show dislocations and X-ray fabric analysis shows preferred crystallographic orientations (White, 1976a).

Development of crystal plasticity is determined by dislocation mobility (Paterson, 1976). Glide, which is thermally insensitive, requires high deviatoric stress. At higher temperatures, thermally activated dislocation climb allows dislocation creep to occur at lower deviatoric stress. In general, crystal plasticity is favoured by relatively high deviatoric stress and homologous temperature, T_H , (where $T_H = T/T_M$; T_M is melting temperature and both T and T_M are in degrees K).

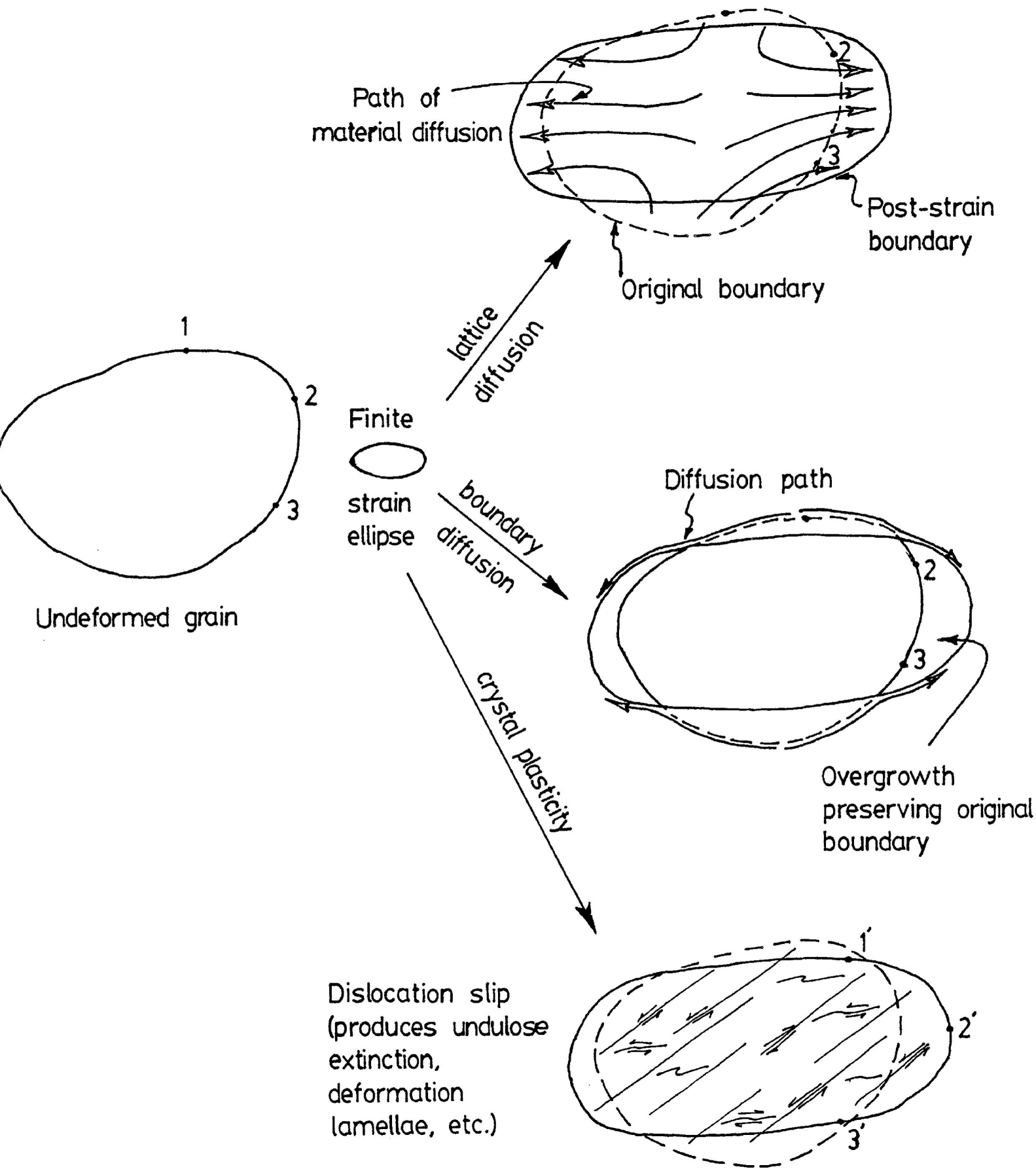
Diffusional mass transfer: Diffusional mass transfer is the diffusion of matter both through grains and along grain boundaries. The former mechanism is also called lattice diffusion

or Nabarro-Herring creep. When coupled with particulate flow the process is known as superplasticity (Ashby and Verall, 1973).

Boundary diffusion occurs in two ways: in the solid state (termed Coble creep), and under the postulated influence of an adsorbed film of water (labelled pressure solution; Rutter, 1976).

Diffusion generally results in change of grain shape, and is often volume conservative. An exception may occur with PS when diffusion distances are great.

Identification of diffusive mass transfer is not entirely straightforward. Nabarro-Herring creep causes the diffused material to be crystallographically continuous with the rest of the grain lattice and so the deformed grain shows no internal record of the former texture (Fig. 2-1). Producing a texture geometrically equivalent to Nabarro-Herring creep are PS and Coble creep (Rutter, 1983) but the latter two tend to show other evidence of the deformation. This includes signs of material removal, resulting in, perhaps, a tectonic cleavage, and overgrowths. Textural differentiation of grain scale PS and Coble creep effects appears to be impossible. The site of material removal, path of transport and site of deposition are the same for both, and it is only the deduction of accompanying conditions which allows the distinction. Ramsay (1977) has summarized the diagnostic effects of PS seen in nature.



The two solid-state diffusional mass transfer mechanisms occur under conditions of low differential stress and intermediate to high T_H . PS occurs at low T_H but is effective over a wide range of stress. PS does not occur significantly in quartz at temperatures over approximately 650°C, or in calcite over 400°C (Rutter, 1976).

Strain-induced recrystallization: Recrystallization in common usage refers to strain-induced recrystallization but not stress-induced recrystallization, i.e. diffusive mass transfer. The latter is understood to involve no change in the internal state of the crystal while the former does. Strain-induced recrystallization ("annealing") occurs at high temperature in the absence of differential stress and so is not a deformational process. It may, however, be a post-tectonic component of many tectonite fabrics. Dynamic recrystallization is the process by which strain-softening may occur; it is favoured by high temperature and differential stress. Dynamically recrystallized grains typically have ragged boundaries and show signs of plasticity ranging up to the development of polygonal substructure. (Statically recrystallized grains have straight borders and undeformed cores.) See Nicolas and Poirier (1976) for a fuller discussion.

2.2.2 Constitutive Equations and Flow Laws

Constitutive equations, also known as equations of state, are the building blocks of DMMs: they describe the relation of strain rate to fundamental physical quantities - stress, temperature, activation energy, etc. - for specific deformation mechanisms. Dorn (1957) has expressed this as

$$\dot{\epsilon} = W f_1(\sigma) f_2(T) f_3(S)$$

where $\dot{\epsilon}$ is strain rate, W is some constant, f_1 , f_2 and f_3 are functions, σ is differential stress, and S is a fundamental value or values describing the microstructure of the material. As constitutive equations are conventionally written for steady-state deformation, the structural state of the material (but not the strain) remains constant and thus the value of this term is included in M with two functions, f_1 and f_2 , remaining. An example of a constitutive equation for PS, made with an approximation for normal intergranular stress less than 30 MPa, is

$$\dot{\epsilon} = \frac{32 V C_0 D_b w}{R T d^3} \quad (2-1)$$

(Rutter, 1976). Both stress and temperature occur explicitly in this equation as well as implicitly determining the reference

solubility, C_0 , and grain boundary diffusivity, D_b . (See subsection 2.4.2 for explanation of the other terms.)

The change in shape (strain) accomplished in any deformation is driven by the non-hydrostatic component of stress (Ramsay, 1967), also referred to as flow stress. White (1976b) has stated that either differential stress or, with an appropriate factor, deviatoric stress may be used in a constitutive equation, where

$$\sigma_{\text{diff}} = \sigma_1 - \sigma_3$$

and in general,

$$\sigma_{\text{dev}} = \sigma - \left(\frac{\sigma_1 + \sigma_2 + \sigma_3}{3} \right)$$

(Presumably, White's reference to deviatoric stress is actually to maximum principal deviatoric stress.) As $\sigma_{1\text{dev}}$ is no greater than two-thirds of σ_{diff} , it is desirable to know which quantity of non-lithostatic stress is called for when calculating the position of a DMM boundary which is moderately or steeply inclined to the stress axis (see below). Raj (1982) has used the von Mises deviatoric stress

$$\sigma_{\text{vM}} = \left\{ 0.5 \left[(\sigma_1 - \sigma_2)^2 + (\sigma_2 - \sigma_3)^2 + (\sigma_3 - \sigma_1)^2 \right] \right\}^{0.5}$$

in his constitutive equations. Elliot (1973) has stated that stress in constitutive equations is octahedral stress, though this is not apparent in derivation of other constitutive equations, e.g. Raj and

Ashby (1972). Octahedral stress is similar in form to von Mises deviatoric stress but less by a factor of 4.24 .

Constitutive equations differ from the Mohr-Coulomb, von Mises and other early failure criteria (Ramsay, 1967). Such criteria, while describing the relationship between stress and strain, indicate that failure only occurs if a specified state of stress is exceeded. Constitutive equations describe steady-state flow for a range of strain rates. Furthermore, failure criteria describe behavior of a crystal aggregate while constitutive equations describe grain-scale transformation.

Constitutive equations are based upon a geometrical model of individual grain behavior. Because only diffusive mass transfer mechanisms have readily defined geometry (Rutter, 1983), these are the only ones to have had constitutive equations developed. Subsequent development of an equation is made using boundary conditions on the model. If, as has been noted for PS, the deformation consists of dependent processes with one process very much slower than the others, it is reasonable to base the equation upon that one process (viz. Rutter, 1976). Another approach for PS is to assume constant mass flux of the dependent processes (viz. Rutter, 1983).

Flow laws are a class of equations related to constitutive equations. Derivation of constitutive equations is based upon

theoretical models, and may include substitution of thermodynamic relationships. In contrast, steady-state flow laws are semi-empirical relationships which describe bulk flow. An example of a flow law is the Dorn equation, shown here with a power law stress term:

$$\dot{\epsilon} = A \exp\left(\frac{-H}{RT}\right) \sigma^n \quad (2-2)$$

where A and n are constants, and H is activation energy. Flow laws are fitted to experimental data. The Dorn equation, for example, has been found useful in fitting experimental data for intracrystalline flow above about $T_H = 0.5$ (Rutter, 1974) for a variety of materials. Both constitutive equations and flow laws may incorporate externally derived parameters and constants, e.g. the gas constant, R, is used in equations (2-1) and (2-2).

2.2.3 Deformation Mechanism Maps

There are several varieties of DMM. Each provides a graphical relationship between strain rate, non-lithostatic stress, grain size and temperature. In simple terms, a DMM is a two-dimensional representation, with a third quantity contoured and the final quantity held constant (Rutter, 1976) showing the

range of conditions for various deformation mechanisms (Paterson, 1976). A DMM is thus useful to geologists as it provides an easily understood presentation of rock deformation under particular conditions. An example of an Ashby-type plot is shown on Figure 2-2. Weertman (1968) was the first to present such a diagram constructed for constant grain size, d . Another variety of DMM, independently produced and initially presented by Elliot (1973), holds temperature constant with nominal axial quantities of stress and grain size (Figure 2-3). Mohamed and Langdon (1974) plotted $\log(\text{normalized grain size})$ against $\log(\text{normalized stress})$ for constant temperature. The advantage of this particular format is that field boundaries are straight. (This is because various temperature dependent quantities remain constant, leaving strain rate to vary only with grain size and stress.) Langdon and Mohamed (1978) devised a variation of the Ashby plot with straight boundaries in which normalized stress is plotted against the reciprocal of homologous temperature. Straight boundaries result at higher temperatures ($T_H > 0.4$) and lower stresses ($(\sigma/G) < 10^{-3}$); outside these conditions departure from linearity is greater.

Construction of a DMM is, in principle, straightforward. At any point in the field defined by the map axes, the total strain rate is the sum of the strain rates due to the individual deformation

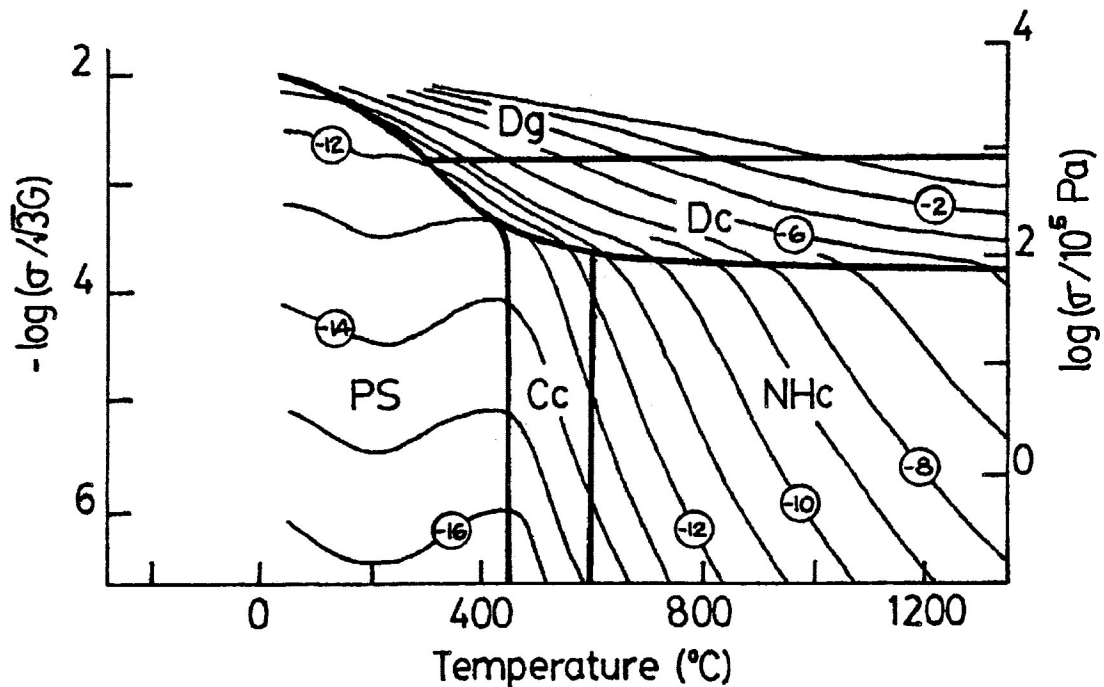


Figure 2-2: Deformation mechanism map (DMM) for calcite; $d=100 \mu\text{m}$. G is the shear modulus; Dg is dislocation glide, Dc is dislocation creep, Cc is Coble creep and NHc is Nabarro-Herring creep; contours are of $\log(\text{strain rate})$. From Rutter, 1976; Fig. 8.

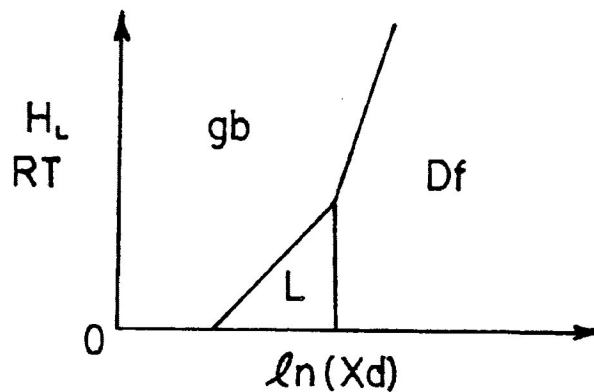


Figure 2-3: Schematic Elliot-type DMM with inverse temperature vs. $\log(\text{grain size and shape})$ where H_L is activation energy of lattice diffusion, X is grain shape and d is grain size; gb and L are grain boundary and lattice diffusional flow, respectively, and Df is dislocation flow. From Elliot, 1973; Fig. 11.

mechanisms (Ashby, 1972). At most points of the entire DMM, however, one particular mechanism will contribute an overwhelming component of the total strain. Thus one speaks of deformation mechanism fields, the extent of which is the stress-temperature space (on an Ashby plot) over which a particular mechanism will be favoured. For example, within the Coble creep field of Fig. 2-2,

$$\dot{\epsilon}_{\text{total}} = \dot{\epsilon}_{\text{Coble creep}} \quad (7)$$

Boundaries between adjacent fields mark the conditions for which the corresponding mechanisms contribute equally to net strain rate. Thus, on any boundary,

$$\dot{\epsilon}_a = \dot{\epsilon}_b$$

where subscripts a and b indicate deformation mechanisms a and b. Ideally, a straightforward determination of field boundaries could be made by equating constitutive relationships and flow laws. However, this usually involves expressions which are awkward to evaluate. Rather than using a lengthy iterative solution, another approach is to calculate values of the contoured quantity - strain rate in the case of an Ashby map - due to the individual mechanisms. Fields are then delimited by the points at which other mechanism strain rates are greater. These points may also be used to produce strain rate contours; more accurate plotting

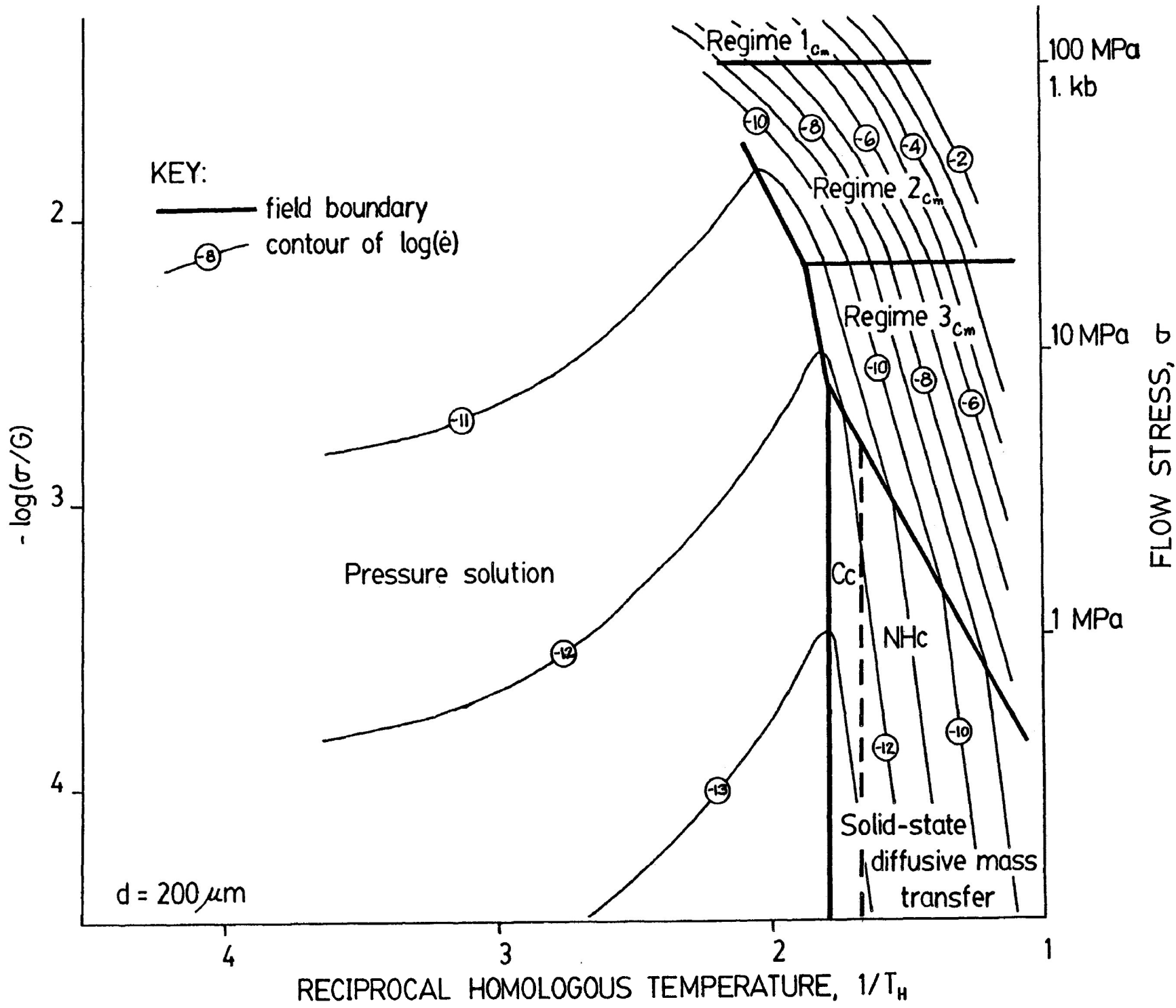
may be accomplished by substitution of the iso-strain rate values in the constitutive equations or flow laws.

The transition between the mechanisms of adjacent fields is shown by the locus of equal strain rates. Representation of the boundary might be more realistically shown as a zone. Mohamed and Langdon (1974) have shown, for aluminum, that complete transition, as calculated with constitutive equations, occurs quickly - within one order of magnitude of normalized stress. Ferguson (1983) has noted, however, that the results of Schmid et al (1977) indicate Solnhofen limestone undergoes more gradual transitions, and has stated that his own work indicates similar behavior predominates in poorly sorted aggregates. Ferguson has described the transition between different mechanisms with composite equations; these are usually additive functions of the flow laws of the two mechanisms.

As previously mentioned, DMM's occur in different forms. Elliot plots, and those of Mohamed and Langdon (1974) are easier to construct because of their linear boundaries. With grain size, d , as an axial quantity on such graphs, it is also possible to see the effects of grain size on deformational behavior. This is convenient for engineers who usually deal with constant temperature applications (Mohamed and Langdon, 1974). Rutter (1976) argues that the Ashby plot is more useful to geologists who

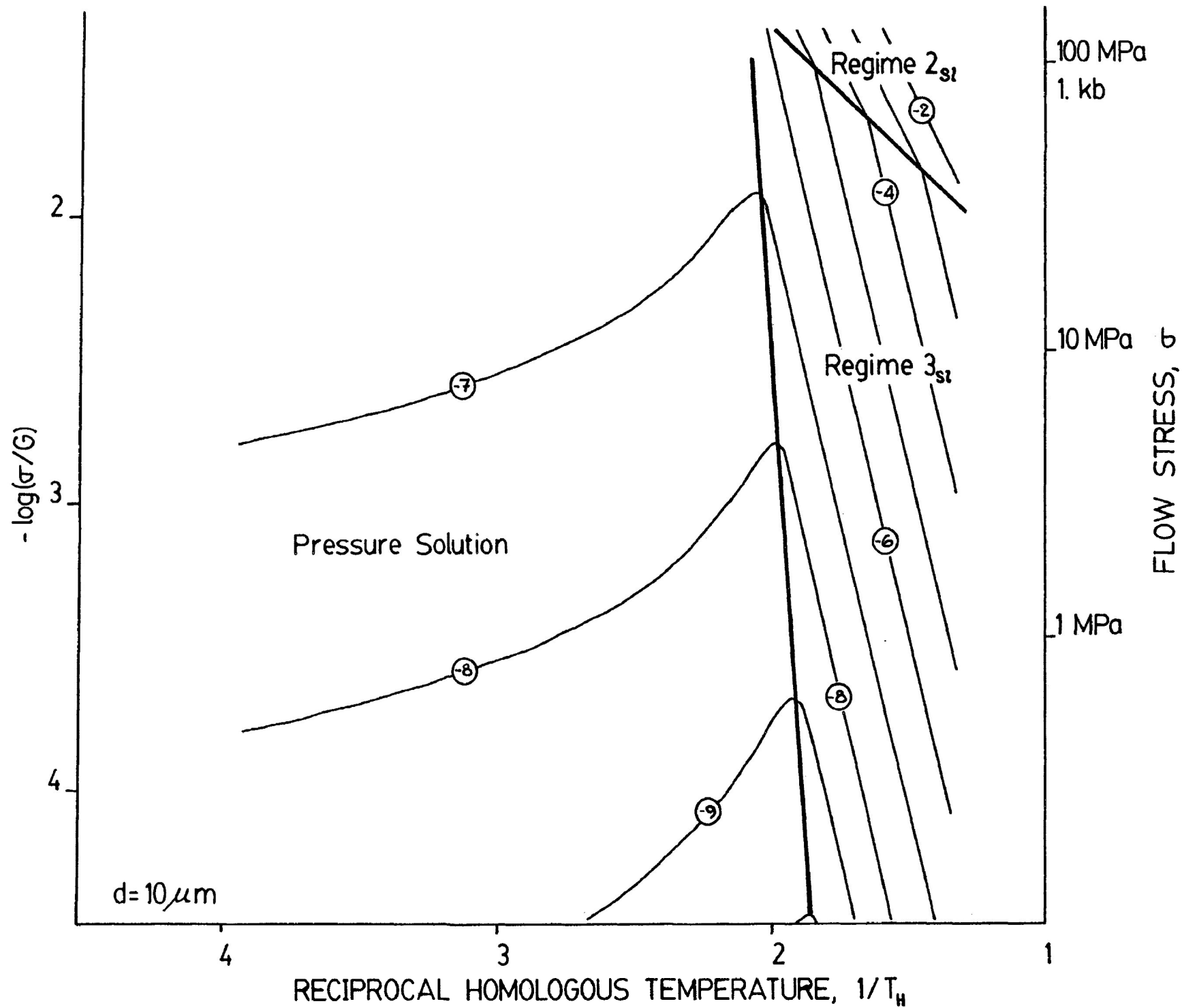
deal with changes in temperature and stress since all processes are temperature and stress dependent but only diffusive mass transfer is strongly sensitive to grain size.

A DMM has been developed for polycrystalline calcite of 200 μm grain size (Fig. 2-4). With the illustrated field boundaries occurring at reciprocal homologous temperatures no lower than slightly in excess of 2, the format of Langdon and Mohamed (1978) was used. The fields for diffusive mass transfer were found using constitutive equations. (Details of the calculations are given in Appendix A.) Stocker and Ashby's (1973) equation describes both Nabarro-Herring creep and Coble creep. Coble creep operates as the dominant mechanism over a narrow range of temperature (approximately 625° to 694°C; see App. A) between PS and Nabarro-Herring creep. PS strain rates were found using an approximation of Rutter's (1976) equation for flow stresses up to about 30 MPa. With differential stresses in nature not exceeding this value (Etheridge, 1983), this is a reasonable natural limit on the DMM. Another mechanism may be operative at higher stresses and lower temperatures. For example, Kerrich and Allison (unpublished) have modified the map by Rutter (1976; Fig. 2-2) to show cataclasis operative under such conditions. The gentle slope of the strain rate contours within the PS field of Figure 2-4 indicates the low temperature dependence of PS.



The fields for regimes 1, 2 and 3 on Fig. 2-4 are taken from Schmid et al (1980) who produced steady-state flow in Carrara marble from 600° to 1050°C. Regime 1 occurred at over 1000 b (100 MPa) flow stress and was best fitted to a Dorn equation with an exponential stress relation, $\dot{\epsilon} \propto \exp(\sigma)$. Deformation in regime 1 was thought to be produced by a complex mechanism of dislocation slip and twinning. Data from regimes 2 and 3 were both fitted to Dorn equations with power law stress relations (eqn. 2-2); $\dot{\epsilon} \propto \sigma^n$ with $n = 7.6$ for regime 2 and 4.2 for regime 3. Regime 2 occurred with flow stresses between 200 and 1000 b (20 and 100 MPa) and produced a core and mantle structure, possibly due to dislocation slip with minor dependent particulate flow. Regime 3 occurred below 200 b and generated equi-axed subgrains. Schmid et al (1980) suggested that dislocation slip with a greater degree of particulate flow was responsible. Rutter (1974) found steady-state flow occurred in Carrara marble from 400° to 600°C, but his transition from deformation by slip to polygonization (corresponding to the regime 2 - regime 3 boundary) was at 800 b (80 MPa). The significance of this inconsistency is that the boundaries between PS and intracrystalline processes are not well established. PS may be superseded at lower temperatures and by other mechanisms than are shown in Figure 2-4.

A second DMM is shown in Fig. 2-5. This map was constructed for calcite with a grain size of 10 μm . The constitutive equation for PS, including the attendant values of parameters, is the same as was used in preparing Fig. 2-4. The two maps show graphically that grain size has a marked effect on PS strain rates. It is also apparent that the finer-grained rock is softer at higher temperatures as well; this has been discussed by Schmid *et al* (1977). These workers found that data from Solnhofen limestone which underwent experimental steady-state flow over the temperature range 600° to 900°C could be given a best fit by multivariate regression in three distinct fields. Regime 1 occurs at unnaturally high differential stresses (1900 b; 190 MPa) at 600°C) and has not been shown here. Regime 2, thought to represent a dislocation creep process, undergoes a stress- and temperature-sensitive transition to regime 3: 300 b (30 Mpa) at 900°C, 1000 b (100 MPa) at 600°. Schmid *et al* (1977) thought regime 3 for Solnhofen limestone resulted from superplastic flow. (None of regimes 1, 2 or 3 is related to Schmid *et al*'s (1980) regimes 1, 2 and 3 for Carrara marble.) Solid-state mass diffusion does not appear on the 10 μm map. The existence of different crystal plastic deformations for Carrara marble and Solnhofen limestone suggests that grain size exerts some control over the operative mechanism, just as it does for diffusive



deformations. This is in addition to deformation mechanism controlling the equilibrium grain size (as shown by Schmid *et al.*, 1980). It is also important to note that Fig. 2-5 may misrepresent the actual deformation that a rock such as Solnhofen limestone would undergo. At 600°C, a limestone having been subjected to regional metamorphism would have been transformed to marble with a greater grain size. The PS field may also be unrealistic. It was determined using Rutter's (1976) constitutive equation for PS which assumes only local diffusive transfer of matter. Outlined in section 2.4 is the argument that PS rarely occurs in nature without the presence of disequilibrium porosity; if so, deformation of Solnhofen limestone at lower temperatures should not be seen in terms of the PS field of Fig. 2-5 when a bulk flow resulting from the development of stylolitic cleavage and extension fractures is more probable (*viz.* Fletcher and Pollard, 1981).

It is customary to normalize the axial quantities of DMM. For example, temperature is usually expressed as T_H . Likewise, differential stress may be normalized by division by the shear modulus, G (see Figs. 2-2,4,5). Grain size is normalized with the Burger vector. Normalization is done to facilitate comparison of the mechanisms in different materials. Similarly, Stocker and Ashby (1973) have constructed an "applied deformation map" on

which geothermometric and geobarometric gradients have been used to substitute depth or lithostatic pressure for temperature as an axial quantity.

Ashby's (1972) original DMM was intended to describe conditions favouring plastic flow and precluding fracture. Subsequently, DMM have been produced for brittle deformation (Ashby et al, 1979, and Ghandi and Ashby, 1979, in Atkinson, 1982).

2.3 Theory of Pressure Solution

2.3.1 Phenomenological Models

The ability of pressure alone to affect the physical state of a substance was reported by Thomson (1862). Having shown earlier that hydrostatic pressure affects the melting point of ice, he proceeded to demonstrate experimentally that differential stress applied to granular salt immersed in saturated brine resulted in deformation of the salt. Thomson made the "general inference that stresses tending to change the form of any crystals in the saturated solutions from which they have been crystallized must give them a tendency to dissolve away, and to generate, in

substitution for themselves, other crystals free from the applied stresses or any equivalent stresses." This process was explicitly distinguished from the effect of hydrostatic pressure applied to the fluid. Thomson also commented on the action of the fluid in this reaction, suggesting that dissolution in pore water might be responsible.

Numerous workers have confirmed Thomson's hypothesis (see Kerrich, 1978). However, the work by Riecke (1894, 1912; in Kerrich, 1978) did not. Riecke stated that if two crystals are in contact with a common saturated solution, stress applied to one will cause its dissolution while the other tends to grow. Riecke has been criticized by Kerrich (1978), Robin (1978) and Paterson (1973), among others, for his experimental design, and also by Robin on thermodynamic grounds. The "Riecke principle" as a premise for PS is invalid, and references to it are absent in recent literature.

Following Thomson's hypothesis of the effect of water on a differentially stressed solid, Sorby (1865, 1879, 1880; in Kerrich, 1978) attributed fabrics such as stylolites, pebble indentation and veins to the action of PS. He suggested that the presence of water in the environment in which these features formed increased the rate of matter transfer. Almost a century later, Weyl (1959) postulated that an intergranular aqueous film provides a route for

diffusion of matter. He argued for the existence of such a film by presenting a PS model involving "stepwise marginal dissolution and crushing". Two grains initially in contact (Fig. 2-6), but without an intermediate solution film, are initially able to dissolve only at the margin of the contact adjacent to the pore space. As dissolution proceeds, pore fluid flows between the two grains. Eventually the remaining grain material in contact is unable to support the load and is crushed. The fine grained detritus will dissolve away until the aqueous film is expelled and the grains are once more in contact, whereupon the process repeats itself.

As Weyl himself recognized, this model is unsatisfactory in several respects, not least of which is that no textures corresponding to this model have been observed. It is also a complicated process. Robin (1978) has argued that when crushing occurs, the grain is liable to come in contact again along the outside edge and so trap the crushed material inside the surface of contact, although it is not clear that this would stop the process. Nevertheless, the sequential nature and variable rate of action renders the model suspect. Furthermore, this model does not acknowledge the literature on the existence of an adsorbed intergranular film with anomalous liquid properties. Weyl noted that his model precludes the existence of such a film, and

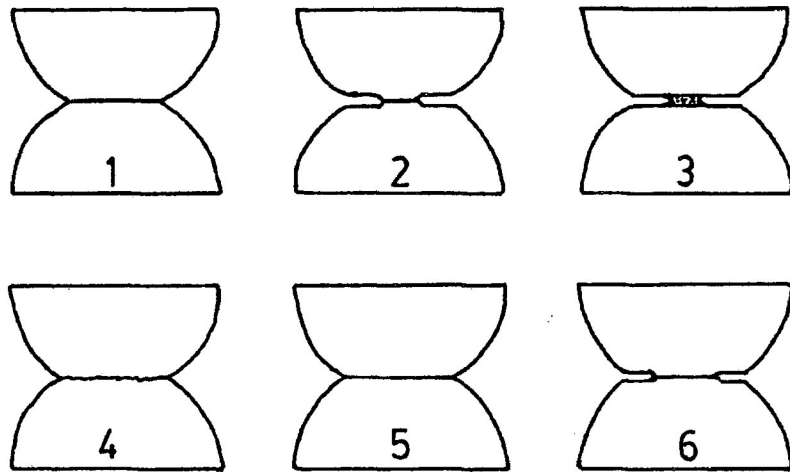


Figure 2-6: Weyl's model of pressure solution by stepwise marginal dissolution and crushing. When dissolution (step 2) has advanced sufficiently, the remaining material crushes (step 3) and dissolves (step 4). The process then repeats (steps 5 and 6). From Weyl, 1959; Fig. 2.

concluded that a true adsorbed film (see below) is actually present during PS.

In a related model, Ostapenko (1968) suggested crystal plasticity and cataclasis would lead to microgranulation of grain surfaces in contact. Preferential dissolution of the crushed material (due to the finer grain size) and precipitation of the dissolved material at sites of lower stress would produce the deformation. Again, there is no petrographic evidence for this process.

The existence of a solvent film along grain contacts during PS is supported by a closely related phenomenon, force of crystallization. This is the opposite of PS. When a crystal in solution is able to grow against an external load (Correns, 1949), the growth is said to have exerted a force of crystallization. This process is interpreted as occurring by diffusion of matter along an adsorbed intergranular film with subsequent precipitation. Experimental work, for example that of Becker and Day (1905) and Correns (1949), has shown that crystal growth against a load does occur.

While force of crystallization has been shown to operate, and is related to PS, its natural occurrence is limited. Growth under pressure will occur if a solution is supersaturated with respect to the grain under pressure (Correns, 1949). (This raises the

interesting question of why precipitation will occur preferentially on a stressed face over an unstressed face in experiments such as those of Correns.) The limits to this growth in nature is the requirement of unrealistically high supersaturation to oppose the tensile strength of the rock plus the minimum effective stress (Kerrick, 1978). Fluid overpressure, as it reduces effective stress, favours force of crystallization but does not guarantee its operation.

If aqueous films are to exist along grain contacts, these films will have properties unlike those of ordinary fluids. This behavior is thought to result from adsorption of the fluid to the surface of the grains. Elliot (1973) has defined pores as void spaces sufficiently large to be unaffected by the surface forces of the enclosing grains. In contrast, intergranular films of water appear to be highly influenced by the enclosing grains. Rutter (1976) has attributed the ability of a film to withstand shear stress to polarization of the water molecules by surface forces of the grains. Crystal growth through force of crystallization and Rutter's (1983) demonstration of clay expansion upon wetting are macroscopic reflections of this.

It is important to know the strength of these surface effects. For example, consider a sedimentary sequence which is sufficiently permeable to avoid fluid overpressure. The ratio of

effective lithostatic stress to hydrostatic stress will be given by the expression $(\rho_r - \rho_w)/\rho_w$, where ρ_r is the average density of the sediment and ρ_w is the pore fluid density. Typically, ρ_r is about 2.7 g cm^{-3} and ρ_w is 1.0 g cm^{-3} . The resultant effective stress is 1.7 times as great as the pore fluid pressure. In sediments with substantial porosity, stress concentration would raise this value considerably. In absolute terms, using the assumptions of an orogenic geothermal gradient of 30°C/km and PS operating at up to 400°C (Rutter, 1974), the maximum effective principal stress supported by a continuous intergranular film may be as much as 220 MPa (2.2 kb).

While the effective stresses experienced under conditions favouring PS are substantial, their magnitude does not appear unreasonable in light of Rutter's (1983) experiments on clay films. In a series of experiments performed by Rutter, dried films of flocculated kaolinite, ranging in thickness from 10 to 150 μm , were compacted under 100 MPa. For the thinnest clay films, addition of water to the clay caused expansion against the load. (Thinning of the thicker layers of clay was attributed to bulk flow of the clay from between the opposing piston faces.) These tests demonstrate clearly that adsorbed fluid is, under the experimental conditions, able to support a bulk effective stress of 100 MPa. Calculations showed the thickness of aqueous films adsorbed by

individual clay particles was in the range of 1 to 2 nm. Rutter noted that the maximum stress sustainable by water adsorbed on clay appears to be much higher (c. 500 MPa), but also that at higher stresses, both film thickness and diffusivity may be reduced. Nonetheless, the existence of adsorbed aqueous films under conditions favouring PS appears possible.

There will be influences on the degree of development of an intergranular film. One factor is the degree of adsorption which varies between different minerals. Clay has a pronounced electrostatic potential which is thought responsible for the strong adsorption of water (Deer et al, 1966). Other minerals may lack a strong polarity and so be less effective in adsorbing water. This suggests why a small proportion of intergranular clay appears to aid PS.

Variation in stress distribution along grain faces is also relevant to the intergranular film. Close packing and parallel alignment of clay crystallites would lead to reasonably uniform stress across the crystallite faces in Rutter's experiments, in contrast to the approximately parabolic stress distribution at the interface between more equant grains (Rutter, 1976; Robin, 1978). In the latter case aqueous film thickness could be expected to vary along such a grain contact, perhaps with the film entirely absent where the stress is greatest.

Thus, one model of an adsorbed intergranular film is of a continuous layer which, in general, can maintain gradients in normal stress. A second model of grain boundaries is referred to as island and channel structure (Elliot, 1973; Raj and Chyung, 1981, in Raj, 1982). Elliot suggested islands with a width of three to five atomic spaces separated by channels of one to two spaces width. Diffusion would occur preferentially along the interconnected channels. The natural roughness of surfaces suggests that two grains coming in contact would not touch completely at their interface but rather where protruding asperities meet the opposing surface. Variation in size of those protrusions, ranging from macroscopic to lattice-scale irregularities, appears to indicate that zones of contact will, at least initially, vary considerably in size. Relatively large and widely separated points of contact could, for example, occur immediately upon deposition of clastic grains. At the earliest stages of compaction, stress concentration across such contacts would be appreciable so that even if bulk effective stress were low, PS would tend to remove the larger irregularities. True lattice-scale islands might thus be expected to form early along a grain contact.

Two problems with this model suggest themselves. How can the island and channel structure be justified with the continuous

film implied by force of crystallization and demonstrated by Rutter's (1983) experiments? Rather than being mutually exclusive, it may be that the aqueous film is continuous at lowest effective stresses, but at higher stresses, protruding bumps punch through the adsorbed film to form the islands.

A second problem is how the island and channel structure would be maintained during PS. Because the islands are only a fraction of the total area of a granular interface, the islands will be subject to stress concentration (Raj, 1982), and so these would normally be expected to be removed by PS first. It seems unlikely, then, that islands and channels will be self-perpetuating. A possible explanation is that as an island is reduced, preferential dissolution would occur at sites of higher free energy: lattice dislocations, subgrain boundaries, microfractures and impurities. New channels would tend to form at this site.

One can extend the island and channel model to the transition to other deformation mechanisms. An increase in effective pressure would tend to thin the film along the channel while an increase in temperature would render the film less viscous and more susceptible to pressure. A thinner film is accompanied by an increased number of contacts and so less fluid is available along the interface to act as a path for diffusion. (Stress concentration will also be reduced.) With greater load being transmitted across

solid-to-solid contacts, cataclasis or crystal plasticity will supersede PS.

2.3.2 Thermodynamics

Another approach to PS is through thermodynamics, more specifically, nonhydrostatic thermodynamics. Paterson (1973) has illustrated how different deformations require different calculations to determine the work done on a system. For example, PS, being a heterogeneous process, i.e. one restricted to a specific site (grain boundaries), is different from crystal plasticity which occurs throughout the grain, and thus different mathematical treatments are required. For all deformations, however, thermodynamics can be used to describe energy balance.

Early work on the conditions favouring PS centred on the relative molar volumes of a component in the solid and in solution. This approach has proved inconclusive (see Robin, 1978). To properly describe equilibrium, and hence the departure from equilibrium which drives a process, one must determine the chemical potential, μ (Paterson, 1973). Robin (1978) has stated that under anisotropic stress, the μ gradient does not parallel the concentration gradient. Because of this, diffusion of mass should not be described by Fick's law as it is usually written, relating

mass flux to concentration gradient. Instead, the appropriate form, for one-dimensional flow, is

$$J = -M (d\mu/dx) \quad (2-3)$$

where J is the mass flux,
 M is the diffusion constant, and
 x is distance.

Because M is a constant, μ is the term of interest in Fick's equation. An unstressed grain under hydrostatic pressure, P_f , is an appropriate reference state in determining μ (Robin, 1978). This is because the system is subject to all the conditions in effect during PS except the differential stress which actually causes the strain. The μ which drives PS is relative to this reference state. It is convenient here to express μ in the form of molar free enthalpy, G :

$$\mu = \left(\frac{\partial G}{\partial n} \right)_{T, P}$$

where n is the number of moles.

At some point along a stressed grain contact, the change in molar free enthalpy is

$$\Delta G = \Delta U - T\Delta S + P\Delta V + P'V_0 \quad (2-4)$$

where U is molar internal energy,
 T is absolute temperature,
 S is molar entropy,
 P is total pressure across the grain contact,

P' is effective pressure across the grain contact; $P' = P - P_f$,

ΔV is the difference in molar volume of a one-component solid between the stressed and unstressed states, and V_0 is the solid molar volume in the unstressed state.

It is ΔG which drives the intergranular diffusion. Robin (1978) has discussed the contributions of the various terms to ΔG . The first three terms on the right hand side are usually small relative to the final term, $P'V_0$. As this last term is dominant, the potential driving diffusion is closely related to the normal stress gradient. Along the margin of the contact, zero effective stress will give this term a value of zero (Robin, 1978). Stress concentration will tend to result in a corresponding μ gradient along the boundary.

Green (1984) has identified contributions to the individual terms of equation (2-4) for the free enthalpy driving diffusion. The terms $(P\Delta V + P'V_0)$ describe the reversible work done by the differential stress on the grain boundary. Contributions to U include elastic strain energy due to the deviatoric stress as well as internal energy generated through local plastic strain and the production of new surfaces, e.g. cracks. In the case of an anisotropic crystal, variation in elastic strain energy will occur with orientation (Paterson, 1973). Plastic strain and surface generation are also responsible for an increase in entropy, ΔS .

Green (1984) has postulated the relative importance of these contributions under different geological conditions. In a diagenetic environment, stress anisotropy will likely be high due to high porosity and irregular grain contacts but the mean stress will be low. Consequently, contributions to ΔG by ΔU and ΔS will be relatively high, especially if the elastic limit of the grains is exceeded. As consolidation proceeds, stress anisotropy drops and the reversible work terms become dominant. In general, however, $P'V_0$ will be the dominant contribution to the μ gradient.

In addition to relating the net μ of PS to change in individual thermodynamic components, it is also possible to relate μ to compression of an actual grain aggregate. By making the approximation that $\mu = P'V_0$, Robin (1978) was able to find a simple expression relating μ_{\max} and bulk effective pressure, P_e . With the assumptions that the intergranular effective force between grains of equal diameter, d , is intermediate between the values for cubic packing and hexagonal packing, and that P'_{\max} is only 1.5 times the average value of P' (a less than parabolic stress distribution), Robin found

$$\mu_{\max} = 0.75 V_0 (d/a)^2 P_e$$

where a is the diameter of a circular intergranular contact.

Recently, it has been suggested that μ is not a scalar but a

tensor, e.g. Bayly (1987). In other words, μ is thought to depend on orientation as well as position. This development does not appear to have great relevance to the thermodynamics of PS. PS is essentially a two-dimensional process: dissolution and diffusion occurring along a grain boundary which is of limited thickness. In a grain aggregate, different grain contacts will have different values of μ driving PS, but this difference in μ will be due to different normal stresses. In contrast to the effect of external variable stress, μ is also affected by crystal anisotropy. This is an internal variable and so would appear to give rise to a μ tensor. As discussed previously, variation in μ due to crystal anisotropy is likely to be small.

2.3.3 Textural and Mineralogical Limitations on Pressure Solution

PS has long been recognized to accomplish negative dilation. This includes both compaction of sediments and non-isovolumetric deformation in low-grade metamorphic rock (Green, 1984). These two occurrences differ in their scale of mass conservancy. The infilling of porosity by local precipitation of PS-derived cement is a locally mass-conservative deformation (if expulsion of pore

fluid is neglected). However, larger PS-generated structures, e.g. stylolites, are not mass-conservative at the scale of individual pores. PS manages to operate at different scales whenever there is a μ between the two sites, and results in significant shortening whenever the product of diffusive mass flux and time is sufficiently large.

PS has been shown to consist of three dependent processes: dissolution, diffusion and precipitation. Each process is driven by some fraction of the net free enthalpy, G_{net} . Arithmetically, this is

$$G_{\text{net}} = G_{\text{dissol}} + G_{\text{diff}} + G_{\text{pptn}}$$

where the right hand terms are the free enthalpies due to dissolution, diffusion and precipitation, respectively. Texture may be expected to influence each process, and the free enthalpy required for it. Dissolution is commonly visualized as occurring between two grains of identical size and shape, but it need not occur this way in nature. For example, stylolite growth involves dissolution of grains which are in contact with much finer grained detritus of the stylolite. Gray and Durney (1979) noted that greatest dissolution in metasediments occurs between grains of quartz and phyllosilicate minerals, but attribute this to ease of diffusion along such a contact, and not to any textural effect on

dissolution. Any variation in dissolution rate, or in μ driving dissolution, are unknown but may exist.

Diffusion and precipitation also occur in different textural environments; in these cases, texture does have an effect. Diffusion moves matter to points of lower free enthalpy. It is usually thought of as occurring along adsorbed films, but diffusion through pore fluid can occur as well (Kerrich *et al.*, 1977b). In the case of grain cementation, diffusion need only transport material to the nearest non-equilibrium pore. Production of the larger structures involves much greater distances of transport. In the latter case, diffused material may be deposited as cement in nearby rock of greater porosity, or within hydraulic tensile fractures, forming veins (Kerrich *et al.*, 1978). Not only distances vary; the diffusion constant, M (in Fick's equation; number (2-3)) will almost certainly vary as well. Rutter (1976) has quantified this with his estimate that M for a 2 nm thick adsorbed film is 5 orders of magnitude less than for free water. M may also vary between films adsorbed on different materials. Because of variations in M , μ gradients will vary between the different textural sites (intergranular contacts vs. equilibrium and non-equilibrium porosity and cleavages) while a constant flux is maintained. This rate argument suggests that long range diffusive transport may be accomplished efficiently in terms of μ .

Like diffusion, precipitation may occur in different textural situations and have different values of G_{pptn} associated with each situation. There are essentially two situations. Precipitation will occur spontaneously, i.e. $G_{\text{pptn}} < 0$, when there is a minimal level of supersaturation. A variation on this occurs when diffusion transports material to a site of fluid flow. This fluid will, if undersaturated, provide a sink for the pressure solved material.

The second site of precipitation is along intergranular contacts. (In Raj's (1982) terminology, this is "creep".) For precipitation to occur along a grain boundary subjected to an intergranular normal stress, a force of crystallization must be involved. As noted previously, force of crystallization is driven by supersaturation of nearby pore fluid, and will not operate except at lowest effective normal stresses. This indicates that precipitation along an intergranular contact is not spontaneous and requires an external driving force, i.e. $G_{\text{pptn}} > 0$. (In addition, diffusion along the contact where precipitation occurs will also be against the free enthalpy gradient.) As equilibrium is described by the minimum value of G_{net} , equation (2-4) shows that pore wall precipitation is favoured over intergranular growth.

This conclusion can be explained in greater detail by

expressing G_{net} for intergranular growth as the difference in free enthalpy between sites of compressive deviatoric stress (where dissolution occurs) and tensile deviatoric stress (where precipitation might occur):

$$G_{\text{net}} = \Delta G_t - \Delta G_c$$

where ΔG_c is the difference in G between the faces under compressive deviatoric stress and the reference state, and ΔG_t is the difference in G between the faces under tensile deviatoric stress and the reference state.

Both ΔG_c and ΔG_t are expressed by equation (2-4). With differential stresses in nature usually less than 20 MPa (Etheridge, 1983), and because conditions under which minimal porosity will occur will tend to be accompanied by relatively great mean stress, the proportional difference in stress between the two faces will be small. As a result, the term $P'V_0$ of (2-4) will be small in comparison to the value it would have in a highly porous aggregate. As noted previously, the quantity $U - T\Delta S + P\Delta V$ usually contributes little to the free enthalpy driving PS with respect to the reference state. Thus, $U - T\Delta S + P\Delta V$ makes a similarly minor contribution to the net free enthalpy between the two faces. Consequently, the term $P'V_0$, although itself small, can

be expected to dominate the difference in potential between the two faces. This indicates that the μ gradient is largely due to the normal stress gradient (which is reasonable). More importantly, however, is the magnitude of G_{net} - compared with the reference state of a hydrostatically stressed grain, the potential between either of the faces and open voids is much greater. A similarly large μ can be expected to exist between stressed grain boundaries and sites of hydraulic extension fracturing because of the zero or near-zero effective stress perpendicular to the walls of these fractures. Thus, PS transfer from surfaces of compressive deviatoric stress to surfaces of tensile deviatoric stress is not favoured. The greater potential between stressed grain boundaries and voids indicates the most energetically stable condition.

This conclusion shows that porosity substantially influences the scale at which PS is isovolumetric. Raj (1982) has determined an expression for this equilibrium pore size. An ideal elongate triple junction (Fig. 2-7) will have cross-sectional geometry given by $r_0 = (\gamma/p_e)$, where r_0 is the equilibrium radius of curvature of the grain wall along the pore, γ is the crystal-fluid interfacial energy, and p_e is mean effective pressure. (This relationship assumes grains are equant, and that γ is isotropic and

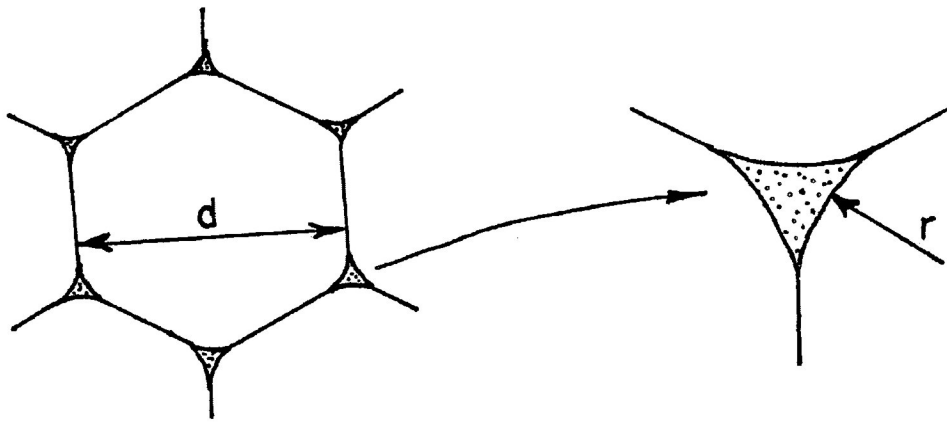


Figure 2-7: Cross-section of an ideal triple junction. d is grain size and r is pore wall radius of curvature. From Raj, 1982; Fig. 2.

independent of size. As written by Raj, p_e includes a correction factor to account for stress concentration due to island and channel boundary structure.) Such triple grain junctions would terminate at four grain junctions.

An incidental note is that PS is unlike the other diffusive mass transfer mechanisms regarding the scale at which grain volume is conserved. Both Coble creep and Nabarro-Herring creep are isovolumetric at the scale of individual grains because solid-state diffusion involves diffusion of vacancies as well as of mass.

2.4 Dynamic Aspects of Pressure Solution

2.4.1 Qualitative Controls on Material Flux During Pressure Solution

Having established that the driving force of PS is μ generated by a normal stress gradient, the kinetics of the process are worth considering. The three processes in PS - dissolution, diffusion along the grain boundary, and precipitation - are dependent, so that all three exert some control over the net rate of transport and in turn the strain rate. It has, however, been commonly supposed that of the three, diffusion is very much slower than dissolution

and precipitation, and exerts dominant control over strain rate (Gratier and Guiguet, 1986). There are reasonable grounds for this. One indication comes from the empirical observation that PS textures are better developed in finer-grained materials (Heald, 1956; Kerrich, 1978). The greater area of contact between larger grains requires diffusion of matter along a greater distance, and suggests diffusion is a major control. An isotopic fractionation study by Kerrich *et al* (1977a) showed quantitatively that the transition temperature from crystal plastic strain to diffusive deformation is strongly grain size dependent; transition temperatures between 200° and 360°C for calcite were accompanied by change in grain size from 1000 to 10 µm.

Another suggestion of rate control by diffusion comes from infinite solution theory. When a liquid is very fluid and a solid has appreciable solubility in the fluid, it is the reaction at the solid-fluid interface rather than diffusion of solute away from the interface which tends to limit the rate at which solid becomes solute (Readey and Cooper, 1966, in Raj, 1982). Along an intergranular film, however, the apparent viscosity of a liquid is much greater than the viscosity of the same liquid in a less confined space. For example, Rutter (1976) has calculated that for a 2 nm thickness of water, apparent viscosity is greater than 10^5 times that of unadsorbed water. This value leads to an estimation,

previously noted, that diffusive flux along the 2 nm film will be five orders of magnitude less than the flux in unadsorbed water. If an island and channel structure is present, the lesser net cross-sectional area of the channels relative to the continuous intergranular film assumed by Rutter to be present would make this a conservative estimate.

Rutter's result indicates that diffusion rates can be expected to be lower along intergranular films than in pore water. In particular, there is the implication that in aggregates with local non-equilibrium porosity, precipitation will not greatly affect mass flux. High porosity provides a large number of sites at which nucleation and growth by precipitation can occur. Even if precipitation is a relatively slow process, rapid transport through pore water to pore walls is possible, and a relatively large area of pore wall is able to accept the mass flux. As porosity is decreased, precipitation will tend to have a greater effect on the rate of net transport. Lower porosity involves shorter distances of diffusion through pore fluid, and a lesser area for precipitation to occur on. Greater levels of saturation of the pore fluid are likely to reflect this change. When equilibrium porosity is attained, precipitation will have stopped entirely within that pore. PS will continue, however, if diffusion is able to transport material to void spaces further away. Thus precipitation will

present greater resistance to net flux, and perhaps begin to exert dominant control over it as equilibrium pore size is reduced.

A third possibility is interface-controlled PS. Raj (1982) has reported data from experiments on saturated rock salt aggregates indicating strain rate is proportional to reciprocal grain size; his constitutive equations for PS controlled by interface reaction (unlike the equations for diffusion control – see below) share this characteristic. As noted by Raj, there is no indication of how applicable the theory of dissolution in an infinite solution is to the same process along an intergranular film. More specifically, what limits matter transfer from the grain to the film? If the interface reaction dominates overall deformation kinetics, then the interface boundary must have a strong negative effect upon dissolution compared to dissolution from a single face bounded only by fluid.

2.4.2 Quantitative Controls on the Rate of Pressure Solution

Diffusive mass transfer, including PS, is unlike other deformations in that the textural geometry is sufficiently constrained to permit derivation of theoretical constitutive equations (Rutter, 1983). The success of such an equation depends

on the validity of the assumptions made. The preceding discussion has illustrated that a fundamental decision in developing a constitutive equation for PS is to identify the relative contributions of dissolution, diffusion and precipitation to the overall strain rate. For example, both Rutter (1976) and Durney (1976) assumed diffusion would be the dominant factor in control of strain rate. This assumption was effected by equating diffusive flux with total flux. Raj (1982) instead produced separate constitutive equations for dominantly interface-controlled and dominantly diffusion-controlled PS, as well as a composite equation derived from both which predicts the strain rate that results when both dissolution and diffusion have a significant effect upon net strain rate.

A second illustration of the importance of assumptions is also given by Raj (1982) who treated PS as occurring in two ways: as densification, which is a negative dilation occurring in the presence of interconnected, non-equilibrium porosity, and as creep, which is bulk strain in the presence of equilibrium sized pores. In light of the argument that PS creep is an unlikely process (see sub-section 2.3.3), the value of these clearly stated assumptions is apparent.

Shown below are the constitutive equations of Rutter (1976) and Durney (1976), and the two equations for each of interface and

diffusion controlled mass transfer by Raj (1982). Note that each of these equations describes grain scale PS and not the development of larger features.

From Rutter (1976):

$$\dot{\epsilon} = \frac{32\sigma V C_o D_b w}{RT \rho d^3} \quad (2-1)$$

From Durney (1976):

$$\dot{\epsilon} = \frac{6 C_o D_b w}{\rho r_c^2} \left[\frac{\exp \frac{4(\sigma - \sigma_0)V}{3RT} - 1}{3RT} \right]$$

From Raj (1982):

For deviatoric creep:

(i) controlled by the interface process,

$$\dot{\epsilon} = \frac{\sigma_{VM} V}{3kT} \frac{k_1 \bar{c}}{d}$$

(ii) controlled by diffusion,

$$\dot{\epsilon} = \frac{\sigma_{VM} V}{1.3\eta d^3} \bar{c} \propto$$

For densification:

(i) controlled by the interface process,

$$\dot{\epsilon} = \frac{(p_e - \frac{\sigma}{r_c} V) k_1' \bar{c}}{k T d}$$

(ii) controlled by diffusion,

$$\dot{\epsilon} = 2.3 \frac{(p_e - \frac{\sigma}{r_c} V) \bar{c} \infty}{\eta d^3}$$

where C_0 is equilibrium concentration of the solid in unadsorbed water,

\bar{c} is an estimate of crystal solubility in the adsorbed fluid,
 D_b is diffusivity of the adsorbed film,

d is grain diameter,

k is Boltzmann's constant,

k_1' is an expression of linear growth velocity per molar driving force. The quantity $k_1'c$ is measurable experimentally (Raj, 1982).

p_e is mean effective pressure,

R is the gas constant,

r_c is the radius of the contact area between grains,

r_p is the radius of the pore wall,

V is the molar volume of the solid,

x is the ratio of area of island contacts to total boundary area (see text),

∞ is a parameter describing the interface boundary:

$$\infty = xh/b, \text{ where } h \text{ is height of the islands, and } b \text{ is the lattice spacing,}$$

σ is the crystal - fluid interfacial energy,

σ is effective normal stress at a grain boundary,

$(\sigma - \sigma_0)$ is an expression of differential stress,
 σ_{VM} is deviatoric stress, and
 η is fluid viscosity.

Inspection of these equations shows which factors can be varied to favour PS:

Stress (σ , $(\sigma - \sigma_0)$, $(p_e - \sigma/r_c)$ and σ_{VM}) All equations show a linear dependence upon stress, although it is expressed in different ways. The ability of stress to raise strain rate is limited. Although the PS field boundary for calcite shown in Figure 2 extends above 10^8 Pa (1. kbar) normal stress, this is probably not correct as (2-1) is the result of an approximation for $\sigma < 30$ MPa, and Rutter shows no comparable applicable equation for $\sigma > 100$ MPa. Kerrich and Allison (unpublished) have placed a cataclastic limit on Rutter's (1976) DMM for quartz which eliminates much of the PS field at the lowest temperatures and highest stresses.

The use of effective stress in these equations shows that pore pressure plays a part in the kinetics of PS. Increasing P_f without a corresponding rise in normal stress will reduce effective stress, and slow PS (McClay, 1977). As well, it will reduce plasticity and cataclasis (Paterson, 1976) and will favour particulate flow.

Another factor that will influence stress is the presence of very fine grained interstitial material, e.g. clay. Higher proportions of matrix will cause coarser grain fractions to embed themselves and so reduce stress concentration (Siever, 1959; Weyl, 1959).

Raj's equations show that mean effective stress is important to densification and bulk deviatoric stress is important to creep. A rock with equilibrium porosity will not be subject to densification, and so only deviatoric stress will cause further strain. However, it is not true to suggest that only mean effective stress will cause densification. A porous solid will undergo both strain and densification if deformed by a deviatoric stress. This is an indication that Raj's analysis for densification is approximate.

Reference solubility (C_0, \bar{c}) All equations presented have an expression for solubility under the conditions of interest but without the normal stress gradient along the grain boundaries. For each equation, this reference solubility is directly proportional to strain rate. One control on solubility is P_f . In general, solubility rises with P_f (see eq. 3, Robin, 1978). Thus, if an increase in total normal stress was equalled by an increase in P_f , the rise in P_f

would have no mechanical effect on strain rate but would still cause the solubility and strain rate to rise. Pore fluid pressure may be shown as a third dimension on a DMM (Borradaile, 1981). Such a representation would incorporate both effects of pore pressure.

A factor affecting solubility is permanent strain. Permanent strain will raise solubility along a free face, and results in higher dissolution rates. Engelder (1982) has reported a natural example in which twinning in calcite has enhanced dissolution, and Bosworth (1981) has calculated that in the case of the halite blocks used by Sprunt and Nur (1977a) in their PS analogue experiments, plastic strain raised the μ of the material more than the elastic strain did. Permanent strain along an intergranular boundary can be expected to have a similar effect. Higher strain energy causes faster dissolution but it is irrelevant whether the cause of this strain energy is elastic or permanent strain (Robin, 1978). (Robin noted cataclasis will also increase solubility.) As long as diffusion alone does not effectively control the PS flux, permanent strain will affect the rate of dissolution and, in turn, the material flux which determines the strain rate. This is the reason for the presence of the k'_1 term, a measure of the so-called "interface velocity", in Raj's equations.

It is also possible to affect grain solubility through changes

in solution chemistry. This approach has been applied experimentally in order to increase strain rates, e.g. Gratier and Guiguet (1986). Formation brines could have the same effect in nature.

Diffusion path width (w) Rutter and Durney have both explicitly included grain boundary width, w , in their constitutive equations. The term \propto in Raj's equations for diffusion-limited strain includes the value of the film thickness. In all of these, path width is linearly proportional to strain rate.

The presence of a term in the constitutive equation to account for boundary width suggests that this value is readily quantifiable. In fact, it is not known whether the fluid-crystal transition is gradual or abrupt (Raj, 1982). Elliot (1973) has referred to a sandwich model: a central band of high diffusivity flanked by zones of lower diffusivity. Whatever the grain boundary structure, the rate of diffusion will vary across its width (Robin, 1978).

Regardless of variation in diffusivity across the interface, use of the equations requires some value be fixed on the width term. Rutter (1976) suggested the effective width is twice the Burger vector. In contrast, McClay (1977) has said a value closer to $100b$ is more realistic. Any value used will be approximate; factors such as the degree of lattice misalignment will cause

individual boundary widths to vary.

Clay is a material which is thought to hasten PS by promoting diffusion (Heald, 1956). This effect is attributable to its very fine grain size which provides many paths for diffusion (Weyl, 1959; Rutter, 1976). According to de Boer (1975), only smectitic (swelling) clays will appreciably aid diffusion. However, studies by Heald (1956) and also Thomson (1959) suggest situations in which illite (a non-smectitic clay) has hastened PS.

Temperature (T) The equations of Rutter and of Durney, and Raj's equations for interface-controlled deformation indicate PS has a low T sensitivity. T appears explicitly in the denominators of these equations while the numerators include terms directly related to T: all four equations include a reference solubility term, and both Rutter's and Durney's include grain boundary diffusivity. An increase in T will cause both numerator and denominator to increase, and these increases will tend to cancel. Rutter (1983) has noted that the T sensitivities of both the viscosity of water, η , and the heat of solution of materials which pressure solve are low, and has suggested that these are related to a low heat of activation, H, in an Arrhenius relation for PS, $\dot{\epsilon} \propto \exp(-H/RT)$.

The absence of T and presence of η in the denominator of Raj's equations for diffusion-controlled PS, and the reference solubility

term in the numerator, indicates diffusion-controlled PS is relatively T sensitive, in contradiction of the equations of Rutter and Durney. Note that Rutter (1976) has suggested that temperatures above the critical point (373 °C) may influence PS by causing breakdown of the intergranular film.

Grain size (d, r_c) Strain rate varies with grain size raised to exponents ranging between -1 and -3. The inverse relationship between strain rate and d is confirmed by petrographic evidence (e.g. Heald, 1956; see Kerrich, 1978). While Rutter's as well as Raj's equations for diffusion-controlled PS (and also Elliot, 1973) indicate strain rate is proportional to the inverse cube of d , Raj's equations for interface-controlled PS have a simple reciprocal relationship with d . The third power reflects greater importance of the length of the diffusion path.

Durney's equation is not readily compared because it uses contact area radius, not grain size, as its dimensional control.

2.4.3 Bulk Behavior During Pressure Solution

In terms of the fabrics produced by PS, there are two scales of operation (Fletcher and Pollard, 1981). PS of porous aggregates

will involve diffusion along adsorbed films no longer than the intergranular contacts. The fabrics that result are textural in scale: for example, truncated and indented grains, and cementing overgrowths. Because of increased grain size (which involves longer diffusion paths) and porosity loss (which lowers stress concentration), strain rate will decline over time.

PS in aggregates with equilibrium porosity operates on a larger scale than in more porous rocks. Thermodynamics indicate material must diffuse longer distances in order to reach a site for precipitation (sub-section 2.3.3). The production of a spaced cleavage may be associated with this longer range diffusion. In some cases these structures will provide paths of easier diffusive flow, e.g. clay-lined stylolites.

Fluid flow can influence the bulk strain regardless of the scale of diffusion. It will raise the strain rate by contributing to greater mass flux. Interstitial fluid expelled during compaction does not have this effect. While dissolved matter will be carried away, the remaining fluid will be at the same concentration and the μ will be unchanged. In comparison, percolating unsaturated fluid has the potential to move much greater volumes of material (Green, 1984). A supersaturated incoming fluid is also possible, thus slowing or halting PS locally.

Also ignored by the constitutive equations is particulate

flow. This will be controlled particulate flow (Borradaile, 1981). Gray (1981) has reported this deformation in a cleaved calcareous mudrock.

Bulk strain can be described by rheological models. When deformation occurs by grain scale diffusion, the rock is thought to behave as an incompressible linear viscous fluid (Elliot, 1973). It has been noted above that PS in a porous aggregate will instead occur with a gradually declining bulk strain rate. Such non-linear behavior results from compression of the solid, and is an illustration of how constitutive equations do not describe bulk behavior. Fletcher (1982) has produced equations which specifically describe bulk behavior. With the assumptions that porosity is constant and that the soluble phase supports the entire load on the rock, Fletcher showed that macroscopic diffusion in a rock results in isotropic linear viscous behavior. This approach yielded results of at least qualitative value but which in the present form do not explain the formation of structures such as cleavage.

Cleavage Development

PS produces spaced cleavages in diagenetic and lower metamorphic grade environments. In order to avoid the

complication of phase change, stylolites are considered first.

Like other PS structures, stylolites do not form in completely unlithified material. They develop in rocks of minimal porosity, as commonly seen in clastic and carbonate rocks. An extreme example of this is stylolites in glassy rhyolites (Bloss, 1954; Goldring and Conolly, 1962). Heald (1956) deduced that stylolite formation was penecontemporaneous with authigenesis in some Appalachian sandstones, another indication that stylolite development is not syndepositional. They are probably initiated by some mechanical anisotropy (Nelson, 1983; Fletcher and Pollard, 1981; Park and Schot, 1968). Diffusion related to the growth of stylolites might occur in two ways. In both cases dissolution will occur at the stylolite, resulting in the accumulation of an insoluble residue.

1. Stylolite growth caused by diffusion away from the stylolite. Non-equilibrium porosity in the rock adjacent to the stylolite will cause material to diffuse away from the stylolite and into the nearby porosity. This is an isovolumetric deformation. Stylolite growth in such a fashion is limited by the infilling of porosity. This extends the diffusion path and lowers the μ gradient. Fletcher and Pollard's (1981) "anticrack" model predicts that compressive stress will be most intense at the edges of stylolites, and suggests that growth of solitary

stylolites will occur in this manner.

Such a path of material diffusion explains the decrease in hardness with separation from stylolites (Nelson, 1983), which is circumstantially supported by the observation of different colour of weathering immediately adjacent to stylolites (e.g. Lockport dolostone; P. Clifford, pers. comm.).

2. Stylolite growth resulting from diffusion along the stylolite. Diffusion along a stylolite is towards a sink of non-equilibrium porosity, including extension fractures (where fibrous vein fillings may form) or towards a conduit for pore fluid flow. The insoluble residue, with its very fine-grained phases, provides a route for easy diffusion and allows longer diffusion paths. Fletcher and Pollard (1981) have modelled stress fields which result in the growth of stylolites paired with the growth of extension fractures. They have also suggested, with reference to natural examples, that the interaction of consumption between matter along stylolites, growth of extension fractures and sliding along shear fractures may result in a macroscopic equivalent of diffusion controlled particulate flow (Raj and Ashby, 1972).

PS and Metamorphism

PS is a powerful agent in lower grades of metamorphism. Under these conditions, PS is manifested through mineralogical differentiation as it is by stylolite growth during diagenesis. For example, Kerrich et al (1977b) showed that following transition from mass-conservative crystal plastic deformation to PS, a large scale shear zone in Yellowknife, N.W.T. experienced significant losses of silica and soda.

The production of mineralogically distinct layering, often associated with PS during metamorphism, is in some cases driven solely by stress gradients without associated phase change. This mass transfer is usually related to folding. For example, cleavage development in crenulated metapsammities and metapelites accompanied by mineralogical segregation has been attributed to diffusional mass transfer (Gray, 1979). Gray and Durney (1979) have discussed the variables in this situation. They suggest that normal stress on the layering is likely to be higher on fold limbs than hinges, especially as folds tighten, and mean stress will be lower, at least in incompetent layers, in the hinges. Together these effects create a μ gradient. (Gray and Durney (1979) also argue that layer-parallel orientation of elongate grains results in higher average normal stress on limbs than on hinges, but this

effect of stress concentration is only local and will not extend from limb to hinge.) Their discussion raises a question regarding the style of deformation which occurs during formation of the crenulation cleavage. Assuming that the cleavage is formed by diffusive mass transfer (and not by simple preferentially oriented growth of micaceous phases), does the mineralogical redistribution occur through precipitation (of quartz) under a substantial effective minor principal stress? This difficulty is avoided if cleavage develops under a high P_f (which results in low effective stresses). Another possible explanation is that folding may be accompanied by minor disaggregation along the hinge (also perhaps aided by elevated P_f). Disaggregation would provide microporosity for sites of material precipitation. A macroscopic equivalent of this process occurs when adjacent layers with little competency contrast form saddle reefs during folding (Ramsay, 1967).

Differentiation may also occur in conjunction with chemical change. Non-isochemical PS in a shear zone reported by Kerrich et al (1977b) and also by Beach (1974) is an example of large scale redistribution of matter. PS differentiation with associated chemical change also produces metamorphic cleavages. For example, Knipe and White (1977) and Knipe (1981), in electron

microscopy studies of slaty cleavage, reported that growth of new phyllosilicate phases was accompanied by PS of detrital quartz grains. These cleavages in metamorphic rocks are not sites of accumulation of insoluble material, unlike stylolites. Beach (1979) has suggested numerous mineralogical reactions that may occur at these sites. These reactions include the breakdown of feldspar and epidote to illite and muscovite, and the generation at higher metamorphic grade of muscovite. Dehydration (which tends to raise P_f and cause fluid flow) and silica production often occur in these reactions, and a decrease in net volume of the solid phases excluding silica is nearly ubiquitous. The reactions may also increase pH sufficiently to elevate silica solubility (an effect suggested previously by Lerbekmo and Platt (1962) and Thomson (1959) to occur in stylolites). The cleavages are thus suggested to be sites of both metamorphic mineralogical reaction and strain. The relation between these reactions and PS ("incongruent" PS in Beach's (1979) terminology) is complex; the differential stress helps drive the reaction (Fyfe, 1976) which in turn may contribute to the μ driving the diffusion of matter (Rutter, 1983).

2.5 Previous Experimental Work

Experimental work relevant to PS has followed two lines of inquiry. The earliest work was concerned with verification of the phenomenon of PS following Thomson's (1862) hypothesis that differential stress will cause preferential dissolution with concomitant precipitation. Experiments by Poynting (1881), Becker and Day (1905), Taber (1916) and Wright and Hostetter (1917; in Kerrich, 1978) confirmed Thompson's prediction. Becker and Day (1905) were able to demonstrate force of crystallization as well as PS. Both Taber (1916) and Wright and Hostetter (1917) showed optically that overgrowths on alum crystals are at the same state of stress as their host crystal. Russell's (1935) use of the photoelastic technique indicated preferential dissolution of an alum crystal occurred at points of high normal stress. Correns (1949) showed that factors controlling dissolution and growth of alum include stress, solute concentration, temperature and the nature of the interface.

A new approach in phenomenological experimentation was made by Rutter (1976) who attempted to show a quantitative relationship for diffusion and strain. In his tests, pressure-solved material did not remain within the pore space of the sample but instead was allowed to diffuse into an adjacent reservoir of

water. Powdered salts were first compacted dry. With the addition of water, a steady displacement rate resulted. Data from the experiments was inconclusive, apparently because of experimental artefacts.

Experiments by Sprunt and Nur (1977a) were performed to establish an experimental relationship between dissolution and stress. Blocks of various materials were each pierced by a single cylindrical hole. The blocks were then submerged in chemically active liquid and a uniaxial load was applied perpendicular to the hole axis. In those tests in which dissolution of the block along the hole was controlled by the surface reaction (as opposed to the process of transport of solute away from the solid surface), it was found that solution rate was proportional to local stress along the circumference of the hole.

Bosworth (1981) repeated Sprunt and Nur's (1977a) experiment with halite. Halite was deformed while dry, and the crystal dissolved after release of the load. Plastic strain, not stress, was found to account for the pattern of preferential dissolution of the halite. Green (1981) has discussed the work by Sprunt and Nur (1977a) as well as that by Bosworth (1981).

A second line of investigation has been concerned with production of PS textures in rock and rock analogues (see Table 2-1). The earliest of such work was done by Spring (1888) and Le

Temperature (°C)	Pc (MPa)	Pf (MPa)	Pore fluid(s)
20° to 345°C	117. to 262.	maximum of 110.	---
305° to 658° plus one test at 212°C;	100., 200. and 300.	Pf < or = Pc	NaCl and NaOH solutions
272° to 560°C	17. to 83.	---	water; NaOH, NaCl and Na2CO3 solutions; and a formation brine
400°C	41. ; applied over 4 weeks	---	0.5 M Na2CO3
340°C	20. at start; raised to 88. over 67 days; Pc then held constant	16	1.0 M NaCl
room temperature	1.6 to 28.	---	carbonic acid of various concentrations
25°, 200°, 260° and 330°C	25., 51. and 76.	0 (?)	1.0 M NaCl
room temperature?	98.	sample dry	---

270° to 280° C	35. to 146.	25. to 99.	water
one test at 22° C; others at 130 to 180° C	50. to 150.	15 to 50.	water
one test at 20° C; all others at 360° C	0.1 and 150.	---	air; water; 0.1, 0.5 and 1. N NaOH for silica; water and 5% NH ₄ Cl for calcite

Chatallier (1892, in Kerrich, 1977). Both workers succeeded in producing cementation at grain boundaries within crystal aggregates which had been subjected to differential stress.

A number of workers in the 1950's and 60's were interested in experimental lithification of clastic sediments. Some of these studies dealt solely with simple dissolution and precipitation, e.g. Heald and Renton (1966), while others encompassed deformation. A series of tests by Maxwell (1960) were performed to simulate the effects of burial upon compaction and cementation. Variables considered by Maxwell included P_c , P_f , temperature and temperature gradient, time, texture, and the presence of fluids and their composition and flow. No bulk differential stress was used and hydrostatic stress was applied almost instantaneously. Maxwell found no textural evidence for PS. Cataclasis occurred even above 300°C, and particulate flow was thought to be partially responsible for the strain. An overall trend towards increase in bulk density with increase in temperature was interpreted by Maxwell to indicate weakening of quartz due to "increasing ease of fracture"; this was more likely due to enhanced crystal plastic behavior of the quartz. Simple dissolution and precipitation of quartz were also responsible for changes in texture. These effects were significant above 270°C, and were favoured by alkaline saline solutions over distilled water.

Ernst and Blatt (1964) investigated the solubility of clastic quartz and the development of authigenic overgrowths by compacting granular samples. To make more silica available for cementation, silicic acid ($\text{SiO}_2 \cdot \text{H}_2\text{O}$) was sometimes added to the samples. "Metamorphic textures" were developed in those samples subjected to non-zero effective stresses (of unknown magnitudes). These included sutured grain boundaries, fractures, undulatory extinction, deformation lamellae and sub-grain development. The latter were produced at 658°C and presumed to be the product of thermal recrystallization. Sutured boundaries appeared to be produced only at temperatures below 360°C . Ernst and Blatt (1964) attributed this texture to PS. In one illustrated sample showing sutured boundaries, other deformation textures were largely absent, suggesting that PS was dominant.

Renton et al (1969) conducted two series of tests. In the first, a quartz crystal or basal plate surrounded by a quartz or zircon sand, and the sample then compressed. Pitting of the quartz crystals by the sand grains was attributed to PS. The zircon sand produced larger pits than the quartz sand. Deformation of a dry sample produced pitting accompanied by fracturing. Fracturing also resulted when "loads were excessive" (p.1109; Renton et al, 1969) but unfortunately no measurement of strain rate was made. Crystal plastic deformation was not discussed, although it seems

possible that the pitting was produced by this mechanism.

A second series of experiments by Renton et al took the conventional approach of compaction of a sand. Little cataclasis was noted; concavo-convex grain contacts were common, and euhedral overgrowths were present. The finer the quartz sand, the greater the compaction that occurred. Chert sands were shown to be more compacted than the quartz sands. These results were attributed to PS, but the effects of simple dissolution and precipitation and of particulate flow, although not discussed, appear to have been dominant.

de Boer (1975) conducted a long term experiment similar to that of the present investigation. The single sample consisted of quartz sand interlayered with separate bands of kaolinite, bentonite, illite and organic matter for which good development of PS textures was claimed. Curved grain contacts were present with interpenetration of up to one-third the grain diameters. Minor local suturing occurred along these contacts. This texture was slightly better developed in the presence of intergranular clay films. Overgrowths of both crystalline quartz and amorphous silica were also present. The quartz overgrowths occurred throughout most of the sample. They were in optical continuity with the host grains, and generally were adjacent to PS contacts. (Albite overgrowths were noted on the accessory feldspar present.) The

amorphous silica rims showed at least three layers. Ferric oxide (due to oxidation of the pressure vessel) had an incomplete spatial association with the silica.

de Boer (1975, 1977) also conducted experiments on the compaction of quartz and calcite sands. A logarithmic relationship between rate of loss of porosity and time was found for the calcite sand. The presence of water clearly aided compaction but the composition of the water had little or no effect. Compaction of the calcite samples was effected primarily by crystal plasticity and cataclasis, with dependent, but not rate-determining, chemical dissolution. Several series of tests were performed on quartz sands leading de Boer to conclude on the basis of rate of porosity loss that PS was active at both 25° and 200°C in samples held at 51. MPa.

Deelman (1975) produced grain indentation in a heterogeneous mixture subjected to hydrostatic pressure. Harder materials were observed to have indented softer ones. Deformation was correctly inferred to have been accomplished by plastic flow of the softer material. A conclusion that water plays no part in PS was drawn from this result, however. Burger (1975) criticized Deelman for not presenting evidence for the presence or absence of plastic strain in his samples, and for omitting strain rate in his discussion of PS in nature. Atkinson and Rutter (1975) further

criticized Deelman for employing conditions of high applied stress and low temperature which would lead to plastic deformation or fracture of grains regardless of the presence of water, and for neglecting to discuss the effect of pore pressure in reducing applied stress in nature.

Sprunt and Nur (1976, 1977b) deformed hollow and solid cylinders of quartz arenite. The geometry of the hollow cylinders led to an effective stress gradient across the cylinder wall. In all but a dry control sample, a loss of porosity occurred without observable cataclasis; PS was inferred to be operative. Porosity reduction showed a strong direct relation to P_f , and was greater in the finer-grained samples. Hydrostatic stress produced much less porosity loss than non-hydrostatic stress, but the data relating porosity loss and effective stress were equivocal, and did not show a direct relationship as would be expected. The decrease with time of the rate of porosity reduction was attributed to an initial silica undersaturation of the pore fluid.

Baker et al (1980) conducted two series of tests, one series to model PS, the other producing hydrothermal recrystallization. Stable isotope data were used to determine the extent of isotopic equilibration, and estimates of porosity and specific surface area were made using a nuclear magnetic resonance technique. Degree of isotopic equilibration was shown to be directly related to

temperature, and appeared to be inversely related to grain size. Mechanical compaction caused some loss of porosity. Although PS was concluded to have been active, no definitive evidence for this was presented.

Gratier and Guiguet (1986) applied differential stress to thin layers of quartz sand held between quartzite blocks under P_c . Particulate flow occurred early in their experiments. Plastic deformation of the grains was minor, and grain indentation and "sealing" of grain boundaries was observed, along with ten micron-scale, void-filling quartz growths. The development of a preferred dimensional orientation was shown to be related directly to both the test duration and the pore fluid solution concentration.

CHAPTER 3: EXPERIMENTAL APPARATUS

3.1 Deformation Machines

Triaxial Rig. The stress relaxation tests of this study were performed in a Donath triaxial rig. This is a hydraulically driven machine with a computer controlled loading capability.

Samples are deformed within the pressure vessel (Fig. 3-1). A maximum working confining pressure (P_c) of 207 MPa (2.07 kb; 30,000 psi) is allowed. Confining pressure is applied laterally by hydraulic fluid surrounding the sample within the vessel and axially (less friction) through the ram which drives the lower piston, and results in a nearly true hydrostatic pressure. Differential load is also applied by the ram and lower piston, and results in a maximum compressive stress being applied axially. The pressure vessel is surrounded by a heating jacket (not shown) which is controlled by a thermostat. The temperature control is set slightly above ambient temperature in order to maintain constant temperature during a test.

Two components present on the pressure vessel were used to monitor sample behavior. A linearly variable differential transformer unit (LVDT) was used to measure changes in sample length. Movement of the ram results in change in analogue signal

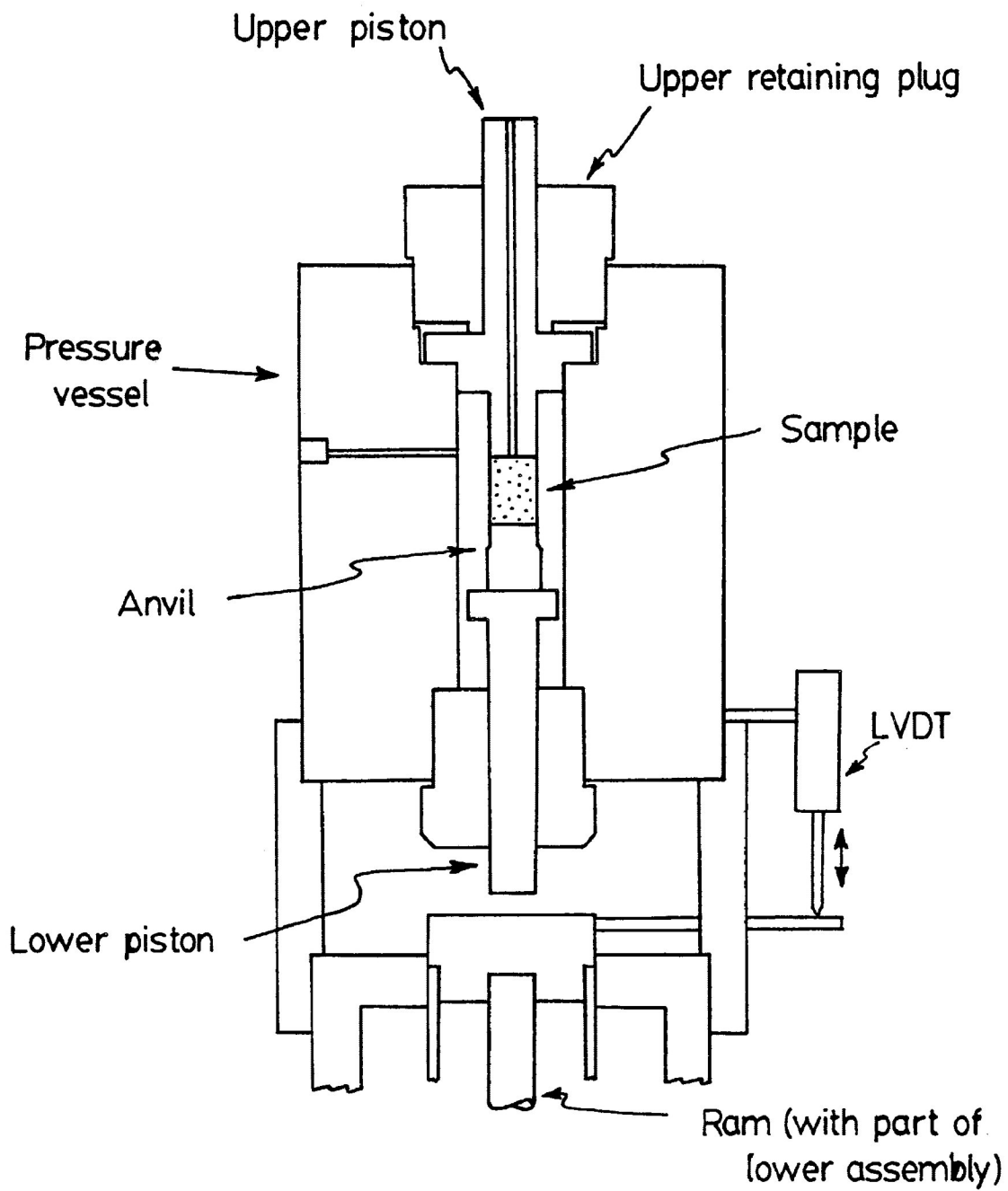


Figure 3-1: Schematic of the pressure vessel and related components.

output from the LVDT. This signal was used to calculate sample shortening. Appendix B outlines the corrections made for machine distortion in arriving at this figure.

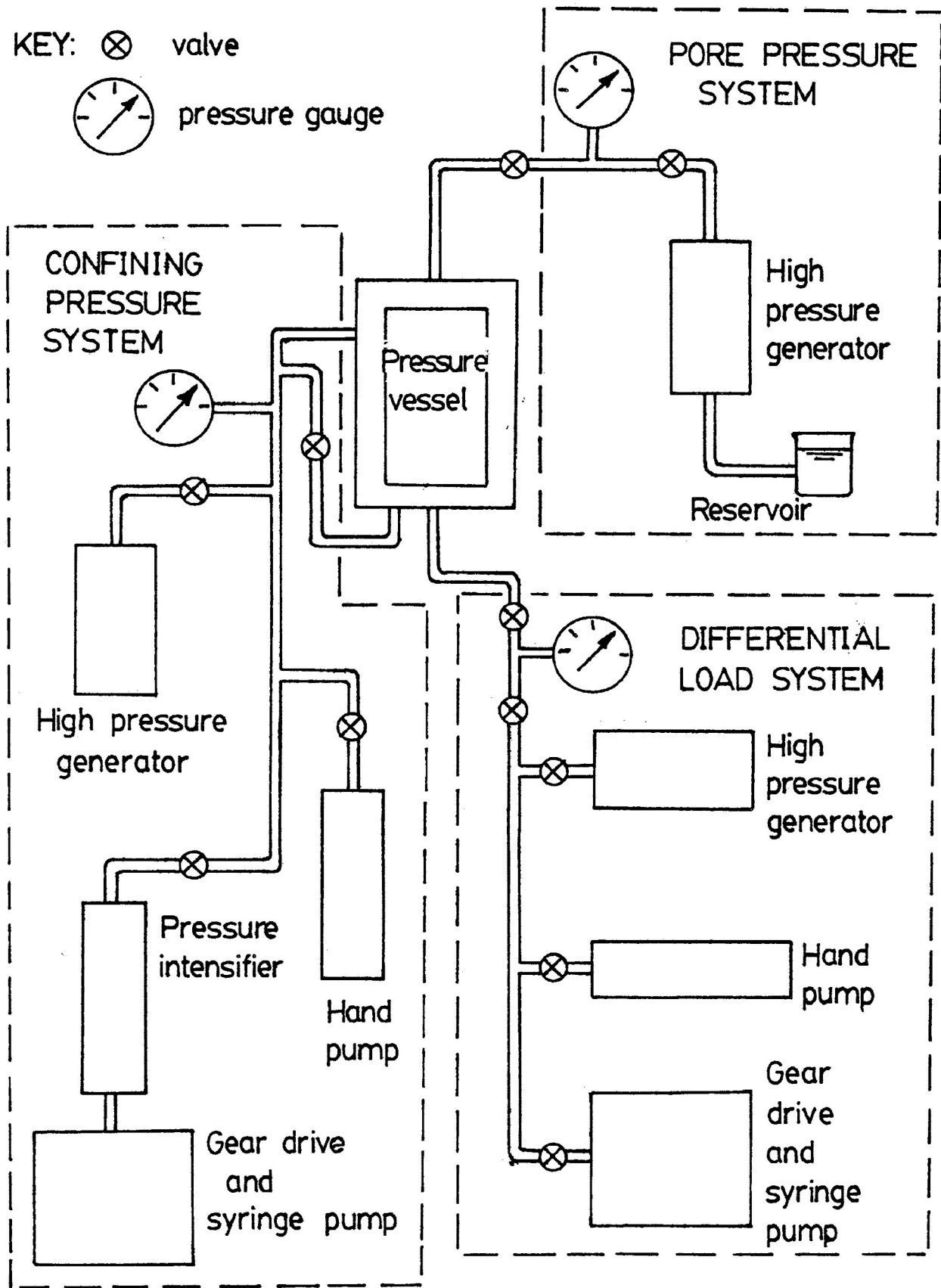
The second measurement device is a load cell. This consists of a strain gauge rosette on a collar within the upper retaining plug. The power supply to the strain gauges was adjusted to give a 1 mV change in output signal for every 1000 lb axial load.

Three hydraulic systems are present on the Donath rig (Fig. 3-2). The 10,000 psi hand pump was used to prime the confining pressure system. Confining pressures up to 30,000 psi were obtained by means of a hand-powered high pressure generator and a syringe pump driven by a multi-gear electrical motor. The hydraulic fluid used in this system is a low viscosity silicone oil. P_c is monitored by means of a pressure transducer (not shown).

The components of the differential load system are similar to those of the confining pressure system. The hand pump, also with a 10,000 psi rating, is used to seat the lower piston and anvil against the sample. Differential loading of the sample is accomplished with the syringe pump. Lower pressures (<10,000 psi) within the hydraulic lines of the differential load system allow an ordinary hydraulic fluid to be used. Higher differential stresses within the specimen, however, are obtained by means of a mechanical advantage (27.0 times for a sample of 0.5 in diameter) between the ram and sample.

KEY: ⊗ valve

⊙ pressure gauge



Pore fluid pressure up to 30,000 psi is produced by a high pressure generator like those of the confining pressure and differential load systems. The pore fluid communicates with the sample by a hole bored in the upper piston.

The stress-strain measurement system has several elements (Fig. 3-3). As a sample deforms, analogue signals from the LVDT and load cell are sent to a chart recorder which provides a record of displacement (X) vs. load (Y). The signals are passed on to an analogue-digital converter and are then received by the computer in digital form. The computer calculates and records the stress and strain experienced by the sample. If the sample is being loaded, the computer then determines an appropriate change in differential load in order to maintain the constant displacement or strain rate desired. A signal is then sent via the analogue-digital converter to a variable speed control unit. This unit controls the electric motor of the differential load hydraulic system.

To minimize the problem of electrical noise, voltage regulators are used to smooth the current powering the load cell, LVDT and computer.

Hydrostatic Rig. The hydrostatic deformation rig (Fig. 3-4) is much simpler than the triaxial rig. The pressure vessel is rated for pressures up to 1 kb (100 MPa). Hydraulic fluid can be pumped into the pressure vessel by means of a hand pump and a high

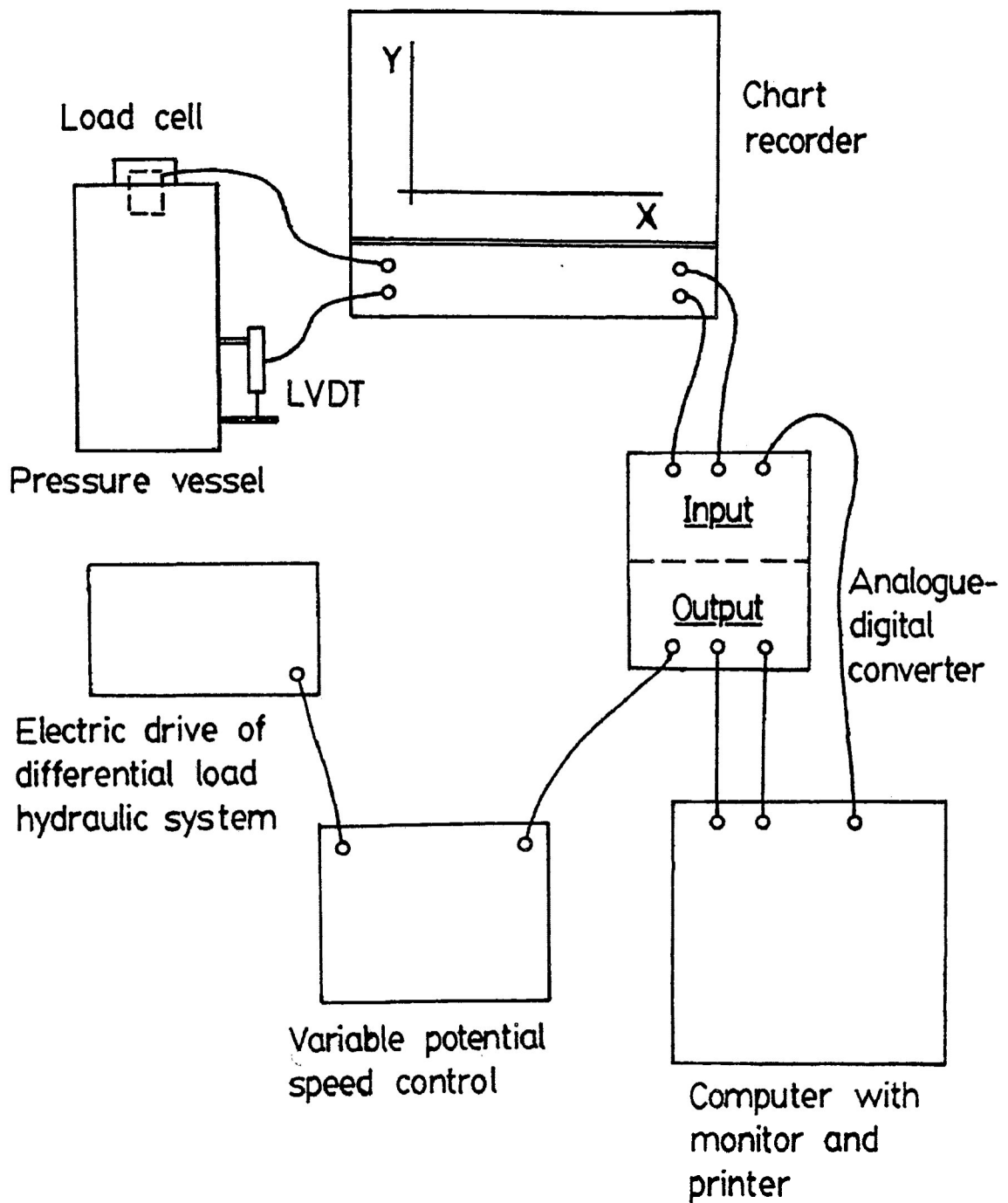


Figure 3-3: Monitor and control system of the Donath triaxial rig.

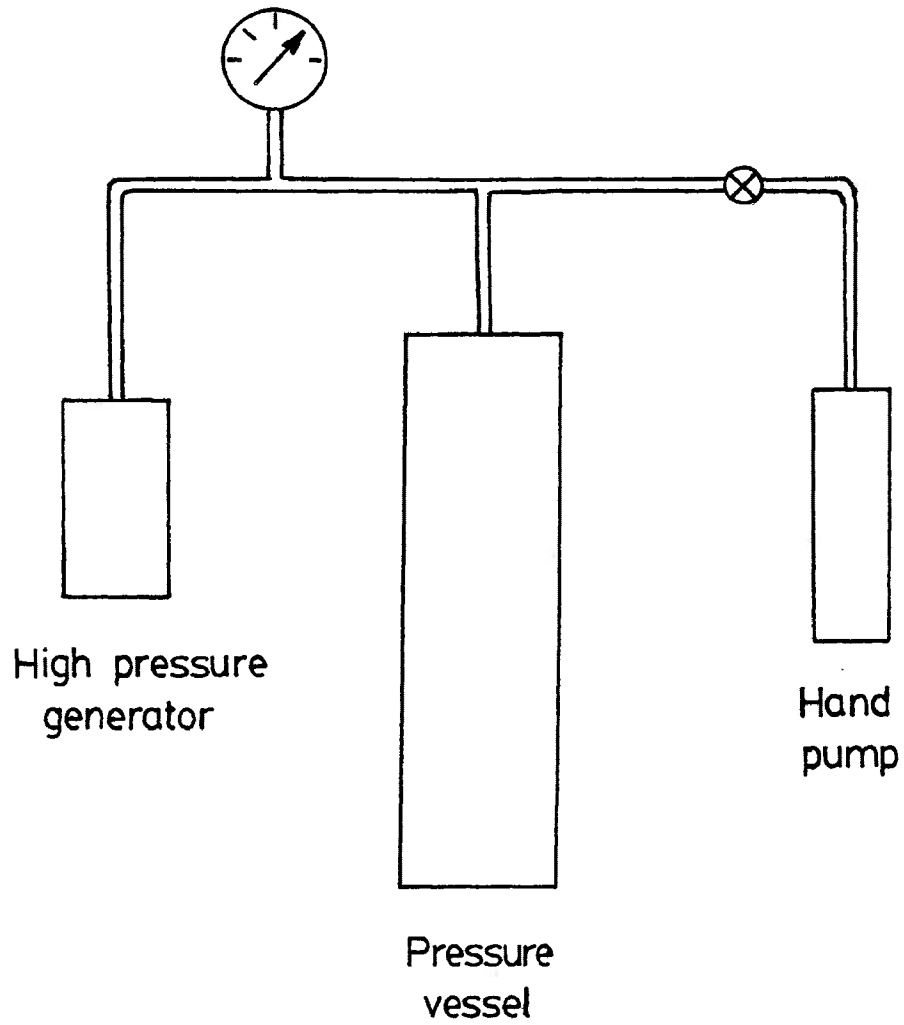


Figure 3-4: Schematic diagram of the hydrostatic rig.
Key as for Fig. 3-2.

pressure generator, both identical to those found on the triaxial rig. Samples are held in a perforated aluminum tube for easy placement and removal of the samples. The perforations ensure that the hydraulic fluid is readily able to circulate around the samples and so apply an hydrostatic stress to the samples.

3.2 Materials and Sample Preparation

Stress relaxation tests were performed on right cylindrical samples of Carrara marble. Samples of the marble were prepared by drilling cores of 0.48 in diameter with a glass cutter's core drill mounted on a drill press. Cores were then mounted in a clamp and the ends were flattened on a grinding wheel. Sample ends were ground to within 0.002 in of parallel. Nominal sample length was 1.0 in.

Calcite sand was used in the preparation of samples deformed in the hydrostatic loading test. This calcite was collected by C. Alford from a vein approximately 6 km west of Stanley, Ontario (see Alford, 1988; Fig. 3-6). After crushing and sieving, a very high proportion of fines (produced by crushing) was found to be present in the desired grain size fraction of very fine sand ($\phi = 3.75$ to 4.0; respective U.S. Standard sieve sizes are 200 and 230

with openings of 74 and 63 μm). Resieving was done in two steps. An initial dry sieving with 200 and 230 mesh brass sieves removed some of the silt- and clay-sized material. Subsequently the sand was wet sieved with a 230 mesh, stainless steel sieve. Washing was done with distilled water. Less than 2% (by visual microscopic estimation) of the remaining material was finer than 4.0 ϕ after wet sieving.

While the vein material preferentially sampled was virtually monomineralic (C. Alford, pers. comm.), some secondary mineral phases were present in the sieved material. Traces of organic material were also present (<0.1%). Removal of the secondary mineral phases was attempted with a Franz model L-1 isodynamic magnetic separator. The following settings on the machine were used:

current 1.2 amperes

vibration level 5

forward slope 25°

side tilt 15°.

Observation of the separated secondary phases revealed three species: a blue-grey mineral with metallic lustre and platy habit, a brassy yellow mineral occurring as sub-spherical grains without obvious cleavage, and smooth-sided, spherical, pink grains. These are tentatively identified as ilmenite, pyrite (or some similar sulphide) and garnet, respectively. Weathering of the

first two had stained and apparently weakly cemented a few calcite grains. The sand produced by the sieving and separation was visually estimated to be better than 99.5% calcite; this was deemed adequate.

Quartz was added (10% by volume) to the purified calcite sand in order to provide a surface against which the calcite could preferentially pressure solve. Laboratory grade quartz in the form of rounded grains was used; grains ranged in size between $\phi = 2.75$ to 3.75 (0.149 to 0.074 mm; sieve sizes 100 to 200).

Kaolinite was taken from a specimen in the Lakehead University Geology Department teaching collection. The clay was reduced to a powder with a mortar and pestle.

The calcite and kaolinite were positively identified by X-ray diffraction (XRD). Both minerals gave traces which accorded very closely with library values. The XRD analyses were made by Dr. T. Griffiths of the Lakehead University Instrumentation Laboratory.

The following procedure was used in the preparation of the hydrostatic samples (see Fig. 3-5):

1. A section of 0.75 in inside diameter teflon tubing was cut to a length of about 1.8 in. This length was sufficient to allow the tubing to extend over the O-rings of the two end-pieces without extending past the ends of the end-pieces. When thus constructed, the end-pieces of adjacent samples could seat firmly against one another. With a total nominal length of 2. in, each

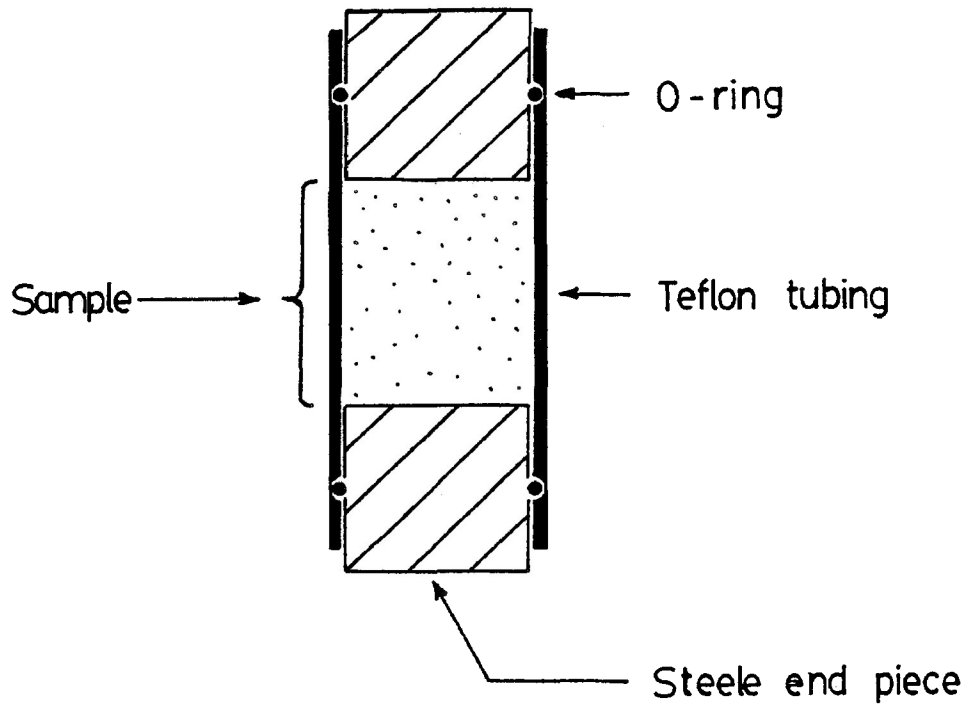


Figure 3-5: Cross-sectional view of hydrostatic test sample. Not to scale.

test piece contained an uncompacted sample of about 0.75 in length with a volume of 0.33 in^3 (5.4 cm^3).

2. A suspension of the kaolinite was prepared by mixing loose kaolinite and distilled water or saline solution in a volume:volume ratio of 1:3. The kaolinite was prepared by scraping it from a large lump and then grinding it in a mortar and pestle. The saline solutions used were prepared with distilled water and laboratory grade salts. The clay-liquid mixture was stirred and allowed to settle several times, thus causing the coarser clay aggregates to settle to the bottom of the mixture.

3. After slipping the section of teflon tubing over the endpiece (of known length), approximately 0.25 in of calcite sand was poured in the tubing. The clay-water mixture was then gently stirred so as to raise the finer clay particles into suspension. This suspension was then immediately poured over the calcite sand and mixed into the sand with a laboratory spatula. Any excess suspension, beyond that necessary to saturate the sand, was drawn off with a syringe.

4. Dry calcite sand was then sprinkled on top of the wetted sand to bring the total sample depth to about 0.75 in. The upper end-piece, with a stamped number kept on the uppermost surface, was then slid into the tubing till it rested snugly against the sand mixture. The total length of the test-piece was then measured and recorded.

CHAPTER 4: STRESS RELAXATION TESTING AND PRESSURE SOLUTION

4.1 The Stress Relaxation Test

4.1.1 Theory

The stress relaxation test (SRT) is a technique which allows study of rheological behavior over a range of strain rates in a single test. It is a relatively rapid procedure which complements loading tests (done at constant strain or displacement rate) and creep tests (done at constant stress or load). During a SRT, dissipation of stress by the sample makes possible the determination of a material's dependence of strain rate upon differential stress, or of the values of parameters relating to dislocation activity during intracrystalline plasticity (Rutter et al, 1978).

In order to begin a SRT, a sample must first be loaded with some differential stress. This loading can be done under any particular conditions of interest - P_c , P_f , T , etc. As loading proceeds, the strain of the sample will increase. Stress relaxation is begun by locking in place the components of the

machine which apply load to the sample. In the case of the Donath rig, this is done by closing the valve closest to the pressure vessel on the differential pressure hydraulic line. Although further loading of the sample is prevented, the existing stress causes the sample to flow and in doing so gradually relieves the load.

A generalized rheological model is helpful in interpretation of the stress - strain - time data obtained during a SRT (Fig. 4-1). (Hart (1979) has presented several rheological models of material behavior during a SRT.) The permanent strain of the sample produced during the SRT is driven by stored elastic strain energy accumulated during the previous loading of the sample (Rutter et al, 1978). Ideally, a SRT is performed on an infinitely stiff machine, i.e. one which does not deform elastically as the sample is stressed. In practice, however, a machine has limited stiffness and undergoes some elastic deformation as the sample itself is loaded and strained. Consequently, the elastic strain energy causing permanent sample deformation is contributed by both the machine and the sample itself (viz. Cook, 1981). This elastic behavior is indicated in the rheological model by springs; machine deformation is exclusively elastic while rock acts in a more complex fashion. Sample strain is only partially recoverable on account of non-elastic response.

In general, the dissipation of elastic strain by the sample is expressed by

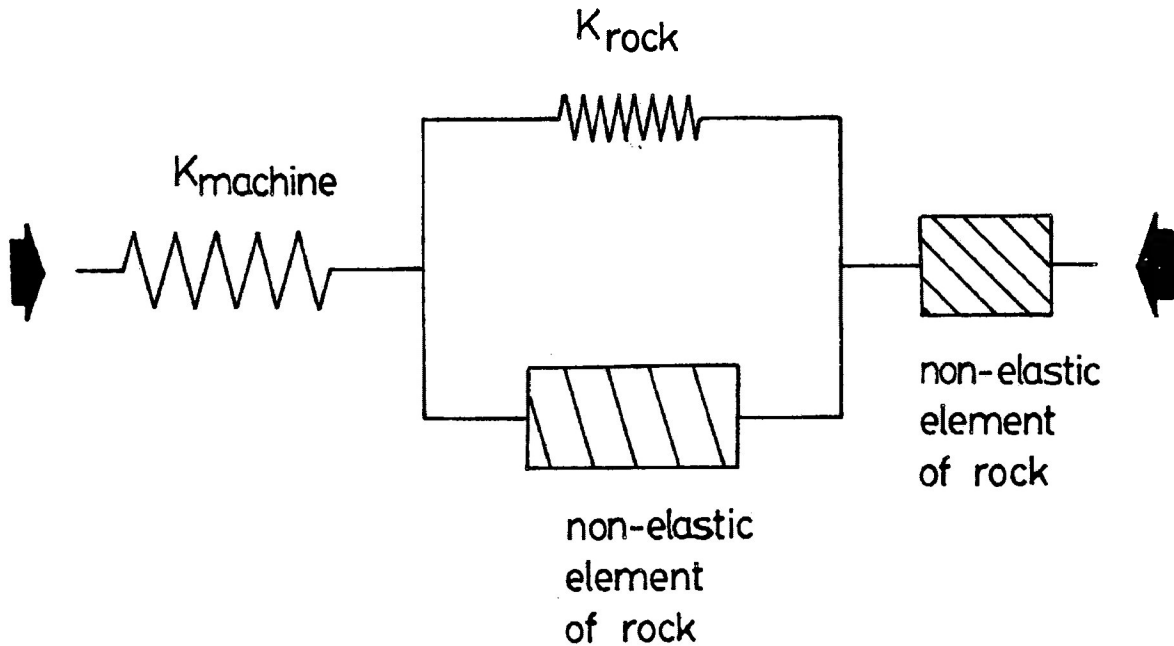


Figure 4-1: Rheological model of machine and sample behavior. Elastic behavior of the machine and sample is indicated by springs; the compliance, K , is the reciprocal of the elastic constant. Permanent strain of the sample is described by the two non-elastic elements which may include viscous and plastic action.

$$\frac{de_p}{dt} = - (K_r + K_m c_m) \frac{d\sigma}{dt} \quad (4-1)$$

where e_p is permanent strain,

K_r is the rock compliance,

K_m is the machine compliance, and

c_m is a correction factor so that elastic strain of the machine corresponds to the differential stress on the sample, (Schmid, 1976; Rutter *et al*, 1978).

Relaxation of the stress can occur in two ways. Anelasticity is imperfect elastic behavior characterized by exponential time dependence (Guin and Pratt, 1964). Both the sample and machine may behave anelastically during a SRT. Note that a sample will only behave anelastically if the prior loading does not produce inelastic deformation. Anelastic relaxation in metals, including the machine, may occur for up to 100 s from the start of a SRT (Rutter *et al*, 1978; Guin and Pratt, 1964). The second form of relaxation, and the one which is usually of interest during a SRT, is relaxation after permanent strain. In such a case relaxed strain has a logarithmic relation with time (Guin and Pratt, 1964).

4.1.2 Application of the SRT

SRTs used to determine values of flow law parameters require steady-state flow of the material (Rutter et al, 1978). Steady-state flow is deformation at constant stress, temperature and microstructure which results in a constant strain rate. In practice, steady-state flow should be achieved during loading of a sample prior to initiation of stress relaxation. Strain and consequently microstructural change during a SRT is minimized by use of very stiff machines.

The generalized expression for flow laws,

$$\dot{\epsilon} = W f_1(\sigma) f_2(T) f_3(S)$$

(Dorn, 1957) shows strain rate, $\dot{\epsilon}$, is a function of flow stress, σ , temperature, T , and microstructure, S . If T and S are held constant during a SRT, the data will be solely a function of strain rate sensitivity. For a power law stress function, $\dot{\epsilon} \propto \sigma^n$, then substitution of equation (4-1), taking logarithms and differentiating with respect to $\log \sigma$ gives

$$n = \partial \log \dot{\sigma} / \partial \log \sigma \quad (4-2).$$

where $\dot{\sigma}$ is stress rate, $\partial \sigma / \partial t$. For an exponential stress relation, $\dot{\epsilon} \propto \exp(p\sigma)$, the same operations yield

$$p = \partial \log \dot{\sigma} / \partial \log \sigma \quad (4-3)$$

(Rutter et al, 1978). Because $\dot{\sigma}$ is linearly proportional to strain rate of the sample, equations (4-2) and (4-3) illustrate the

logarithmic relation between relaxed strain and time referred to in subsection 4.1.1 . In practice, treatment of SRT data involves a correction of elastic effects. Force applied by both P_c and axial load causes elastic distortion of the machine and sample which must be accounted for. The calculations used are outlined in Appendix B.

The treated data from a SRT may be plotted on a graph of \log vs. $-\log \dot{\epsilon}_p$, where $\dot{\epsilon}_p$ is the permanent strain rate (Fig. 4-2). Ideally, successive points will occur at progressively lower strain rates and will define one or more linear segments. If more than one linear trend is present, the slopes of the successive segments will progressively increase. This increase indicates that the deformation mechanisms which are successively responsible for strain of the sample have a decreasing strain rate sensitivity to stress.

4.1.3 Limitations of the SRT

As with any experimental procedure, there are a number of factors leading to error in SRT data. There are two general sources of error: the machine and the sample.

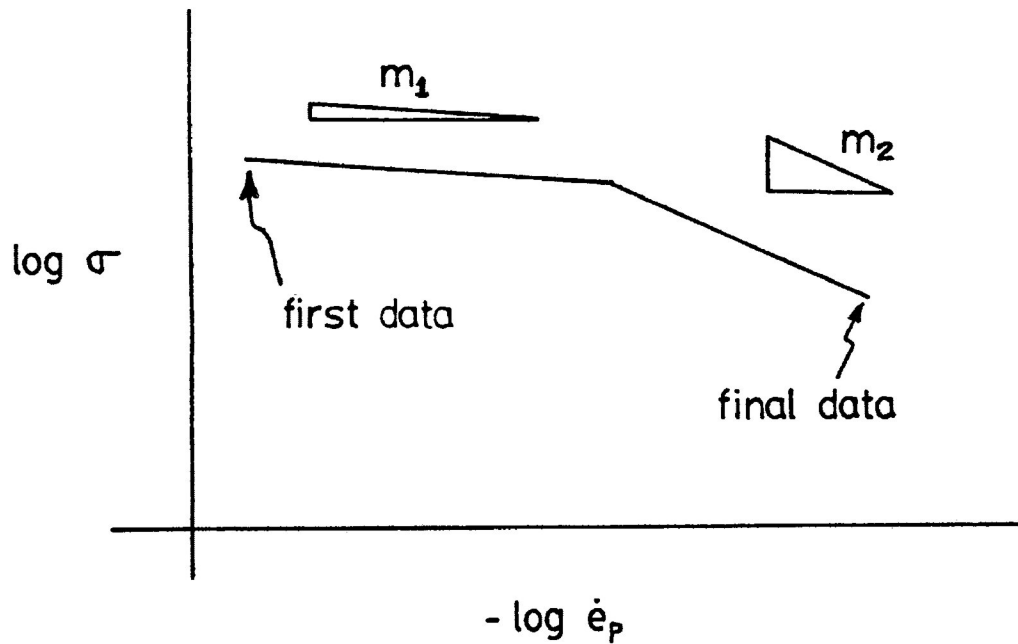


Figure 4-2: Graph of $\log(\text{differential stress})$ vs. $-\log(\text{permanent strain rate})$ showing trends defined by SRT data. The first trend, with slope m_1 , indicates a deformation mechanism with a greater strain rate sensitivity to stress than the second mechanism, illustrated by the line segment with slope m_2 .

Note that $m_2 > m_1 > 0$ and that

$$\frac{1}{m} = \frac{\partial \log \dot{\sigma}}{\partial \log \sigma}$$

Machine generated error. There are two categories of machine generated error. One contains error due to the measurement and control devices. A leading cause of this error is the accuracy of the LVDT (see section 3.1) which depends on axial displacement. For any sampling interval the change in LVDT signal is required to correspond to the equivalent of at least 0.0005 in (0.013mm) shortening for a reliable result. At faster strain rates, this displacement will occur quickly. As a SRT progresses, however, strain rates will fall and so progressively longer intervals are required for a minimal reliably measured strain.

The delay of an interval is calculated according to the equation

$$\text{delay} = \frac{0.0005}{\text{strain rate}}$$

using the assumption of initial unit sample length. The value of strain rate is taken from the previous measurement interval. For example, for a strain rate of $10^{-7.0} \text{ s}^{-1}$, the subsequent interval is run for 1 hour, 23 minutes. Even if a SRT is progressing ideally, it is impractical to continue it once a strain rate much less than $10^{-8.0} \text{ s}^{-1}$ has been obtained. This is because the exponential nature of strain rate results in a very long delay. For example, for a strain rate of $10^{-8.2} \text{ s}^{-1}$, a delay of 22 hours is needed. At

these lower strain rates, a paucity of data on graphs of quantities plotted against time can make interpretation difficult.

Complicating the problem of longer intervals is electronic stability. For the LVDT used in the SRTs described below, Alford (1988) has reported drift of up to ± 50 parts in 4,096 ($\pm 1.2\%$). He noted that the worst drift occurred at times of greatest electrical demand (despite regulation of the current used to power the LVDT). Stable current allows optimal performance of the LVDT (± 1 part in 4,096; see Alford, *op. cit.*), but lengthy interval delays and protracted SRTs make this preferred behavior difficult to obtain.

Load cell sensitivity was not considered a major source of error in this study. Alford (*op. cit.*) reported drift of ± 1 part in 4,096 for the load cell used in this study. Furthermore, data from calibration of the load cell output against P_c and axial load (not reported here) indicates behavior is highly linear and repeatable.

The second general limitation on SRT's is dimensional instability which arises from change in temperature. Heating and cooling will cause indirect change in forces applied to the machine and sample. Thus, variation in ambient temperature appears responsible for SRT data giving (highly) non-linear distributions of $\log \sigma$ vs. $-\log \dot{\epsilon}_p$ (for example, Fig. 4-9c). This effect is greatest at lower strain rates when sample intervals are longer. Two approaches to this problem present themselves.

a) Compensation for temperature fluctuation during treatment of data. Just as raw SRT data is treated to compensate for elastic flexure of machine and sample, corrections for thermal expansion could be made by applying empirical relations. There are several possible corrections. The effects of temperature change directly upon the LVDT and load cell are unknown, and would have to be determined. Expansion and contraction of the pressure vessel may change the vessel volume, and consequently change P_c which is known to affect load cell output. Dimensional change in the pressure vessel may also directly affect load cell and LVDT output. A correction for sample expansion or contraction may be made. Calculations made using a value of $7 \times 10^{-6} \text{ } ^\circ\text{C}^{-1}$ for the linear thermal expansion coefficient of marble (Skinner, 1966; Table 6-10) suggest this is a minor correction. Finally, the effect of time upon these corrections would need to be known. Clearly, compensation for temperature change by means of calculated corrections is an awkward and lengthy process with the potential for substantial errors remaining.

b) Maintenance of triaxial rig ambient temperature A reasonably straightforward and inexpensive approach to the problem of thermal expansion is to control ambient temperature. This was done by surrounding the pressure vessel with a heating

jacket. This arrangement appears to have regulated P_c with some success over the temperature fluctuations typically experienced in the laboratory (see App. C).

Sample generated error. One type of sample error arises from variation in elastic modulus. Elastic modulus varies from sample to sample, both because of the variability of natural material and because it may be altered during deformation. It is possible to correct this by obtaining the elastic constant from the unloading of the sample after a SRT and then using this value to recalculate the SRT data. This correction may be important if the transition stress and strain rate between two competing deformation mechanisms are to be known accurately.

Sample error is also important to a SRT if the sample is not undergoing steady-state flow. Ideally, data from a SRT define linear trends of progressively increasing positive slope on a graph of $\log(\text{differential stress})$ vs. $-\log(\text{permanent strain rate})$ (Fig. 4-2). These quantities are shown individually in Fig. 4-3: differential stress and permanent strain rate decline continuously and concurrently over time. In some SRTs, however, permanent strain rate does not progressively decline. This gives rise to what is here termed "cycling" of the data. Fig. 4-4a shows a generalized representation of how strain rate varies over time during cycling. This may be explained in terms of changing microstructure. While

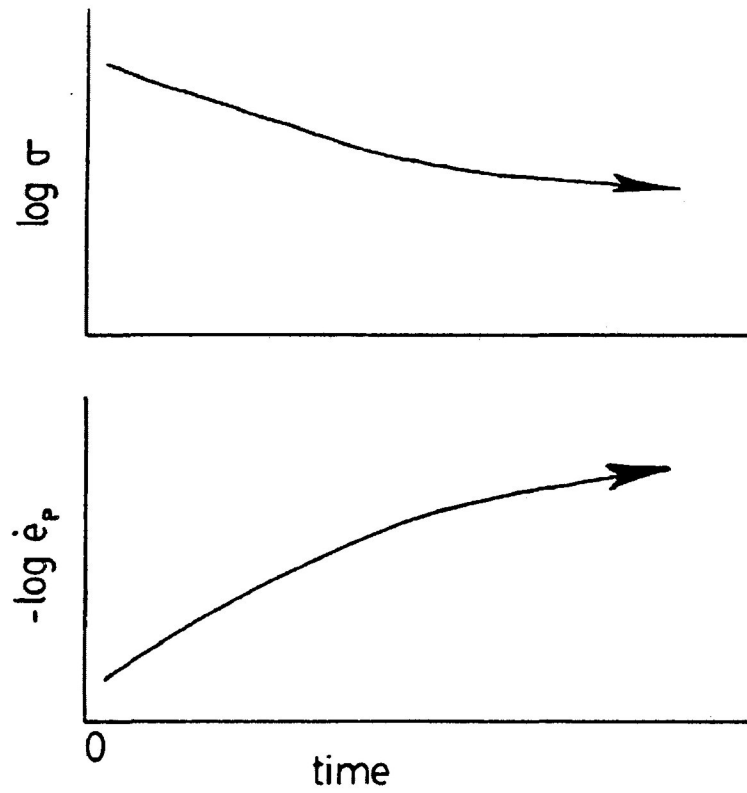


Figure 4-3: Variation of $\log(\text{differential stress})$ and $-\log(\text{permanent strain rate})$ over time during a SRT without the occurrence of cycling.

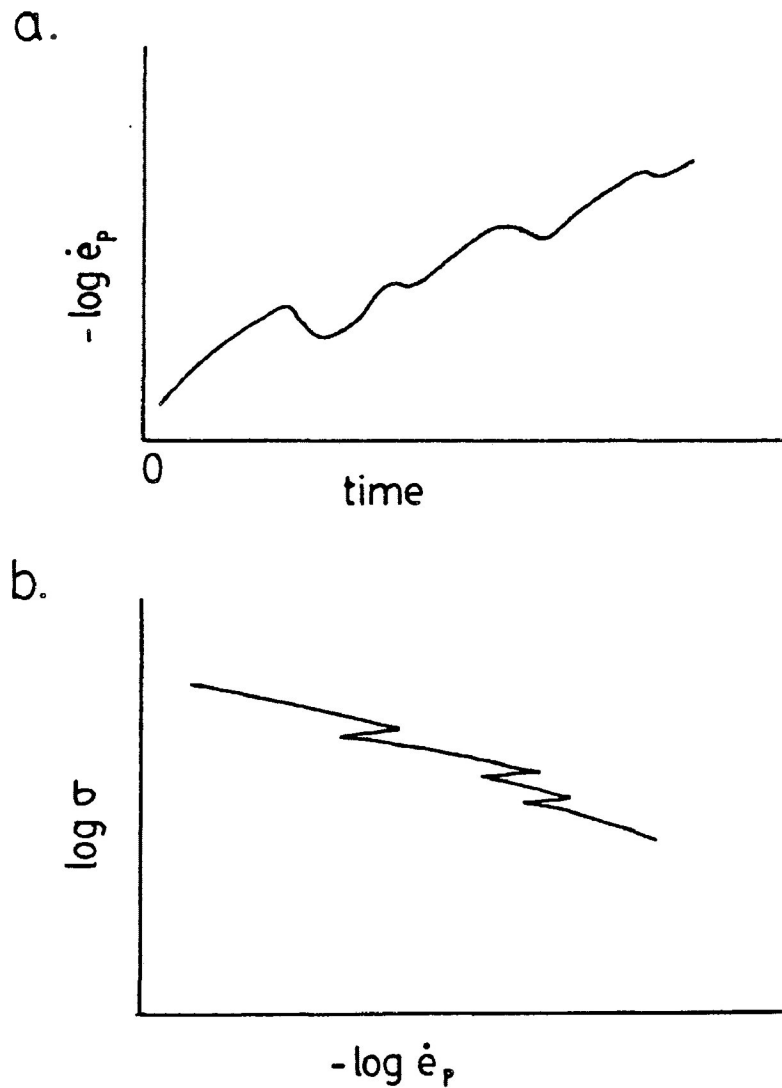


Figure 4-4: Graphical representation of cycling. a. An overall decline over time in permanent strain rate is marked by short-lived increases. b. A graph of $\log(\text{differential stress})$ vs. $-\log(\text{permanent strain rate})$ shows a curve subject to abrupt changes in slope. Differential stress continually declines during the SRT.

differential stress will continue to decline during cycling, alternate phases of hardening and softening of the sample cause permanent strain rate to fall and rise. The result is a sawtooth curve on a graph of $\log(\text{differential stress})$ vs. $-\log(\text{permanent strain rate})$ (Fig. 4-4b). Fig. 4-8d shows typical SRT data illustrating cycling.

A third error which is attributable to sample behavior (and also to thermally generated change in pressure vessel volume) is the effect of change in P_c upon axial load. Sample dilation or contraction will cause P_c to rise or fall, and consequently change the load on the load cell. With no change in differential stress, the change in load is given by (for load cell TP795) $\Delta L = (9.1 \times 10^{-7}) \Delta P_c$, where change in load cell output, ΔL , is in volts and ΔP_c is in psi (see App. B). The computer program which monitors the SRT, however, treats ΔL as the result of a change in differential stress ($\Delta D.STRESS$, in MPa). Substitution into the relation $\Delta D.STRESS = (\Delta L K2) / 145 AR$, where $K2$ is the load cell load-output constant (10^6 lb/V) and AR is the circular cross-sectional area of the sample, shows that a 1. MPa change in P_c results in an apparent change of 4.6 MPa in differential stress for a sample of 0.5 in diameter.

4.2 Stress Relaxation Tests on Carrara Marble

4.2.1 Introduction

A series of SRTs were performed on Carrara marble with the hope of obtaining quantitative data on PS. Carrara marble was chosen for several reasons. Being an essentially monominerallic rock with a regular, virtually isotropic lithologic fabric, it is highly uniform. This uniformity is desirable as the effects of sample variation upon deformational behavior are minimized. Grain size is sufficiently large to allow optical observation of the effects of deformation of individual grains. Furthermore, Carrara marble has, on account of its composition and fabric, been used by other workers concerned with deformation of (calcite) rocks; recent work done on Carrara marble includes Rutter (1974), Schmid *et al* (1980), and Ferguson (1983). Published SRT data on marble is not extensive, however.

Prior to recognition of the magnitude of thermal expansion, seven samples of Carrara marble were successfully loaded and entered into stress relaxation. A total of twelve SRT's were performed on these samples. The absence of temperature regulation equipment on the triaxial rig during these early tests

requires that the results be interpreted with caution. In the absence of a continuous or periodic record, knowledge of the usual pattern of ambient temperature change allows some constraints to be placed on the reliability of the data.

Two samples of Carrara marble (CM-11 and 13) were tested following the installation of a heating jacket, with thermostat, around the pressure vessel of the rig. No output is produced by the temperature regulation equipment and so no record of temperature fluctuation during the SRTs is available. Along with the installation of a temperature regulator, a pressure transducer was connected to the computer which controls and monitors sample deformation. It was thus possible to record P_c along with other data. This record of P_c should reflect changes in temperature and sample volume. The conditions of loading of the Carrara marble samples are presented in Table 4-1.

4.2.2 Results of Deformation of Carrara marble

CM-11

Three tests were performed upon sample CM-11. The sample was first deformed after drying at ordinary room conditions. The

TABLE 4-1: Conditions of loading of Carrara marble

Sample	Pc (MPa)	Pf (MPa)	loading strain (%)
CM-1	148.	dry	1.8
reload	148.	dry	1.4
CM-3	193.	dry	7.0
CM-4	193.	dry	2.7
reload	193.	19.	2.6
CM-5	193.	dry	7.1
CM-6	193.	19.	6.8
CM-7	193.	dry	10.9
CM-8	193.	dry	11.4
CM-11	193.	dry	4.6
reload	186.	19.	1.9
reload	186.	19.	2.6
CM-13	193.	dry	4.9
reload	193.	dry	2.4
reload	191.	0; wet	2.0
reload	191.	48.	1.8

second and third tests were performed at a pore pressure of 19. Mpa (0.19 kb). The fluid used, as with sample CM-13, was distilled water.

Loading: The graphs of strain, e , against time (see Figures 4-5a, 6a, 7a) show every fourth data pair. The slope of these plots thus provides a broad indication of how well the control system of the deformation rig was able to maintain a constant strain rate during loading. The increase in e was nearly linear over time for the first two tests (Figs. 4-5a, 6a), and was gently curved during the third loading (Fig. 4-7a). Each of these curves can be seen to steepen briefly beginning at the point corresponding to the yield point on the differential stress vs. e graphs (Figs. 4-5b, 6b, 7b). (The yield point typically occurred at 1.% strain for CM-11 and CM-13. An exception to this occurred during the second loading (see Fig. 4-6b): axial load from the previous test had not been released, thus resulting in an ostensibly low yield point.) The temporary increase in strain rate corresponding to the yield point is a machine effect; several cycles of the controlling program RIG6.BAS are required to respond to the softening of the sample as it passes through the yield point. The third loading shows this most clearly; this loading appears to have resulted in steady-state permanent flow, unlike the work-hardening of the first two loadings, and it is the third loading which shows the greatest steepening of the e -time curve.

Fig. 4-5a: CM-11, first loading: P_c , strain vs. time

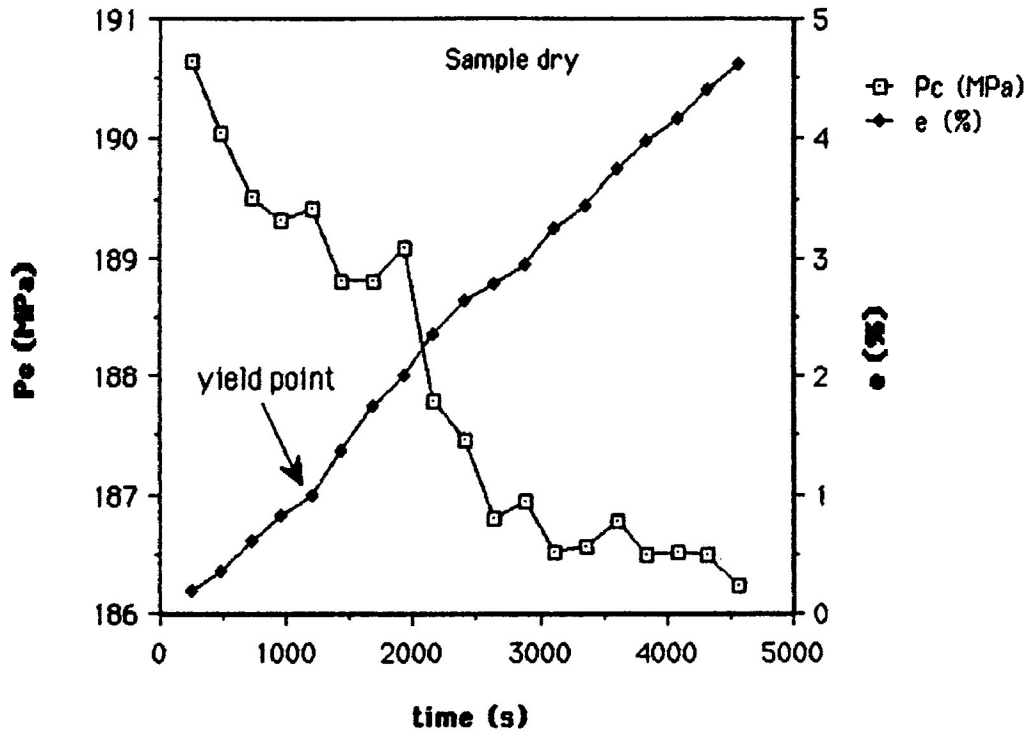
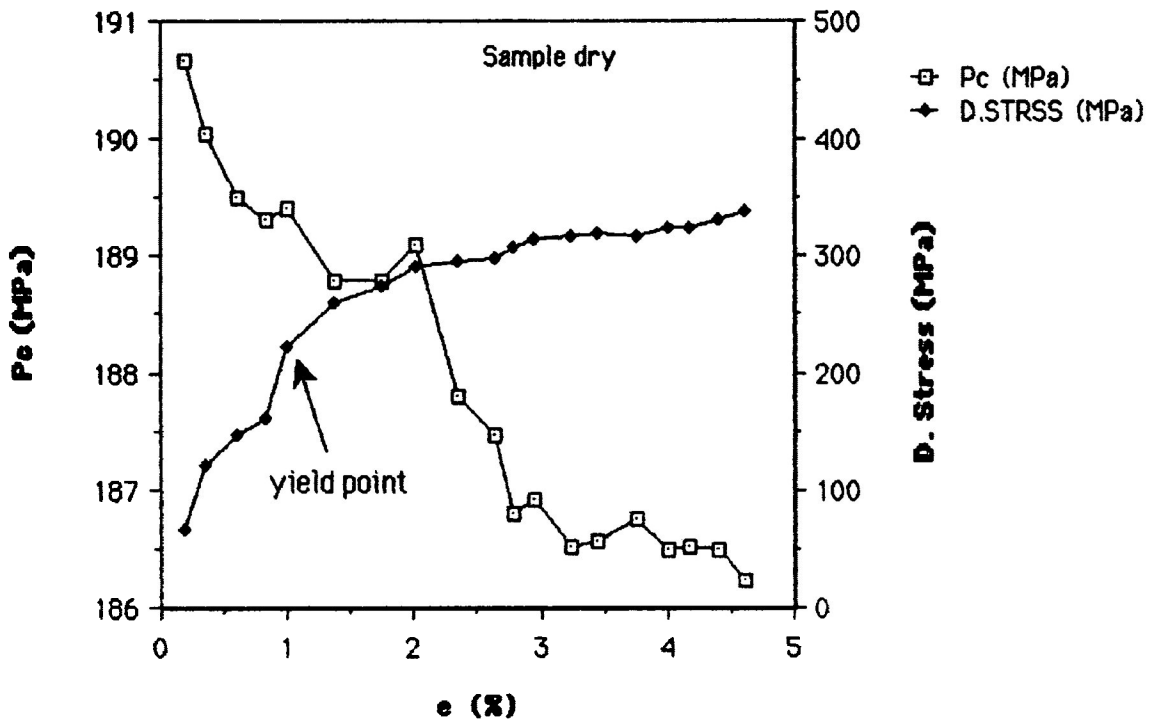
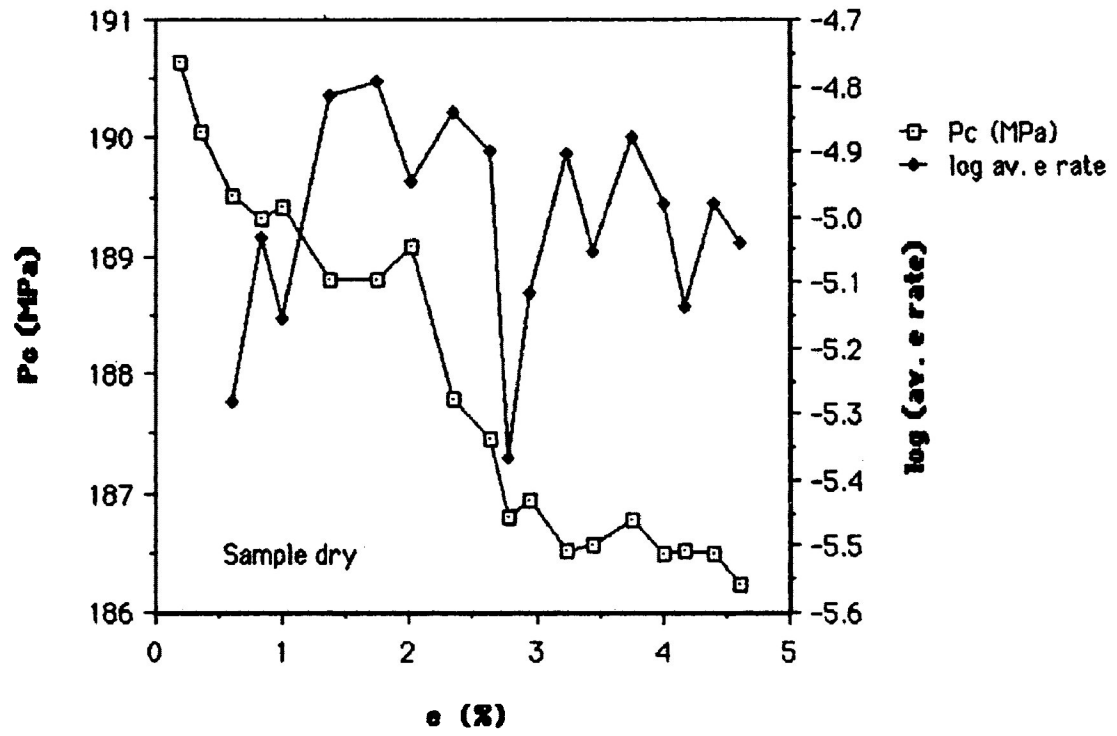


Fig. 4-5b: CM-11, first loading; P_c , differential stress vs. strain



**Fig. 4-5c: CM-11, first loading;
 Pc, log(average strain rate) vs. strain**



**Fig. 4-6a: CM-11, second loading;
Pc, strain vs. time**

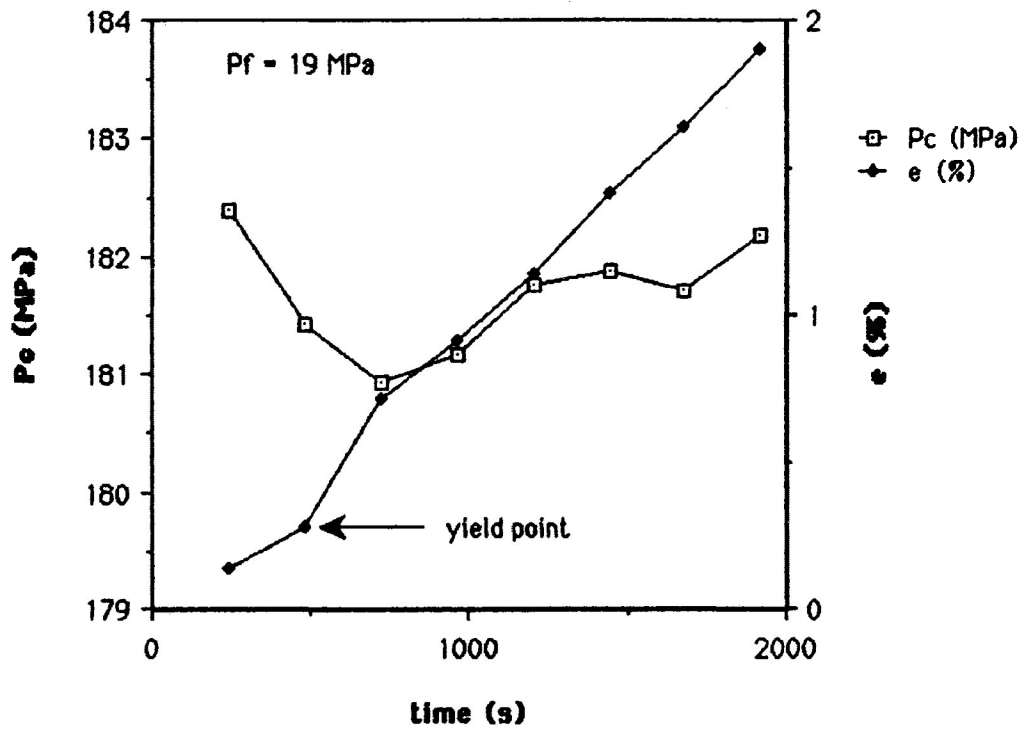


**Fig. 4-6b: CM-11, second loading;
Pc, differential stress vs. strain**

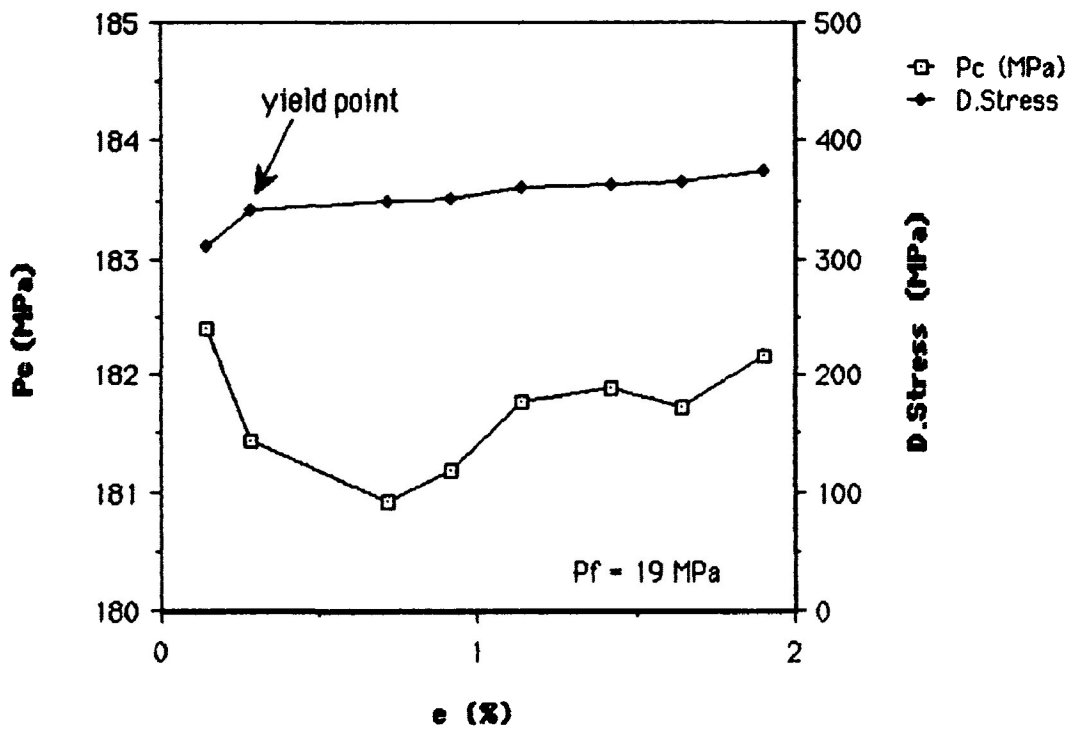


**Fig. 4-6c: CM-11, second loading;
Pc, log(average strain rate) vs. strain**

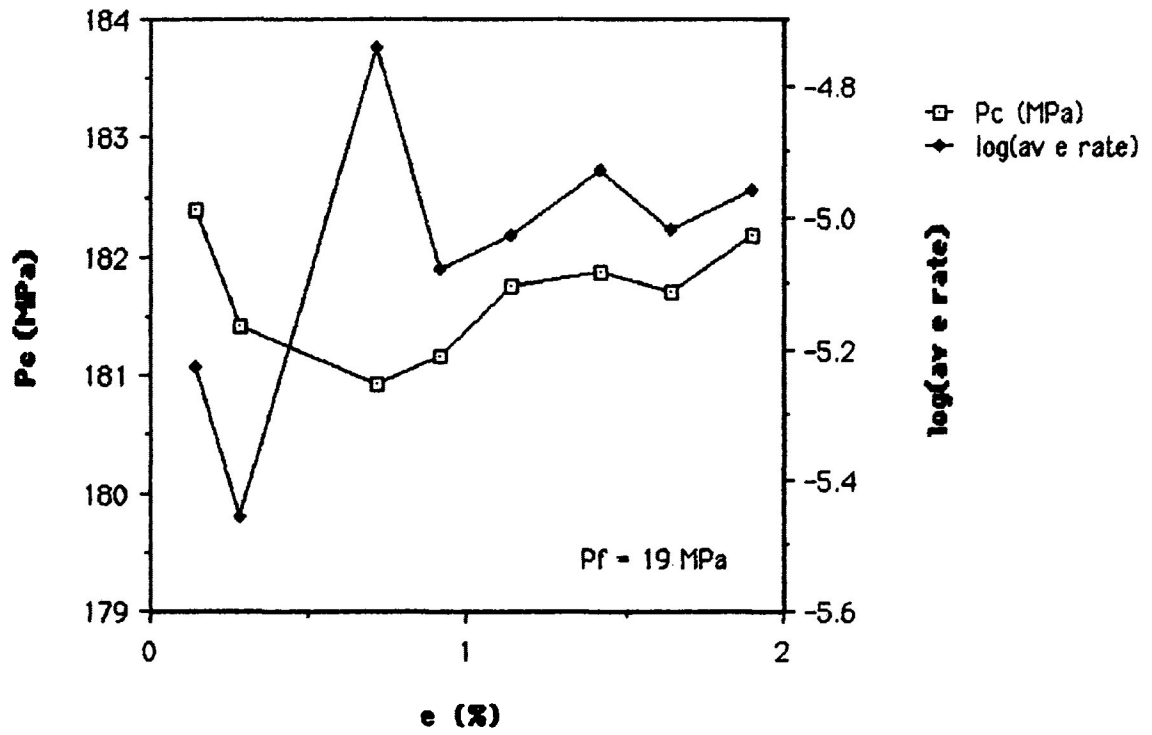


**Fig. 4-7a: CM-11, third loading;
Pc, strain vs. time**

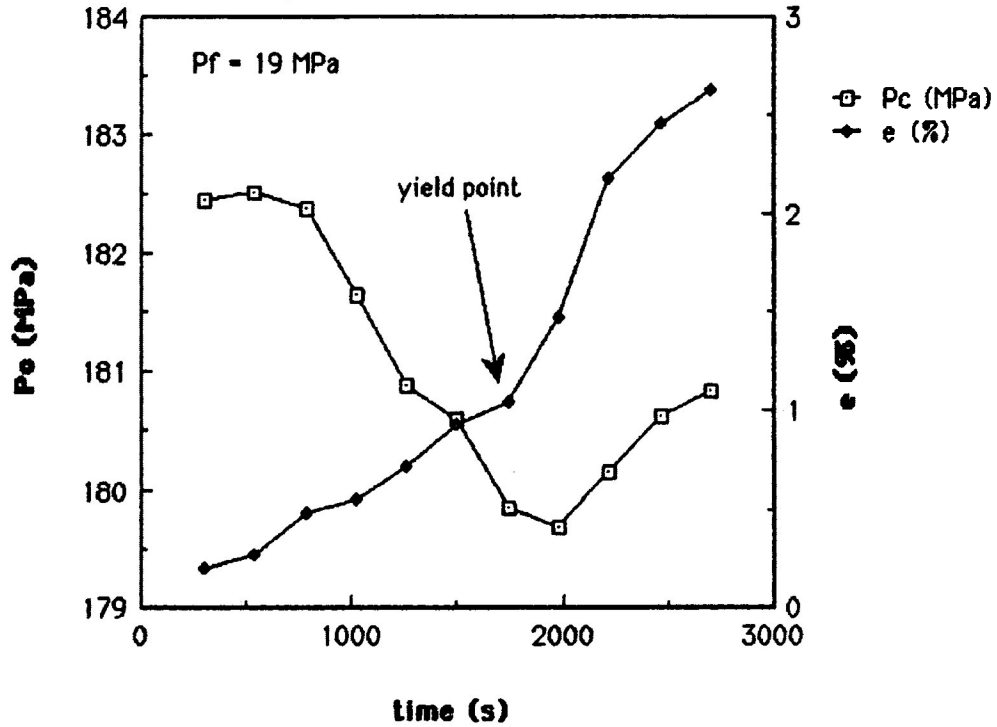


**Fig. 4-7b: CM-11, third loading;
Pc, differential stress vs. strain**

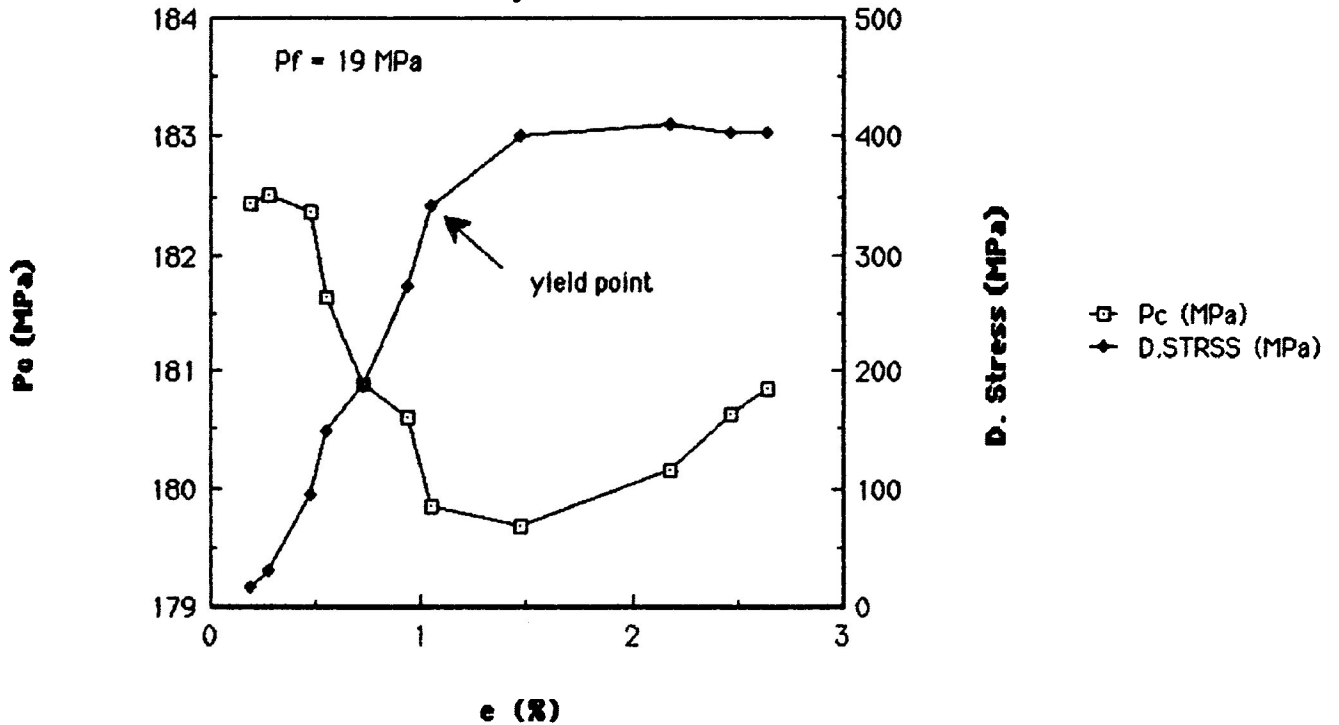


Fig. 4-7c: CM-11, third loading;
Pc, log(average strain rate) vs. strain

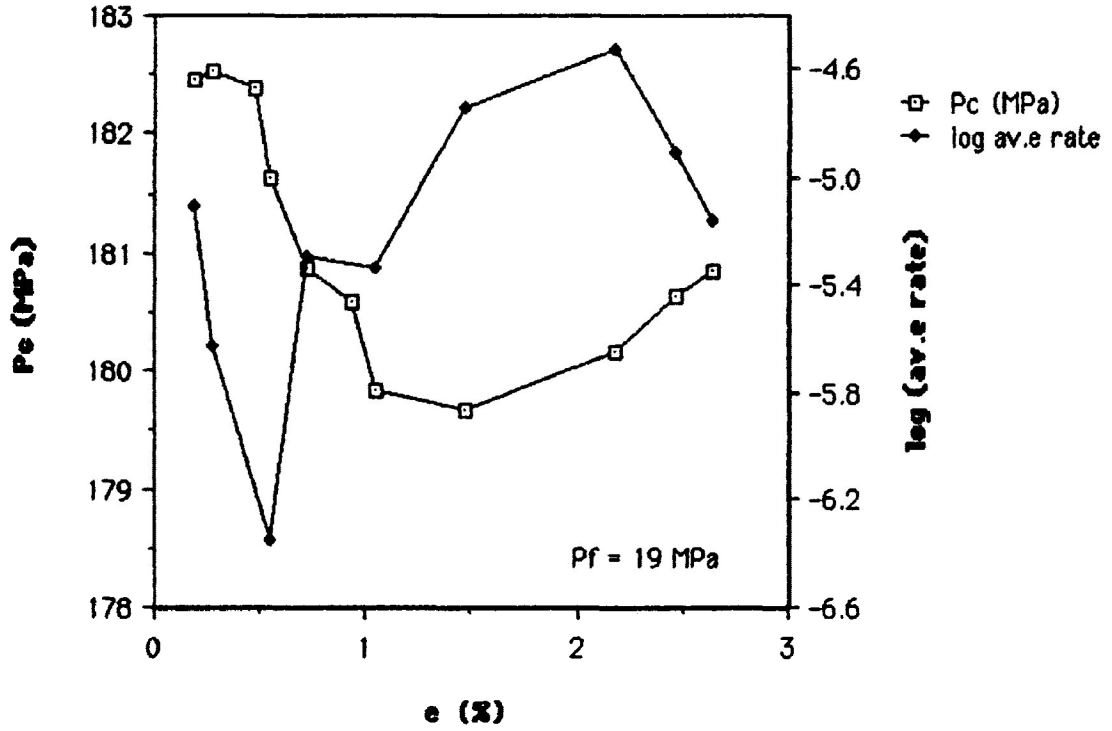


Figure 4-5a shows that P_c varied on two scales during the first loading. First, it is seen to have generally declined during the test, and did so at a decreasing rate. Some of this decline may be due to compaction of the sample. However, this effect is likely minimal as application of over 180 MPa (1.8 kb) prior to axial loading should close any voids opened during geological uplift and sample preparation. Furthermore, experimental loading typically results in an initial dilation at high strain rates and low temperatures (Rutter, 1974; Donath and Fruth, 1971) and would be reflected by a rise in P_c , not a drop. A machine effect may be (largely) responsible. As this test was relatively brief, and was performed at a time of day when ambient temperature is generally stable, it is unlikely that thermal expansion or contraction is responsible. A possible explanation for this gradual decline is an increase in pressure vessel volume due to application of axial load; this has not been confirmed independently and remains speculative.

P_c also varied episodically over shorter intervals of the initial loading. Figure 4-5c shows an initially inverse correlation between the minima and maxima of P_c vs. time and $\log(\text{average strain rate})$ vs. time. Comparison of Figures 4-5c and 4-5b suggests that while bulk expansion of the sample increased P_c , the grain-scale process by which the dilation was accomplished served to strengthen the sample and lower the strain rate. The

absence of bulk longitudinal fractures, and minimal intragranular fracturing seen in thin section suggests the dilation is due to intergranular separation. Some intergranular gaps are present; twinning of the grains has occurred and may be responsible. The inverse relation between P_c and $\log(\text{average strain rate})$ tends to confirm this interpretation; strain rate should decrease as the sample hardens.

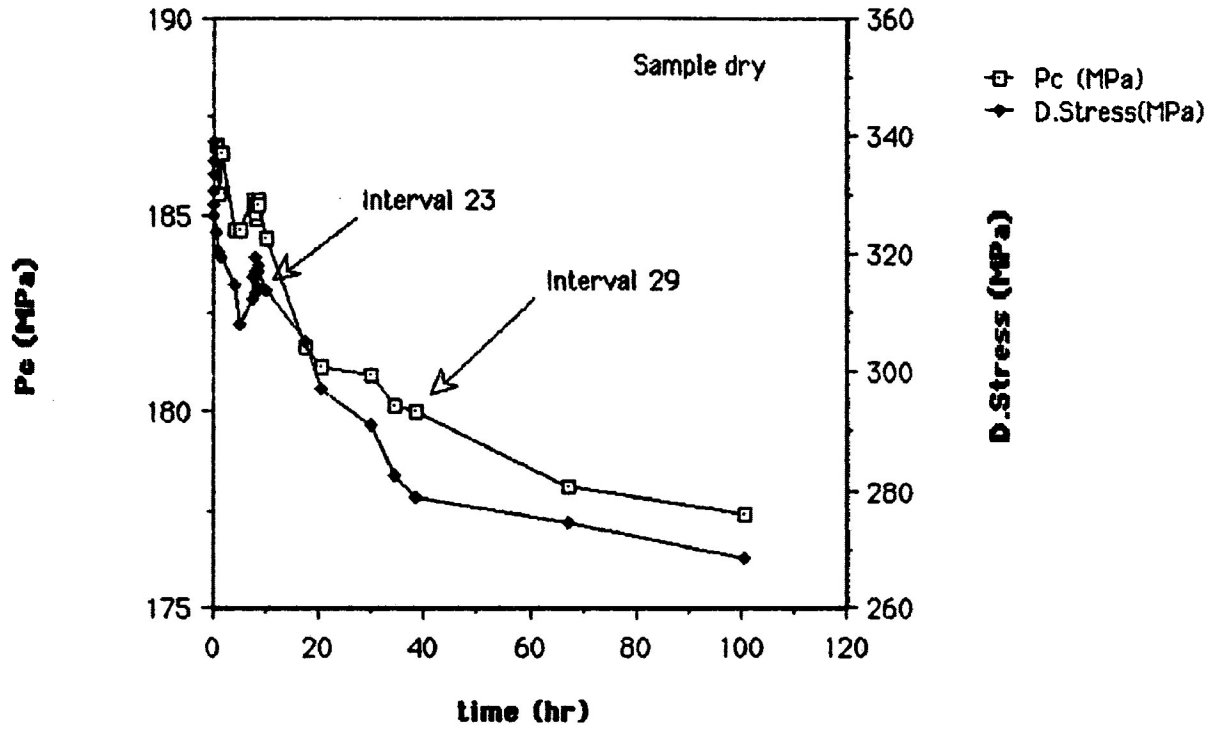
After 2.5% strain during the first loading, P_c did not fall so rapidly as before. This is attributable to the decreased loading rate while the specimen underwent work-hardening permanent flow. Breakdown of the inverse relation between P_c and $\log(\text{average strain rate})$ also occurs. While steady-state flow was not occurring in the sample, presumably strain was sufficiently high that work-hardening was not occurring so quickly as before.

The second loading of CM-11 (Figs. 4-6a,b,c) was performed after the first SRT on the sample. As the remaining axial load was not backed off prior to reloading, the differential stress - ϵ curve (Fig. 4-6b) shows only a small range of elastic strain, and the P_c - ϵ curve likewise shows only a small variation. P_c reached a minimum after the yield point was passed, as it did during the first loading, and then rose slightly overall as loading continued. Figure 4-6b shows CM-11 work-hardened at a slow and steady rate. This may be because the strain is produced through twinning of increasingly non-preferentially oriented grains.

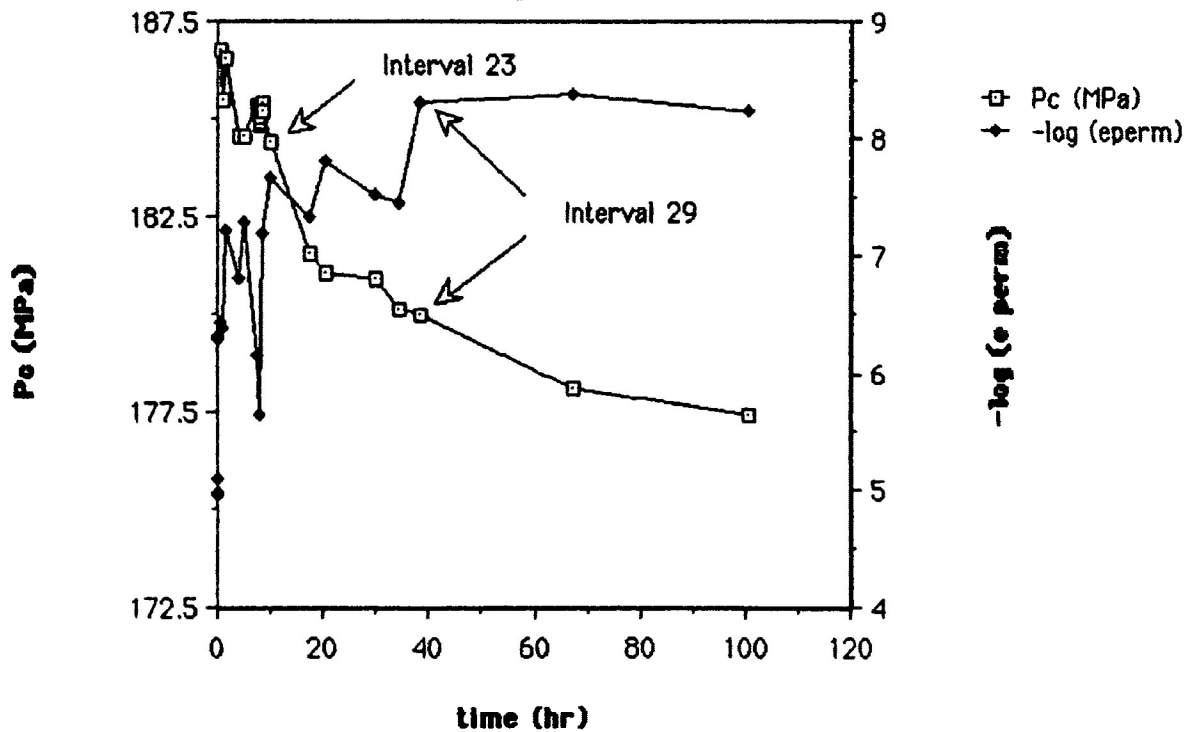
The behavior of CM-11 during the third loading (Figs. 4-7a,b,c) was very similar to that of the second loading. Axial loading was begun from zero, however, so the transition from elastic to permanent flow is more apparent on the graph of differential stress vs. ϵ (Fig.4-7b). Permanent flow during the third loading differed from the first two loadings; the sample appears to have begun steady-state flow, not work-hardening. As before, P_c declined as differential stress rose, and the P_c minimum occurred as the sample passed the yield point. The subsequent increase in P_c is interesting as it indicates sample dilation concurrent with steady-state flow. This may be interpreted to indicate hardening due to grain-scale dilation was balanced by some softening mechanism which did not produce compaction equal to the bulk dilation.

SRTs: The first SRT performed on CM-11 while dry has given generally acceptable results. Two reasonably linear trends were obtained on the graph of $\log(\text{differential stress})$ vs. $\log(\text{permanent strain rate})$ (Fig. 4-8c), indicating that two general processes were responsible for deformation of the sample during this test. (Best linear fits for SRT data were obtained by the reduced major axis method; linear regression was not applicable on account of subequal uncertainty in the values of $\log(\text{differential stress})$ and $\log(\text{permanent strain rate})$. Davis (1986) has presented the

**Fig. 4-8a: CM-11, first SRT:
Pc, differential stress vs. time**



**Fig. 4-8b CM-11, first SRT;
Pc, -log permanent strain rate vs. time**



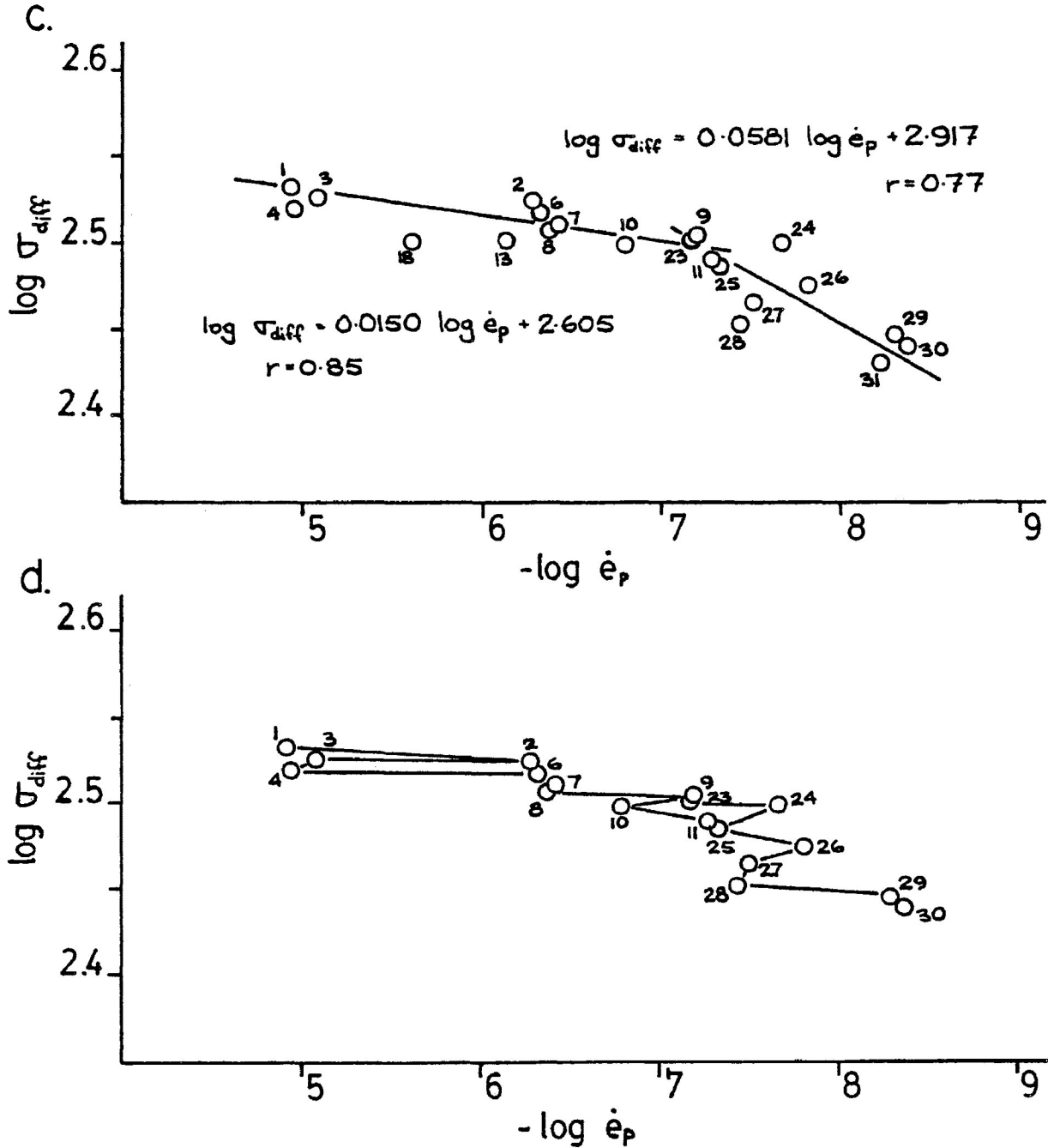


Figure 4-8c,d: Data from the first SRT on CM-11 are shown with two interpretations of the $\log(\text{differential stress})$ vs. $-\log(\text{permanent strain rate})$ graph. In c, two linear fits (data in red and green) by the reduced major axis method are shown. In d, cycling of the data is indicated. (Note: the number beside each point is the interval number.)

essentials of the reduced major axis method.)

Figures 4-8a and b indicate that, with one apparent exception, both strain rate and differential stress fell at a decreasing rate through the test. The exception occurred about 8 hours after the start of the test. Because it occurred at a time that ambient temperature is known to fall, thermal distortion is suspected. The rise in differential stress is presumably due in part to machine contraction. The rise in P_c (approximately 1. MPa) accounts for an apparent rise in differential stress of about 5. MPa (subsection 4.1.3); differential stress rose overall about 15. MPa, leaving a difference of 10. MPa. In response to the added differential stress, strain rate would have risen. The minimal number of points plotted on Figure 4-8c reflects this irregularity. The value of strain rate calculated from the raw data is negative, and so cannot be plotted. Points for intervals 13 and 18, which are plotted, are clearly not of significance.

Additional thermal variation may have occurred later but the differential stress vs. time curve does not show it. There was certainly, however, a thermal effect following interval 29 (Fig. 4-8a). This value was obtained on a Sunday morning; interval 30 was completed at 9:04 am Monday, after the ambient temperature rose. Consequently, a decrease in differential stress may have occurred (depending on the effectiveness of the heating jacket

used to maintain rig temperature) which is not shown by the data of Figure 4-8a. Similarly, there is no apparent change in strain rate and P_c (Fig. 4-8b).

Cycling of the data is shown to have occurred by Figure 4-8b. Over the first linear trend (intervals 1 to 11; see Figure 4-8c), the correlation coefficient, r , of $\log(\text{differential stress})$ against $\log(\text{permanent strain rate})$ is relatively good (0.85) as compared to the value of r , 0.77, for the second trend (intervals 23 to 31). The data of Figure 4-8c which show a linear trend are reproduced in Figure 4-8d with data connected successively, rather than with a single best fit line. A pattern similar to that of Figure 4-4b is present. Line segments joining successive interval data points are very close to horizontal over the first linear trend. Consequently, the overall distribution of the data, as seen in Figure 4-8c, is close to linear. The steady decrease of differential stress causes slope of the line segments to alternate between negative and positive as strain rate increases and decreases, respectively.

Cycling is also occurred over the second linear trend (intervals 23 to 30; Fig. 4-8c). The greater slope of the data overall leads to greater scatter; the successive line segments are at a greater angle of incidence to the overall trend than is the case for the first linear trend.

It is of interest to compare the relative magnitudes of slope of the individual line segments from the two linear trends.

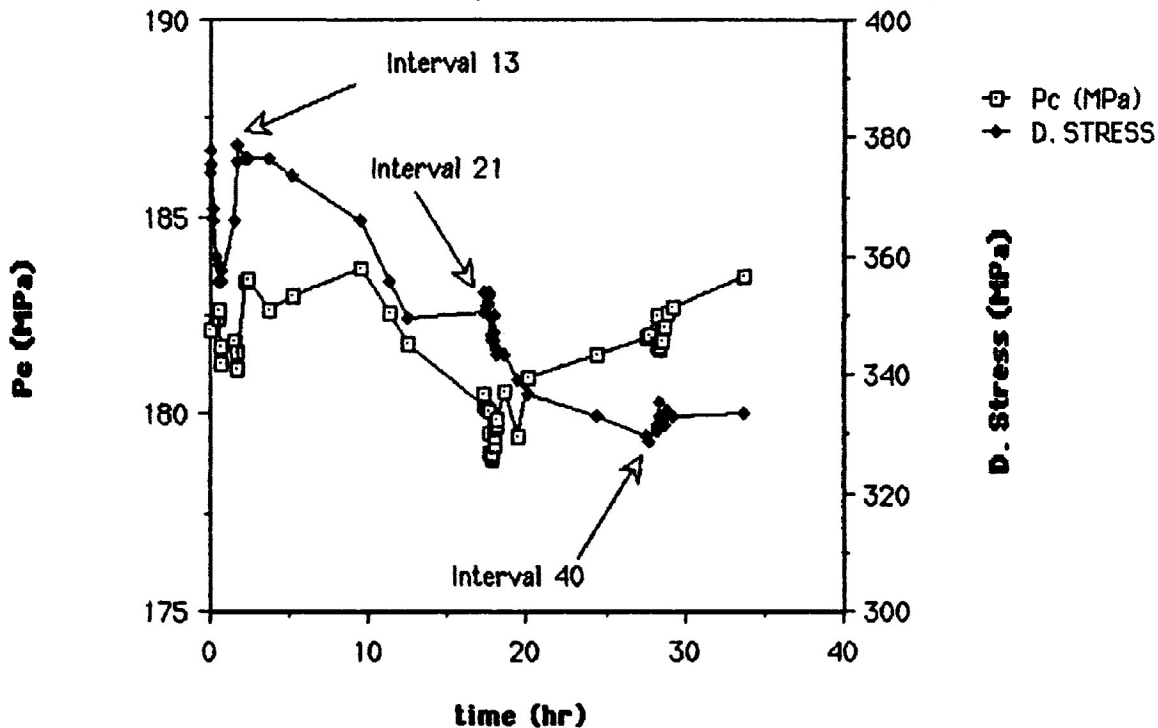
Limited data makes this difficult, at least for an individual test. Inspection does suggest, however, that of line segments showing increasing strain rate, those from the second linear trend are steeper, i.e. more negative. This indicates that during the periods of strain rate increase, the sample displayed greater strain rate sensitivity to stress over the second linear trend than the first. Note also that there is no overlap of the two zigzag curves, suggesting that the sample passed through two distinct stress-strain regimes.

Pc showed a steady decline through the first SRT of CM-11 except while differential stress rose (hours 8 to 10; Fig.4-8a). Presumably this overall trend reflects continuing compaction during the test. Changes associated with compaction may be in part responsible for the difference in deformation indicated by the discussion above. Thermal expansion causing a drop in Pc could also have resulted in an apparent drop in differential stress (subsection 4.1.3).

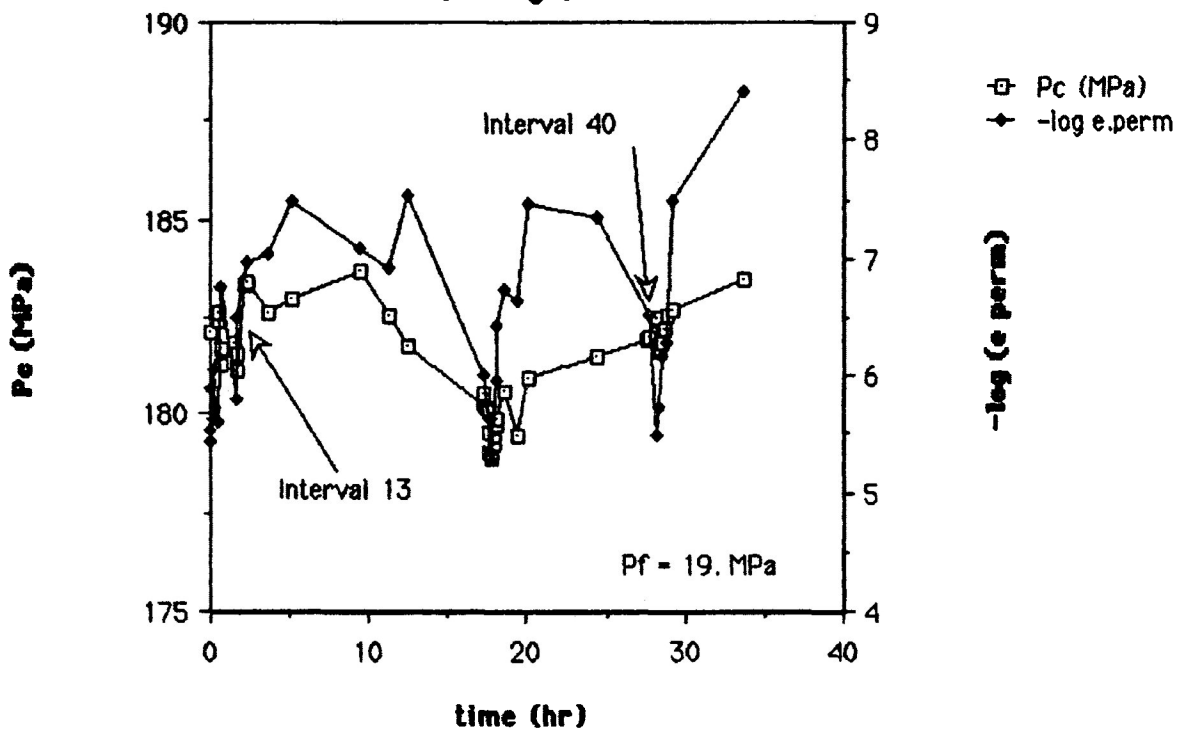
The second SRT on CM-11, performed at $P_f = 19$ MPa (0.19 kb), has given unsatisfactory results. A total of nine intervals define two linear trends, both with a range of less than one order of magnitude of strain rate (Fig. 4-9c). The majority of the data define no readily recognizable pattern.

Although differential stress does fall overall during the second test (Fig. 4-9a), the curve is sufficiently irregular for the

**Fig. 4-9a: CM-11, second SRT;
Pc, differential stress vs. time**



**Fig. 4-9b: CM-11, second SRT;
Pc, $-\log(\text{permanent strain rate})$ vs. time**



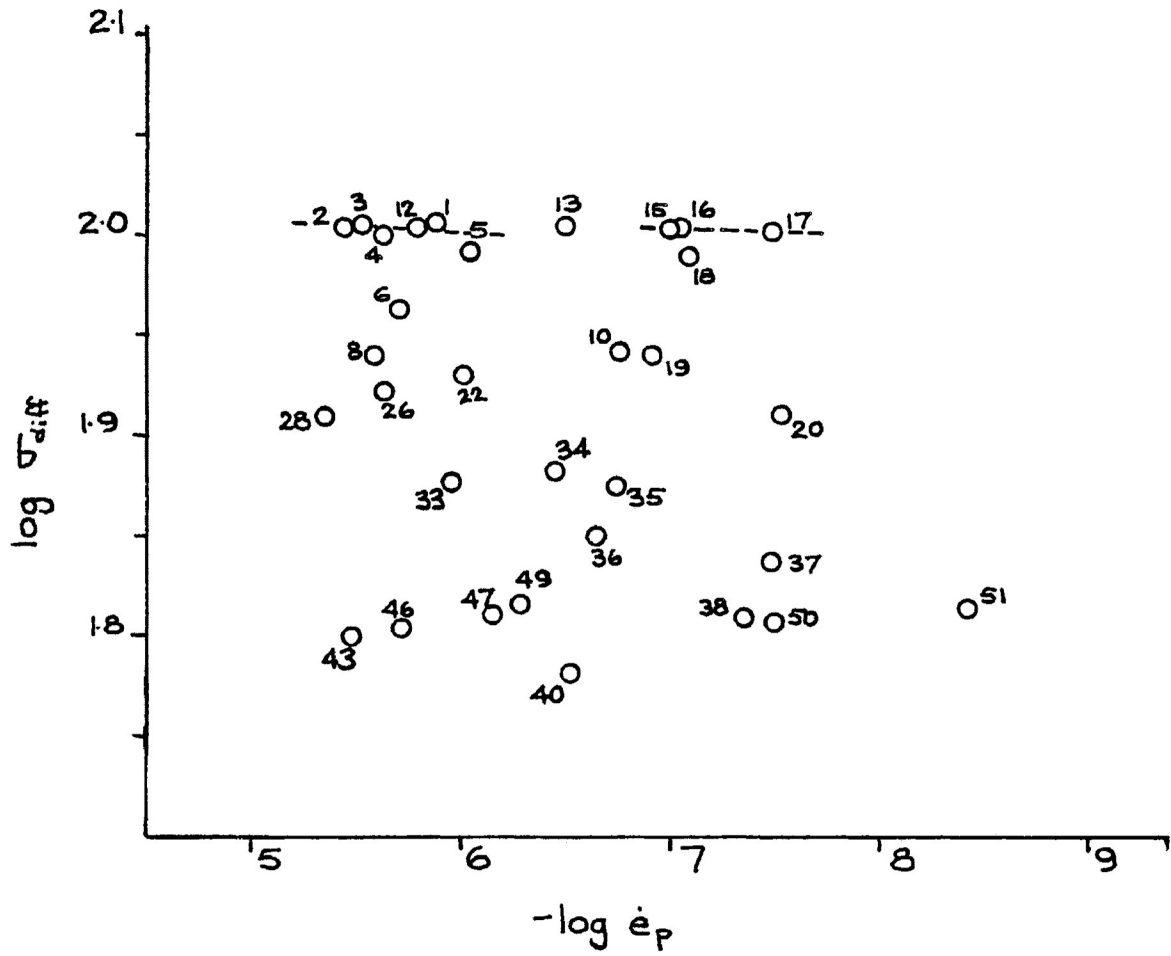


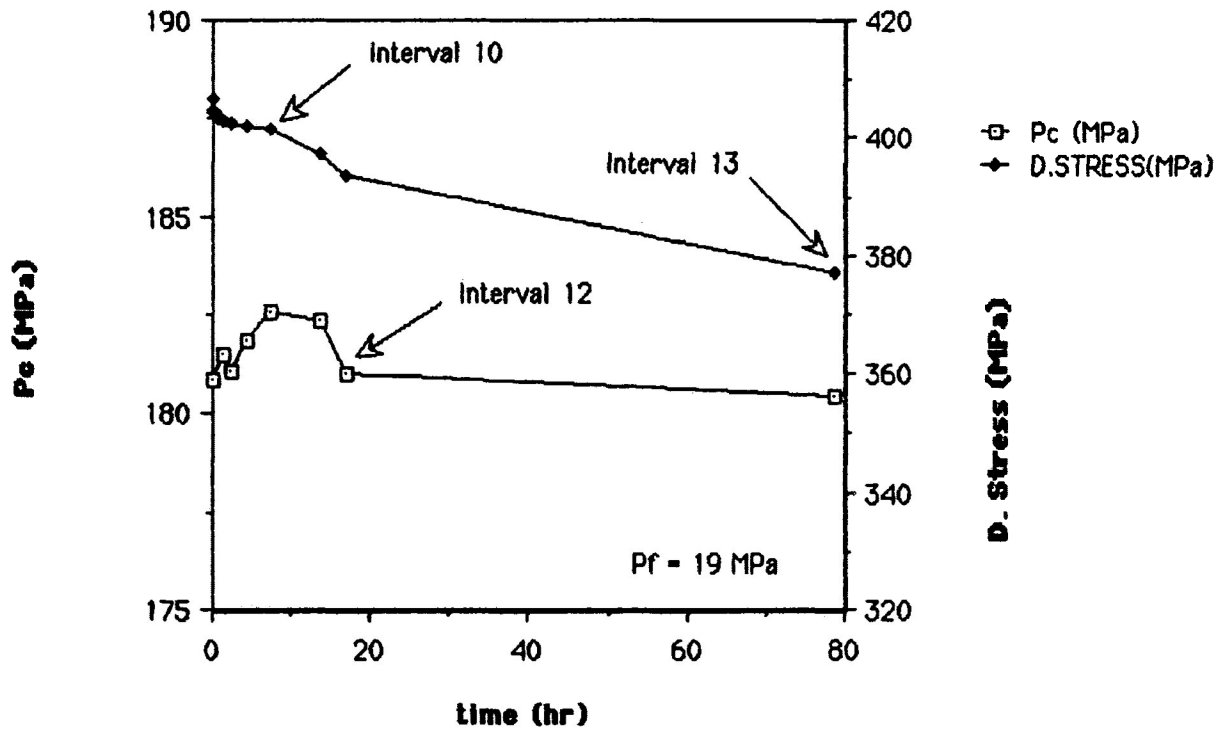
Figure 4-9c: Data from the second SRT on CM-11. Approximate linear trends are shown for intervals 1 to 5 and 15 to 17; these trends are of dubious value.

results to be assigned little value. Following an initial quick drop, differential stress behaved unexpectedly by rising rapidly until interval 13. The minimum of this segment of the differential stress vs. time curve occurred at 1:03 pm, and so it is possible that the drop is related to lunch-hour fluctuation in electrical power supply. Such an effect might similarly explain the sympathetic variation in P_c and strain rate (Fig.4-9b). The clustering of points beginning with interval 21 (at 5:41 am, Wednesday) is possibly explained by ambient temperature rise. If warming is to account for this, it is unexpected that strain rate rose, just as it did during the sudden cooling at the beginning of the first SRT on CM-11. Another cluster of points occurred later, beginning with interval 40 at 4:03 pm, Thursday. This could be due to power fluctuation at the end of the working day.

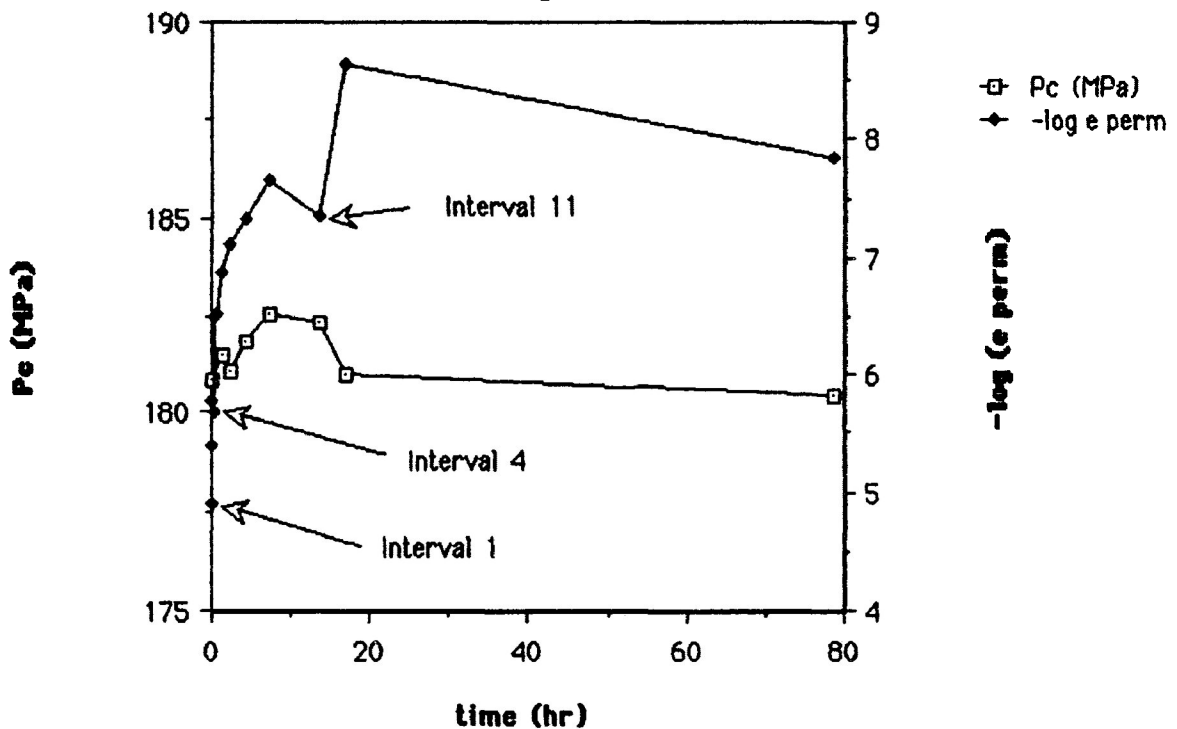
Another possible explanation for (some of) the variability of this test is that sample behavior is responsible. If this is the case, the interpretation appears to be very difficult. Whatever the cause, the best approach appears to be to disregard the results.

Data from the third SRT on CM-11 are unusual and instructive. The initial fast decline of differential stress over time (Fig.4-10a), possibly due to anelastic relaxation, was considerably smaller than that of the first two tests. Also, differential stress vs. time for the third SRT (Fig. 4-10a) has a relatively gentle slope in comparison to the previous two tests. This probably reflects the

**Fig. 4-10a: CM-11, third SRT;
Pc, differential stress vs. time**



**Fig. 4-10b: CM-11, third loading;
Pc, log(permanent strain rate) vs. time**



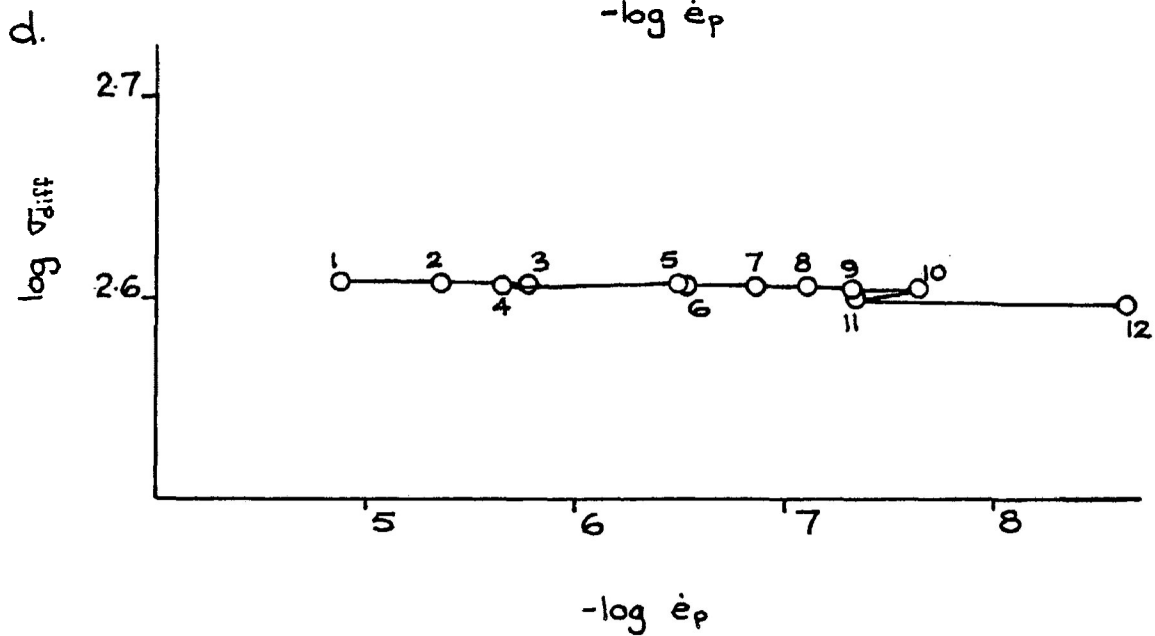
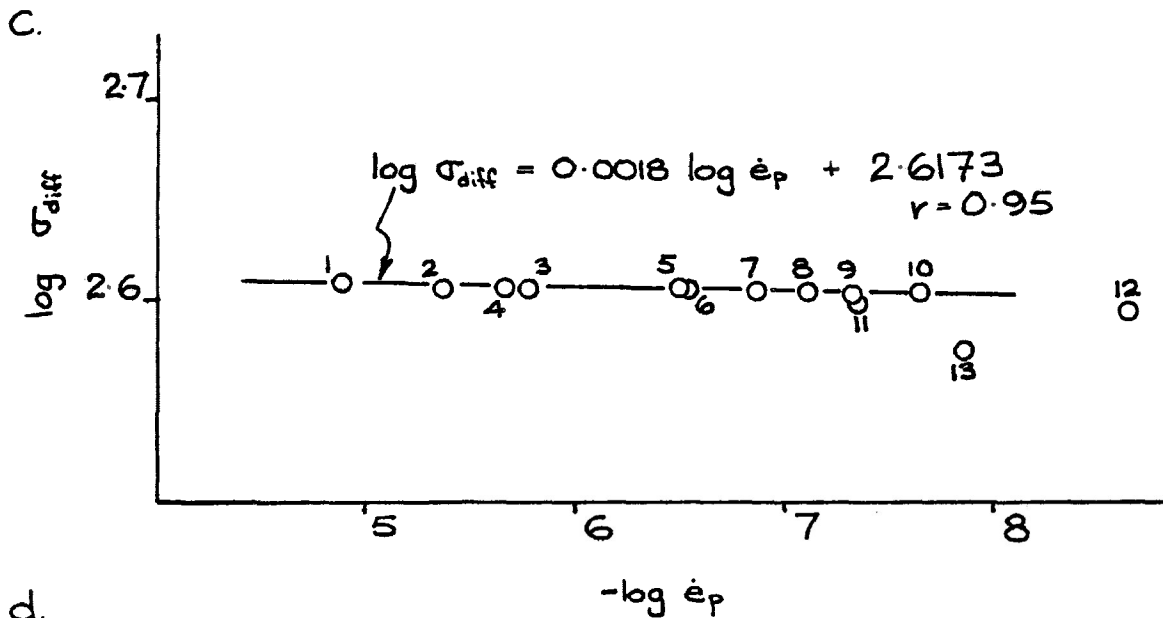


Figure 4-10c, d: $\log(\text{differential stress})$ vs. $-\log(\text{permanent strain rate})$ data from the third SRT on CM-11. Fig. 4-10c shows a best linear fit; 4-10d shows the trend of the data over time.

type of permanent deformation during the third loading, namely steady-state flow, in contrast to the work hardening of the earlier two.

Differential stress was very well-behaved during the first twelve intervals of the test. The absence of any irregularity during the first day of this test indicates no thermal effect has influenced the test. Accompanying the apparently ideal pattern of differential stress is an increase and subsequent decrease in P_c . This appears to be a sample effect on P_c , indicating the sample first dilated and then compacted. Note that the curve of $\log(\text{permanent strain rate})$ over time (Fig. 4-10b) has a sawtooth form. The transition from increasing to decreasing strain rate, at interval 10, coincides with the maximum of the P_c vs. time curve. This appears to be a clear indication that cycling does occur, and that it is accomplished by different (bulk) deformation processes. Note also that Figure 4-10d shows intervals 1 to 12 include two phases when strain rate increased (3 to 4 and 10 to 11), and that the data do not define a simple continuous trend as fitting a single line suggests (Fig. 4-10c). Evidently the microstructural adjustments are very sensitive to strain; the strain accumulated over interval 11 was 0.1%.

Inspection of data from the three SRT's done on CM-11 suggest that the SRT is not able to indicate directly what grain-scale deformation process is occurring in a sample so much

as it indicates what bulk sample deformation is occurring. There are two reasons for this. One is change in P_c , which was observed in all three tests. Some of this change is a machine effect, but sample volume change is partially responsible. With a volume change, deformation must be partly intergranular. A second reason is the cycling of data. This phenomenon indicates that, even if only one overall linear trend is present, there is more than one process active in deforming a sample. Clearly the data are characteristic of the sample behavior, and not of some particular granular deformation mechanism. This is particularly so if change in sample volume is related to this process, as the third SRT suggests.

A problem raised by this interpretation of the data is the identification of the particular deformation mechanism responsible for deformation at the level of individual grains. The cycling of strain rate during the continuous drop of differential stress of a SRT indicates that the sample is alternating between two processes. Either or both of these processes may be individual deformation mechanisms operating exclusively, or be a combination of deformation mechanisms. The transition to another process occurs when the sample is softer in response to that other process.

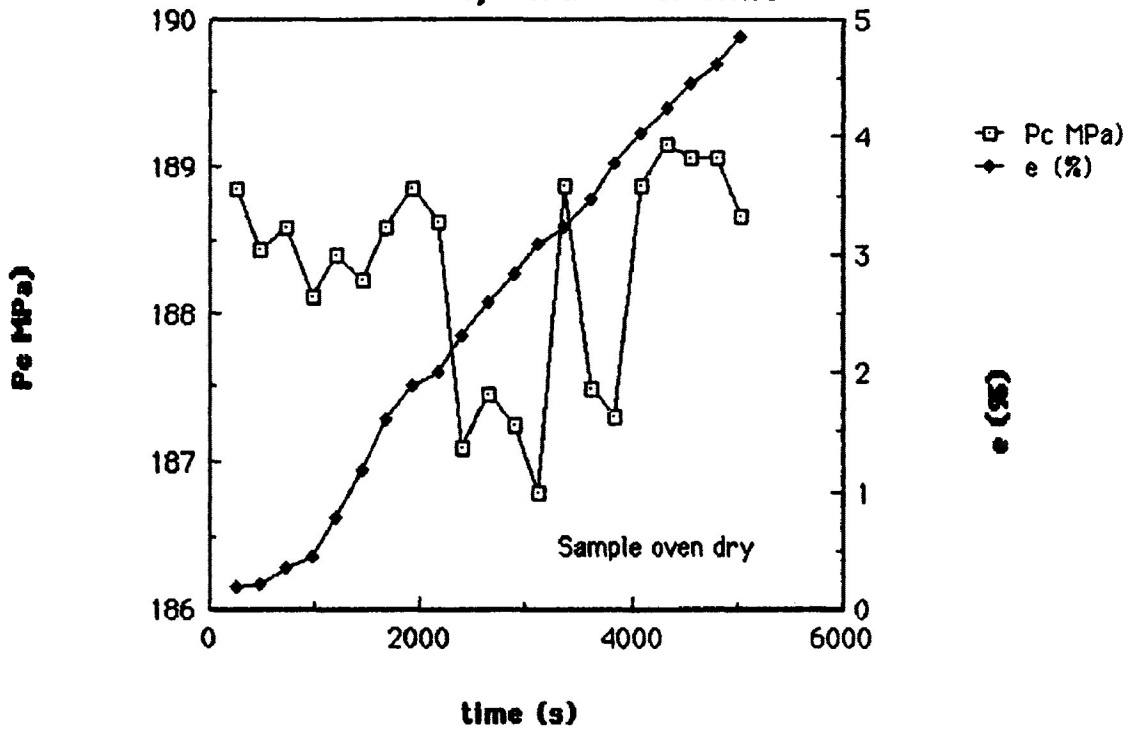
CM-13

A total of four tests were run on sample CM-13. The first two were performed on the sample after oven drying, the third with the sample saturated with water at $P_f = 0$, and the fourth at $P_f = 48.3\text{MPa}$ (0.48 kb).

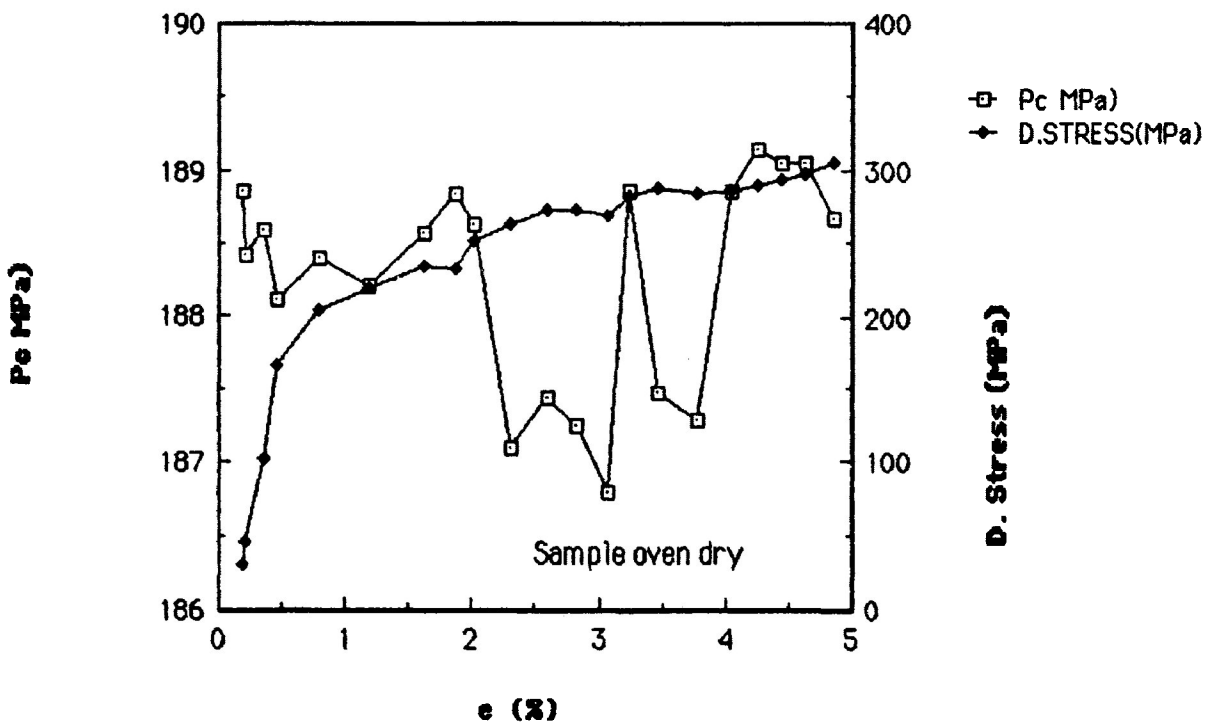
Loading: Graphs of e vs. time (Figs. 4-11a, 12a, 13a and 14a) show that e accumulated more quickly as the sample passed through the yield point but otherwise increased approximately linearly. This behavior is consistent with that observed in CM-11. P_c does not, however, display uniform behavior through this series of tests. During the second and fourth loadings (Fig. 4-12b, 14b) P_c dropped during elastic straining of the sample and then remained approximately level during permanent flow. Again, this is generally similar to CM-11 behavior in loading. The first and third loadings (Fig. 4-11a, 13a) are, in contrast, very much different. During both loadings, P_c was approximately constant but subject to fluctuation, especially during the first. It is difficult to account for this behavior: it is very different from that of the other two loadings which follow the pattern of CM-11.

SRTs: Machine effects appear to have been the cause of the irregularity of results from the first SRT. Differential stress declined overall (Fig. 4-15a) but local increases did occur. Likewise, permanent strain rate (Fig. 4-15b) does not vary smoothly. Irregularities of data from the start of the test (12:35

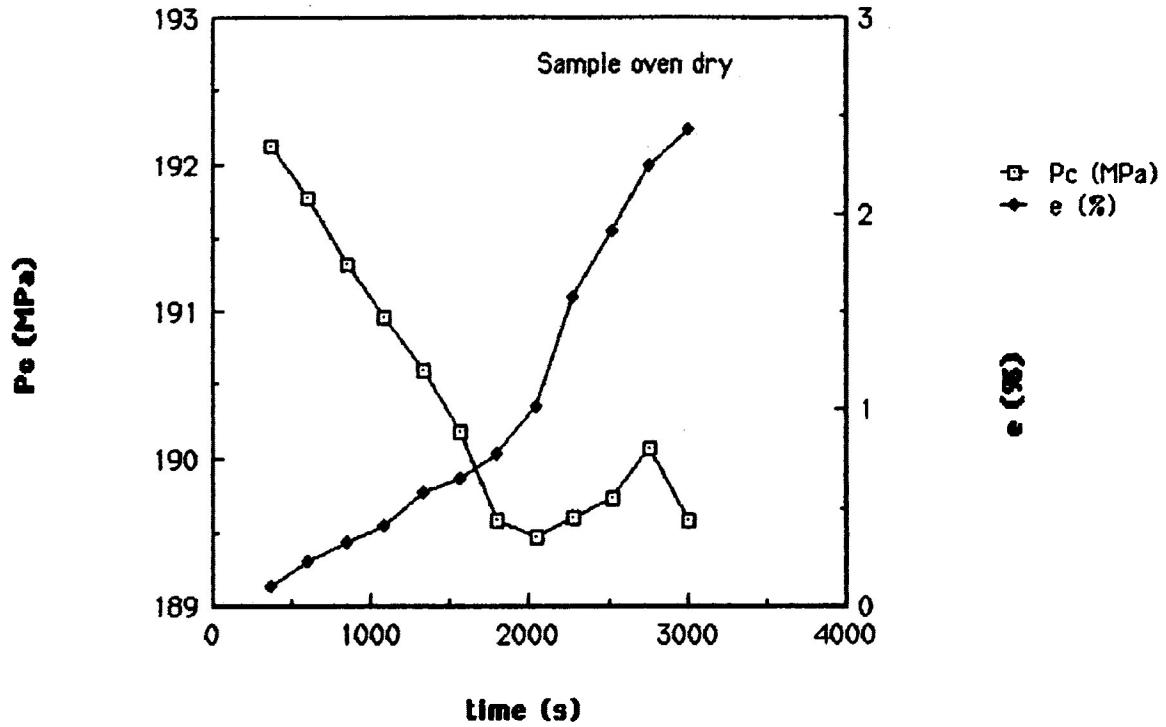
**Fig. 4-11a: CM-13, first loading;
Pc, strain vs. time**



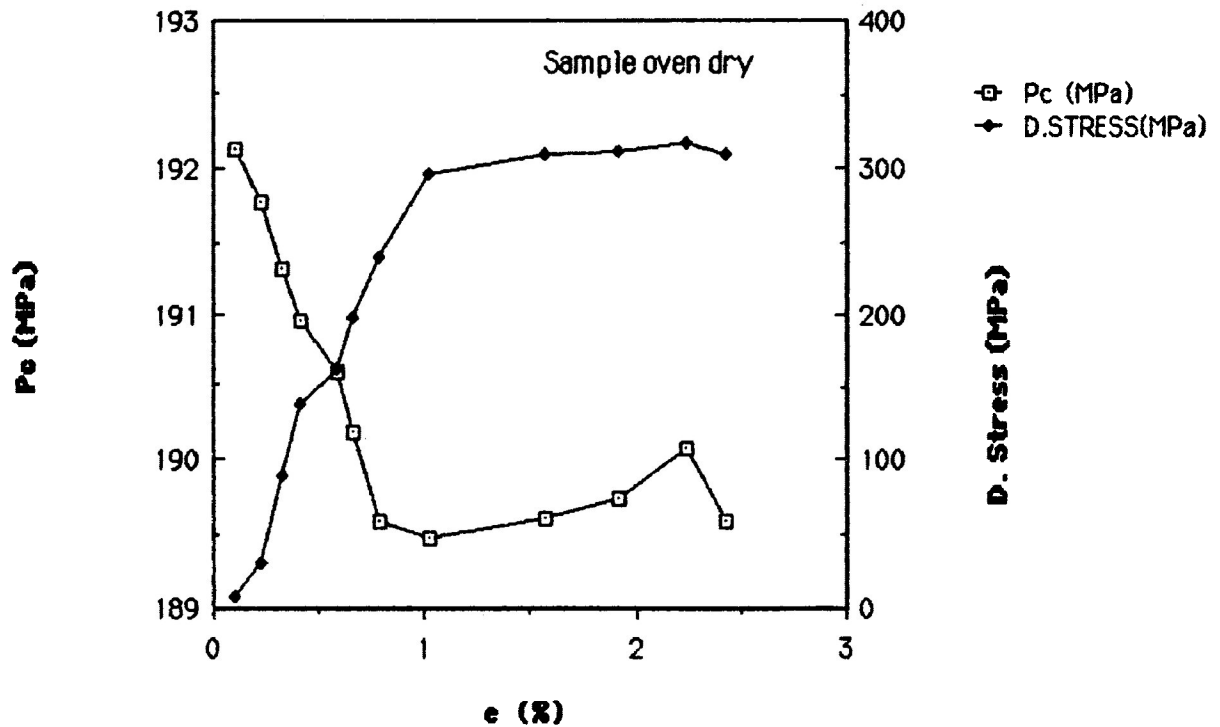
**Fig. 4-11b: CM-13, first loading;
Pc, differential stress vs. strain**



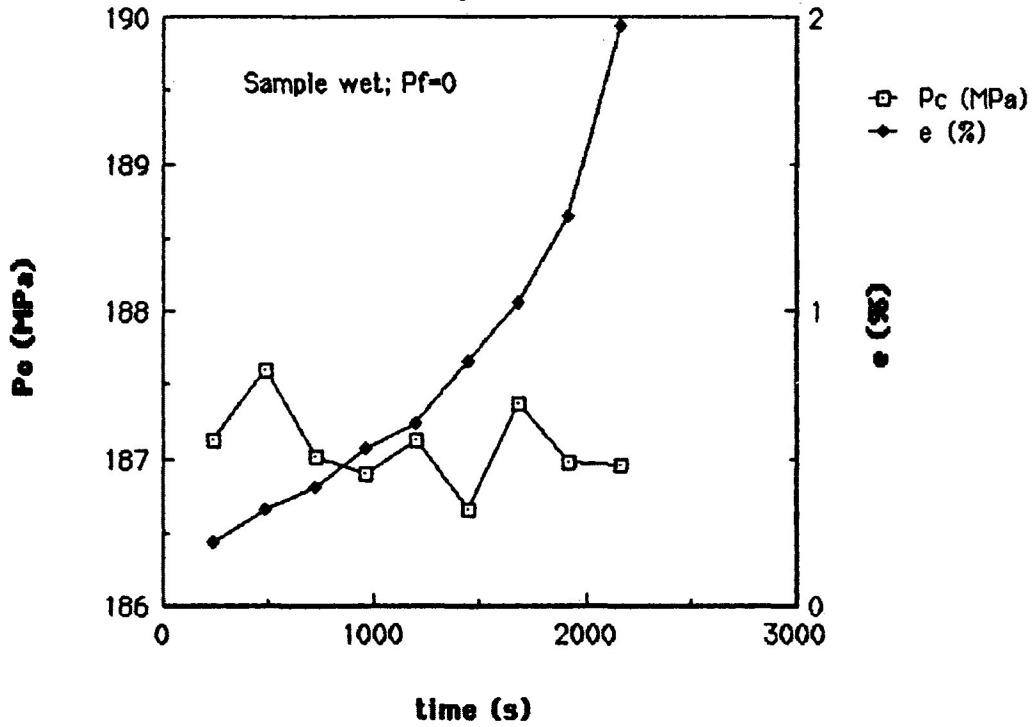
**Fig. 4-12a: CM-13, second loading;
Pc, strain vs. time**



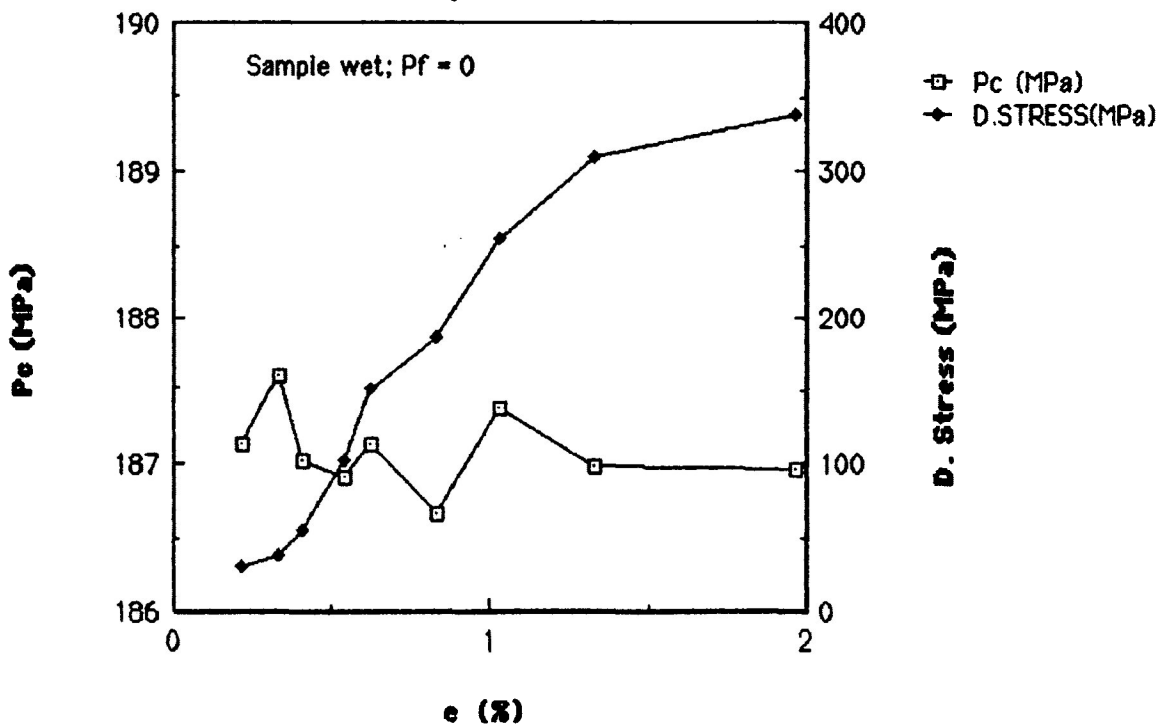
**Fig. 4-12b: CM-13, second loading;
Pc, differential stress vs. strain**



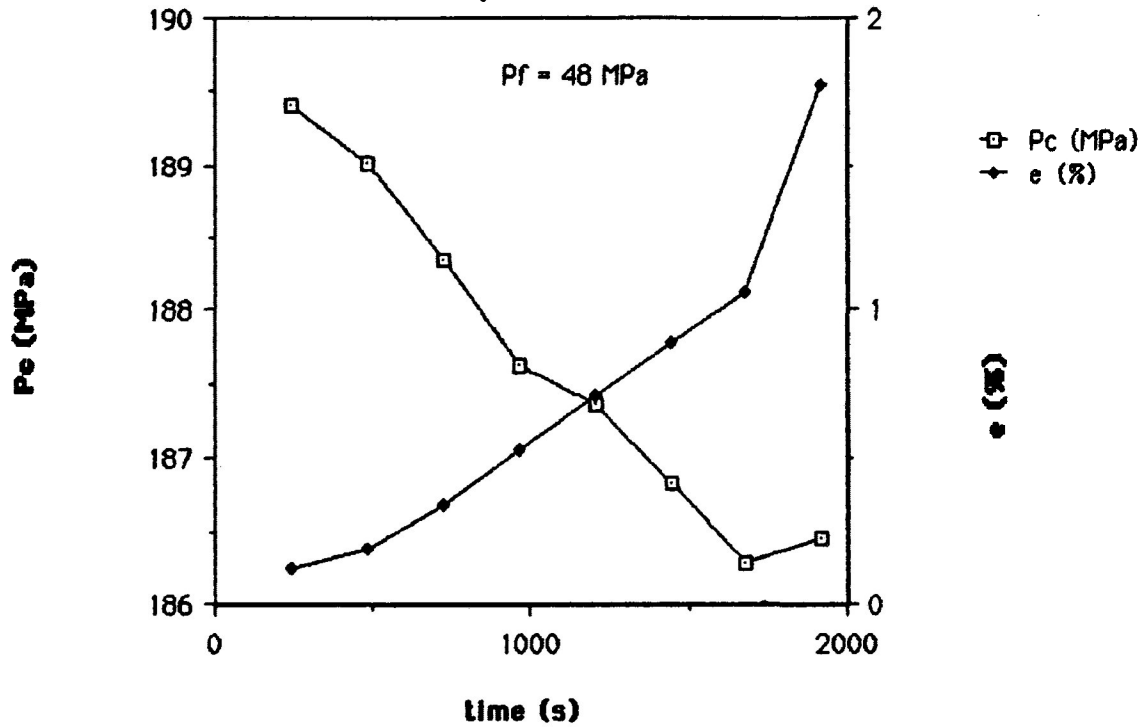
**Fig. 4-13a: CM-13, third loading;
Pc, strain vs. time**



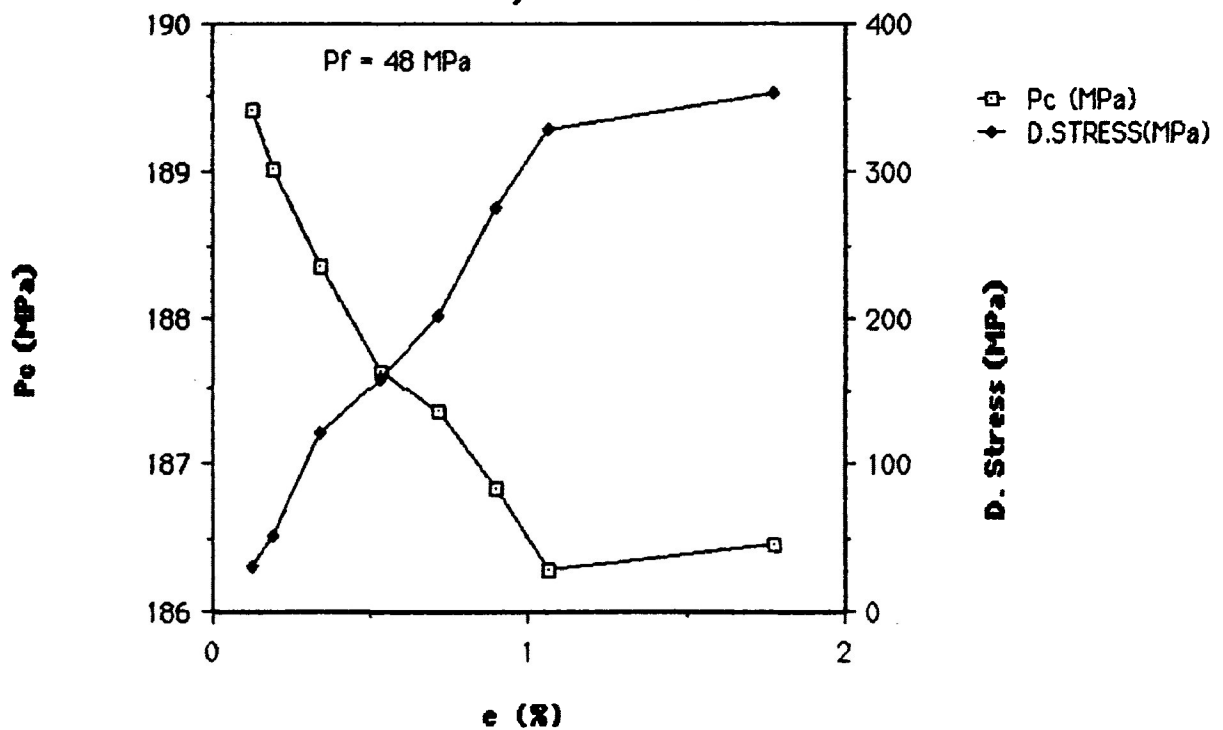
**Fig. 4-13b: CM-13, third loading;
Pc, differential stress vs. strain**



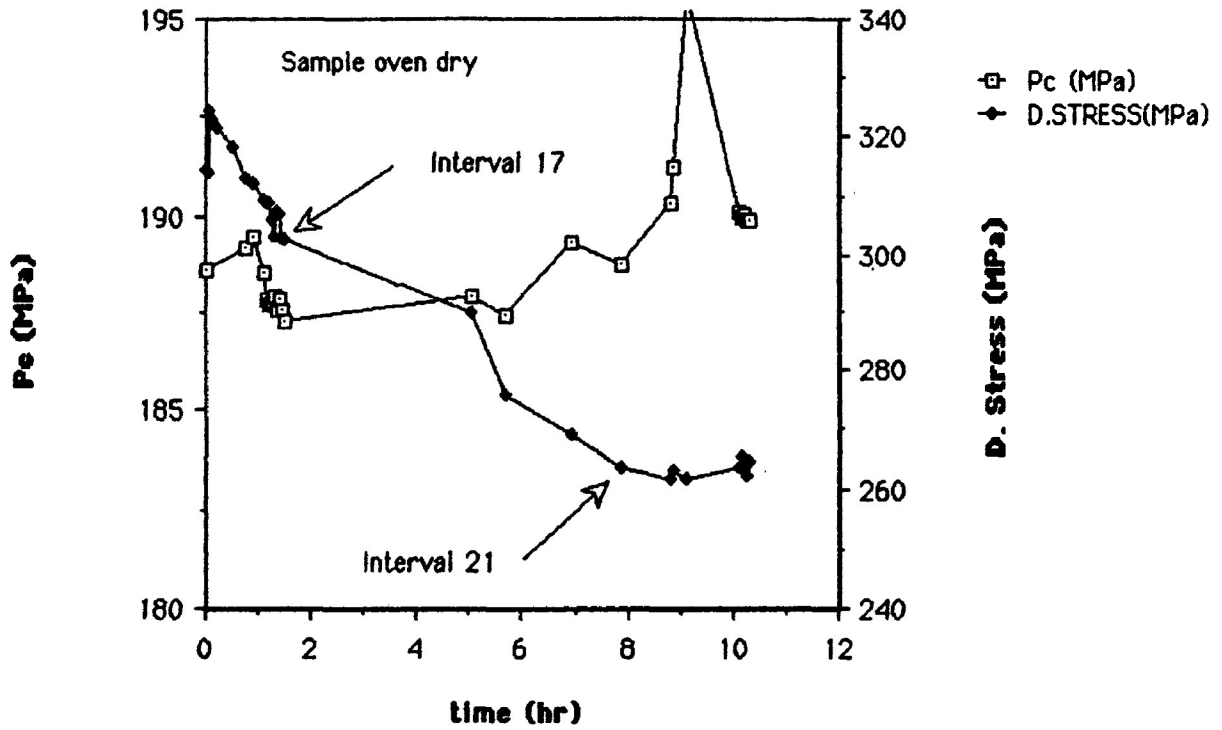
**Fig. 4-14a: CM-13, fourth loading;
Pc, differential stress vs. strain**



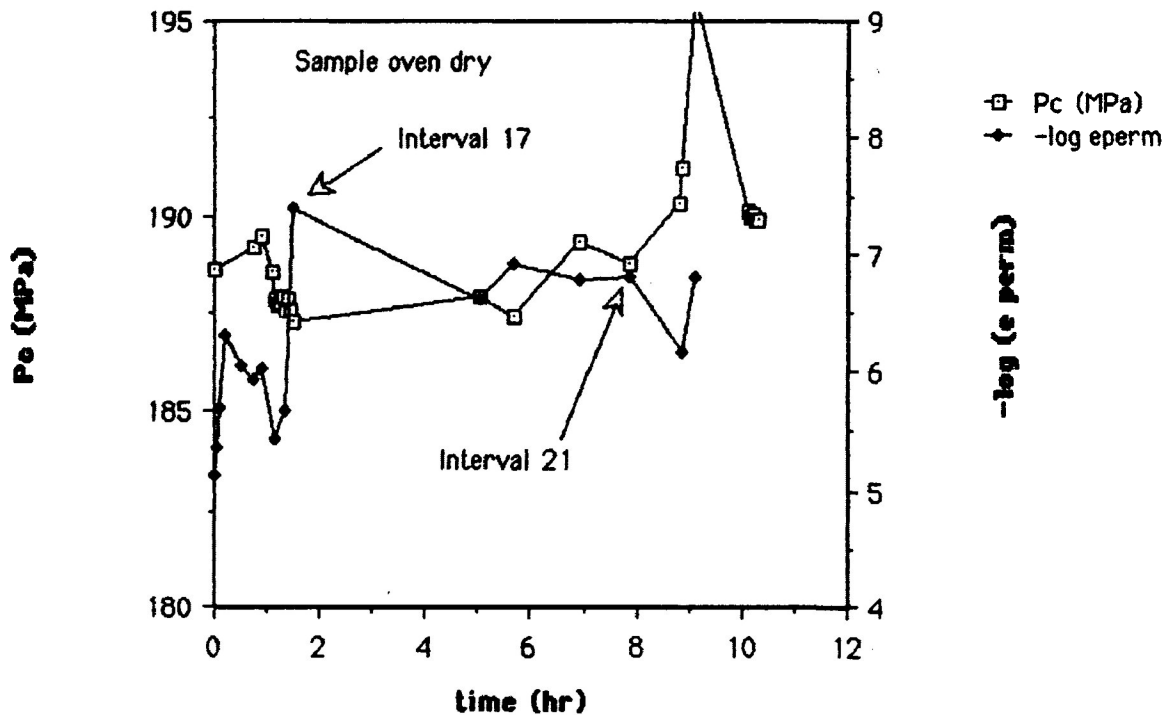
**Fig. 4-14b: CM-13, fourth loading;
Pc, differential stress vs. strain**



**Fig. 4-15a: CM-13, first SRT;
Pc, differential stress vs. time**



**Fig. 4-15b: CM-13, first SRT;
Pc, log(permanent strain rate) vs. time**



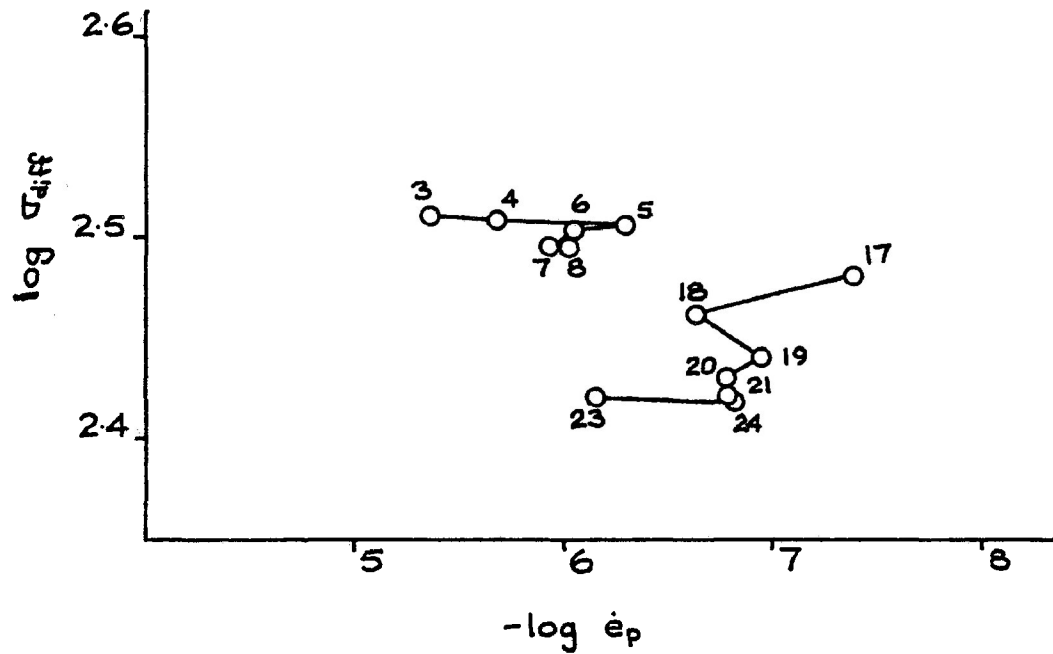


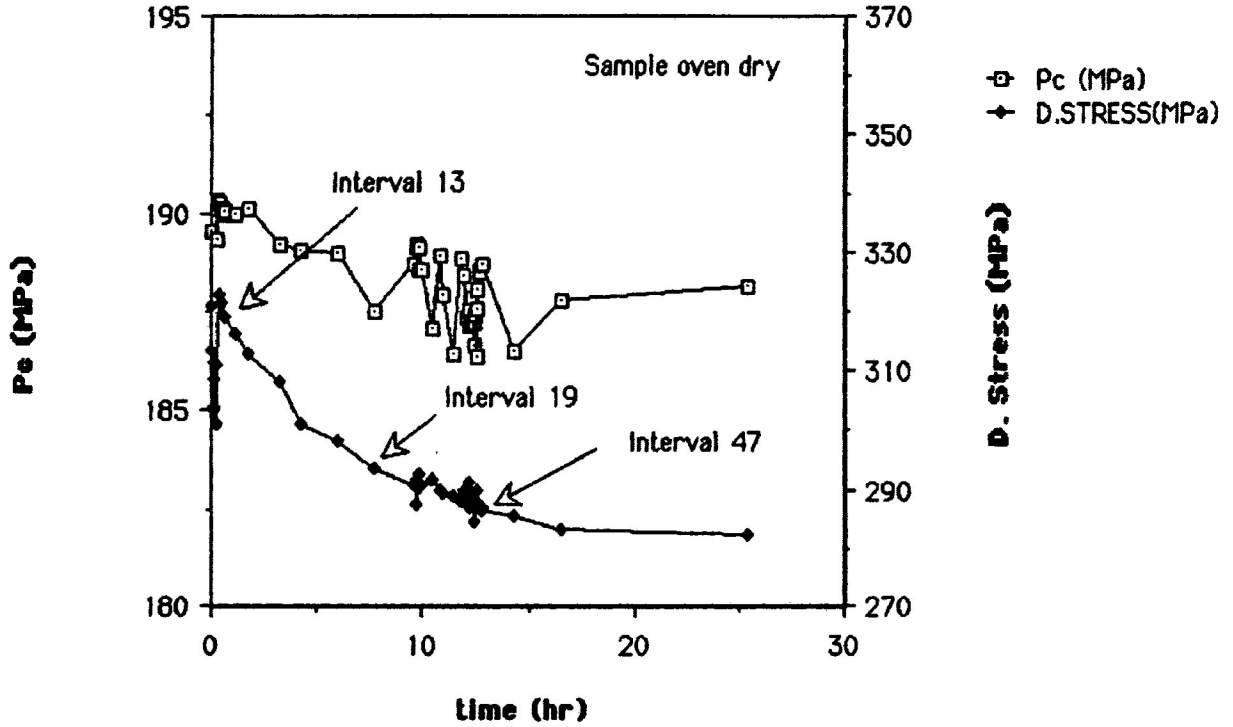
Figure 4-15c: $\log(\text{differential stress})$ vs. $-\log(\text{permanent strain rate})$ for the first SRT on CM-13. Only data which are subject to cycling are shown; other data show no discernable trend. Note that points 17 to 21 and 23 to 24 are not continuous; there appears to have been a thermal interruption.

pm, Wednesday) until interval 17 (2:05 pm) are perhaps due to lunch time power fluctuation. Similarly, the general increase in differential stress and rejection of permanent strain rate data after interval 21 may be attributable to ambient temperature drop. Despite no general decrease of strain rate, some cycling is apparent (Fig. 4-15c).

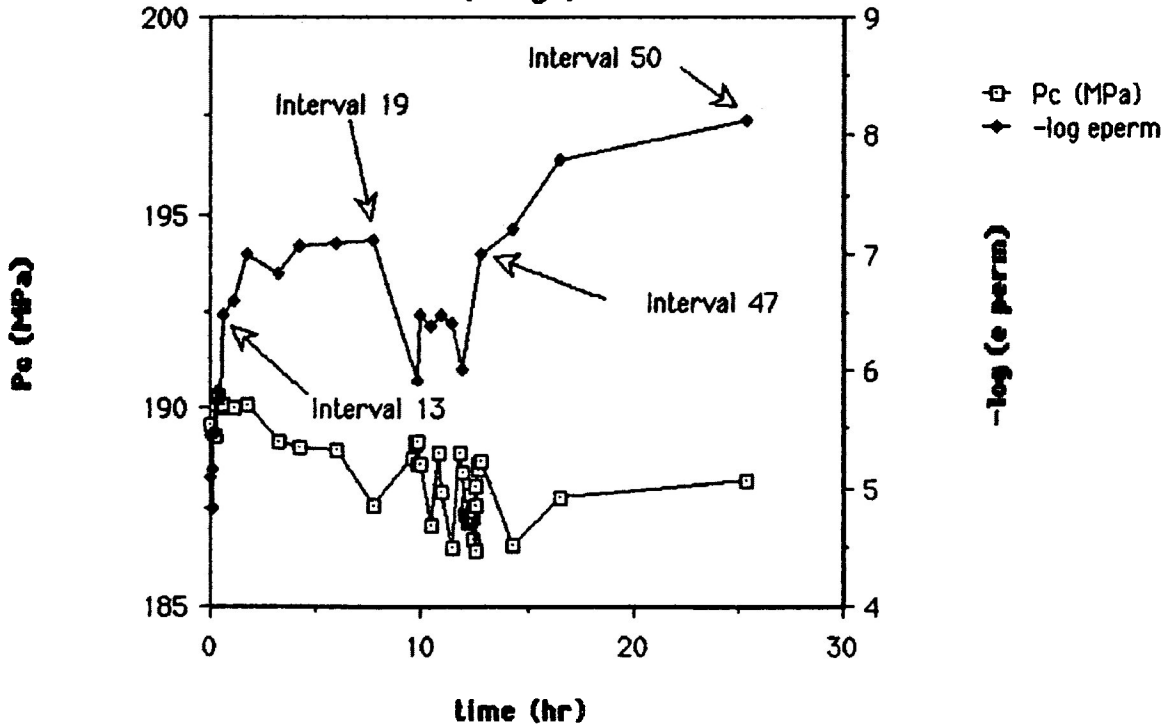
Data from the second SRT on CM-13 are of similar quality to that of the first test. Differential stress (Fig. 4-16a) dropped over most of the test except during intervals 20 to 47 (10:16 am to 1:27 pm, Thursday) when it underwent considerable minor fluctuation. Mirroring this change were both P_c and permanent strain rate (Fig. 4-16b). It is possible that mid-day current fluctuation is responsible, but some rapidly changing, perhaps alternating sample behavior, could have been occurring. Cycling did occur over intervals 13 to 19 (Fig. 4-16c). The steeper trend of intervals 17 to 19, occurring over a period of 3 hours, 29 minutes, apparently suggests some process is operative which is different than that over intervals 13 to 16, and over the other periods of continuous data (intervals 1 to 4 and 47 to 50).

Results from the third SRT on sample CM-13 indicate very regular behavior until interval 15 (at 10:16 am, Friday; Figs. 4-17a,b). Presumably this interruption is due to falling ambient temperature. Data taken subsequently do not appear to be reliable with the possible exception of the final three intervals, 46 to 48.

**Fig. 4-16a: CM-13, second SRT;
Pc, differential stress vs. time**



**Fig. 4-16b: CM-13, second SRT;
Pc, log(permanent strain rate) vs. time**



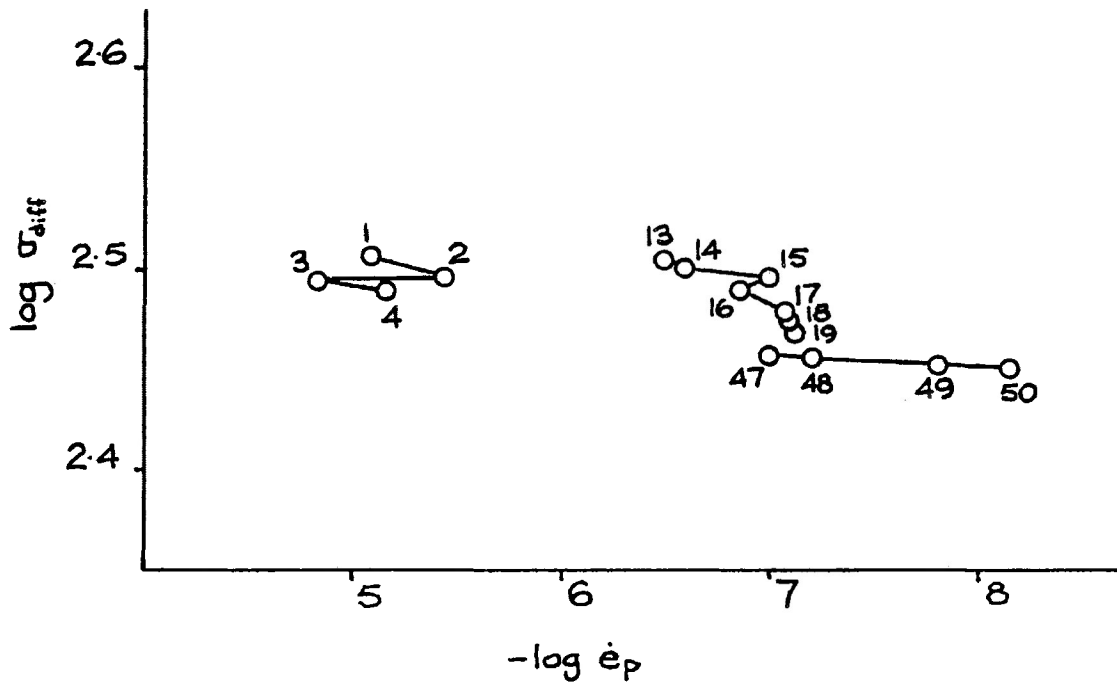
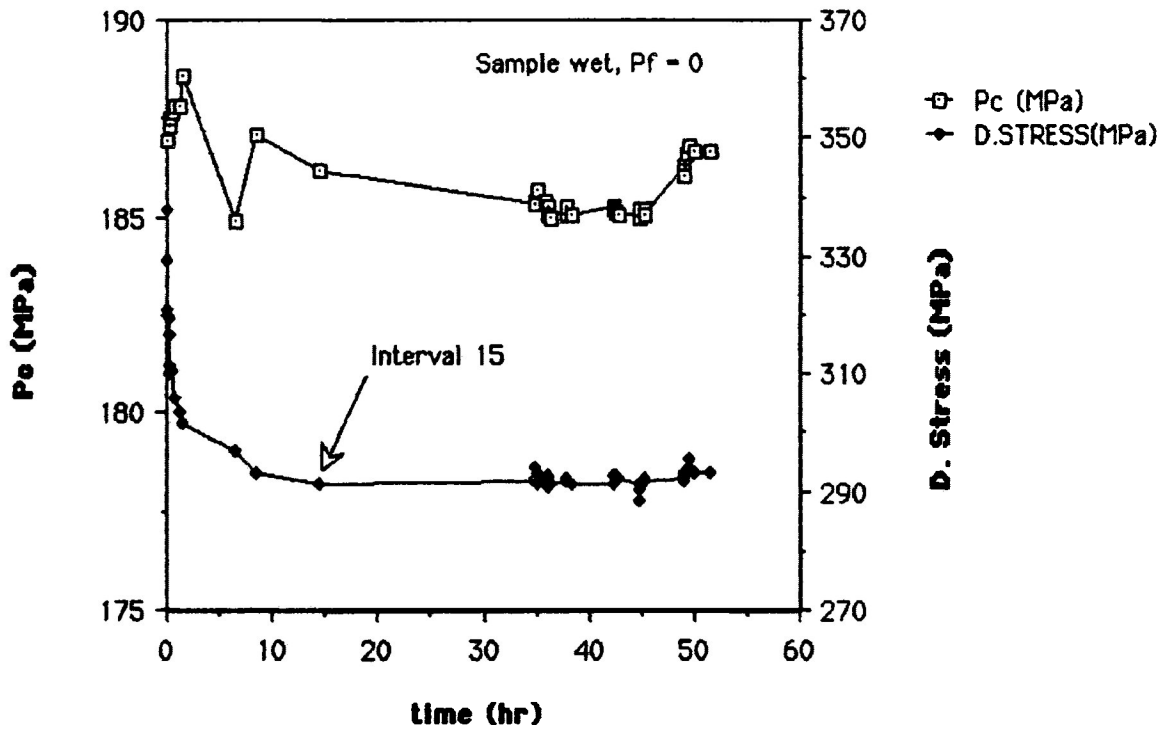
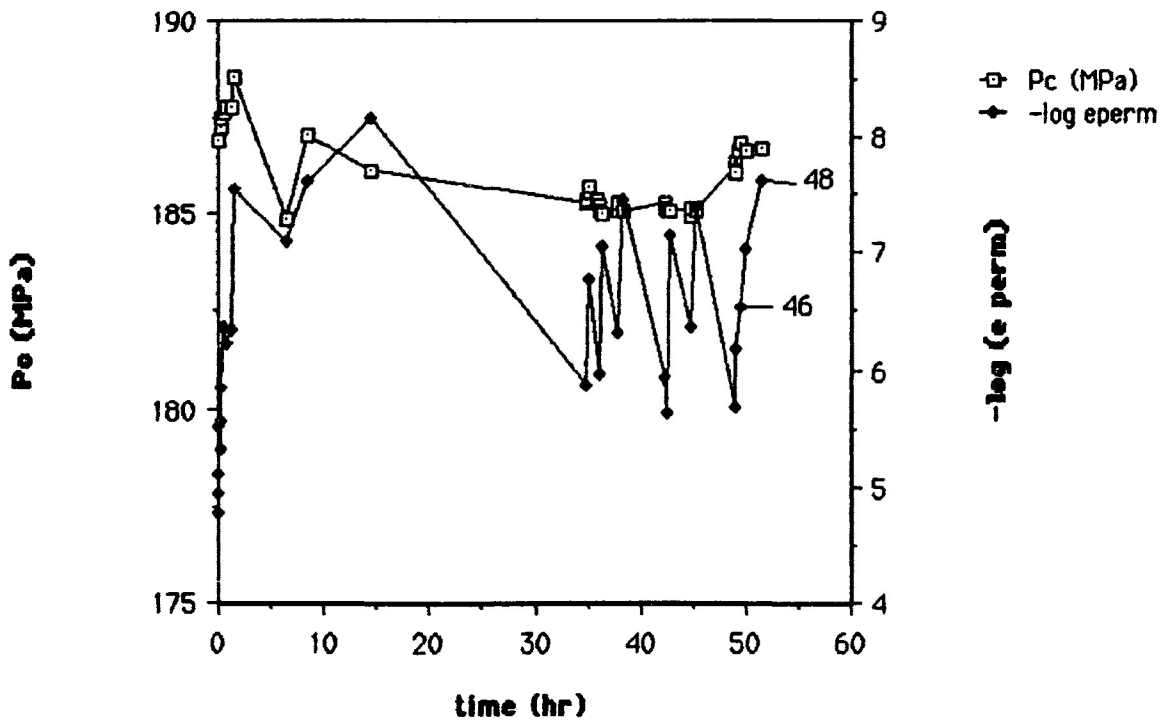


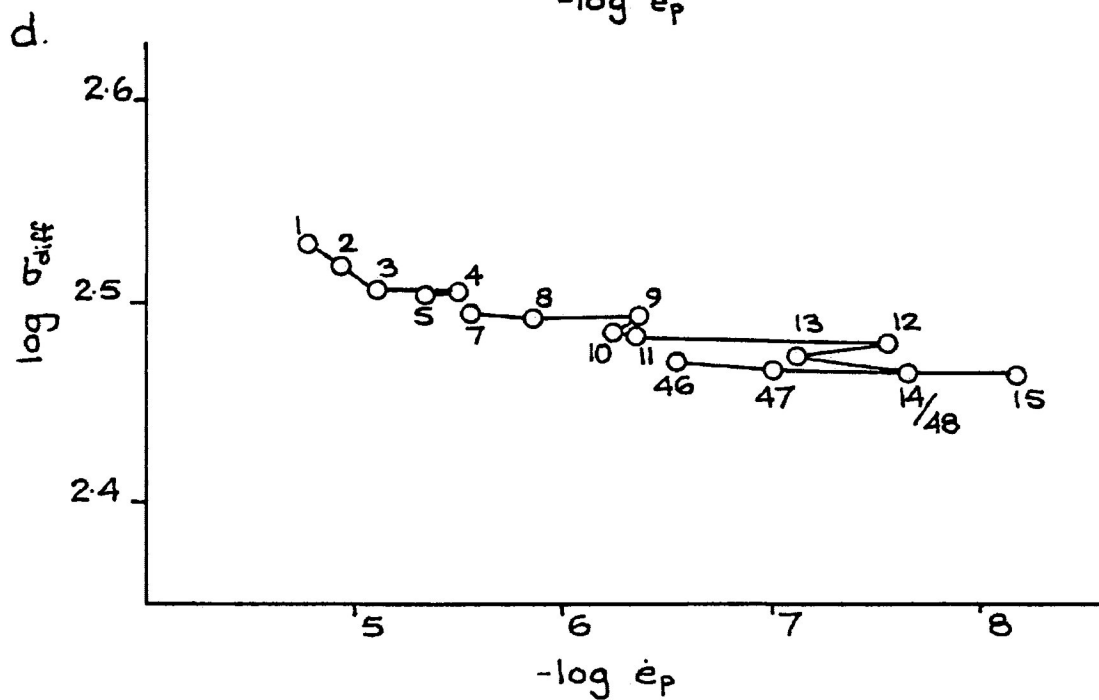
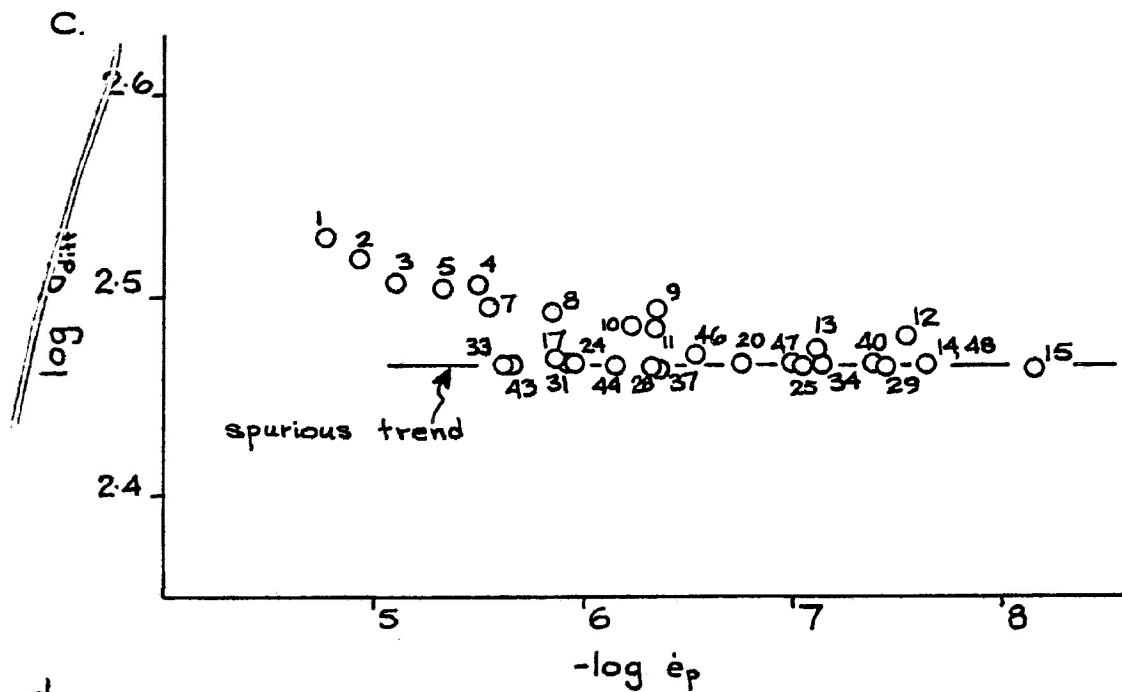
Figure 4-16c: $\log(\text{differential stress})$ vs. $-\log(\text{permanent strain rate})$ for the second SRT on CM-13. Note that because the differential stress for interval 13 is greater than that for interval 4, one may infer that a (thermally generated) interruption has occurred between these intervals.

**Fig. 4-17a: CM-13, third SRT;
Pc, differential stress vs. time**



**Fig. 4-17b: CM-13, third SRT;
Pc, log(permanent strain rate) vs. time**





Figures 4-17c, d: $\log(\text{differential stress})$ vs. $-\log(\text{permanent strain rate})$ for the third SRT on CM-13. Fig. 4-17c shows all the data; note the nominal linear trend. Fig. 4-17d shows data for which differential stress steadily drops.

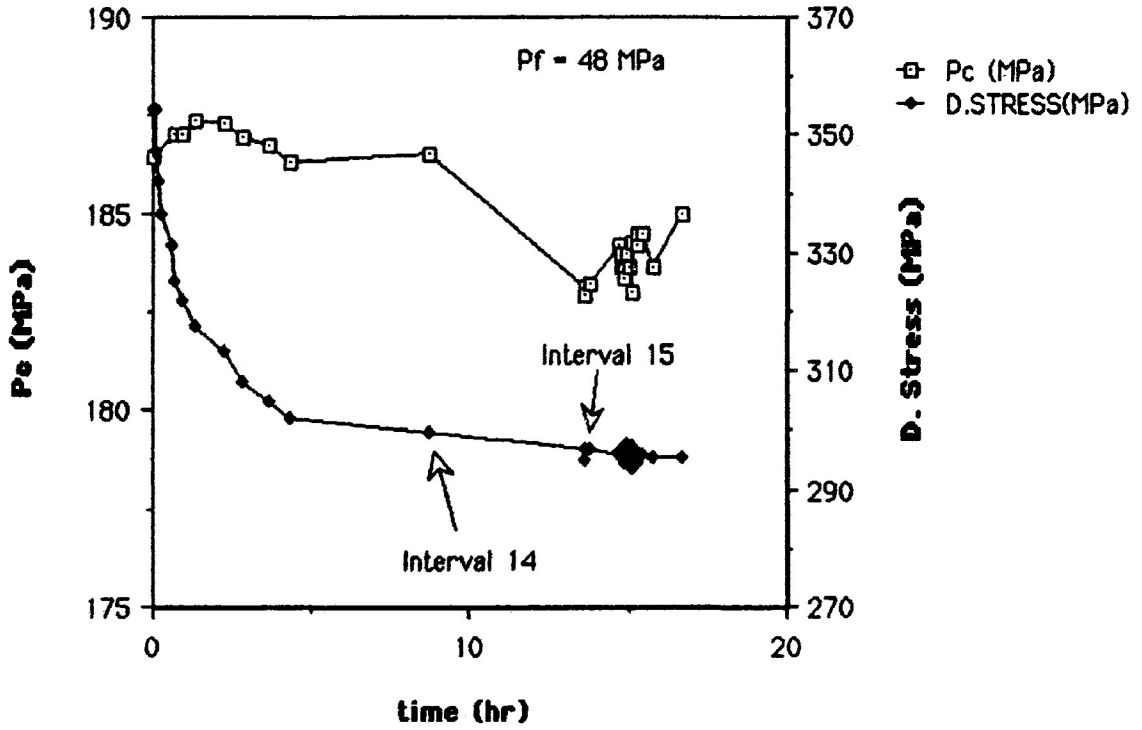
The intermediate interval points show a linear trend (Fig. 4-17c) which is suspect; the irregular pattern of differential stress, which includes increases (Fig. 4-17a), is not meaningful. Strain rate (Fig. 4-17b) is similarly variable, and includes a number of null results which do not appear on the graph.

Cycling has occurred several times (Fig. 4-17d) over the first 15 intervals. The general form of the curve is concave up (but note that interval 6 gave a null value for strain rate). The overlap of intervals 14 and 48 is a consequence of the irregularity of differential stress; it has risen during the intervening intervals.

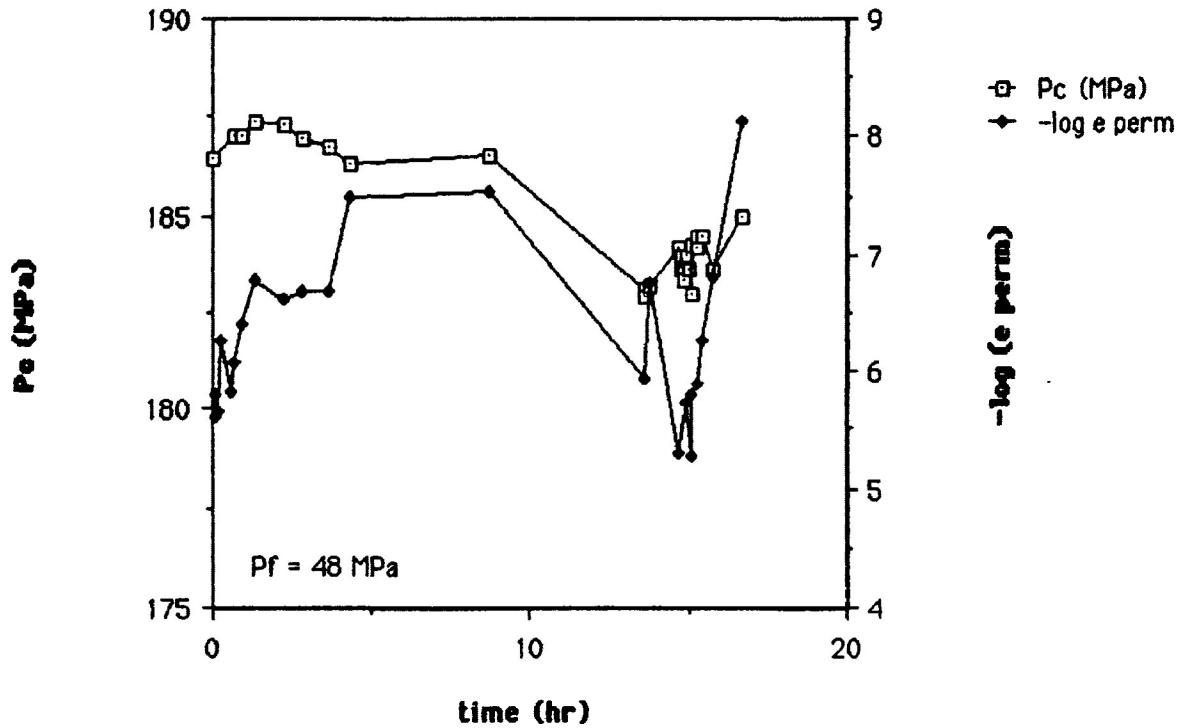
Good results were obtained from intervals up to and including number 14 during the fourth SRT. Differential stress (Fig. 4-18a) showed a steady decline while strain rate (Fig. 4-18b) was stepped, giving rise to a pattern of cycling (Fig. 4-18c). Ambient heating would have occurred between intervals 14 (4:50 am, Monday) and 15 (9:39 am), thus explaining the irregularity in differential stress, strain rate and P_c .

Results of SRT's on CM-13 resemble those of CM-11. Both groups of tests were subject to interruption due to machine effects, and possibly also due to complex sample behavior. The first and second SRT's on CM-13 show a curious pattern; differential stress increased sharply within a few minutes of the start of the test. The cause of this is not clear; presumably it is a machine effect. Despite these extraneous effects, the true

**Fig. 4-18a: CM-13, fourth SRT;
Pc, differential stress vs. time**



**Fig. 4-18b: CM-13, fourth SRT;
Pc, log(permanent strain rate) vs. time**



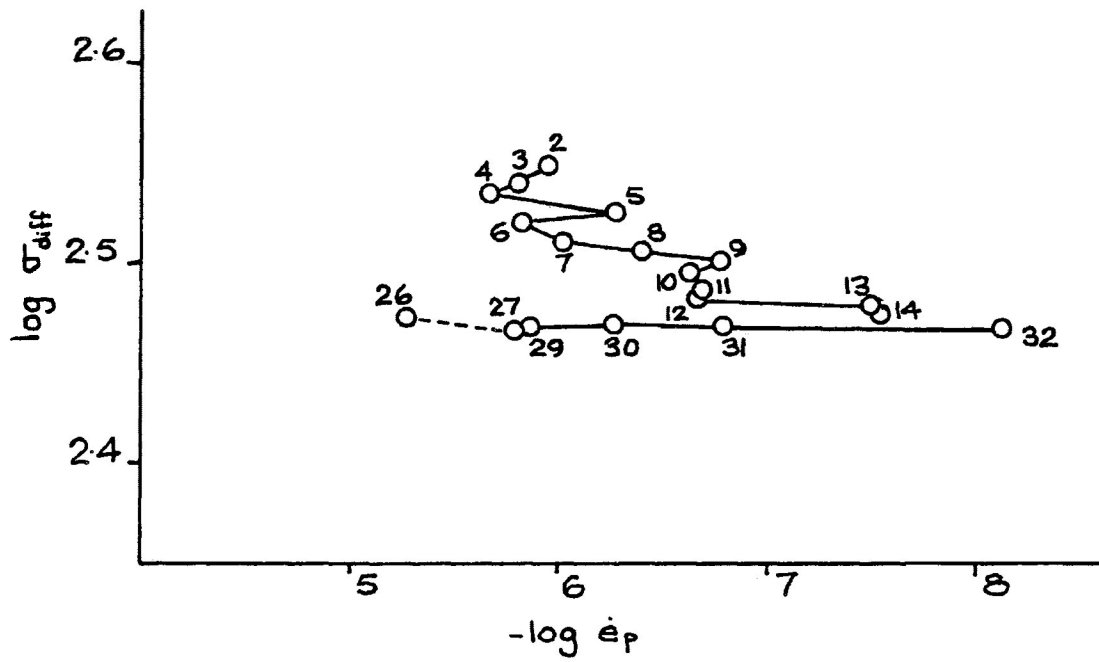


Figure 4-18c: log(differential stress) vs. -log(permanent strain rate) for the fourth SRT performed on CM-13.

sample behavior of cycling is apparent. Unlike CM-11, these results do not show overall linear trends with increasing slope from any one test. It is notable that the final SRT on CM-13 shows a linear trend with nearly stress-independent attitude (intervals 29 to 32). This trend resembles that obtained during the third SRT performed on CM-11. In both cases the samples had been strained over 10%, indicating this deformation is structurally controlled.

CM-1 to 8

Testing of samples CM-1 to 8 was performed without the use of a heating jacket on the pressure vessel and without recording P_c . Because of this, only a brief discussion of the results is given.

Loading: Behavior of the Carrara marble during loading (Figs. 4-19 to 25) was reasonably consistent. Elastic strain, indicated by the initial sub-linear locus of differential stress vs. strain data points, ended at differential yield stresses ranging from approximately 100 (for CM-1) to 270 MPa (for CM-7). While the initial segment of the differential stress-strain curves for some of the samples (CM-4, 6, 7 and 8) is not markedly linear, the load-displacement curves (not shown) produced by the chart recorder during the tests indicate a (near-)linear relation does in fact exist. All of the samples underwent work-hardening (indicated by a positive slope of the stress-strain curve) after passing the yield point. Irregularities during this permanent

Fig. 4-19a: CM-1, first loading; Differential stress vs. strain

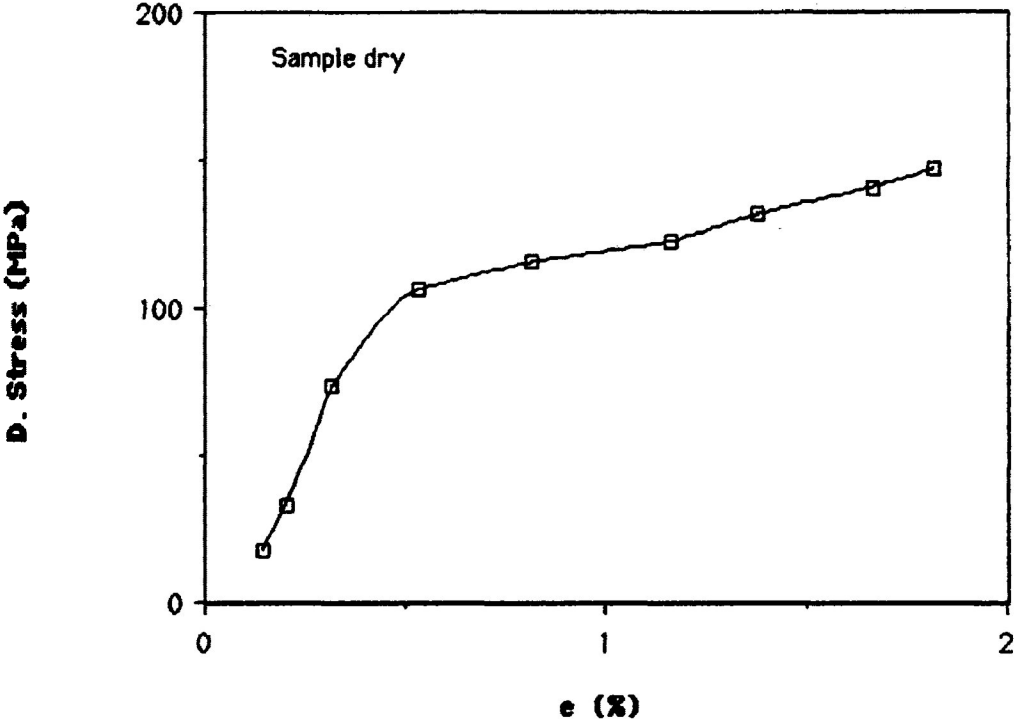


Fig. 4-19b: CM-1, second loading; Differential stress vs. strain

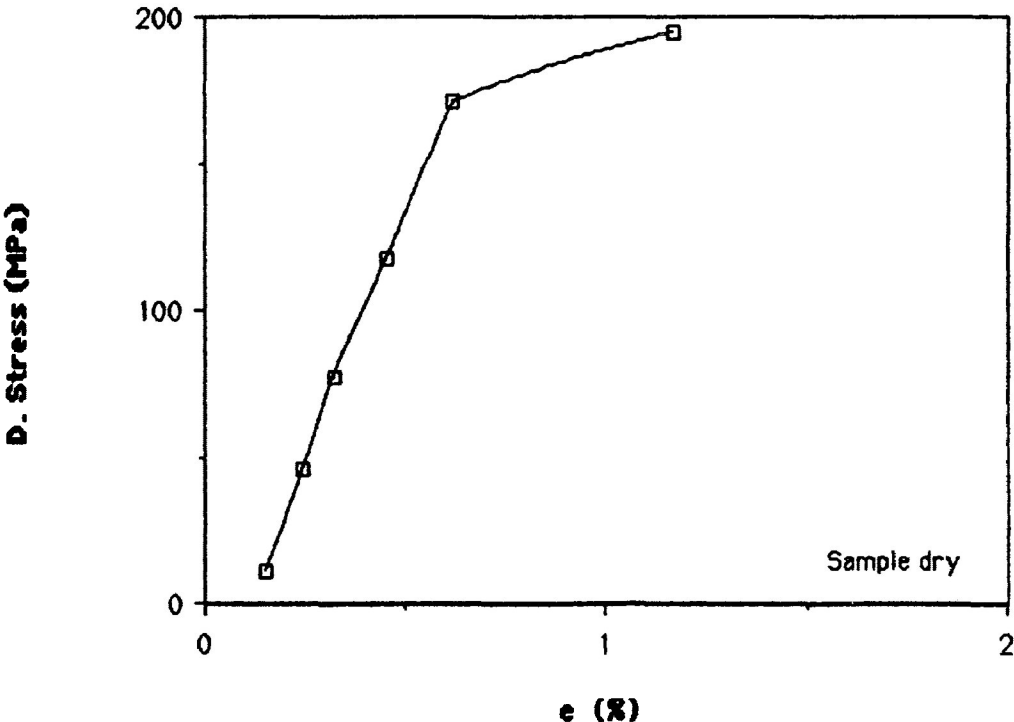


Fig. 4-20: CM-3 loading; Differential stress vs. strain

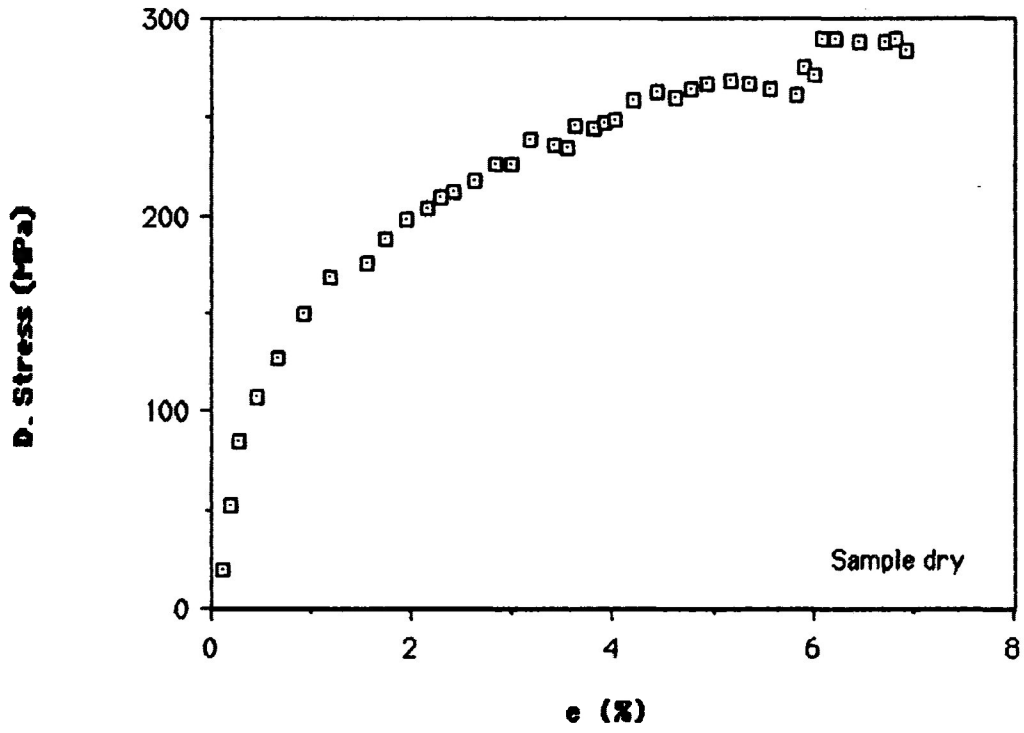


Fig. 4-21a: CM-4, first loading; Differential stress vs. strain

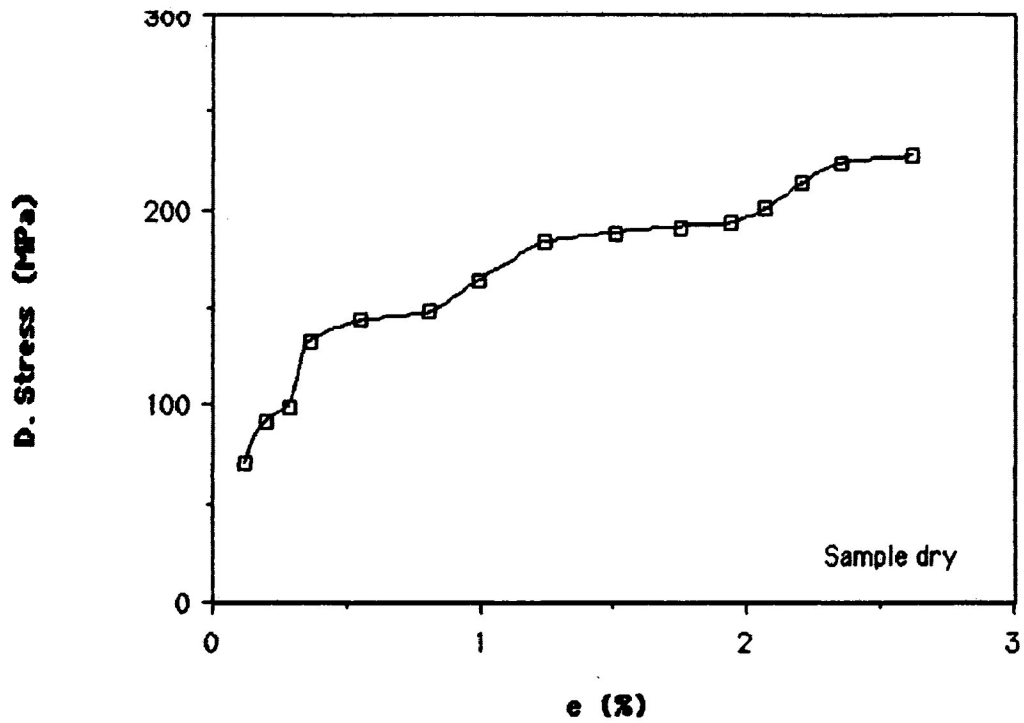


Fig. 4-21b: CM-4, second loading; Differential stress vs. strain

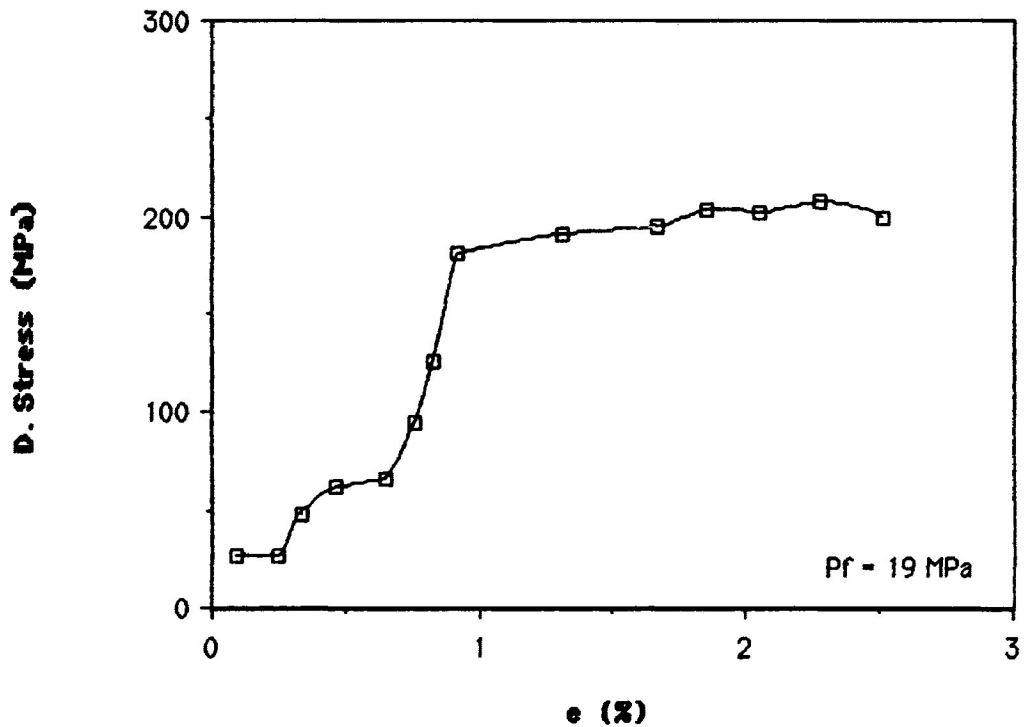


Fig. 4-22: CM-5 loading; Differential stress vs. strain

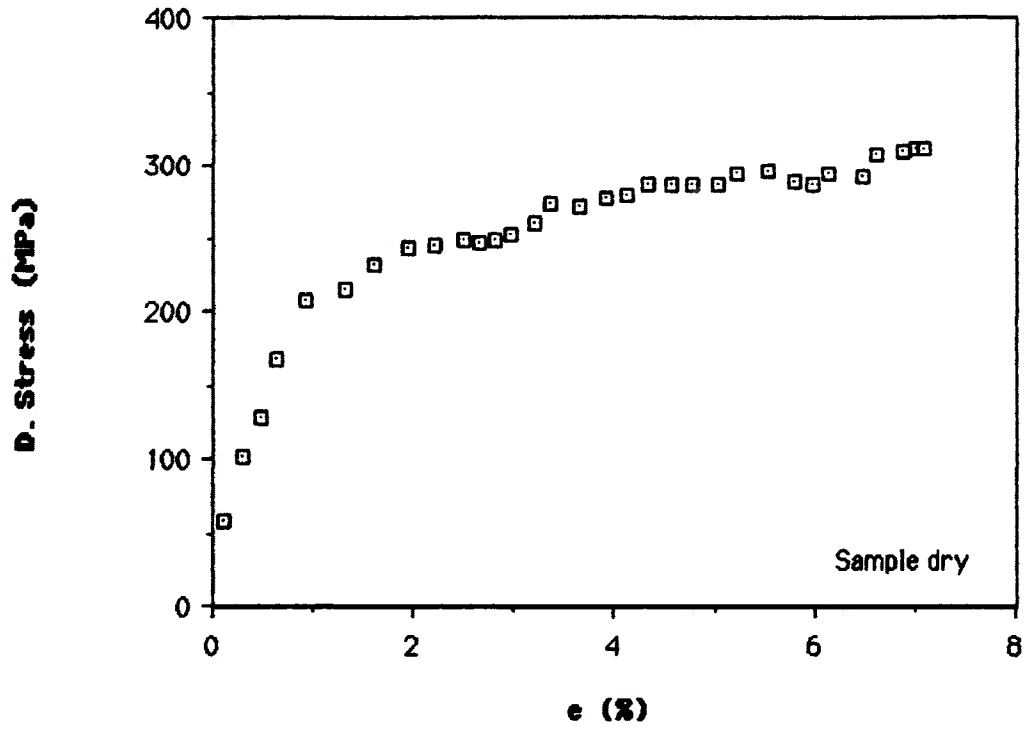


Fig. 4-23: CM-6 loading; Differential stress vs. strain

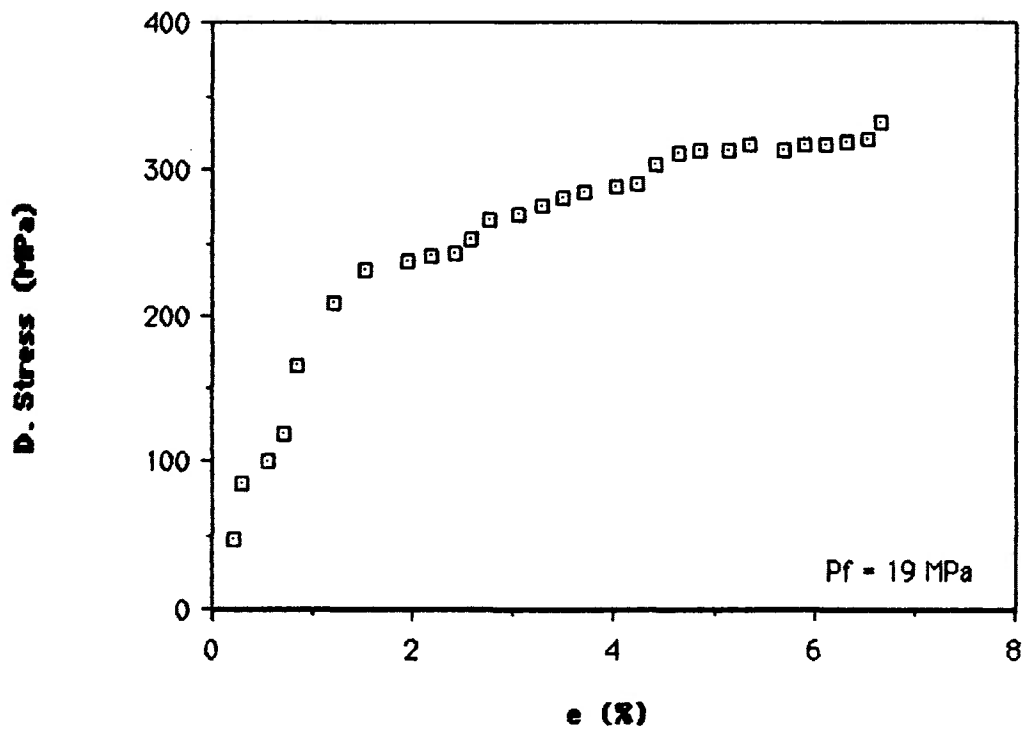


Fig. 4-24: CM-7 loading; Differential stress vs strain

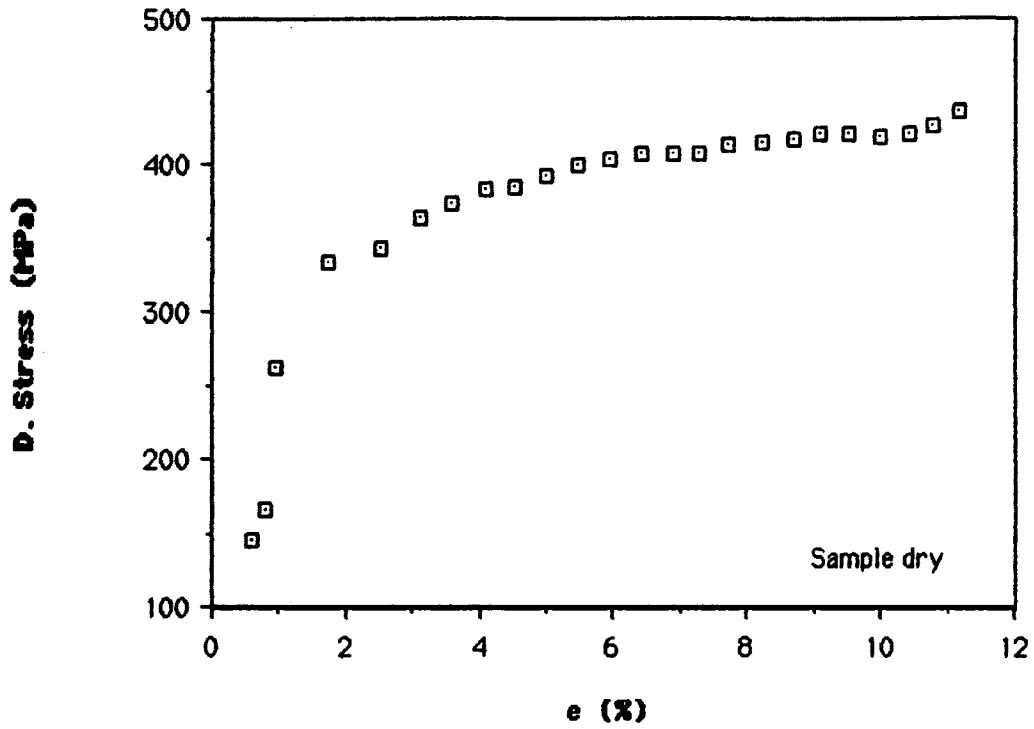
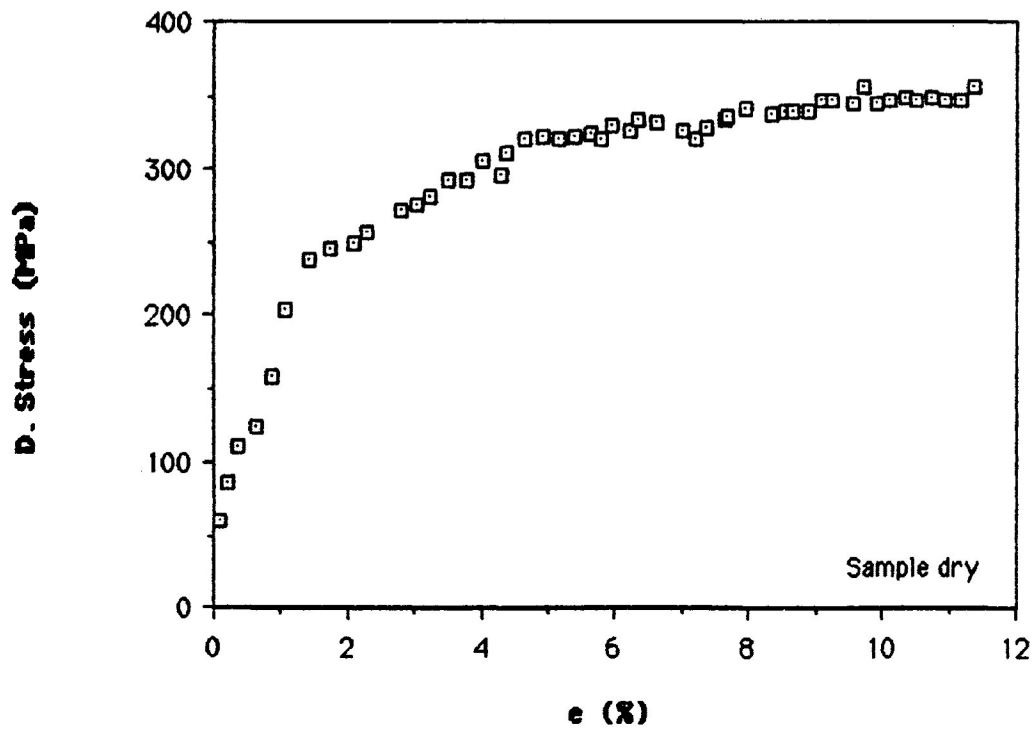


Fig. 4-25: CM-8 loading; Differential stress vs. strain



deformation are evident from the curves for CM-3, 5, 6 and 8, and indicate perturbations of the overall work-hardening flow. No effect of the presence of pore pressure is evident from these loadings of Carrara marble.

SRTs: The SRTs performed on samples CM-1 to 8 (Figs. 4-26 to 34) generally confirm the findings from CM-11 and 13. Cycling of the data is evident in some cases, and thermal expansion and contraction appears to have disrupted some of the data.

Thermal fluctuation has affected the SRTs on samples CM-1 (both the first and second SRTs), CM-4 (second test), and CM-6 to 8. Differential stress is shown to have suffered at least temporary increases during these tests (see graphs of $\log(\text{differential stress})$ vs. time); this is attributed to thermally driven contraction of the deformation rig. A limited number of intervals from these tests show a trend on graphs of $\log(\text{differential stress})$ vs. $-\log(\text{permanent strain rate})$ except for CM-8 (not shown). SRTs on samples CM-3, 4 (first test) and 5 appear to have avoided thermal complications. These tests show a continuous decline in differential stress over time. Cycling is evident in the data for these tests.

Fig. 4-26a: CM-1, first SRT; log(differential stress) vs. time

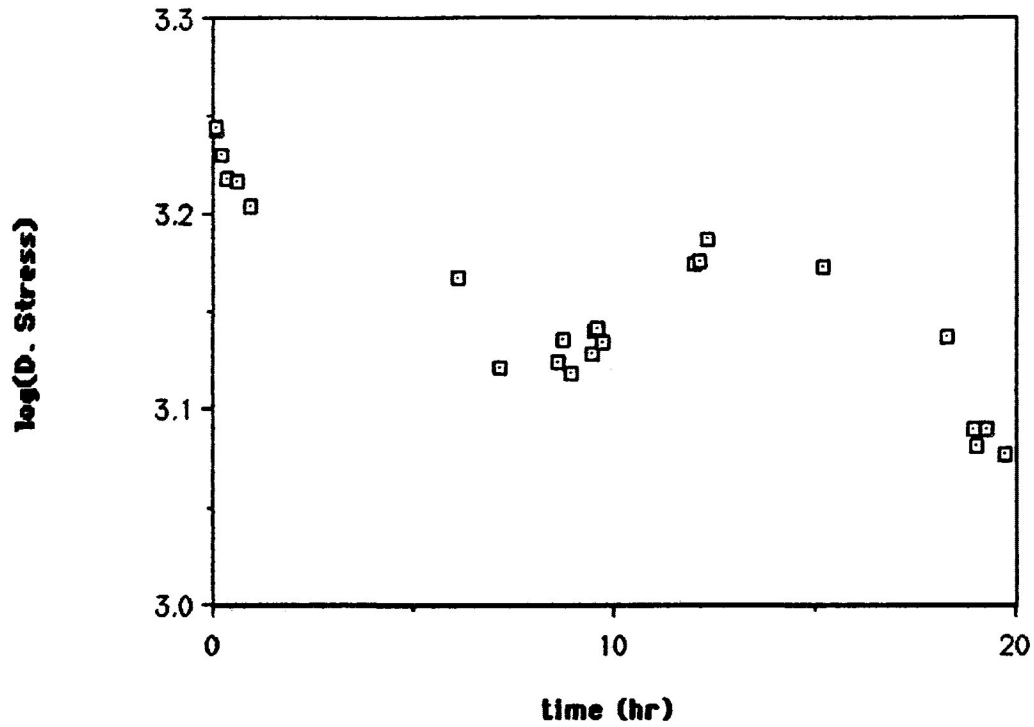
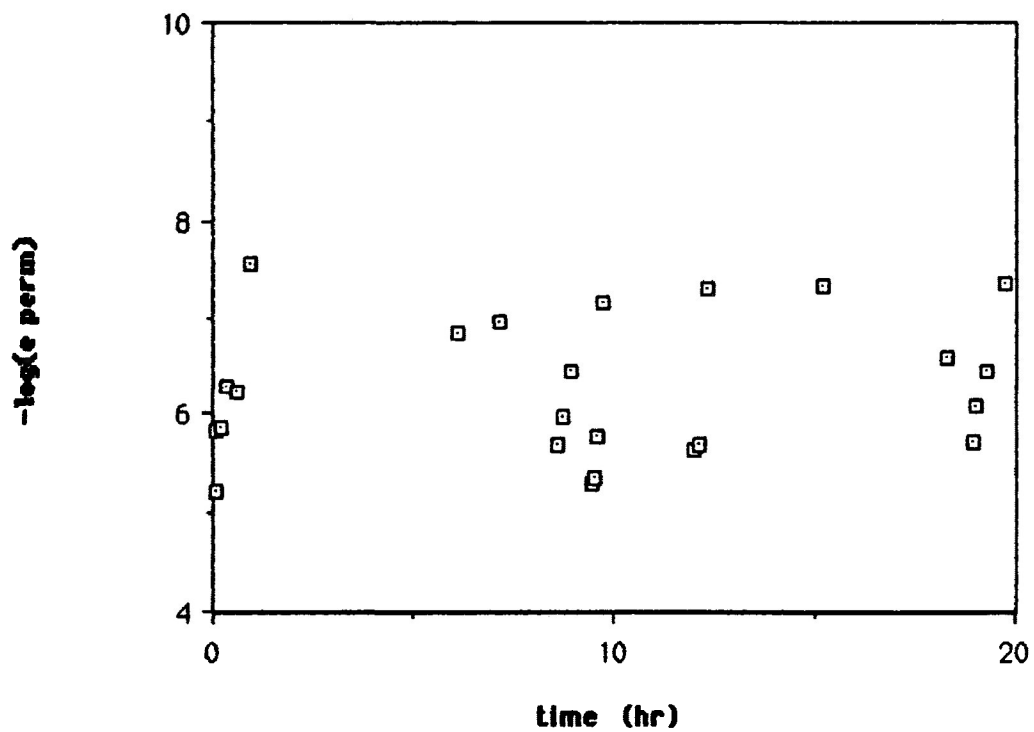


Fig. 4-26b: CM-1, first SRT; -log(permanent strain rate) vs. time



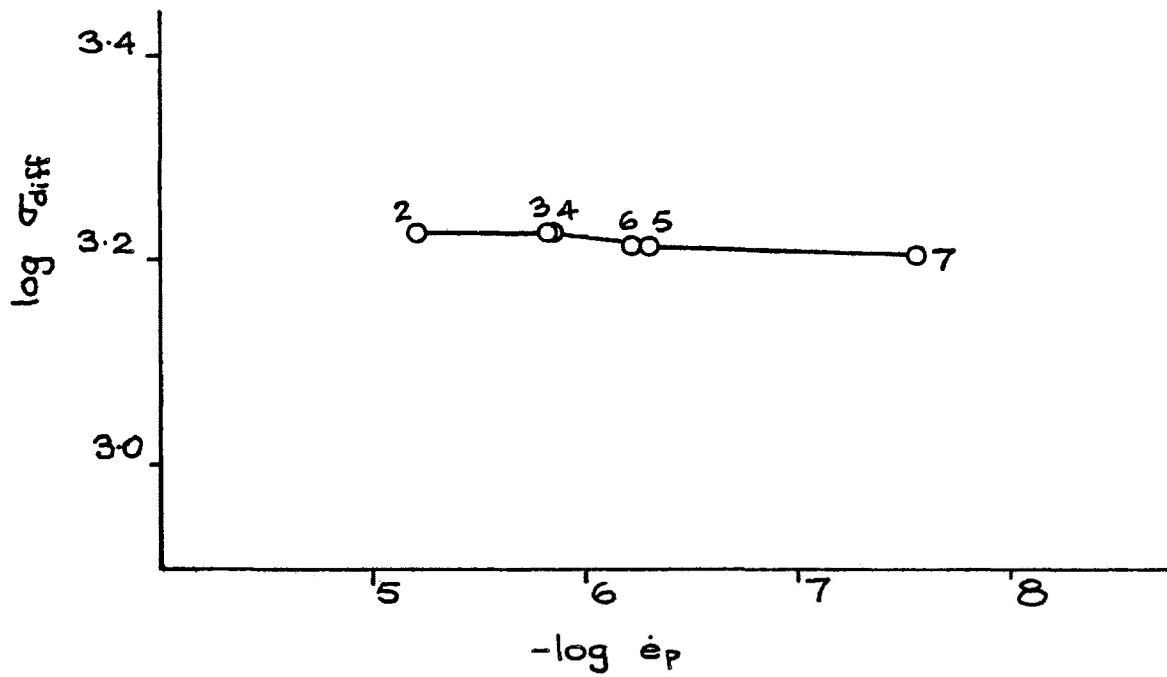
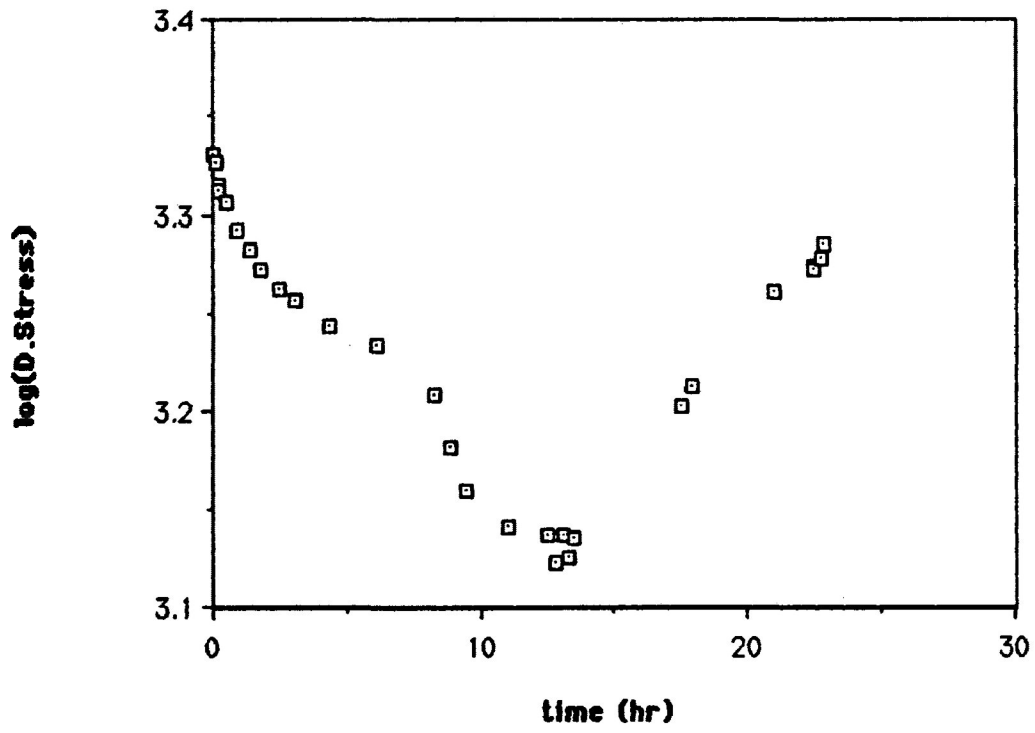


Figure 4-26c: Data from the first SRT on CM-1 plotted on $\log(\text{differential stress})$ vs. $-\log(\text{permanent strain rate})$. Except for intervals 5 to 6, this is a single trend.

Fig. 4-27a: CM-1, second SRT; log(differential stress) vs. time



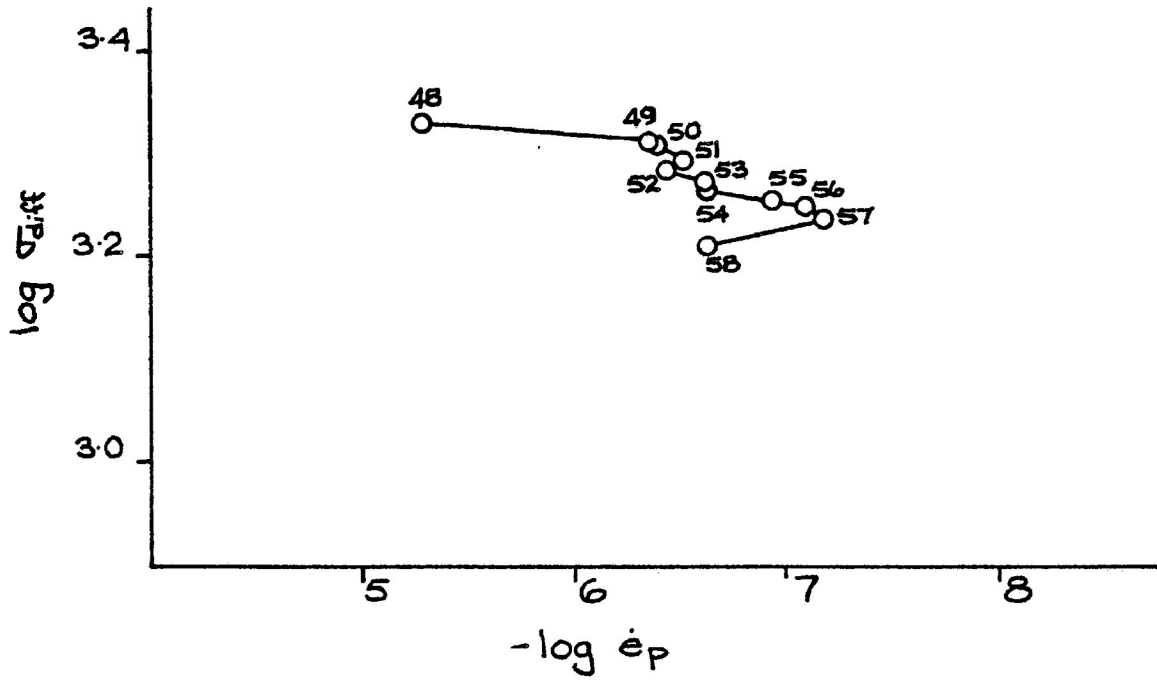


Figure 4-27c: $\log(\text{differential stress})$ vs. $-\log(\text{permanent strain rate})$ for the second SRT on CM-1.

Fig. 4-28a: CM-3 SRT; log(differential stress) vs. time

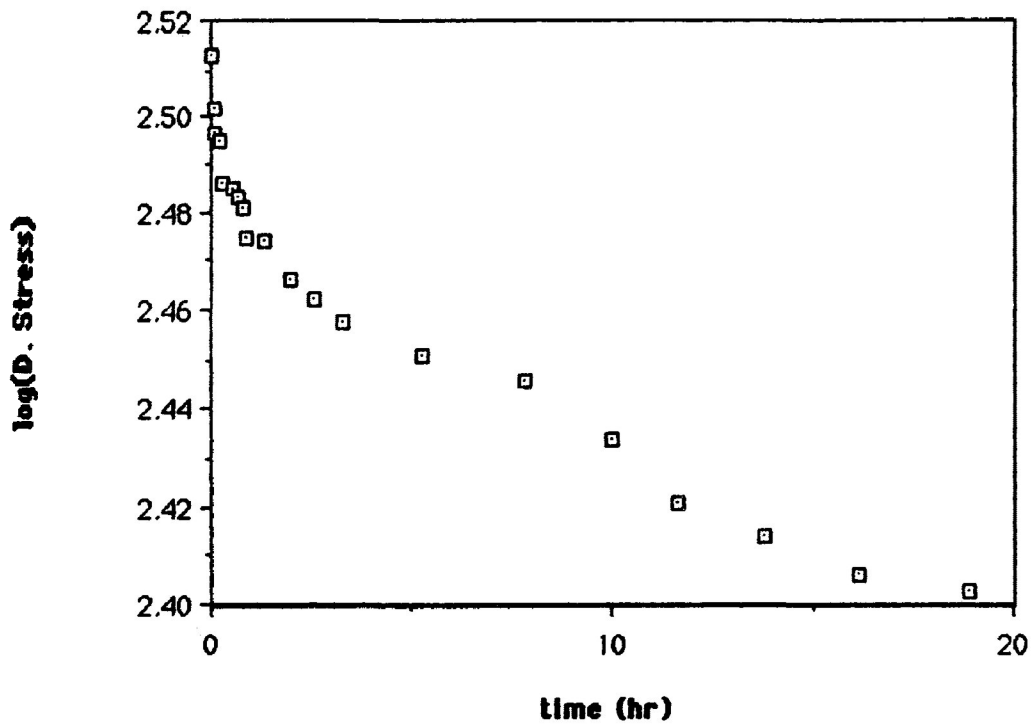
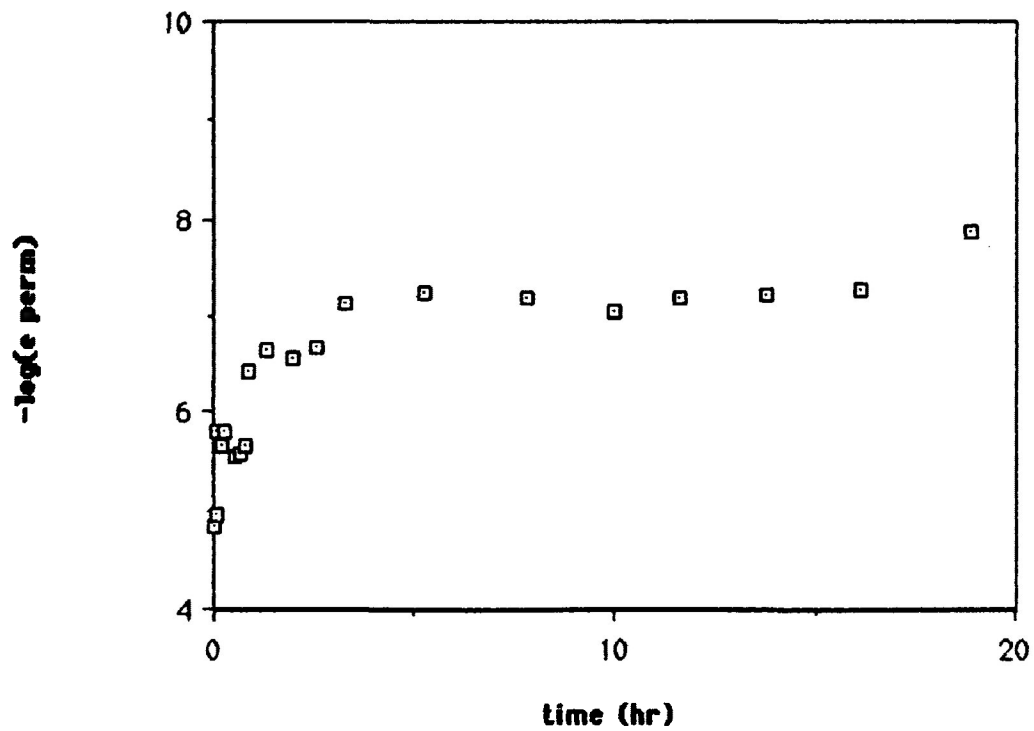


Fig. 4-28b: CM-3 SRT; log(permanent strain rate) vs. time



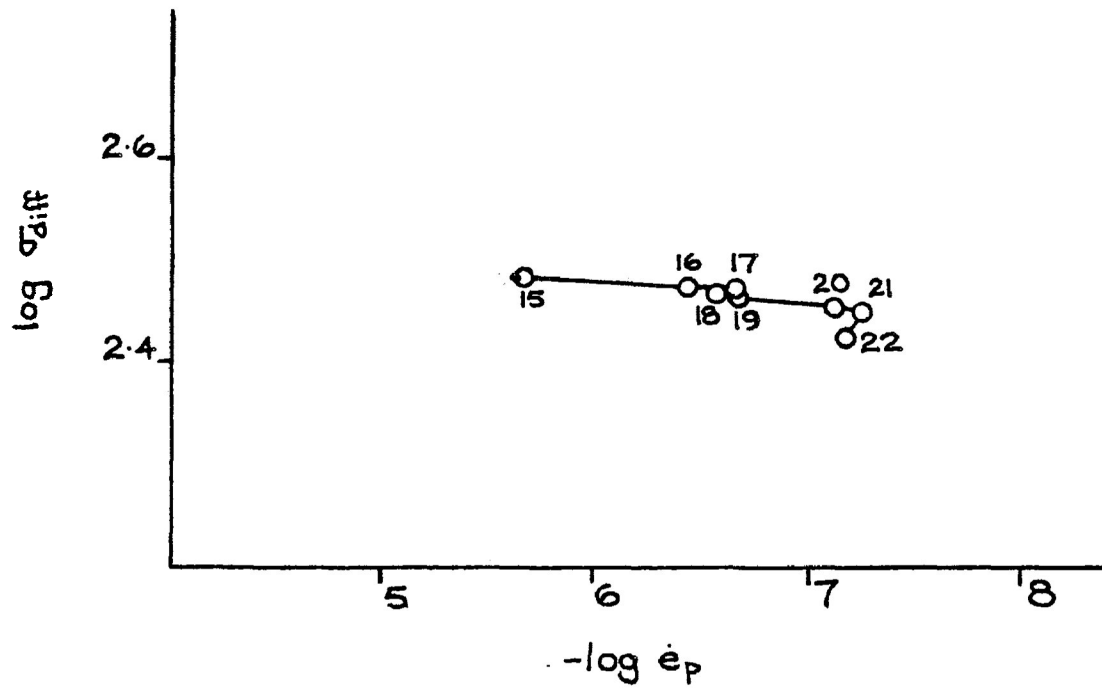


Figure 4-28c: SRT data from CM-3 plotted on $\log(\text{differential stress})$ vs. $-\log(\text{permanent strain rate})$.

Fig. 4-29a: CM-4, first SRT; log(differential stress) vs. time

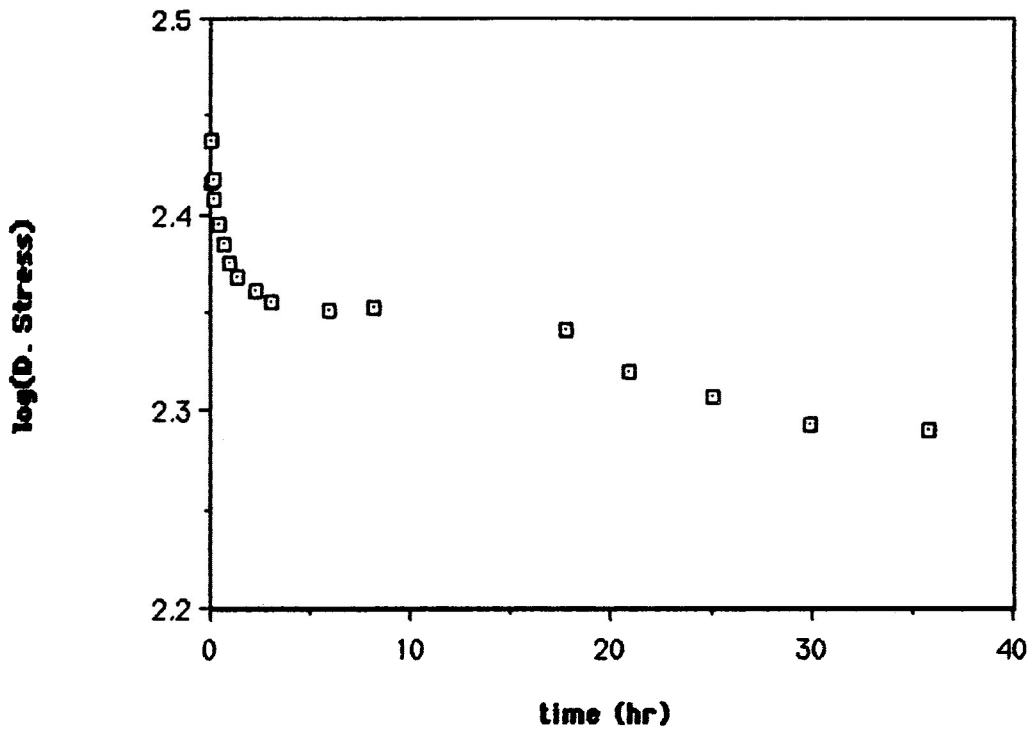
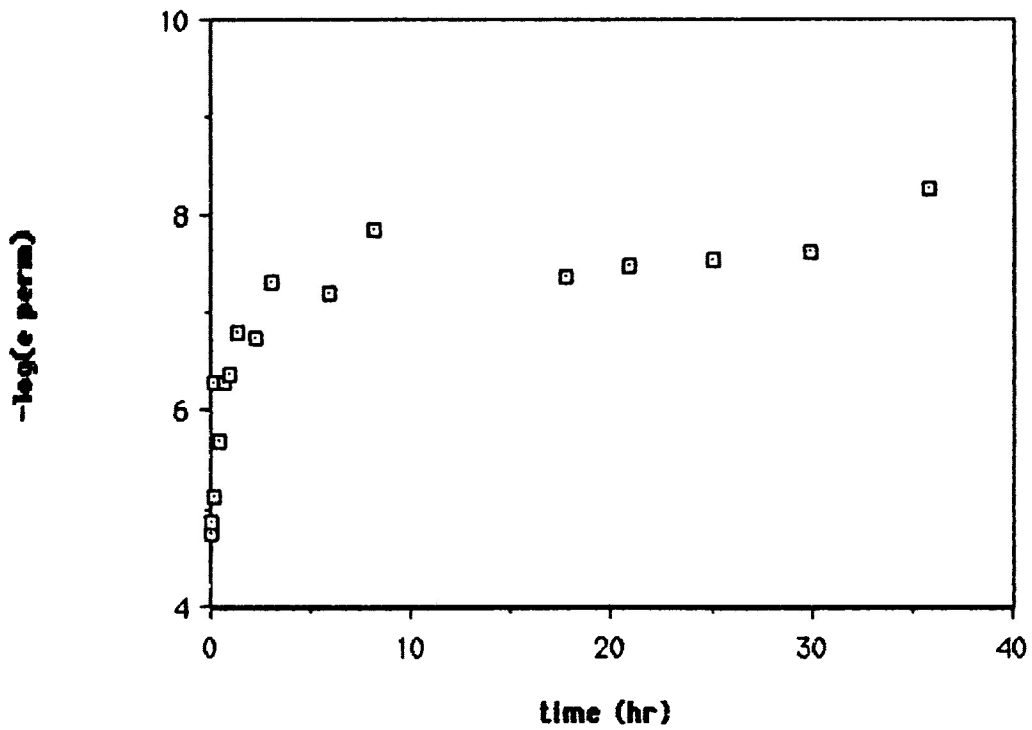


Fig. 4-29b: CM-4, first SRT; log(permanent strain rate) vs. time



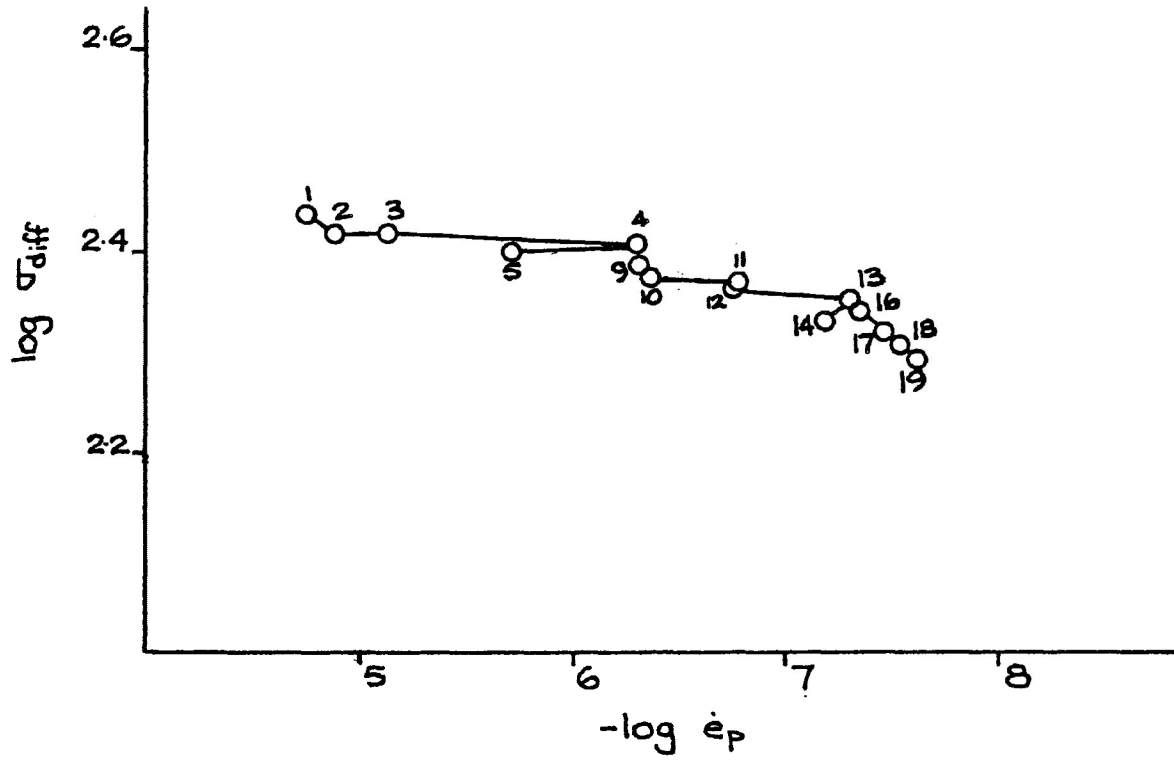


Figure 4-29c: Data from the first SRT on CM-4. Intervals 1 to 14 and 16 to 19 may define two different trends.

Fig. 4-30a: CM-4, second SRT; log(differential stress) vs. time

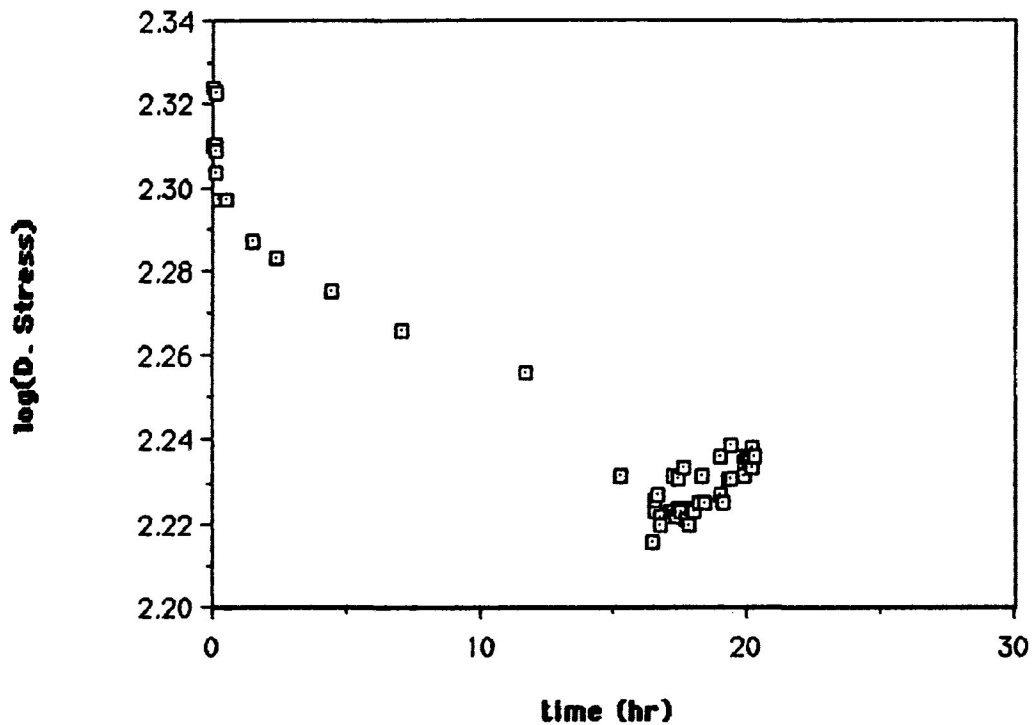
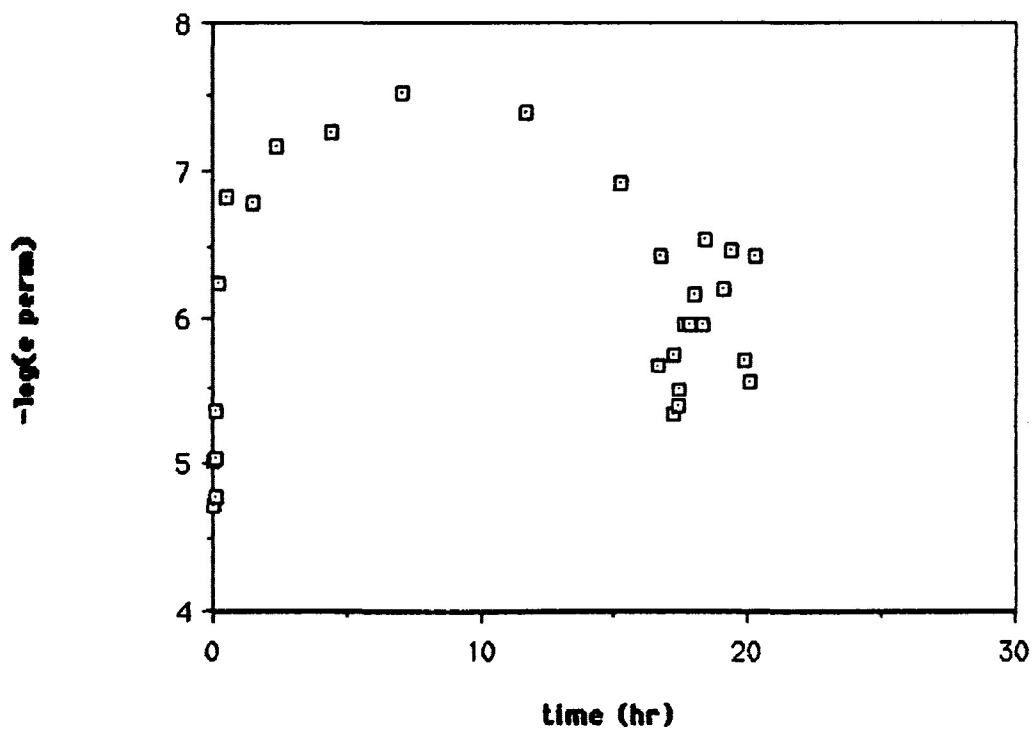


Fig. 30b: CM-4, second SRT; log(permanent strain rate) vs. time



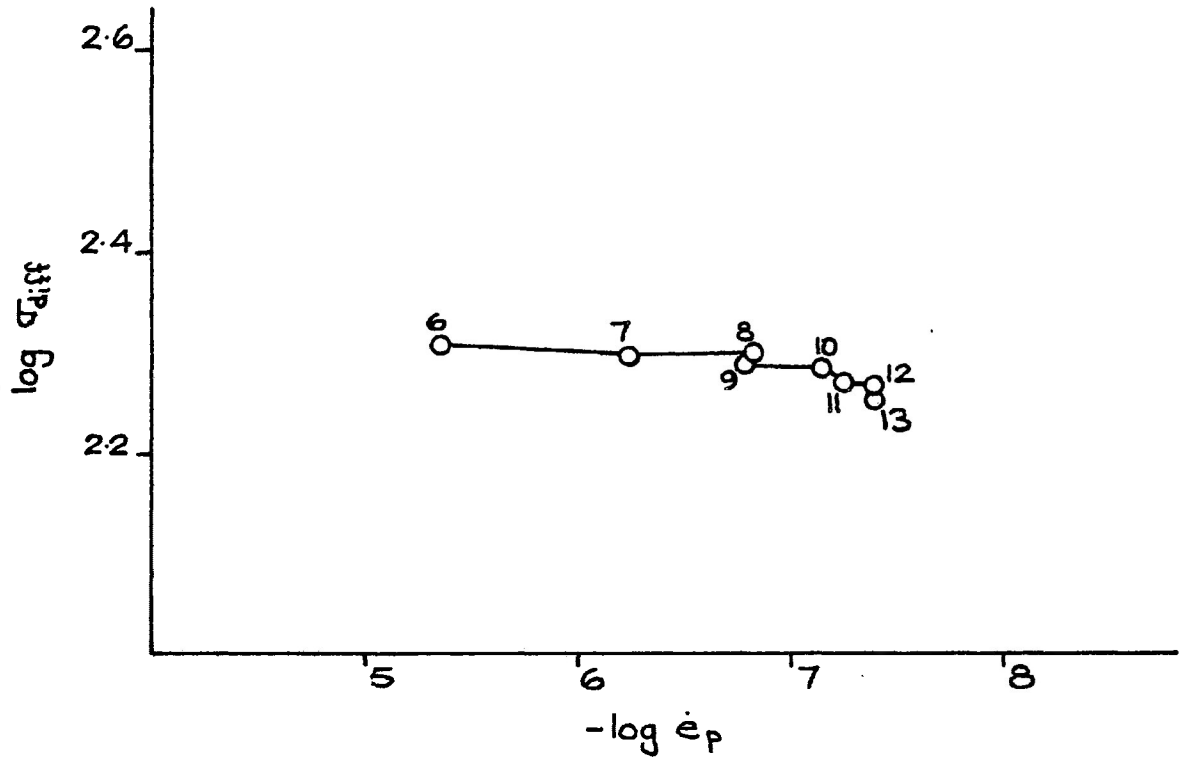


Figure 4-30c: Second SRT on CM-4. Intervals 6 to 10 and 10 to 13 may indicate two different trends.

Fig. 4-31a: CM-5 SRT; log(differential stress) vs. time

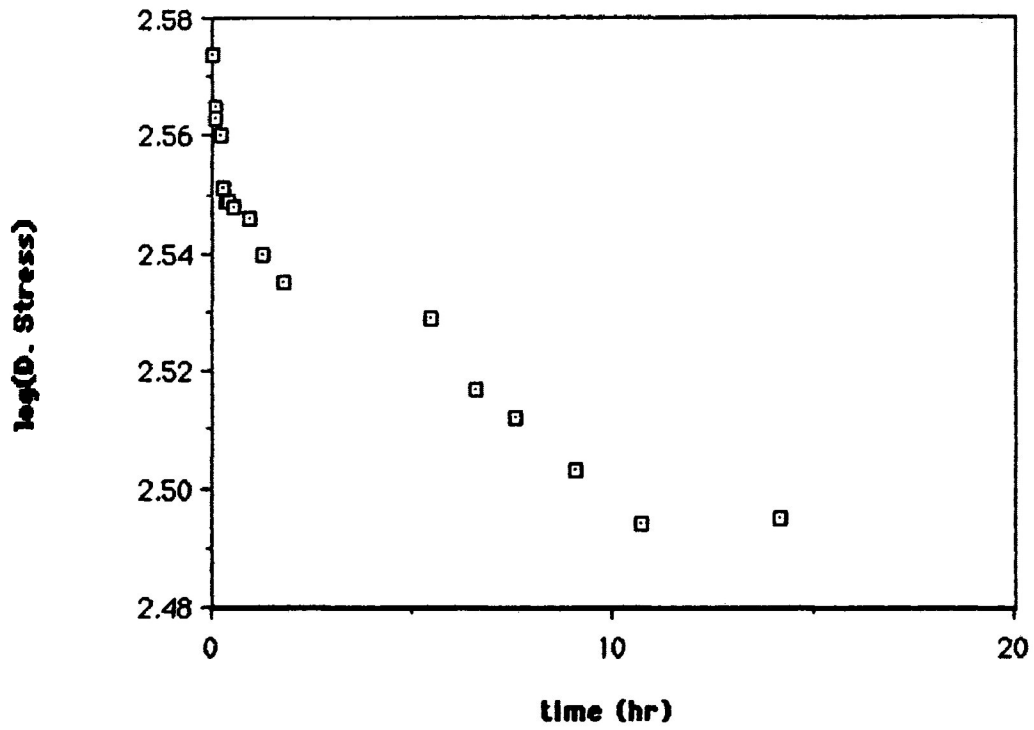
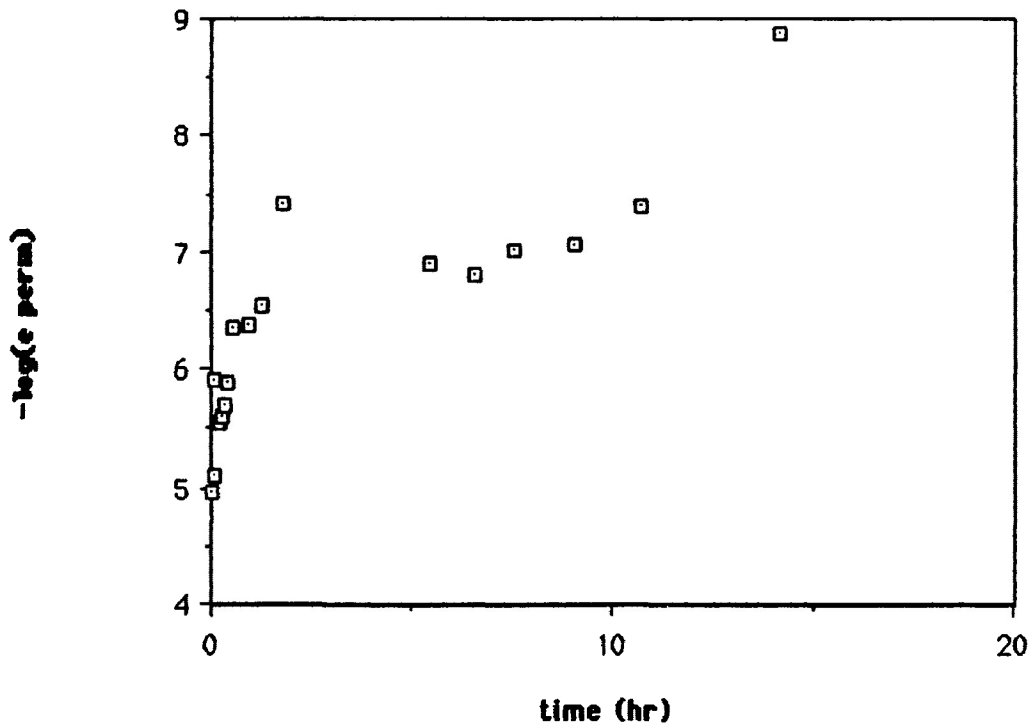


Fig. 4-31b: CM-5 SRT; log(permanent strain rate) vs. time



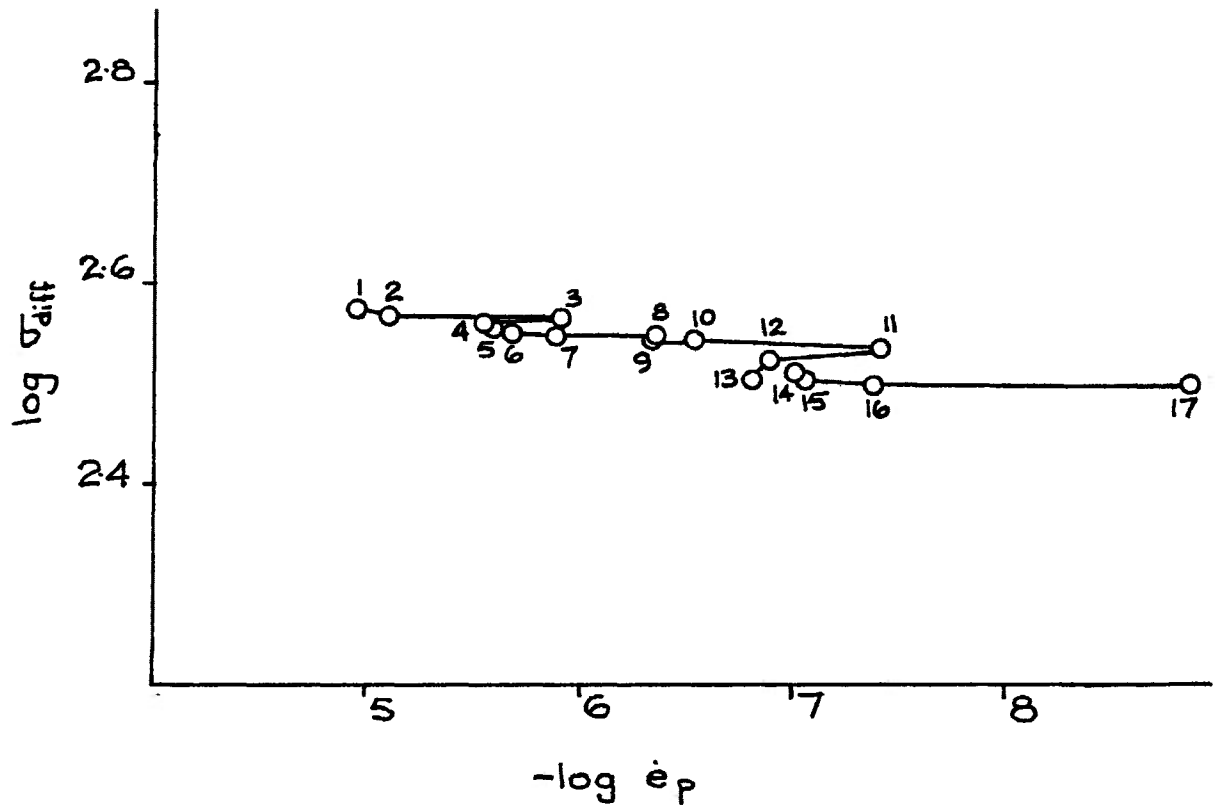


Figure 4-31c: log(differential stress) vs. -log(permanent strain rate) for SRT on CM-5.

Fig. 4-32a: CM-6 SRT; log(differential stress) vs. time

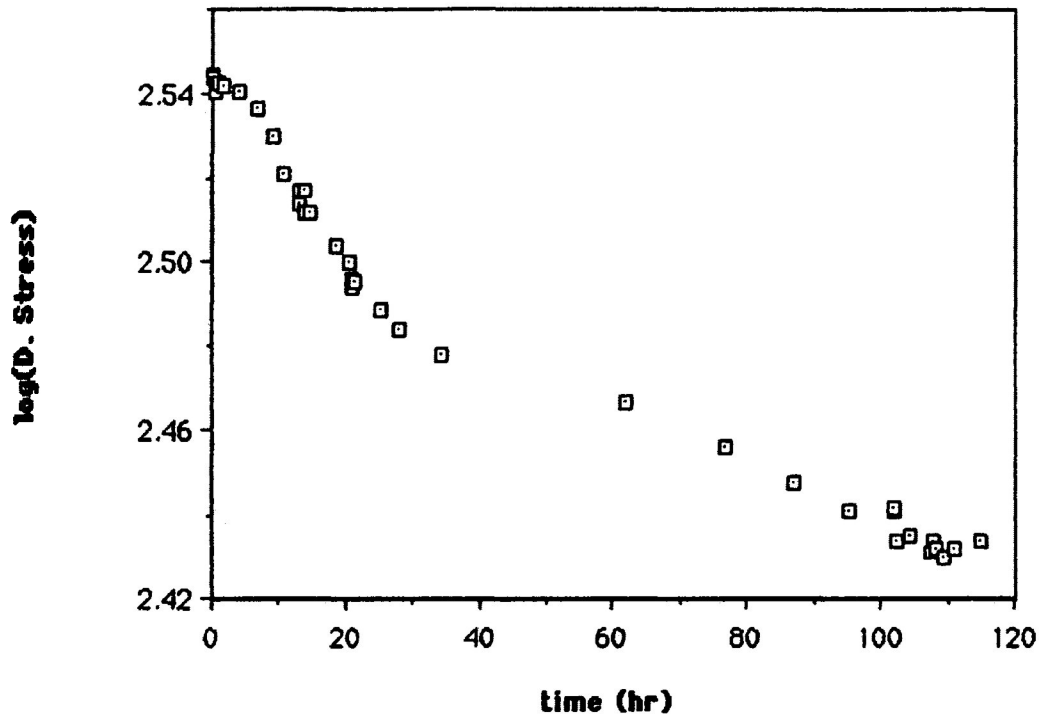
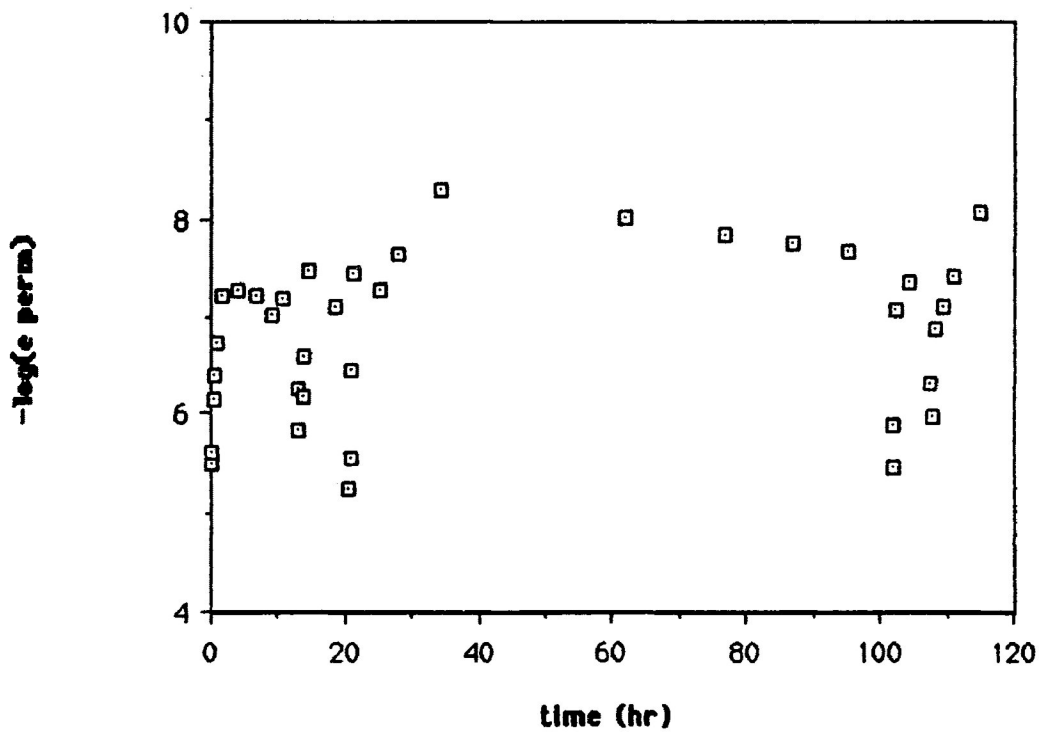


Fig. 4-32b: CM-6 SRT; log(permanent strain rate) vs. time



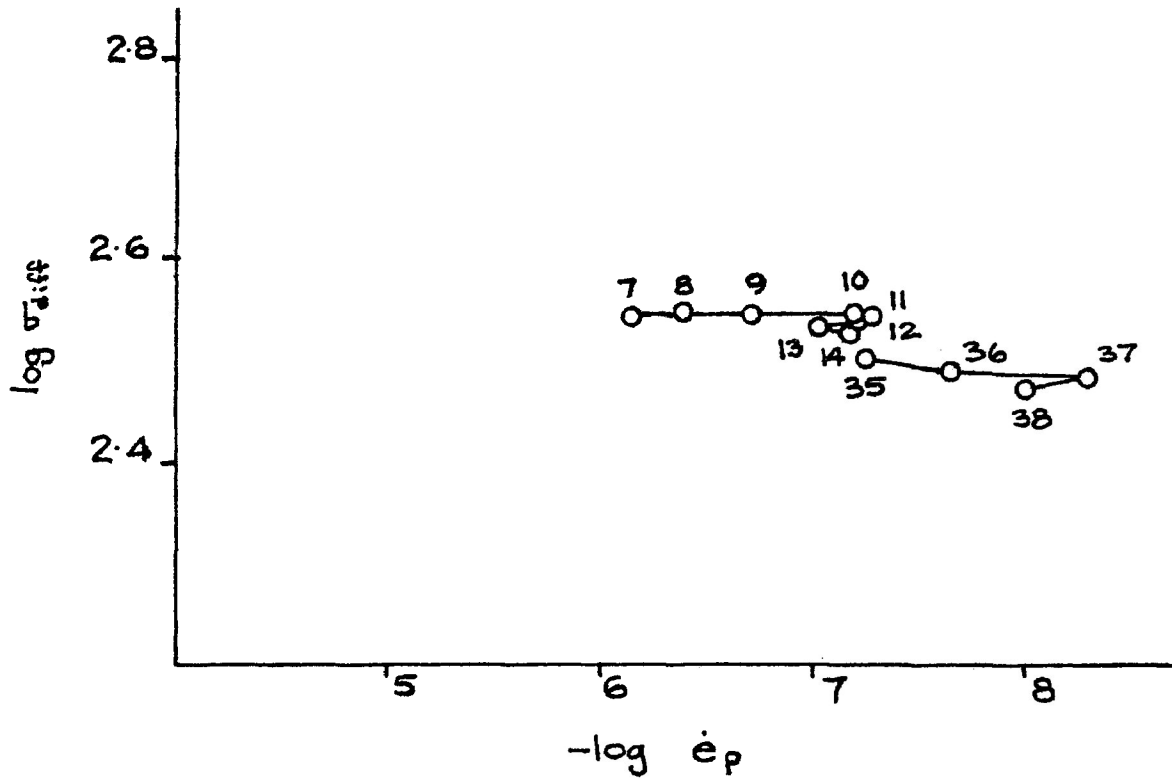


Figure 4-32c: $\log(\text{differential stress})$ vs. $-\log(\text{permanent strain rate})$ for SRT data from CM-6. Two sets of consecutive intervals with declining differential stress are shown.

Fig. 4-33a: CM-7 SRT; log(differential stress) vs. time

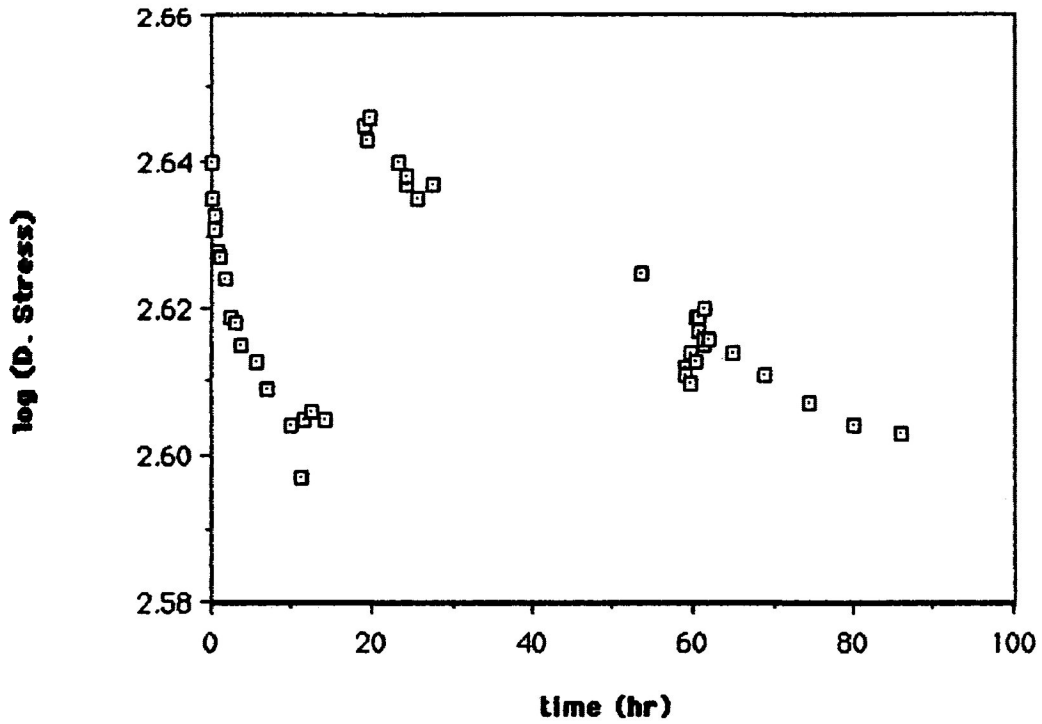
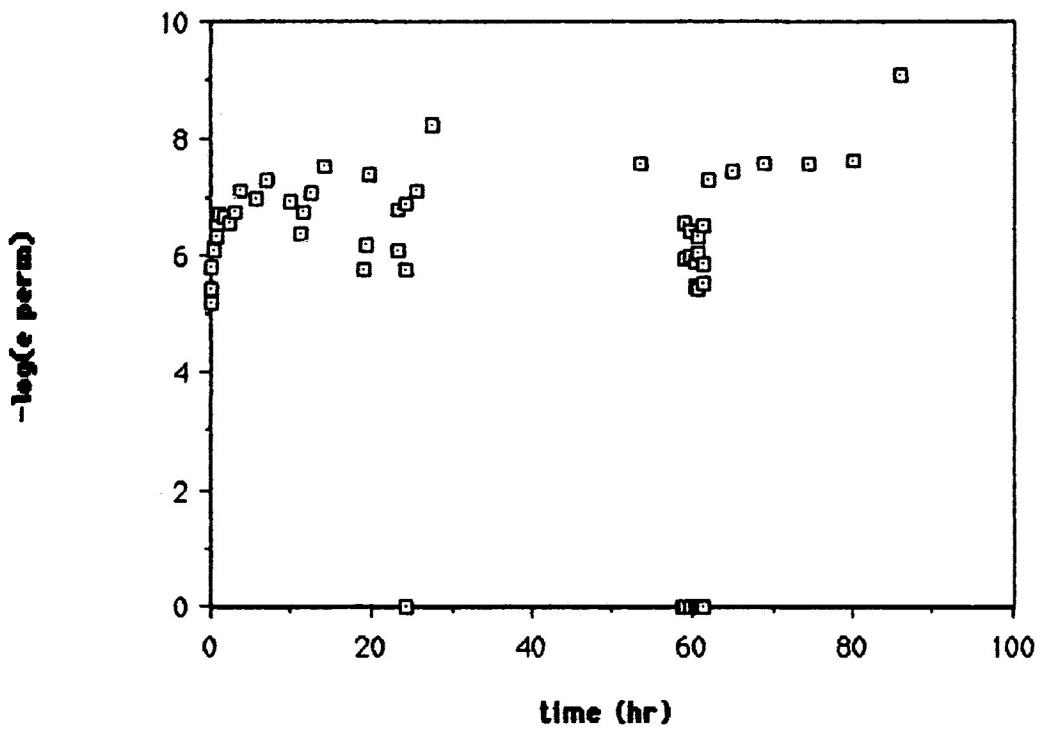


Fig. 4-33b: CM-7 SRT; log(permanent strain rate) vs. time



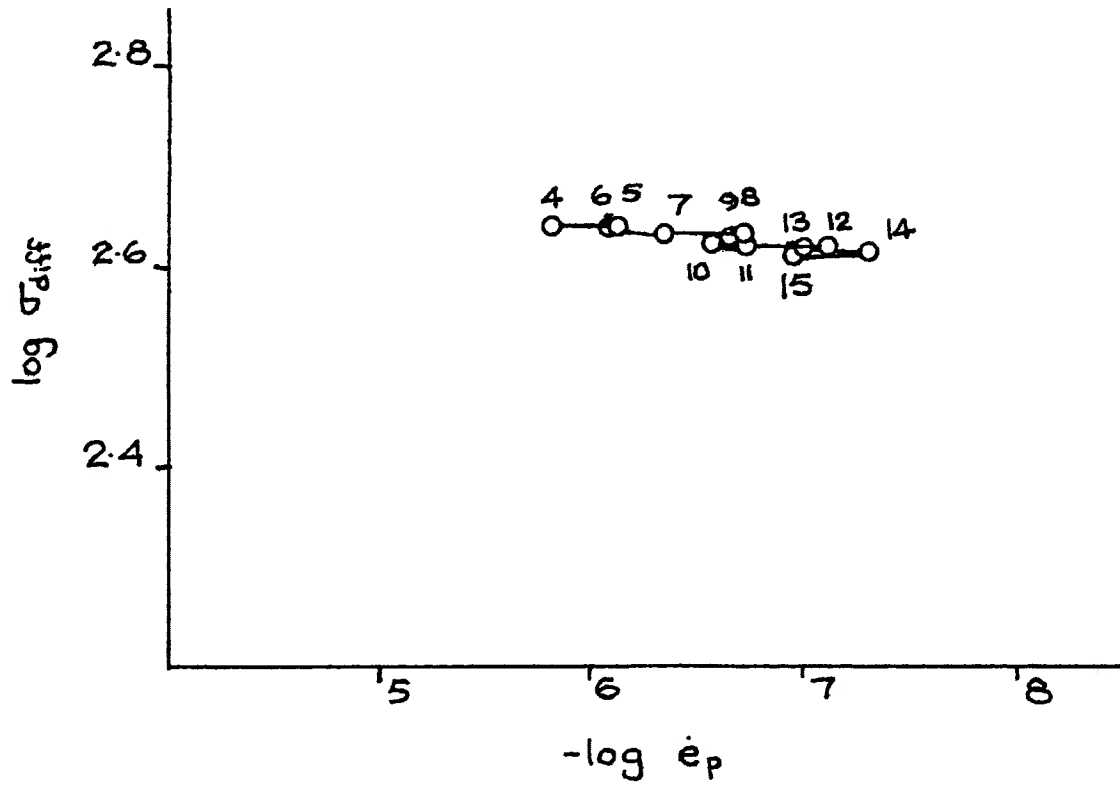
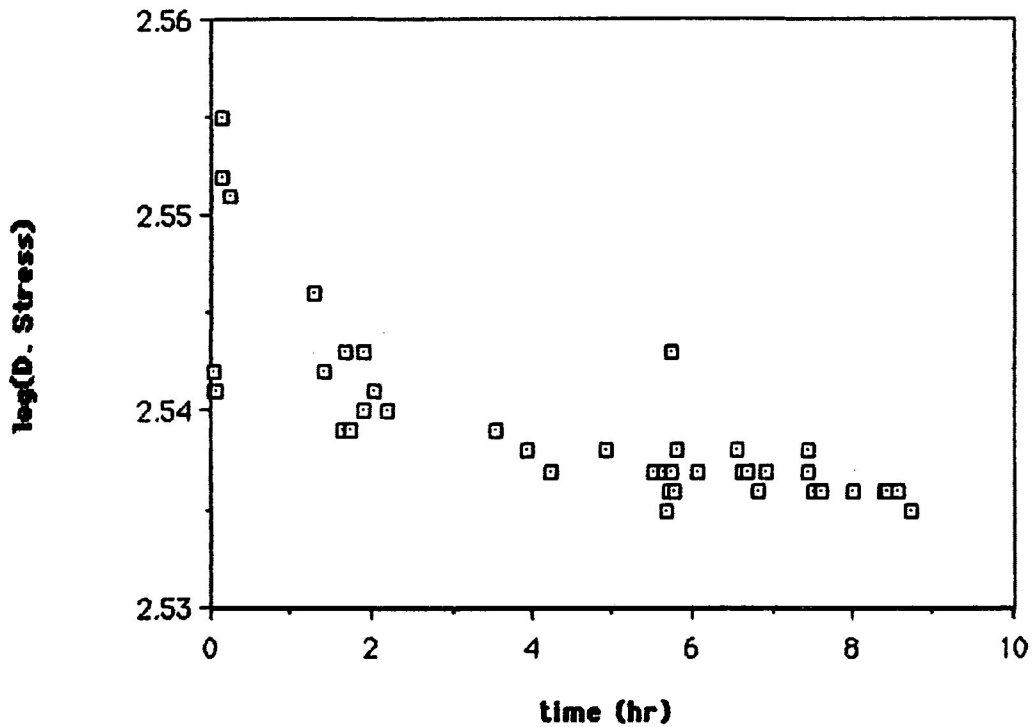


Figure 4-33c: $\log(\text{differential stress})$ vs. $-\log(\text{permanent strain rate})$ for SRT on CM-7.

Fig. 4-34a: CM-8 SRT; log(differential stress) vs. time



4.2.3 Discussion

Two factors caused the data from SRTs on Carrara marble to depart from the idealized pattern discussed in subsection 4.1.2 . One of these, temperature variation, appears to have a pronounced effect on dimensional stability of the deformation rig. Stabilization of temperature is essential for successful application of the SRT at lower strain rates, or in general over long measurement intervals.

Those SRT results on Carrara marble not affected by temperature fluctuation showed signs of the complex behavior referred to here as cycling. This phenomenon appears related to the microstructure of the material. Rutter (1974) has shown that Carrara marble does not undergo steady-state flow below 400°C. This is confirmed by the observation of work-hardening during loading of samples CM-1 to 13 which was done at room temperature (nominally 25°C). Under this condition, strain rate (during both loading and stress relaxation) is a function not only of flow stress but also of microstructure. Carrara marble has shown considerable sensitivity to microstructure during SRTs. For example, during the third SRT on CM-13, one reversal from increasing strain rate to decreasing strain rate occurred after 0.1% strain accumulated during the phase of increasing strain rate. (The average strain developed during individual SRTs on CM-11 and

13 was 0.5%.) Thin sections of the Carrara marble samples show greater twinning than in the undeformed marble, and minor gaps between grains which indicate that particulate flow has occurred. It is not possible to say, however, what alternation in deformation occurred during the cycling.

4.3 Stress Relaxation Tests on Calcite-Quartz Aggregates

4.3.1 Introduction

Three SRTs were performed on samples similar to those deformed in the long-term hydrostatic test. The calcite is the same used in the hydrostatic test samples: a highly angular sand ranging in size between 74 and 63 μm ($\phi = 3.75$ to 4.00). The quartz used was in the form of rounded grains ranging in size between 200 and 177 μm ($\phi = 2.25$ to 2.5). Calcite and quartz were mixed in a volumetric ratio of 10:1. No other material (such as kaolinite) was used in the preparation of the samples. Sample preparation was begun by slipping a length of teflon jacket over a cylindrical steel endpiece. The seal between the endpiece and jacket was maintained by an O-ring. The calcite-quartz mixture was then poured into the jacket to a depth of about 1 inch, and the

top anvil, also with an O-ring, was then slipped into the upper end of the teflon jacket. The cross-section of the calcite-quartz aggregate samples deformed in the stress relaxation tests thus was the same as the cross-section of the hydrostatic test samples (Fig. 3-5). The calcite-quartz sample was then placed in the triaxial rig and compacted under confining pressure; this was raised to the desired level in steps over about twenty minutes. No axial load was applied during compaction. Samples CQA-2, 3 and 4 were all compacted dry.

This material was chosen because as an experimental material because it was thought to be more susceptible to PS than Carrara marble. Being a loose aggregate of angular grains rather than a mass of interlocking grains, it is likely to have sufficient porosity to provide a site for precipitation of any pressure solved material produced during a SRT. Furthermore, the calcite sand is much finer grained than Carrara marble; if PS does occur, it will occur much faster (see Ch. 2) and will therefore be easier to detect during a SRT.

4.3.2 Results of Deformation of CQA samples

Loading: The differential stress - ϵ curves for the CQA samples (Figs. 4-35, 36 and 37) do not have the form typical of coherent geological material. Elastic behavior is not well

Fig. 4-35a: CQA-2, first loading; Differential stress vs. strain

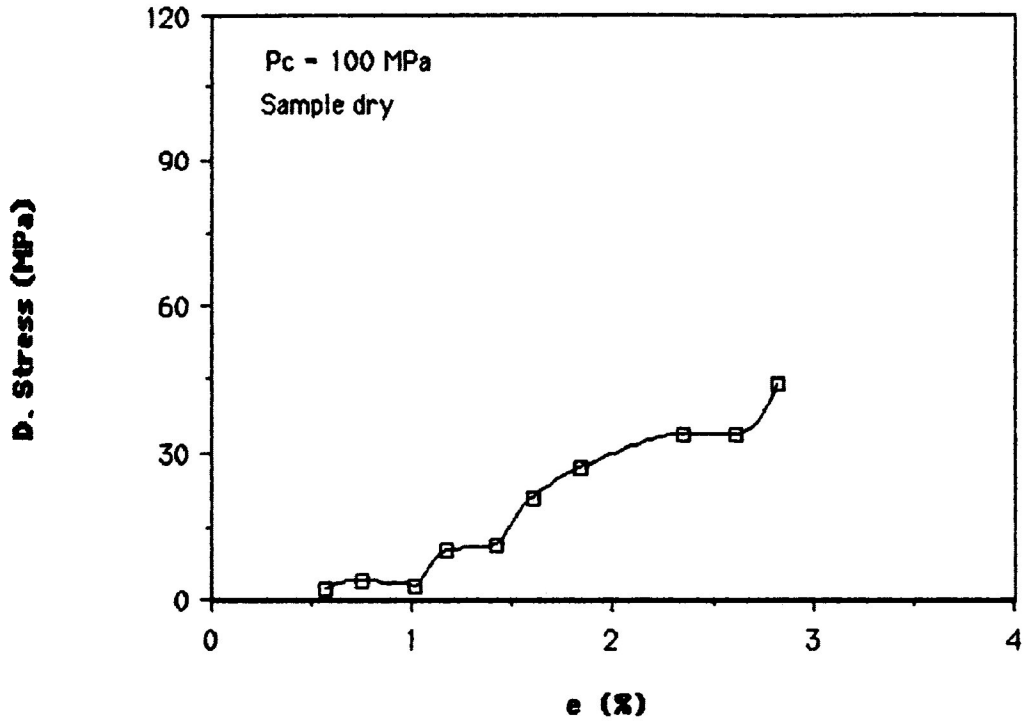


Fig. 4-35b: CQA-2, second loading; Differential stress vs. strain

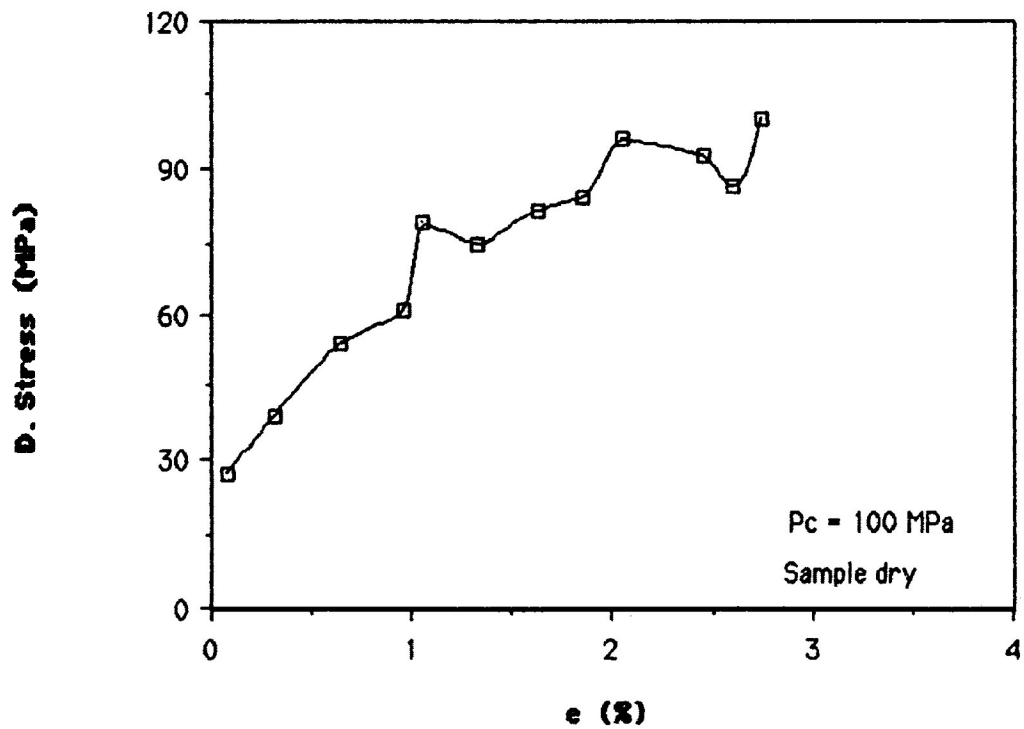


Fig. 4-36: CQA-3 loading; Differential stress vs. strain

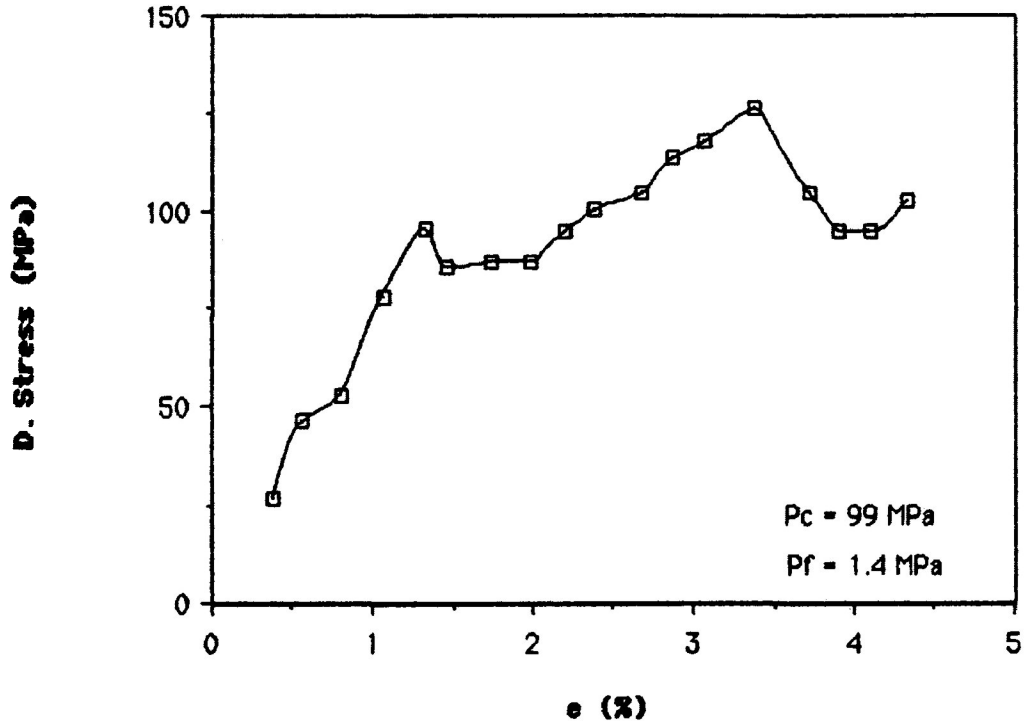
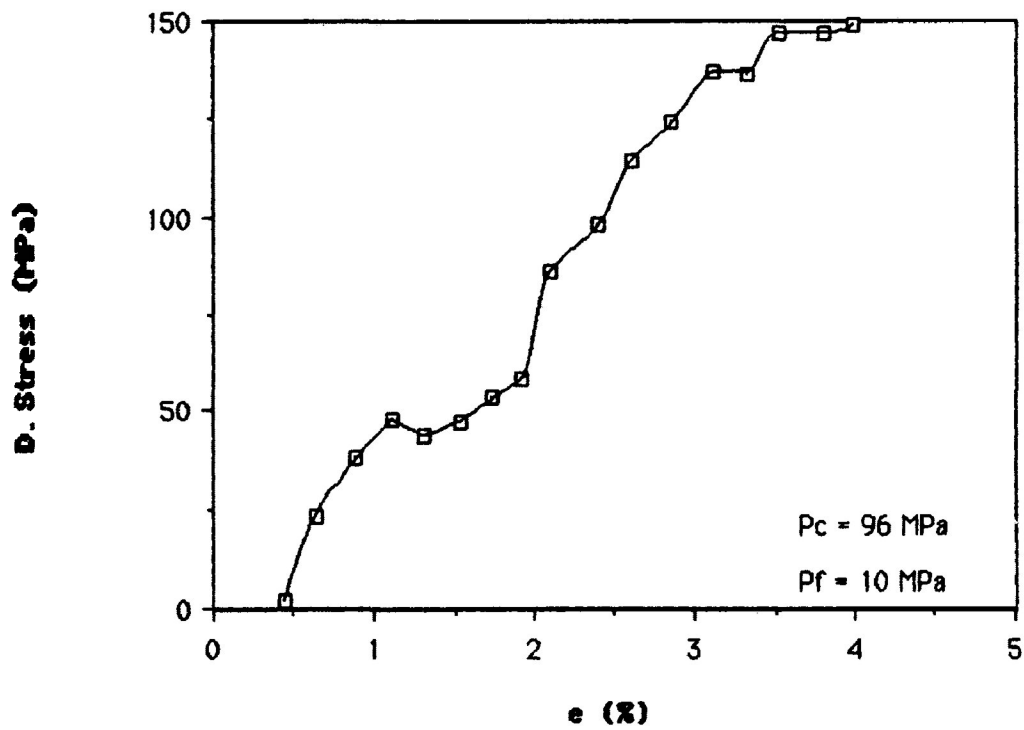


Fig. 4-37: CQA-4, loading; Differential stress vs. strain



developed. During the first loading of CQA-2, which was compacted and deformed at the same P_c (100. MPa; see Table 4-2), the sample underwent permanent strain without first showing any elastic behavior. Overall work hardening was interrupted by brief phases of steady-state flow or strain softening. The second loading of CQA-2, which followed a failed SRT, shows a continuation of this behavior but with a slight concave-down curve. During this second loading, the sample was able to sustain higher differential stresses than in the first test. This is an effect of the work hardening flow of the first loading.

Samples CQA-3 and 4 (Figs. 4-36, 37) were deformed at the same nominal P_c as for CQA-2 but were compacted at 150. MPa. This appears to account for higher differential stresses during the loadings of CQA-3 and 4. These have weakly defined yield points (approximately 95 (?) and 50 MPa, respectively, at just over 1% strain), in contrast to CQA-2 which shows no such change. In addition to different yield stresses, CQA-3 and 4 loaded in different fashions during this permanent flow: CQA-4 deformed mostly through work hardening at a relatively constant and rapid rate while CQA-3 had a more irregular path, twice undergoing considerable strain softening. This difference is attributable to the higher pore pressure of CQA-4 (10. MPa versus 1.4 MPa for CQA-3).

TABLE 4-2: Conditions of compaction and loading of CQA samples

Sample	Compaction	Pc (MPa)	Pf (MPa)	e (%)
CQA-2 reload	1 day at 100. MPa -	100. 100.	dry dry	2.8 2.8
CQA-3	8 hours at 100. MPa, then 15 hours at 150. MPa	99.	1.4	4.3
CQA-4	1 day at 150. MPa	96.	10.	4.0

SRTs: One SRT was performed on each of the three samples. Each test suffered increases in differential stress; this was interpreted as being the effect of thermally generated contraction of the triaxial rig, and the data was rejected. All the data from the test on CQA-2 was rejected. Although measurements following interval 51 showed a steady decline in differential stress, strain rate showed no accompanying drop (Figs. 4-38a,b), and consequently the data was not accepted.

The results of the SRT on CQA-3 are little better than those of the previous sample. Intervals 7 to 12, which occurred within the first 1.5 hours of the start of the test, are the only points defining a linear trend on the graph of $\log(\text{differential stress})$ vs. $-\log(\text{permanent strain rate})$ (Fig. 4-39c). Intervals 58 to 70 are also shown on this graph; like intervals 51 onwards from the test on CQA-2, these data show a continuous decline in differential stress without a similar trend in strain rate (Figs. 4-39a,b) and were rejected.

The final SRT (CQA-4) had the greatest success. Although a regular progression of data was interrupted at about 18 hours (Figs. 4-40a, b), intervals 20 to 32 show a continuous drop in differential stress and a similar trend in strain rate. Minor cycling is evident on the graph of $\log(\text{differential stress})$ vs. $-\log(\text{permanent strain rate})$. This figure shows that for this test, the

Fig. 4-38a: CQA-2 SRT; log(differential stress) vs. time

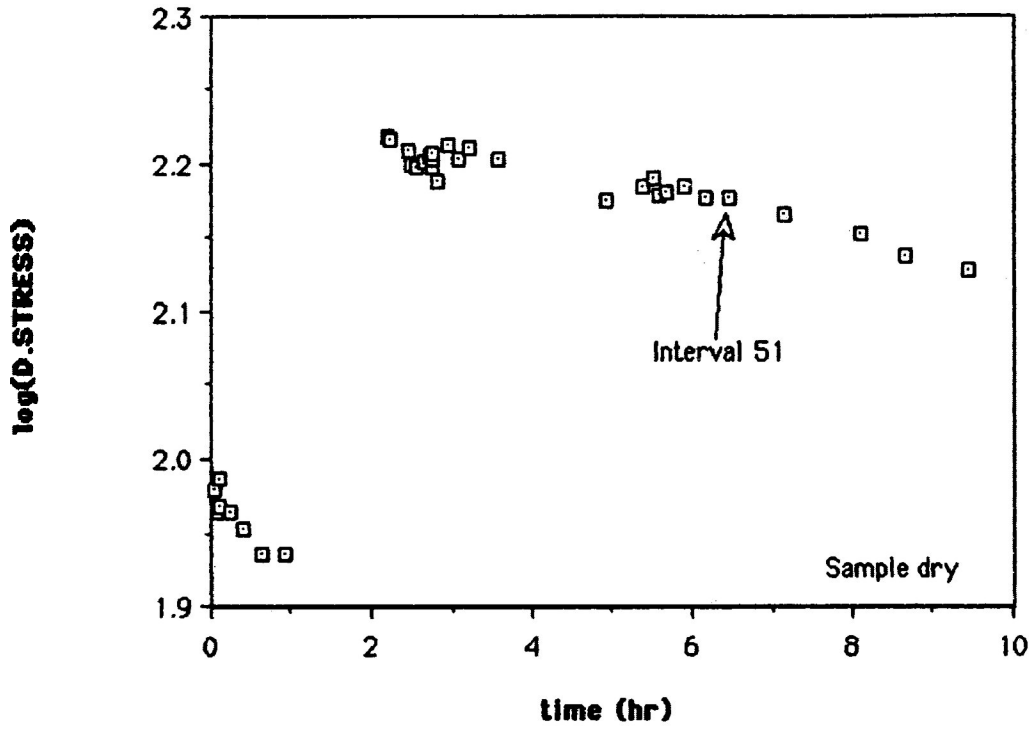


Fig. 4-38b: CQA-2 SRT; log(permanent strain rate) vs. time

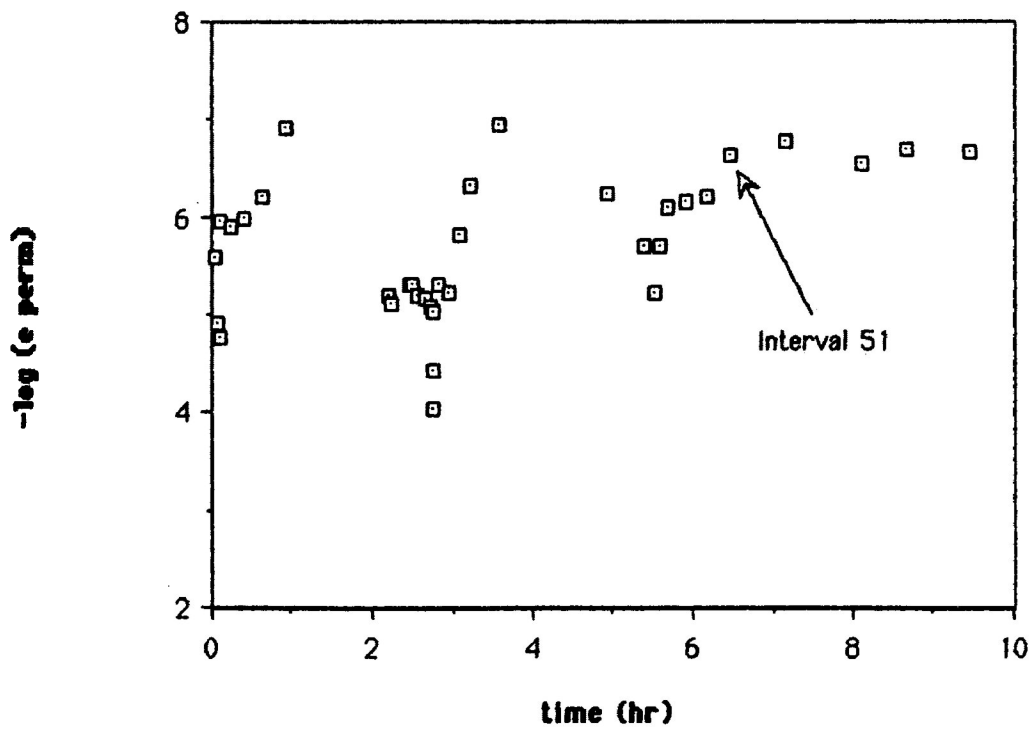


Fig. 4-39a: CQA-3 SRT; log(differential stress) vs. time

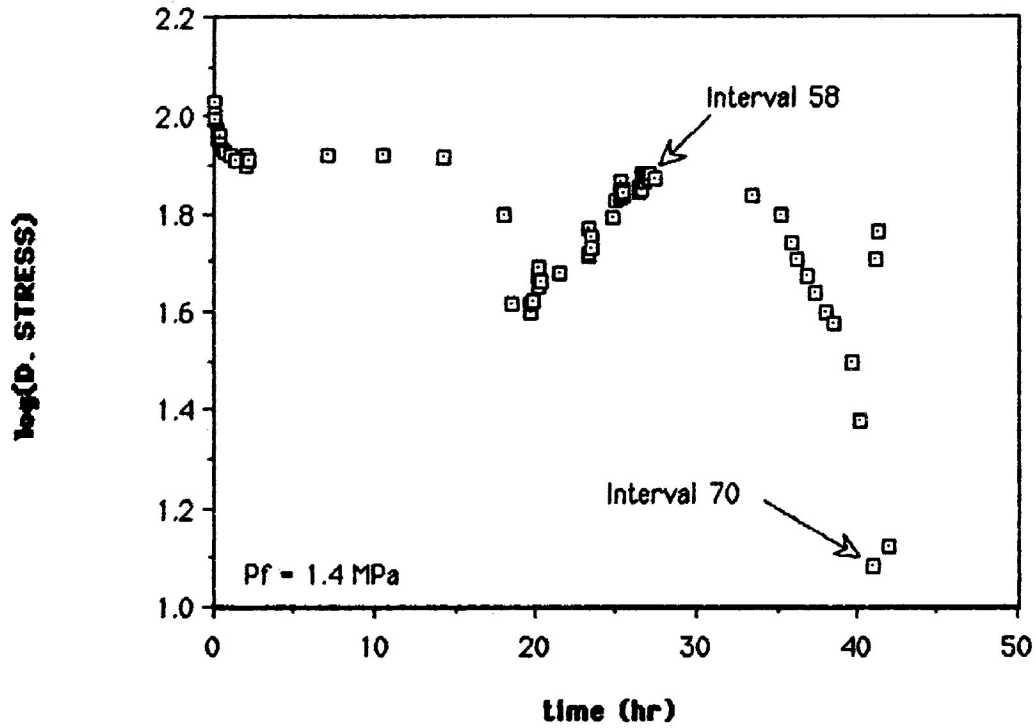
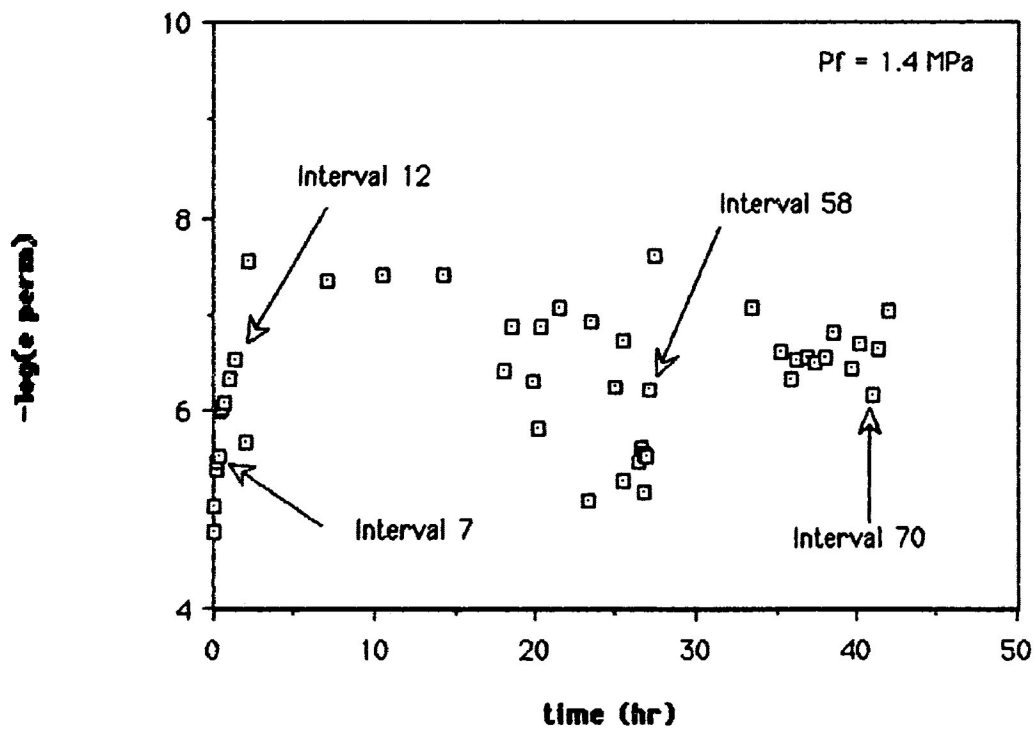


Fig. 4-39b: CQA-3 SRT; log(permanent strain rate) vs. time



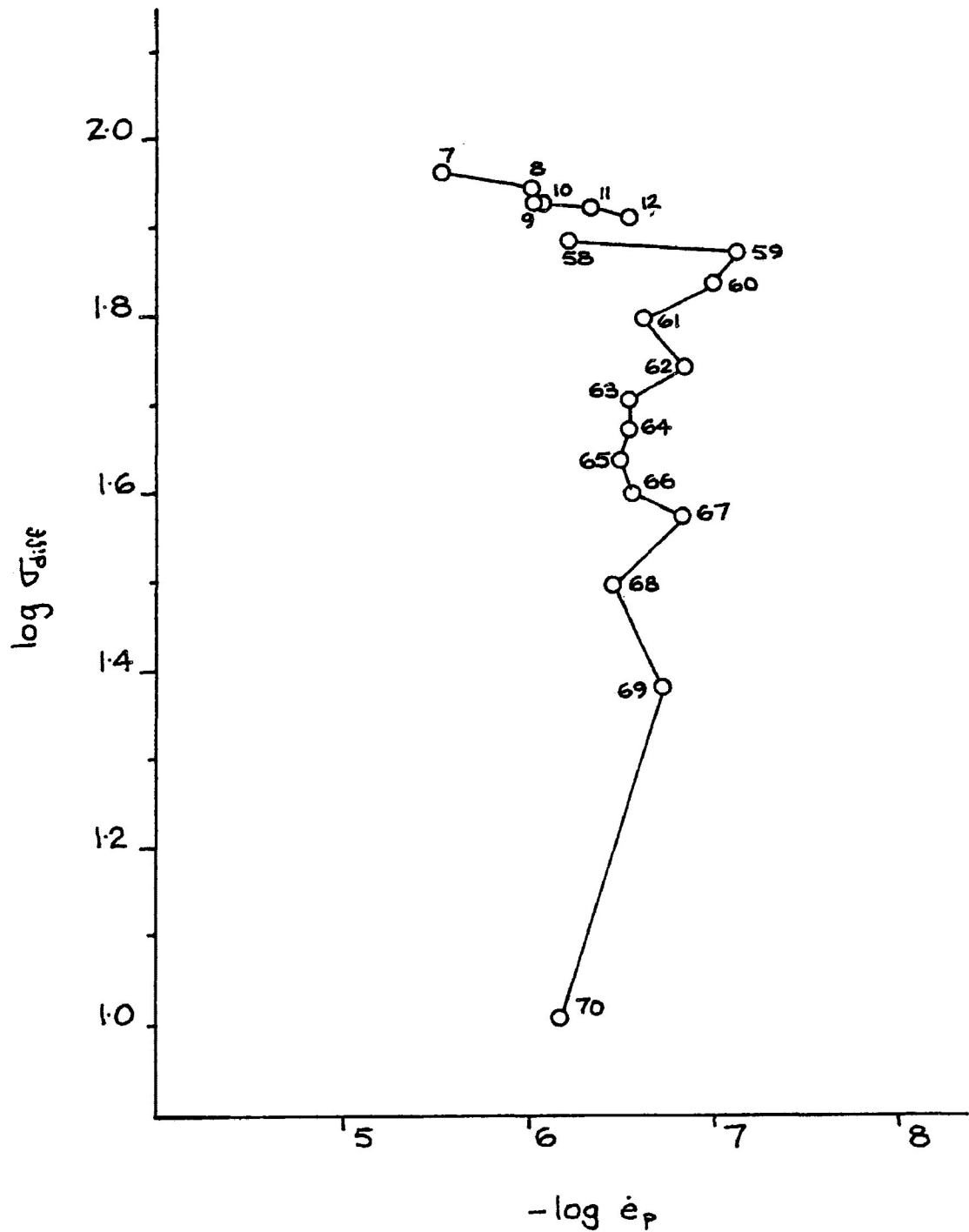


Figure 4-39c: Selected data from SRT on CQA-3. The trend over intervals 7 to 12 is apparently valid; data from intervals 58 to 70 is spurious despite a continuous drop in differential stress.

Fig. 4-40a: CQA-4 SRT; log(differential stress) vs. time

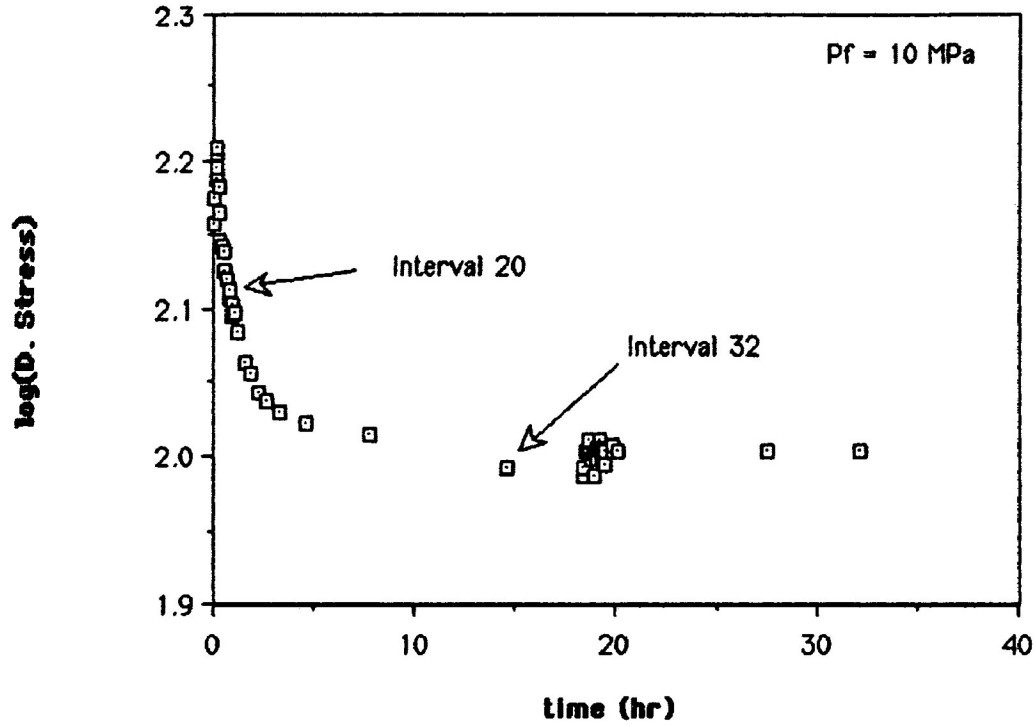
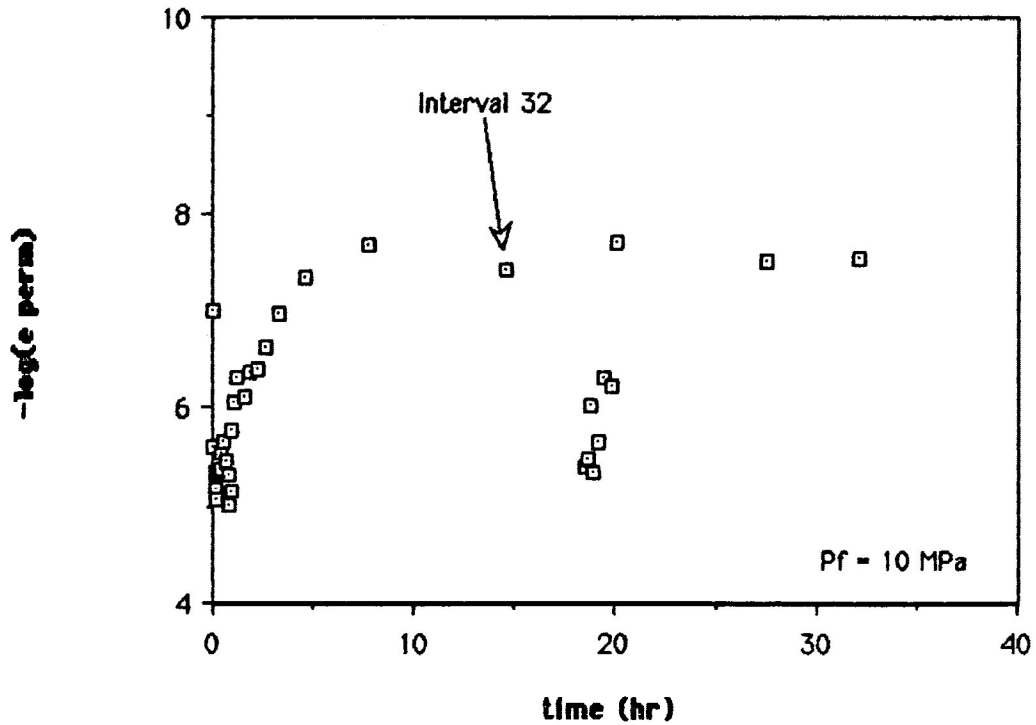


Fig. 4-40b: CQA-4 SRT; log(permanent strain rate) vs. time



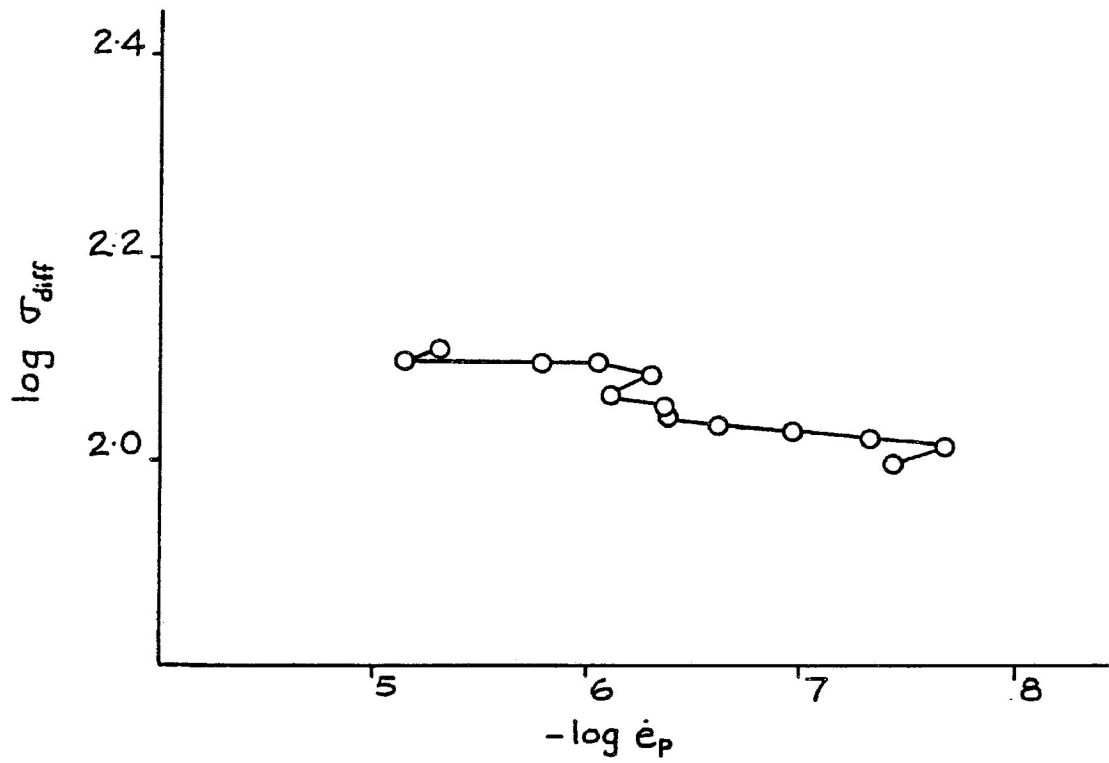


Figure 4-40c: Data showing continuous decline in differential stress during SRT on CQA-4.

lowest strain rate obtained which can be given credence is $10^{-7.7}$ s^{-1} . If not so great as to exclude PS entirely, this strain rate is almost certainly too high to permit this deformation mechanism to generate a series of points on Fig. 4-40c.

4.3.3 Discussion

The calcite-quartz samples have not deformed in a manner typical of lithified material. This is shown by the absence or imperfect development of an initial linear relationship between stress and strain (indicating elastic behavior) and the lack of local smoothness of the loading curves. This atypical bulk behavior is a reflection of grain scale deformation mechanisms. The lack of cementation suggests that substantial fractions of the total strains of samples CQA-2, 3 and 4 have been accomplished by particulate flow. Crystal plasticity, cataclasis and twinning may also have contributed to the total strain. The work-hardening of each sample (indicated by the positive slope of the stress - strain curves) shows that the net effect of these processes was to cause an overall change in microstructure. The finer scale irregularities of the loading curves also are a result of microstructural change and presumably in addition indicate short-term alternation of the dominance of competing mechanisms of deformation.

Aside from the interference of thermal fluctuation, the poor

SRT results obtained from the calcite-quartz aggregate samples are a result of the non-steady state deformation which the samples underwent. It is important to note that this style of deformation occurred at strain rates greater than 10^{-8} s^{-1} . Possibly at some lower strain rate PS could begin to operate as the sole deformation mechanism affecting such an incoherent grain aggregate. Thus the capability of detecting lower strain rates would merit a second attempt of this experimental approach.

CHAPTER 5: CONCLUSIONS

1. The operation of PS requires either greater than equilibrium radius pore space or fluid overpressures approaching the magnitude of the lithostatic load.

When local intergranular porosity has been reduced to the extent that individual pore walls have an equilibrium radius of curvature, further PS requires a new site of precipitation. Consequently diffusion must move the dissolved material a greater distance. The free enthalpy gradient, which the diffusive flux is proportional to, is greatest when precipitation occurs within void space of greater than equilibrium pore size. Diffusive flux may also be affected by conditions of the diffusion path. Stylolites, besides being a site of dissolution, may provide a preferred route for diffusive flow.

If non-equilibrium pore space is not available, precipitation may also occur along a grain contact through force of crystallization. This process is able to overcome only minimal resistance (due to either compressive stress or tensile strength of the material). This condition implies that PS requires high fluid pressure for precipitation to occur along intergranular contacts or, more commonly, extension fractures. The difference in normal stress between the site of dissolution (grains along a stylolite)

and the site of precipitation (an extension fracture) is approximately the bulk differential stress. This difference will tend to be less than the difference in normal stress between grain contacts and pore walls when pores are greater than equilibrium size because of stress concentration. Furthermore, in the case of grain scale diffusion, lower pore pressure will result in greater effective stresses across grain contacts. The lower difference in normal stress between stylolites and fractures will result in a lower strain rate because the free enthalpy gradient is closely related to the stress gradient. Heightening the contrast between gradients in the two situations are the different diffusion distances. In the presence of greater than equilibrium size pores, diffusion distances range up to one half of a grain contact diameter while for stylolites, diffusion may move material several tens of centimetres. Apparently this does not present a problem; the cogenetic development of stylolites and extension fractures (Fletcher and Pollard, 1981) indicates that shortening by PS is able to occur while the effective minimum principal stress is equal to the tensile strength of the rock. At present, it is not known whether dissolution, diffusion or precipitation is the controlling process in this situation, nor what factors may affect the process.

2. Carrara marble does not undergo steady state flow under the experimental conditions of loading.

This is in agreement with Rutter (1974) who found that the lowest temperature at which steady state flow was induced in Carrara marble was 400°C. Rutter found that at 200°C and lower, Carrara marble would work harden while loading.

3. For a sample undergoing stress relaxation to experience a continuous decline in permanent strain rate, the sample must, prior to the initiation of stress relaxation, undergo steady state loading.

Steady state loading corresponds to a constant microstructure. Loading at a constant strain rate and constant differential stress indicates that the rate of the grain scale process(es) by which the sample strains is also constant. This implies that microstructure of the sample - described by grain size, shape, crystallographic fabric and internal grain structure - is constant as well. A SRT begun under this condition thus will be testing the equilibrium response of the sample to a gradual decline in differential stress. Data obtained from such a test will indicate the continuous decline of permanent strain rate and may be interpreted in the conventional manner (cf. Guiv and Pratt, 1964).

4. A sample which work-hardens during loading prior to a SRT will display the phenomenon of "cycling" during a SRT. Cycling refers to the alternating increase and decrease of permanent strain rate while differential stress continuously declines.

During non-steady state flow, microstructure and the deformation processes which determine the microstructure are changing. This change continues if a SRT is begun during non-steady state flow. Results from the SRTs on Carrara marble show that the variable microstructure results in the alternating increase and decrease of permanent strain rate. It is perhaps significant to understanding this phenomenon that strain rate tends nevertheless to decline overall, and that this process of alternation occurs over very small strains. The occurrence of cycling results in a non-linear trend of consecutive data on a graph of $\log(\text{differential stress})$ vs. $\log(\text{permanent strain rate})$, and defies conventional analysis.

5. Temperature fluctuation is a serious obstacle in experimental investigation of deformation at low strain rates.

Experimental deformation machines, such as the Donath triaxial rig used in this study, are made of steel. Because steel has a relatively high thermal expansion coefficient, these deformation machines are subject to appreciable dimensional

instability. This instability hinders accurate determination of lower permanent strain rates (approaching 10^{-9} s^{-1} on the Donath apparatus). Because the strains produced in the laboratory are so small at the lower strain rates, a minimum measured displacement of the sample and machine is required. This guarantees a continued level of accuracy but there are two associated drawbacks. One is that measurements of strain take longer to complete as strain rate falls, and eventually become impracticable on account of their length. The second difficulty is that as measurement intervals increase, there is a greater possibility of ambient temperature change with an accompanying dimensional change in the machine. Experience has shown that for the present apparatus, temperature of the pressure vessel must be held to within $\pm 1^\circ\text{C}$ for SRTs to give satisfactory values of permanent strain rate as low as $10^{-8.5} \text{ s}^{-1}$.

6. Experimental determination of PS strain rates requires materials which are susceptible to rapid deformation by PS.

The lack of success in producing PS during the SRTs is attributable to a combination of two things: machine limitations and material behavior. The Donath rig is at present restricted to detection of permanent strain rates greater than 10^{-9} s^{-1} , and natural materials will tend to pressure solve at lower strain rates. Experimental success will thus require a material which

will deform rapidly by PS. PS strain rates may be maximized by using a material which is fine grained with greater than equilibrium radius pores, by choosing a grain material which is relatively susceptible to PS, by using high intergranular contact pressures, and by using materials such as clay which will hasten the rate of dissolution and/or diffusion along the intergranular boundary. Composition of the interstitial fluid will also affect strain rate, but this variable appears to be a secondary influence on strain rate.

REFERENCES

- Alford, C.S. 1988. "Tectonic" magnetic fabrics in pure and simple shear: experimental investigations. M.Sc. thesis, Lakehead University.
- Ashby, M.F. 1972. A first report on deformation mechanism maps. *Acta Metall.* **20**, 887-897.
- Ashby, M.F., and Verall, R.A. 1973. Diffusion-accomodated flow and superplasticity. *Acta Metall.* **21**, 149-163.
- Ashby, M.F., Ghandi, C. and Taplin, D.M.R. 1979. Fracture-mechanism maps and their construction for F.C.C. metals and alloys. *Acta Metall.* **27**, 699-729.
- Atkinson, B.K. 1982. Subcritical crack propagation in rocks: theory, experimental results and applications. *J. Struct. Geol.* **4**, 41-56.
- Atkinson, B.K. and Rutter, E.H. 1975. "Pressure solution" or indentation?: Comment. *Geology* **3**, 477-478.

- Baker, P.A., Kastner, M., Byerlee, J.D. and Lockner, D.A. 1980. Pressure solution and hydrothermal recrystallization of carbonate sediments - an experimental study. *Mar. Geol.* **38**, 185-203.
- Bayly, B. 1987. Nonhydrostatic thermodynamics in deforming rocks. *Can. J. Earth Sci.* **24**, 572-579.
- Beach, A. 1974. A geochemical investigation of pressure solution and the formation of veins in a deformed greywacke. *Contr. Mineral. Petrol.* **46**, 61-68.
- 1979. Pressure solution as a metamorphic process in deformed terrigenous sedimentary rocks. *Lithos* **12**, 51-58.
- Becker, G. F. and Day, A.L. 1905. The linear force of growing crystals. *Proc. Wash. Acad. Sci.* **7**, 283-297.
- Bloss, F. D. 1954. Microstylolites in a rhyolite porphyry. *J. sed. Petrol.* **24**, 252-254.
- Borg, I., Friedman, M., Handin, J. and Higgs, D.V. 1960. Experimental deformation of St. Peter sandstone: a study of cataclastic flow. In Rock Deformation; D. Griggs and J. Handin,

- eds. Geol. Soc. Am. Mem. 79, 133-192.
- Borradaile, G.J. 1981. Particulate flow of rock and the formation of cleavage. *Tectonophysics* **72**, 305-321.
- Bosworth, W. 1981. Strain-induced preferential dissolution of halite. *Tectonophysics* **78**, 509-525.
- Brace, W.F. 1968. The mechanical effects of pore pressure on fracturing of rocks. In Proceedings, Conference on research in tectonics; A.J. Baer and D.K. Norris, eds. Geol. Surv. Can. Pap. 68-52, p.113-123.
- Burger, H.R. 1975. "Pressure solution" or indentation?: Comment. *Geology* **3**, 294.
- Cook, N.G.W. 1981. Stiff testing machines, stick-slip sliding and the stability of rock deformation. In Mechanical Behavior of Rocks; N. L. Carter, ed. Am. Geophys. Union, Geophys. Monogr. 24, 93-102.
- Correns, C.W. 1949. Growth and dissolution of crystals under linear pressure. *Discuss. Faraday Soc.* **5**, 267-271.

Davis, J.C. 1986. Statistics and Data Analysis in Geology, 2nd ed.
John Wiley, New York. 646p.

de Boer, R.B. 1975. Influence of pore solutions on rock strength
with emphasis on pressure solution. Ph.D. thesis, State
University of Utrecht (The Netherlands); 119p.

----- 1977. Pressure solution: theory and experiments.
Tectonophysics **39**, 287-301.

Deelman, J.C. 1975. "Pressure solution" or indentation? *Geology*
3, 23-24.

Deer, W.A., Howie, R.A. and Zussman, J. 1966. An Introduction to
the Rock Forming Minerals. Longman Group, London. 528 p.

Donath, F.A. and Fruth, L.S. 1971. Dependence of strain rate
effects on deformation mechanisms and rock type. *J. Geol.* **79**,
347-371.

Dorn, J.E. 1957. The spectrum of activation energies for creep. In
Creep and recovery. Am. Soc. for Metals, Cleveland, Ohio, p.259.

Durney, D.W. 1972. Solution-transfer, an important geological

deformation mechanism. *Nature* **235**, 315-317.

----- 1976. Pressure-solution and crystallization deformation.
Phil. Trans. R. Soc. Lond. **A283**, 229-240.

Elliot, D. 1973. Diffusion flow laws in metamorphic rocks. *Geol. Soc. Am. Bull.* **84**, 2645-2664.

Engelder, T. 1982. A natural example of the simultaneous operation of free-face dissolution and pressure solution. *Geochim. cosmochim. Acta* **46**, 69-74.

Ernst, W.G. and Blatt, H. 1964. Experimental study of quartz overgrowths and synthetic quartzites. *J. Geology* **72**, 461-469.

Etheridge, M.A. 1983. Differential stress magnitudes during regional deformation and metamorphism: upper bound imposed by tensile fracturing. *Geology* **11**, 231-234.

Ferguson, C.C. 1983. Composite flow laws derived from high temperature experimental data on limestone and marble. *Tectonophysics* **95**, 253-266.

Fletcher, R.C. 1982. Coupling of diffusional mass transport and

deformation in a tight rock. *Tectonophysics* **83**, 275-291.

Fletcher, R.C. and Pollard, D.D. 1981. Anticrack model for pressure solution surfaces. *Geology* **9**, 419-424.

Frank, F.C. 1965. On dilatancy in relation to seismic sources. *Rev. Geophys.* **3**, 484-503.

Fyfe, W.S. 1976. Chemical aspects of rock deformation. *Phil. Trans. R. Soc. Lond.* **A283**, 221-228.

Ghandi, C. and Ashby, M.F. 1979. Fracture mechanism maps for materials which cleave: F.C.C., B.C.C. and H.C.P. metals and ceramics. *Acta Metall.* **27**, 1565-1602.

Goldring, H.G. and Conolly, J.R. 1962. Stylolites in volcanic rocks. *J. sed. Petrol.* **32**, 534-538.

Gratier, J.P. and Guiguet, R. 1986. Experimental pressure solution-deposition on quartz grains: the crucial effect of the nature of the fluid. *J. Struct. Geol.* **8**, 845-856.

Gray, D.R. 1979. Geometry of crenulation-folds and their relationship to crenulation cleavage. *J. Struct. Geol.* **1**,

187-205.

----- 1981. Compound tectonic fabrics in singly folded rocks from southwest Virginia, U.S.A. *Tectonophys.* **78**, 229-248.

Gray, D.R. and Durney, D.W. 1979. Crenulation cleavage differentiation: implications of solution-deposition processes. *J. Struct. Geol.* **1**, 73-80.

Green, H.W. 1981. On the thermodynamics of non-hydrostatically stressed solids. *Philos. Mag. A* **41**, 637-647.

----- 1984. "Pressure solution" creep: some causes and mechanisms. *J. Geophys. Res.* **89**, B6, 4313-4318.

Gulu, F. and Pratt, P.L. 1964. Stress relaxation and the plastic deformation of solids. *Physica status. solidi* **6**, 111-120.

Hart, E.W. 1979. Load relaxation testing and material constitutive relations. In *Stress Relaxation Testing*, ASTM STP 676; Alfred Fox, ed. American Society for Testing and Materials, 5-20.

Heald, M.T. 1956. Cementation of Simpson and St. Peter sandstones in parts of Oklahoma, Arkansas, and Missouri. *J.*

Geol. **64**, 16-30.

Heald, M.T. and Renton, J.J. 1966. Experimental study of sandstone cementation. *J. Sed. Petrol.* **36**, 977-991.

Heard, H.C. and Raleigh, C.B. 1972. Steady-state flow in marble at 500° to 800°C. *Geol. Soc. Am. Bull.* **83**, 935-956.

Kerrich, R. 1978. An historical review and synthesis of research on pressure solution. *Zbl. Geol. Palaont. Teil I* **5/6**, 512-550.

Kerrich, R., Beckinsale, R.D. and Durham, J.J. 1977a. The transition between deformation regimes dominated by intercrystalline diffusion and intracrystalline creep evaluated by oxygen isotope thermometry. *Tectonophys.* **38**, 241-257.

Kerrich, R., Fyfe, W.S., Gorman, B.E. and Allison, I. 1977b. Local modification of rock chemistry by deformation. *Contrib. Mineral. Petrol.* **65**, 183-190.

Kerrich, R., Beckinsale, R.D. and Shackleton, N.J. 1978. The physical and hydrothermal regime of tectonic vein systems: evidence from stable isotope and fluid inclusion studies. *N. Jb. Miner. Abh.* **131**, 225-239.

- Knipe, R.J. 1981. The interaction of deformation and metamorphism in slates. *Tectonophys.* **78**, 249-272.
- Knipe, R.J. and White, S.H. 1977. Microstructural variation of an axial plane cleavage around a fold - a H.V.E.M. study. *Tectonophys.* **39**, 355-380.
- Langdon, T.G. and Mohamed, F.A. 1978. A simple method of constructing an Ashby-type deformation mechanism map. *J. Mat. Sci.* **13**, 1282-1290.
- Le Chatallier, H. 1892. Über das Gleichgewicht chemischer Systeme bei ungleichförmigen Druck. *Z. Phys. Chem.* **9**, 335-338.
- Lerbekmo, J.F. and Platt, R.L. 1962. Promotion of pressure-solution of silica in sandstones. *J. Sed. Petrol.* **32**, 514-519.
- Maxwell, J.C. 1960. Experiments on compaction and cementation of sand. In Rock Deformation; D. Griggs and J. Handin, eds. *Geol. Soc. Am. Mem.* **79**, 105-132.
- McClay, K.R. 1977. Pressure solution and Coble creep in rocks and

- minerals: a review. *J. geol. Soc. Lond.* **134**, 57-70.
- Miller, I. and Freund, J.E. 1985. Probability and statistics for engineers, 3rd ed. Prentice-Hall, New Jersey, U.S.A., 530 p.
- Mohamed, F.A. and Langdon, T.G. 1974. Deformation mechanism maps based on grain size. *Met. Trans.* **5**, 2339-2345.
- Nelson, R.A. 1983. Localization of aggregate stylolites by rock properties. *Am. Assoc. Petrol. Geol. Bull.* **67**, 313-322.
- Nicolas, A. and Poirier, J.-P. 1976. Crystalline plasticity and solid state flow in metamorphic rocks. J. Wiley, New York, 444 p.
- Ostapenko, G.T. 1968. Recrystallization of minerals under stress. *Geochem. Int.* **12**, 126-135.
- Park, W.C. and Schot, E.H. 1968. Stylolites: their nature and origin. *J. Sed. Petrol.* **38**, 175-191.
- Paterson, M.S. 1973. Nonhydrostatic thermodynamics and its geologic applications. *Rev. Geophys. Space Phys.* **11**, 355-389.

- 1976. Some current aspects of experimental rock deformation. Phil. Trans. R. Soc. Lond. **A283**, 163-172.
- 1978. Experimental rock deformation. Springer-Verlag, 254 p.
- Poynting, J.H. 1881. Change of state: solid - liquid. Philos. Mag. **12**, 33-48.
- Raj, R. 1982. Creep in polycrystalline aggregates by matter transport through a liquid phase. J. Geophys. Res. **87**, B6, 4731-4739.
- Raj, R. and Ashby, M.F. 1972. On grain boundary sliding and diffusional creep. Metall. Trans. **2**, 1113-1127.
- Raj, R. and Chyung, C. 1981. Solution precipitation creep in glass ceramics. Acta Metall. **29**, 159-166.
- Raleigh, C.B. 1965. Glide mechanisms in experimentally deformed materials. Science **150**, 739-741.
- Ramsay, J.G. 1967. Folding and fracturing of rocks. McGraw-Hill, New York, 568 p.

- 1977. Pressure solution - the field data. *J. geol. Soc. Lond.* **134**, 72.
- Readey, D.W. and Cooper, A.R. 1966. Molecular diffusion with a moving boundary and spherical symmetry. *Chem. Eng. Sci.* **21**, 917-922.
- Renton, J.J., Heald, M.T. and Cecil, C.B. 1969. Experimental investigation of pressure solution of quartz. *J. Sed. Petrol.* **39**, 1107-1117.
- Riecke, E. 1894. Über das Gleichgewicht zwischen einem festen homogenen Deformationskörper und einer flüssigen Phase, insbesondere über die Depression des Schmelzpunktes durch einseitige Spannung. *Nachr. Ges. Wiss. Math.-Phys. Göttingen* **49**, 278-284.
- 1912. Zur Erniedrigung des Schmelzpunktes durch einseitigen Zug oder Druck. *Zbl. Miner. Geol. Palaont.* **22**, 97-104.
- Robin, P.-Y.F. 1978. Pressure solution at grain-to-grain contacts. *Geochim. Cosmochim. Acta* **42**, 1383-1389.

- Russell, G. A. 1935. Crystal growth and solution under local stress. *Am. Mineral.* **20**, 733-737.
- Rutter, E.H. 1974. The influence of temperature, strain rate and interstitial water in the experimental deformation of calcite rocks. *Tectonophysics* **22**, 311-334.
- 1976. The kinetics of rock deformation by pressure solution. *Phil. Trans. R. Soc. London, Ser. A*, **283**, 203-219.
- 1983. Pressure solution in nature, theory and experiment. *J. geol. Soc. London* **140**, 725-740.
- Rutter, E.H., Atkinson, B.K. and Mainprice, D.H. 1978. On the use of the stress relaxation testing method in studies of the mechanical behavior of geological materials. *Geophys. J. R. astr. Soc.* **55**, 155-170.
- Rutter, E.H. and Mainprice, D.H. 1978. The effect of water on stress relaxation of faulted and unfaulted sandstone. *Pageoph* **116**, 634-654.
- Schmid, S.M. 1976. Rheological evidence for changes in the

deformation mechanism of Solnhofen limestone towards low stresses. *Tectonophysics* **31**, T21-T28.

Schmid, S.M., Boland, J.N. and Paterson, M.S. 1977. Superplastic flow in finegrained limestone. *Tectonophysics* **43**, 257-291.

Schmid, S. M., Paterson, M. S. and Boland, J. N. 1980. High temperature flow and dynamic recrystallization in Carrara marble. *Tectonophysics* **65**, 245-280.

Sharp, W. E. and Kennedy, G. C. 1965. The system $\text{CaO-CO}_2\text{-H}_2\text{O}$ in the two phase region calcite and aqueous solution. *J. Geol.* **73**, 391-403.

Siever, R. 1959. Petrology and geochemistry of silica cementation in some Pennsylvanian sandstones. *Soc. Econ. Paleontologists Mineralogists, Spec. Pub.* **7**, 55-79.

Skinner, B. J. 1966. Thermal Expansion. In Handbook of Physical Constants, revised edition; S.P. Clark, Jr., ed. *Geol. Soc. Am. Mem.* **97**, 75-96.

Sorby, H.C. 1865. On impressed limestone pebbles, as illustrating a new principle in chemical geology. *West Yorks. Geol. Soc.*

Proc. **14**, 458-461.

----- 1879. Structure and origin of limestone. Q. J. Geol. Soc.,
Lond. **35**, 39-95.

----- 1880. Structure and origin of non-calcareous stratified
rocks. Q. J. Geol. Soc., Lond. **36**, 46-92.

Spring, W. 1888. The compression of powdered solids. Am. J. Sci.
36, 386-389.

Sprunt, E.S. and Nur, A. 1976. Reduction of porosity by pressure
solution: experimental verification. Geology **4**, 463-466.

----- 1977a. Experimental study of the effects of stress on
solution rate. J. Geophys. Res. **82**, 3013-3022.

----- 1977b. Destruction of porosity through pressure solution.
Geophysics **42**, 726-741.

Stocker, R.L. and Ashby, M.F. 1973. On the rheology of the upper
mantle. Rev. Geophys. Space Phys. **11**, 391-426.

Taber, S. 1916. Growth of crystals under external pressure. Am.

J. Sci. **41**, 532-556.

Thomson, J. 1862. On crystallization and liquefaction, as influenced by stresses tending to change of form in the crystals. Royal Soc. Lond. Proceedings **11**, 473-481.

Thomson, A.F. 1959. Pressure solution and porosity. In Silica in sediments; H.A. Ireland, ed. Soc. Econ. Paleontol. Min., Spec. Publ. No. 7, p. 92-110.

Weertman, J. 1968. Dislocation climb theory of steady state creep. Am. Soc. Metals Trans. **61**, 681-694.

Weyl, P.K. 1959. Pressure solution and the force of crystallization - a phenomenological theory. J. Geophys. Res. **64**, 2001-2025.

White, S. 1976a. The effects of strain on the microstructures, fabrics, and deformation mechanisms in quartzites. Phil. Trans. R. Soc. Lond. **A283**, 69-86.

----- 1976b. Estimation of strain rates from microstructural features. Q. J. Geol. Soc. Lond. **133**, 577-583.

Wright, F.E. and Hostetter, J.C. 1917. The thermodynamic reversibility of the equilibrium relations between a strained solid and its liquid. *J. Wash. Acad. Sci.* 7, 405-417.

APPENDIX A: CALCULATION OF A DEFORMATION MECHANISM MAP FOR CALCITE

There are four quantities presented on a deformation mechanism map (DMM): differential stress, strain rate, grain size and temperature (Elliot, 1973). It is possible to present these quantities in a variety of ways (see subsection 2.2.3). The maps illustrated in Chapter 2 have axes of (normalized) flow stress and reciprocal normalized temperature, and have contours of strain rate. The fourth quantity, grain size, has been held constant. For the two maps shown, grain size is 200 μm (Fig. 2-4) and 10 μm (Fig. 2-5).

Outlined below are the equations used in preparing Figures 2-4 and 5. Boundaries were found using the method outlined in subsection 2.2.3.

Pressure solution The constitutive equation used, for differential stresses less than 30 MPa, and with a substitution for the temperature and pressure dependence of calcite (Sharp and Kennedy, 1965) is (Rutter, 1976):

$$\dot{\epsilon} = 74 \sigma' D_b w C_0 (0.00006 T + 0.0075) / \rho d^3$$

where $\dot{\epsilon}$ is strain rate,

σ' is effective differential stress across the grain boundary,

D_b is the boundary diffusivity,
 w is effective grain boundary width,
 C_0 is the reference solubility of calcite in CO_2 solution at
 a reference pressure of 10^8 Pa (1 kb),
 T is absolute temperature,
 ρ is the density of calcite, and
 d is grain size.

D_b was determined with an Arrhenius relation (see solid-state diffusive creep); a value of $3.7 \times 10^{-12} \text{ m}^2\text{s}^{-1}$ was used for the standard boundary diffusivity and 13.4 kJ mol^{-1} for the activation energy (both values from Rutter, 1976). w was taken to be 2 nm, also from Rutter (1976). Values for C_0 were taken from Sharp and Kennedy (1965).

Solid-state diffusive creep A constitutive equation for diffusive creep (Nabarro-Herring creep and Coble creep) was developed by Stocker and Ashby (1973). In Rutter's (1976) notation the equation is

$$\dot{\epsilon} = \frac{21 V \sigma D_v}{R T d^2} \left(1 + \pi \frac{w D_b}{d D_v} \right) \quad (\text{A1})$$

where V is activation volume (assumed equal to molar volume),
 σ is differential stress,
 D_b and D_v are the solid-state boundary and volume diffusivities, and
 w is effective solid-state width of the grain boundary.

The bracketed term on the right-hand side of equation (A1) describes the contribution by Coble creep to the strain rate. With an assumption of equal strain rate due to both deformation mechanisms, it is possible to derive the relation describing the Nabarro-Herring creep - Coble creep boundary:

$$D_b = \frac{d D_v}{\pi w}$$

Substitution for the diffusivity terms may be made with Arrhenius relations of the form

$$D = D_0 \exp(-H/RT)$$

where D_0 is the standard diffusivity, and H is the activation energy.

Following Stocker and Ashby (1973) and Rutter (1976), assume the standard diffusivities for boundary and volume diffusion are equal. The equation obtained is

$$\frac{(H_v - H_b)}{RT} = \ln\left(\frac{d}{\pi w}\right)$$

where H_v and H_b are the activation energies of boundary and volume diffusion, respectively.

With the assumption that $H_b = 2H_v / 3$ (Stocker and Ashby, 1973; Rutter, 1976), and using a value of 250 kJ mol^{-1} for H_v (Rutter, 1976, after Heard and Raleigh, 1972), the stress-

insensitive transition temperature is 694°C for a grain size of 200 μm . While Nabarro–Herring creep and Coble creep are independent processes, they undergo a gradual transition (as shown by Stocker and Ashby's constitutive equation). For this reason, they are shown divided by a dashed rather than a solid line.

Nicolas and Poirier (1976; p. 120) have stated that H_b is usually about half the value of H_v . The boundary temperature corresponding to this relative proportion of activation energies is 1177°C.

On the DMM for 10 μm grain size, no field for simple solid-state diffusion appears. Instead, the field to the right of the PS field is for a related complex diffusional mechanism, superplasticity.

Crystal plasticity. The equations used for $d = 200 \mu\text{m}$ were flow laws taken from Schmid et al (1980). The mechanisms were described briefly in subsection 2.2.3.

Regime 1 ($\sigma > 1000 \text{ b}$):

$$\dot{\epsilon} = A \exp\left(\frac{-H}{RT}\right) \exp\left(\frac{\sigma}{\sigma_0}\right)$$

with $A = 5.9 \times 10^5 \text{ s}^{-1}$,
 $H = 62 \text{ kcal mol}^{-1}$, and
 $\sigma_0 = 114 \text{ b}$.

Regime 2 ($200 < \sigma < 1000$ b):

$$\dot{\epsilon} = A \exp\left(\frac{-H}{RT}\right) \sigma^n$$

with $A = 3.2 \times 10^{-5} \text{ (s b)}^{-1}$,
 $H = 100 \text{ kcal mol}^{-1}$, and
 $n = 7.6$.

Regime 3 ($\sigma < 200$ b):

$$\dot{\epsilon} = A \exp\left(\frac{-H}{RT}\right) \sigma^n$$

with $A = 7.9 \times 10^{+3} \text{ (s b)}^{-1}$,
 $H = 102 \text{ kcal mol}^{-1}$, and
 $n = 4.2$.

The flow laws used for the $d = 10 \mu\text{m}$ DMM were taken from Schmid *et al* (1977). These equation were fitted to data obtained from experimental deformation of Solnhofen limestone (nominal grain size $10 \mu\text{m}$). The three fields of best fit - regimes 1, 2 and 3 - are not the same as those fitted by Schmid *et al* (1980) to experimental data from Carrara marble. Regime 1 for Solnhofen limestone is not shown on Fig. 2-5 because it occurs at unnaturally high differential stresses (1900 b at 600°C).

Regime 2:

$$\dot{\epsilon} = A \exp\left(\frac{-H}{RT}\right) \sigma^n$$

with $A = 0.0468 \text{ (s b)}^{-1}$,
 $H = 71.1 \text{ kcal mol}^{-1}$, and
 $n = 4.70$.

Regime 3:

$$\dot{\epsilon} = A \exp\left(\frac{-H}{RT}\right) \sigma^n$$

with $A = 468. \text{ (s b)}^{-1}$,
 $H = 50.9 \text{ kcal mol}^{-1}$, and
 $n = 1.66$.

APPENDIX B: TREATMENT OF SRT DATA

As with a load test, two devices are monitored during a SRT on the Donath deformation apparatus: the linearly variable differential transformer (LVDT) provides a measure of ram piston displacement (D), and the load cell reading (L) is directly related to total load on the specimen. The output from both devices is used during a SRT to calculate inelastic strain rate ($\dot{\epsilon}_p$) and differential stress (σ_{diff}).

Calculation of inelastic strain rate

The relevant equation for inelastic or permanent strain rate, $\dot{\epsilon}_p$, is

$$\dot{\epsilon}_p = \frac{\Delta l_{S/p} / l_0}{\Delta t} \quad (B1)$$

where, over the particular measurement interval of the SRT, $\Delta l_{S/p}$ is displacement due to permanent sample distortion, l_0 is the initial sample length, and Δt is the interval duration.

Calculation of the inelastic strain rate may be considered in two cases.

1. Ideal SRT

Such a test is performed on an infinitely stiff machine, i.e. one which does not displace elastically under a load. Sample length thus does not change during such a SRT. In this hypothetical case, load slowly decays as sample elastic stress produces permanent strain. Over any measurement interval,

$$\Delta l_{S/p} = - \Delta l_{S/e}$$

where $\Delta l_{S/e}$ is change in sample length due to sample elasticity.

As no net displacement would occur, it would be necessary to calculate the elastic strain of the rock as the product of the rock's elastic constant and the change in load over the interval.

Calculation of $\dot{\epsilon}_p$ is then straightforward using equation (B1).

2. SRT on a machine of limited stiffness (without thermally generated distortion)

In the laboratory, the researcher must contend with elastic distortion of his deformation apparatus. This affects calculation of $\Delta l_{S/p}$. Because the LVDT measures total change of length, the following relation is written:

$$\Delta l_{total} = \Delta l_{M/e} + \Delta l_{S/e} + \Delta l_{S/p} \quad (B2)$$

where Δl_{total} is displacement recorded by the LVDT, and $\Delta l_{M/e}$ is displacement due to machine flexure.

Note that $\Delta l_{M/e} > 0$,

$$\Delta l_{S/e} > 0,$$

$\Delta l_{S/p} < 0$, and, because permanent sample strain is so great,

$$\Delta l_{total} < 0.$$

Equation (B2) may be written

$$\Delta l_{S/p} = \Delta l_{total} - \Delta l_{M/e} - \Delta l_{S/e}$$

Because the LVDT measures displacement such that shortening gives a positive value, and in order to give $\dot{\epsilon}_p$ a positive value, each quantity in equation (B2) is multiplied by -1 . The resulting equation, in the terminology of the program RIGx.BAS used to control SRT's, is

$$PD = DD - (Z + ED)$$

where $PD = -\Delta l_{S/p}$,
 $DD = -\Delta l_{total}$,
 $Z = -\Delta l_{M/e}$, and
 $ED = -\Delta l_{S/e}$.

Because sample length changes during the test, the initial sample length, l_0 , must be calculated for successive intervals:

$$(l_0)_{\text{new}} = (l_0)_{\text{previous}} + (\Delta l_{\text{total}})_{\text{previous}}$$

(The value of l_0 used for the first interval of a SRT is gotten at the end of the loading of the sample.) Program RIGx.BAS thus calculates the new initial length using the formula

$$LO_{\text{new}} = LO_{\text{previous}} - DD \quad (\text{B3})$$

Calculation of \dot{e}_p is now straightforward. In RIGx.BAS notation, equation (B1) is written

$$ISR = \frac{(PD / LO)}{DT}$$

where ISR is \dot{e}_p ,
 LO is l_0 , and
 DT is Δt

Calculation of differential stress

Differential stress, σ_{diff} , is found according to the formula

$$\sigma_{\text{diff}} = \frac{\text{axial load}}{\text{area}}$$

The RIGx.BAS program calculates differential stress, D.STRESS, using

$$D.STRESS = \frac{(LAV - LNULL) K2}{145 AR}$$

where LAV is the average of load cell outputs, in volts, at the beginning and end of the measurement interval,
 LNULL is the load cell output at zero load,
 K2 is the load cell constant (expressed in lb force / V output),
 AR is the sample cross-sectional area in in², and
 145 is the factor required to convert stress from psi to MPa

Note that AR is recalculated for each SRT measurement interval. Assumptions of volume conservation and of uniform lateral sample expansion are made in estimating the cross-sectional area according to the formula

$$AR = \frac{A_0 l_0}{l'}$$

where A_0 is the undeformed sample cross-sectional area,
 l_0 is the undeformed sample length, and
 l' is the current sample length.

The deformed sample length, l' , has the value of quantity LO_{new} in equation (B3).

APPENDIX C: DEPENDENCE OF T AND P_c DURING THE LONG-TERM HYDROSTATIC TEST

Semi-periodic variation in P_c during the long-term hydrostatic loading test was observed after incremental loading of the sample had been completed. Because this fluctuation appeared to have a diurnal cyclicity, changes in ambient temperature were suspected to be responsible. In order to test this hypothesis, a total of 82 measurements of T and P_c were taken periodically over 12 days. This data, shown graphically in Figure C-1, was then statistically analyzed. Changes in P_c were thought to have occurred after changes in T because the thermal response of the hydrostatic rig would not have been instantaneous. However, because the delays were relatively short compared to the period over which T and P_c varied, a more complicated cross-correlation analysis was rejected in favour of a simpler χ^2 test (Davis, 1986).

The particular χ^2 test used makes use of a contingency table (Table C-1). Each cell of the table contains two values: an observed frequency, O (which is the actual number of observations) and an expected frequency, E. For any cell, E is found by

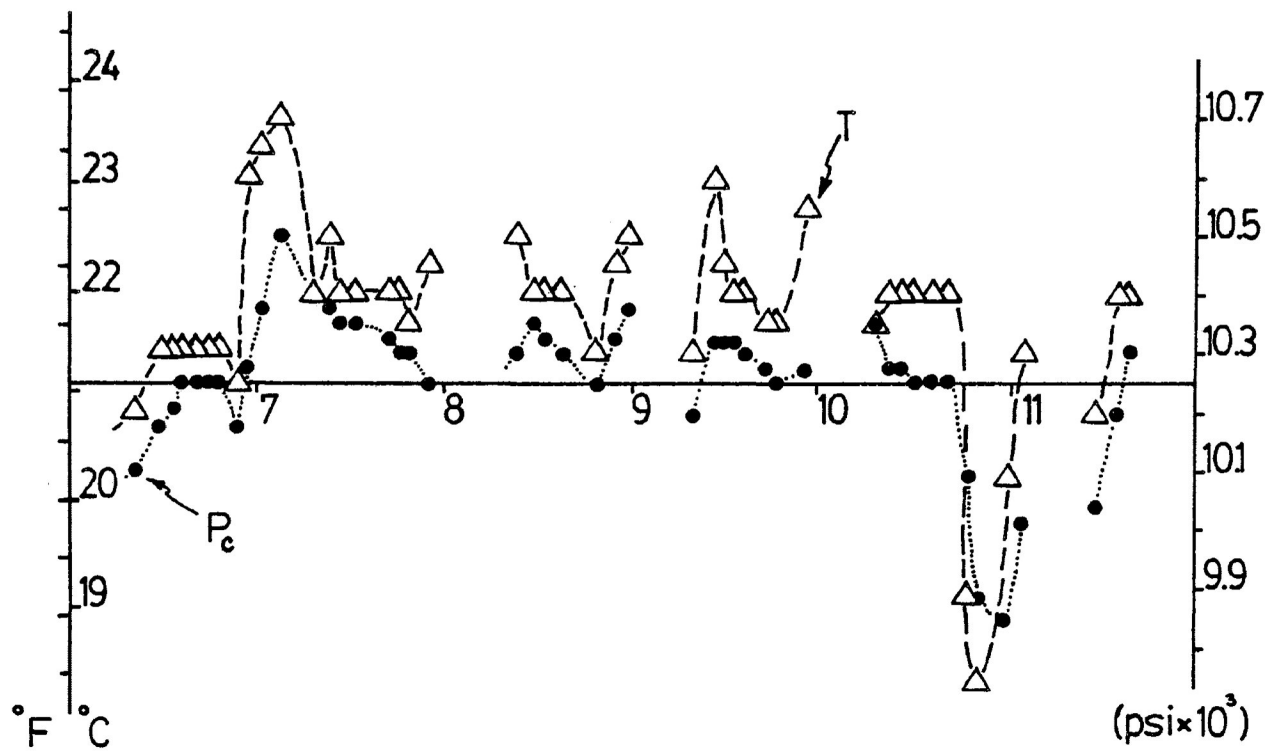
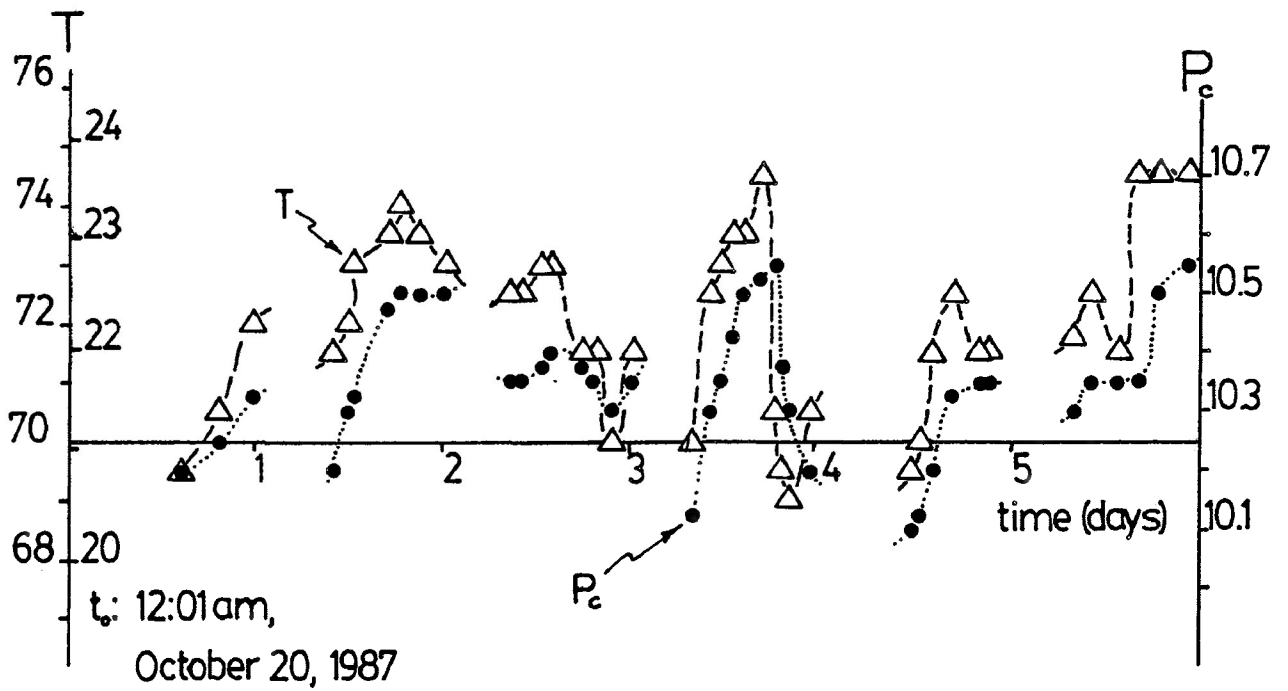


Figure C-1: Graph of hydrostatic rig pressure (solid circles) and ambient temperature (open triangles) vs. time. Data taken over 12 days after loading was complete.

Ambient Temperature, T (°F)

		Ambient Temperature, T (°F)			Total observations
		68.8 - 70.7	70.8 - 72.7	72.8 - 74.7	
Confining Pressure, Pc (psi)	10,100 - 10,299	16 7.1	11 14.9	2 7.1	29
	10,300 - 10,599	4 12.9	31 27.2	18 12.9	53
	Total observations	20	42	20	82

Table C-1: Contingency table of T-Pc data from the long-term hydrostatic test. Observation frequency, O, is in the upper left of each cell; expected frequency, E, is in the bottom right.

multiplying the total number of observations in the column containing the cell by the total number of observations in the row containing the cell and then dividing by the total number of observations in the entire table. The χ^2 statistic is the sum of the expression $(O-E)^2/E$ found for every cell in the table. Because the χ^2 statistic has only approximately a true χ^2 distribution, a standard precaution is to ensure no cell has a value of E less than 5 (Miller and Freund, 1985). Table C-1 is a condensation of an earlier table of the same data, made in order to meet this requirement.

For this test, the null hypothesis, H_0 , is that P_c and T are independent. The alternate hypothesis is that P_c and T are not independent. The number of degrees of freedom is $(3-1)(2-1) = 2$. For a level of significance, α , of 0.01, the critical value of χ^2 is 9.2 . The value of the χ^2 statistic is 27.4 . Because the statistic exceeds the critical value, H_0 is rejected (at the 1% significance level) and the conclusion is that changes in P_c are related to changes in ambient temperature.